DOE/ER/40321--10

DE93 013384

THE DECAY OF HOT NUCLEI FORMED IN LA-INDUCED REACTIONS AT E/A=45 MeV

by

Bruce Libby

Dissertation submitted to the Faculty of the Graduate School
of the University of Maryland in partial fulfillment
of the requirements for the degree of
Doctor of Philosophy
1992

Advisory Committee:

Professor Alice C. Mignerey, Chair/Advisor
Professor James Kelly
Assistant Professor Janice Reutt-Robey
Professor William B. Walters
Professor John Ondov

Work supported by the U.S. Department of Energy

Grant # DEFG05-87ER40321

ABSTRACT

Title of Dissertation: THE DECAY OF HOT NUCLEI FORMED IN LA-INDUCED REACTIONS AT E/A = 45 MeV

Bruce Libby, Doctor of Philosophy, 1992

Dissertation directed by: Professor Alice C. Mignerey, Department of Chemistry and Biochemistry

The decay of hot nuclei formed in the reactions $^{139}La + ^{27}Al, ^{51}V$, ^{nat}Cu, and ^{139}La were studied by the coincident detection of up to four complex fragments ($Z > 3$) emitted in these reactions. Fragments were characterized as to their atomic number, energy and in- and out-of-plane angles. An attempt was made to measure target-like fragments emitted to large laboratory angles, but the results were not conclusive.

The probability of the decay by an event of a given complex fragment multiplicity as a function of excitation energy per nucleon of the source is nearly independent of the system studied. Additionally, there is no large increase in the proportion of multiple fragment events as the excitation energy of the source increases past 5 MeV/nucleon. This is at odds with many prompt multifragmentation models of nuclear decay. Correlation functions of the relative velocity and angle between pairs of fragments in events with 3 complex fragments are similar to those of other reactions in which a sequential mechanism for the emission has been proposed. There is also some evidence

that a fast-fission reaction mechanism may be occurring in the reaction La + Al (and possibly La + V). This is indicated by the well characterized binary decay of the source and anisotropic angular distributions of the emitted fragments.

The reactions $^{139}La + ^{27}Al$, ^{51}V, and ^{nat}Cu were also studied by combining a dynamical model calculation that simulates the early stages of nuclear reactions with a statistical model calculation for the latter stages of the reactions. For the reaction $^{139}La + ^{27}Al$, these calculations reproduced many of the experimental features, such as fragment cross sections, and total charge and source velocity distributions for multiple fragment events. Other features, such as charge-Dalitz plots and branching ratios of the multiple fragment events were not reproduced. For the reaction $^{139}La + ^{51}V$, the shape of the fragment cross section distribution, and the total charge and source velocity distributions were reproduced by the model. However, the calculation failed to reproduce the magnitude of the cross sections, charge-Dalitz plots, and branching ratios.

The calculation failed to reproduce any of the experimental features of the reaction $^{139}La + ^{nat}Cu$, with the exception of the source velocity distributions. This indicates that the early stages of the reaction are being well represented by the dynamical calculations, but not the fragmentation stage. In central collisions, there is some indication that multifragmentation may be occurring in the dynamical calculations, but the mechanism of this multifragmentation is still unclear.

ACKNOWLEDGEMENTS

There are many people who helped make this work possible. First and foremost, I would like to thank my advisor, Dr. Alice Mignerey, for providing the support, both financial and moral, that enabled me to complete this thesis. I also would like to thank my collaborators at Berkeley who helped perform the experiment that this thesis is based on. Special consideration has to go to Dr. Gordon Wozniak, who always seemed to be able to squeeze more money out of the budget of the Nuclear Science Division at LBL to enable me to spend a considerable portion of my graduate school career at Berkeley.

I would also like to thank my family and friends for their support as I continually whined about the trials and tribulations of a graduate student. Special thanks go to Gudrun Kleist, Dori Johnson and Johnny and Ginger Gibbons.

Finally, I would like to thank Bob Dylan for his continuing inspiration.

TABLE OF CONTENTS

LIST OF FIGURES

LIST OF TABLES

CHAPTER I INTRODUCTION

I.A INTERMEDIATE MASS FRAGMENT EMISSION - AN OVERVIEW

Early studies of nuclear reactions led to their classification by different models which depended on the projectile energy and the impact parameter. In central collisions at low energies, the projectile interacts with the entire target, leading to fusion and the formation of a compound nucleus. The compound nucleus then decays by the emission of light particles (protons, neutrons, and alpha particles) or by fission (for heavy compound nuclei). In peripheral reactions, the projectile interacts only with a portion of the target. These nucleons can then be emitted, or transfer their relative kinetic energy to the rest of the target nucleus. The target can then de-excite by the emission of light particles, leading to a heavy target-like residue. The excited target can also fission if it is heavy.

Intermediate mass fragments (IMF's), with masses between those of alpha particles and fission fragments, were first detected radiochemically in high energy proton-induced reactions (WOL56, CAR58, CUM64). These fragments bore no obvious genetic relationship to either the projectile or target, and a variety of mechanisms were proposed for the production of IMF's. These mechanisms included fragmentation (WOL56, CAR58) and fission (CUM64) of the target. As experiments with electronic counters began to study nuclear reactions, IMF's with Z up to 20, including neutron rich isotopes such as ^{11}Li, ^{15}B, and ^{17}C, were detected (POS71, HYD71). In these reactions, a two-step reaction mechanism was proposed. In the first step, the proton interacts with the individual nucleons

of the target, leading to the emission of nucleons and even small clusters. During the second stage, equilibrium is reached and the excitation energy is dissipated by fission or evaporation of light particles.

At this time, the descriptions of the mechanisms of nuclear reactions were clearly defined as either being low energy or high energy mechanisms. In low energy mechanisms (E/A<10 MeV), the projectile and target see each other as a whole, so that the mechanisms are described using mean field effects. On the other hand, high energy mechanisms (E/A>100 MeV) are described using nucleon-nucleon interactions. The exit channels range from binary (two fragments) at low energy to many body at high energy. At some point, called the intermediate energy region, there should be a transition from low energy to high energy mechanisms. The production of IMF's at intermediate energy has been thought to provide a signal of this transition in reaction mechanisms.

As experiments produced more and more IMF's, theories arose to explain their presence. In one model, the emission of IMF's was considered to be due to the asymmetric fission of a compound nucleus. This was just an extension of the general theory of fission to the mass asymmetry coordinate (MOR75). In other words, light particle evaporation and symmetric fission of a compound nucleus could be considered to be the extreme cases of a single compound nucleus decay mechanism. It was also proposed that IMF's could be emitted by a hot nuclear "fireball" formed by the overlap region of target and projectile in peripheral collisions at bombarding energies up to several hundred MeV/nucleon or more (WES76, JAC83, JAC85). In this prescription, nucleons emitted close to each other in space are said to coalesce into fragments, with masses as high as fourteen.

While many new explanations arose for the increased presence of IMF's at intermediate energies, it was also clear that lower energy mechanisms, such as

compound nucleus decay, continued to play an important role at intermediate energies (CHA88a, CHA88b, BOW87, BOW89, BOW91b). What made matters even more confusing was the explanation of the data in the reaction La + C at E/A=50 MeV (BOW87, BOW89, BOW91b) by a dynamical model (PI91) and a statistical multifragmentation model (GRO88). These model calculations may or may not be consistent with the incomplete fusion-compound nucleus mechanism for this reaction proposed by Bowman (BOW87, BOW89, BOW91b). Using a multifragmentation model, Gross (GRO88) reproduced many of the experimental features of this reaction, such as fragment cross sections and fragment-fragment correlations. In this calculation, only two IMF's and several H and He isotopes were produced, which many would not consider true multifragmentation. However, the important consideration is the simultaneous production of all fragments (both IMF's and light particles), which showed that the conclusion that Bowman reached of statistical decay of a compound nucleus formed in this reaction is not definitive. The simulation of this reaction by a dynamical calculation allowed the conclusion that an incomplete fusion product in this reaction reaches thermal equilibrium, which is a result that Bowman reached and an assumption of Gross's model (PI91). However, the dynamical calculation performed cannot account for the emission of fragments due to statistical processes.

The experimental and theoretical study of the reaction La + C at E/A=50 MeV shows how foggy the picture of nuclear decay can be in this energy region. In the study of the reaction Ca + Ca at E/A=35 MeV, for example, the multiple fragment events were successfully interpreted by using both a sequential model that treated expansion of the source and a multifragmentation model (HAG92).

For multifragmentation, emission of fragments should be isotropic in the center of mass, so the envelope of the energy flow should be spherical in shape. On the other hand, sequential decay should lead to an elongated event shape due to the kinematical constraints of sequential decay and the time between subsequent decays. Event shape analysis of the reaction Ar + V at bombarding energies from E/A = 35 to 85 MeV showed that there is some evidence for the onset of multifragmentation as the bombarding energy is increased, because the event shape becomes more spherical (CEB90). However, the lack of a clear transition indicated that there may be a competition between sequential and prompt decay channels.

On the other hand, study of the reaction Ne + Au at E/A = 60 MeV led to the conclusion that multifragmentation was not occurring. This conclusion was based on comparing the relative velocities and angles between pairs of fragments produced in events with three IMF's to simultaneous and sequential decay simulations. (BOU89) The time scale between the subsequent emission stages in this reaction was found to be fairly short. Time scale analysis for the emission of complex fragments in the reaction Ar + Au at E/A = 35 MeV reached a similar conclusion (KIM91). As the time between the emission of IMF's decreases in a sequential mechanism, the signature, such as the event shape, of the mechanism may become more like the signature of multifragmentation. This can lead to erroneous conclusions concerning the decay mechanism.

It is clear that the mechanism for the production of IMF's is still a question of great concern to researchers, and has not been clarified (and has possibly become more confused) by experimental studies over the past ten years. These experiments have shown that it is possible to produce highly excited nuclei in heavy-ion reactions at intermediate energy. A nucleus can accommodate only a

certain amount of excitation energy (around 8 MeV/nucleon, the average binding energy of a nucleon in the nucleus) before it will completely disintegrate into its constituent protons and neutrons. This limiting excitation energy is thought to be somewhat lower than 8 MeV/nucleon, because of the formation of clusters of nucleons (IMF's).

In the experimental studies discussed, the hot nuclei may have been produced in a region of excitation energy in which there is a competition between decay channels. This competition can be illustrated by examining Figure I.1 (BON85). In this figure, the term T near the different lines (for different decay processes) refers to the nuclear temperature. The temperature T is a parameterization of the excitation energy and is equal to $(E^*/a)^{1/2}$, in which E^* is the excitation energy of the nucleus and a is the level density parameter (usually taken to be A/8 to A/10, where A is the mass of the nucleus).

As shown in Figure I.1, fragments in the mass range of less than $A_o/2$ can be produced by several different mechanisms, including competition between fission-like and fragmentation processes. The onset of fragmentation occurs at temperatures of about 4 MeV, while threshold for the domination of the IMF cross section by fragmentation is about 7 MeV, which corresponds to an excitation energy of about 5 MeV/nucleon. In other words, there should be a sharp increase in the cross section for fragments lighter than fission fragments and the probability of multiple fragment events as the excitation energy increases past 5 MeV/nucleon. As the temperature increases even higher, to 15 MeV, the nucleus completely vaporizes into its constituent nucleons.

This onset of multifragmentation at temperatures around 7 MeV has been linked to a possible liquid-vapor phase transition near the critical temperature in nuclear matter (PAN84, LEV85). The nucleon-nucleon interaction is repulsive at

Figure I.1: Schematic diagram of nuclear decay processes that can occur at intermediate energies. N_A is the yield (in arbitrary units) and A_O is the mass of the nucleus studied. The scale of N_A is logarithmic (BON85).

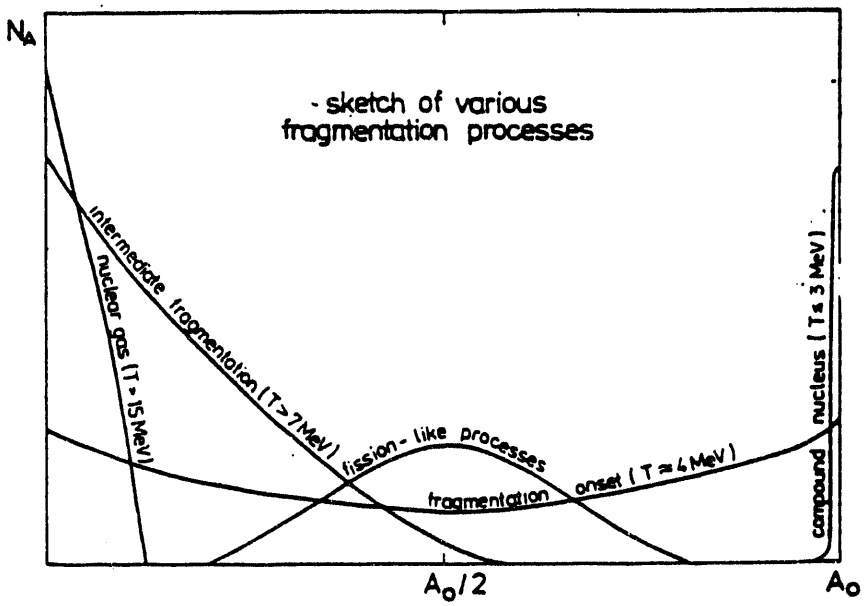
N_A
- sketch of various
fragmentation processes
intermediate fragmentation (T > 7 MeV)
nuclear gas (T ≈ 15 MeV)
fission - like processes
fragmentation
onset (T ≈ 4 MeV)
compound nucleus (T ≤ 3 MeV)
$A_o/2$
A_o

short distances (less than 0.5 fm) and attractive at longer distances (up to 2-3 fm). This is similar to the behavior of atoms in a van der Waal's gas. Because of this, it is thought that nuclear matter can exhibit a phase transition from liquid to vapor at excitation energies readily attainable at intermediate energy (GEL87). This type of mechanism was proposed when it was observed that the mass distribution of IMF's in some nuclear reactions followed a power law dependence $P(A) \propto A^{-k}$, in which P(A) is the probability of emitting a fragment of mass A and k is the critical exponent, with values ranging from 1.5 to 4 (PAN84). The critical exponent is equal to 2.33 for a van der Waal's gas.

However, a power law mass distribution is not unique to a phase transition. This type of mass distribution has also been predicted by percolation models, in which a nucleus is considered to be a composite of nucleons on a lattice, connected by bonds. Excitation of the nucleus leads to a breaking of some of the bonds, with subsequent fragment formation (MOR88). Additionally, sequential decay calculations of a mass 100 nucleus at temperatures ranging from 6 to 20 MeV also produced a power law distribution of the fragment mass for small (A<30) fragments (MOR88). Percolation, sequential decay, and liquid-vapor phase transitions can all be considered to be statistical decay models. The power law mass distribution may then be a feature of all statistical decay models, not any particular one.

It is also possible to explain IMF formation through the use of dynamical models. During nuclear reactions, severely deformed and/or compressed nuclei may be produced. Dynamical fluctuations can then lead to some type of multifragmentation. A pancake-shaped system can undergo Rayleigh-Taylor-like surface instabilities. These instabilities are caused by the interactions between the two surfaces of the pancake. Spherical fragments then form because of the

reduction in the surface energy of the system (as opposed to the high surface energy of the pancake) (MOR92). A compressed nucleus can also undergo some type of expansion. This expansion is likely to be isentropic, and internal energy (or excitation energy) will be converted into translational kinetic energy. If the nucleus then enters a region of dynamical instability, it will fragment (BER83, LOP84).

This experimental and theoretical work can be summarized as a series of interrelated research problems. These questions include:

1) What is the maximum excitation energy that a nucleus can accommodate?

2) Do these highly excited nuclei decay into several fragments sequentially or simultaneously?

3) Are the decay processes due to dynamical (non-equilibrium) or statistical (equilibrium) considerations, or a combination of the two?

4) Is there a smooth evolution in the mechanism of IMF emission as the bombarding energy and/or the mass of the system is increased, or is there an abrupt transition of the reaction mechanism?

5) Is the increase in IMF cross section related to a liquid-vapor phase transition in nuclear matter?

It is hoped that by studying heavy-ion induced nuclear reactions on a series of targets, and then by comparing those reaction systematics to those obtained for similar systems at different bombarding energies, that at least some of these research problems can be explored.

I.B SCOPE OF THE EXPERIMENT

Much of the experimental work of the Maryland-LBL collaboration over the past several years has involved the study of IMF emission at intermediate energies. At one point it was thought that features consistent with compound nucleus decay may exist at bombarding energies even higher than E/A=50 MeV (BOW87, BOW89, BOW91b). However, even for the very asymmetric system La + C at E/A=80 MeV, non-equilibrium processes become very important (BOW89, BOW91b). Gold-induced reactions were also studied at E/A = 50 MeV, but the low fission barrier of the projectile led to a large fraction of events with IMF emission due to asymmetric fission of the projectile in peripheral reactions. With these two problems in mind, a research program that focused on IMF emission in La-induced reactions at lower energies was started. Because the lanthanum projectile is not highly fissile, only central collisions cause lanthanum to fission.

An experiment involving the reaction La + Al, V, and Cu at E/A = 45 and 55 MeV was performed. This was a continuation of experiments studying the reactions La + C, Al, V or Ti, and Cu or Ni at E/A = 35 and 40 MeV. These allowed an available energy (in the center of mass, assuming complete fusion) ranging from 385 MeV for the reaction La + C at E/A=35 MeV to 2410 MeV for the reaction La + Cu at E/A=55 MeV. In this way, the available energy easily surpassed the proposed limit for the onset of multifragmentation. Additionally, the symmetric reaction La + La was studied at E/A= 45 and 55 MeV. However, the detector system used was not well suited for studies involving reactions of symmetric systems.

The goal of this research is to explore the mechanism of IMF emission at intermediate energies. Chapter II explains the experimental techniques used to study complex fragment emission in these reactions. Chapter III presents the

experimental results, both inclusive and for coincident IMF's. Chapter IV discusses the modeling of the reactions studied by dynamical and statistical calculations. Reaction systematics and discussion of the results (both experimental and modeled) will be presented in Chapter V. The conclusions of this study are made in Chapter VI.

CHAPTER II EXPERIMENTAL PROCEDURES

II.A EXPERIMENTAL PHILOSOPHY

In the 1970's, with the advent of a new generation of heavy ion accelerators, it became possible to accelerate ions throughout the entire range of the periodic table. By the use of inverse kinematics reactions, in which the projectile is heavier than the target, the design of experiments to detect complex fragments (or intermediate mass fragments (IMF's)) (Z>2) emitted in nuclear reactions induced by heavy ions became simplified. In nuclear reactions, fragments can be emitted over the entire range of 4 π steradians in the center of mass. In normal kinematics reactions, the complex fragments are emitted both forward and backward in the laboratory system. A full 4π array of detectors in the laboratory is needed in order to reconstruct a reaction that led to complex fragment emission. On the other hand, complex fragments emitted in inverse kinematics reactions are emitted to forward laboratory angles. This can be illustrated by examining Figure II.1.

If a source of complex fragments is moving at a laboratory velocity V_s, a fragment can be emitted with a velocity V_e (which is Coulomb-like in magnitude) either forward or backward in the source frame. The "Coulomb circle" is the locus of all angles to which the fragment can be emitted. If the fragment is emitted forward in the source frame, then it is detected at a laboratory angle $\Theta 2$. If it is emitted backward in the source frame, then it is

Figure II.1: Vector diagram showing the emission of a fragment with a velocity V_e from a source moving with a velocity V_s. Emission of the fragment both forwards and backwards in the source frame leads to detection at forward laboratory angles.

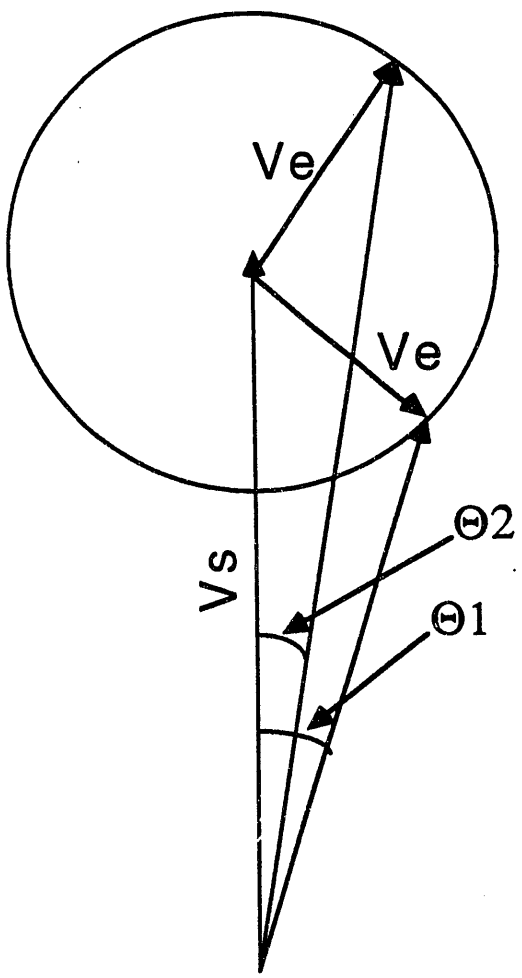
Ve
Ve
Θ2
Θ1
Vs

detected at angle Θ1. It should be noted that all emission in the source frame leads to emission of the fragments to forward laboratory angles. It then becomes necessary to place detectors only at forward angles to obtain a good (though not complete) coverage of 4 π in the center of mass for detection of complex fragments. Additionally, the high velocity of the center of mass provides a kinematic boost to the complex fragments, so that only fragments emitted backwards in the center of mass with very large emission velocities are below the detector energy thresholds. However, the heaviest fragments and evaporation residues are emitted in a narrow cone about the beam. Therefore, detection efficiency for these fragments is low because of the limited detector coverage at small laboratory angles.

The choice of a reacting system to study and a detector system to study that reaction with is almost always a trade-off. By using inverse kinematics reactions, complex fragment emission can be studied with a fairly inexpensive, modular detector system that covers a large angular range in the center of mass while only covering a small angular range in the laboratory system. This array can be reconfigured and then mated to a nearly full 4π detector to study complex fragment emission in reactions in normal kinematics (BOW91a).

Heavy-ion beams are used to induce nuclear reactions for several reasons. Although use of light ions (^{3}He, for example) as projectiles avoids ambiguity of determining the identity of projectile-like fragments, the light ions do not provide much compressional energy for heating up the nucleus. Compressional energy is more efficient at heating up a nucleus than collisional energy because compression is a collective mode, meaning that the entire nucleus is heated at one time by the compressional energy. On the other hand, collisional energy can be spread by individual nucleon-nucleon collisions. The

choice of a Lanthanum beam was made for several reasons. The advantages of using inverse kinematics reactions to study complex fragment emission have been previously discussed. In addition, since one of the goals of the experiment was to determine the mechanism(s) responsible for complex fragment emission, it was necessary to use a projectile with a high fission barrier, so that even binary fission would come from central collisions. This contrasts with what would occur with U or even Au beams, with very peripheral reactions leading to fission of the projectile. For practical reasons, La was used as a projectile because it is monoisotopic and can be delivered to the scattering chamber at a relatively higher intensity (5×10^8 particles per spill, or pps) than other heavy beams. Also, La-induced reactions had been previously studied with the same detector system at E/A=35 and 40 MeV and at E/A=55 MeV during this running period. Thus, the mechanism(s) responsible for complex fragment emission can be easily compared and contrasted over a range of available energy of over 2 GeV.

II.B. ACCELERATOR AND BEAM LINE CONFIGURATION

Experiment 941H was performed in February and March, 1990 using the Beam 44 beamline and the 60" scattering chamber at the Lawrence Berkeley Laboratory BEVALAC complex. In this experiment, La was accelerated to E/A = 45 MeV and impinged on self-supporting targets of ^{27}Al, ^{51}V, ^{nat}Cu, and ^{139}La.

The BEVALAC uses a linear accelerator (the SuperHILAC) capable of accelerating ion species throughout the periodic table to E/A= 8.5 MeV as an injector for the Bevatron synchrotron. The Bevatron is able to accelerate protons

to 4.9 GeV and ^{238}U to E/A=960 MeV. During this experiment, the circulating beam was approximately 5 x 10^{8} particles per spill (pps). A spill is defined as the time it takes to extract the beam into the experimental area. This process usually takes 6 seconds. Hence, there are 10 "spills" of ions per minute, with a flat-top (the period of time during which the beam is actually being directed into the experimental area) for this experiment of 500 ms. This flat-top period can be extended to up to one second for detector systems with a high duty factor.

The beamline configuration for experiment 941H is shown in Figure II.2. The beam is extracted from the Bevatron and steered down the beamline using a series of bending (labeled S1M7, M1, etc.) and focusing (labeled Q1, Q2, etc.) magnets. Wire chambers (labeled WC1, WC2, etc.) are placed along the beamline and can be moved into and out of the beam to check both the x and y positions of the beam. Due to the presence of satellite beams, a scattering chamber entrance collimator was placed inside the beampipe as it entered the chamber to ensure that only a single beam was delivered to the chamber. A local collimator was placed inside the scattering chamber between the beampipe and the target to deliver a beamspot less than 1 cm in diameter on target. The size and shape of the beamspot at the target was checked by placing a phosphor in the target position. A video camera pointing into the chamber detected the phosphor glow as the beam passed through it. By monitoring the glow as the beam was adjusted by changing the current in the bending and focusing magnets (usually just the M1 bending magnet was adjusted), the optimal beamspot was produced. The beam focus was checked periodically throughout the experiment. Additionally, a Faraday cup was placed at the back of the scattering chamber to provide the integrated beam current.

Figure II.2: Beamline configuration of the Beam 44 beamline at the Lawrence Berkeley Laboratory Bevalac. The labels are as follows: WC- wire chamber, M6, etc.- bending magnet, QA, etc.- focusing magnet, DP- diffusion pump, GV1, etc.- gate valve.

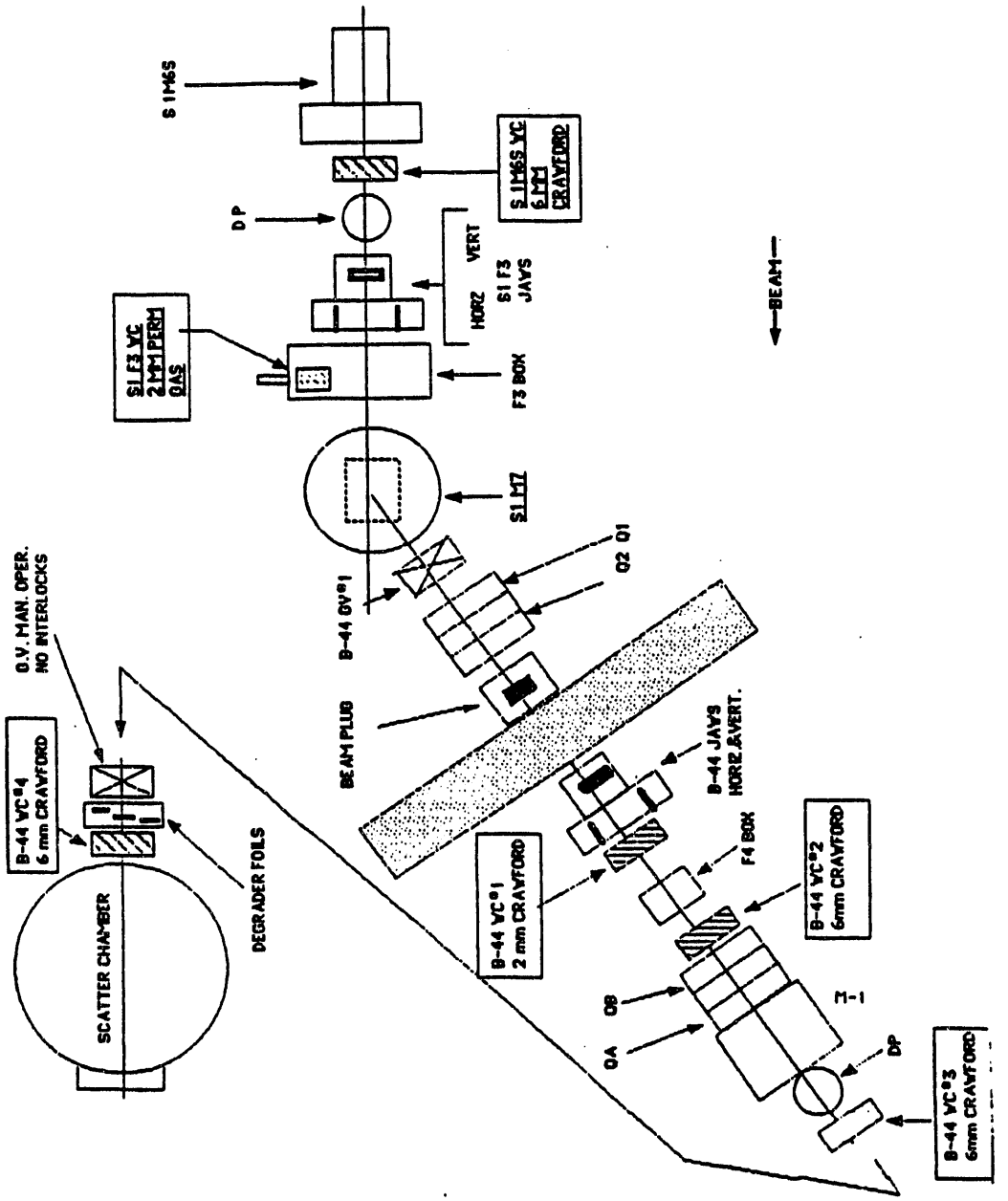
S 1H6S
S1H6S VC
6 MM
CRAWFORD
DP
VERT
HORZ
S1 F3
JAWS
S1F3 VC
2 MM PERM
GAS
F3 BOX
S1 H7
B-44 GV°1
Q2 Q1
BEAM PLUG
B-44 JAWS
HORIZ.&VERT.
F4 BOX
B-44 VC°1
2 mm CRAWFORD
B-44 VC°2
6mm CRAWFORD
M-1
DB
DA
DP
B-44 VC°3
6mm CRAWFORD
B-44 VC°4
6 mm CRAWFORD
G.V. MAN. OPER.
NO INTERLOCKS
DEGRADER FOILS
SCATTER CHAMBER
BEAM

Figure II.3: View of the scattering chamber for Experiment 941H as seen from above.

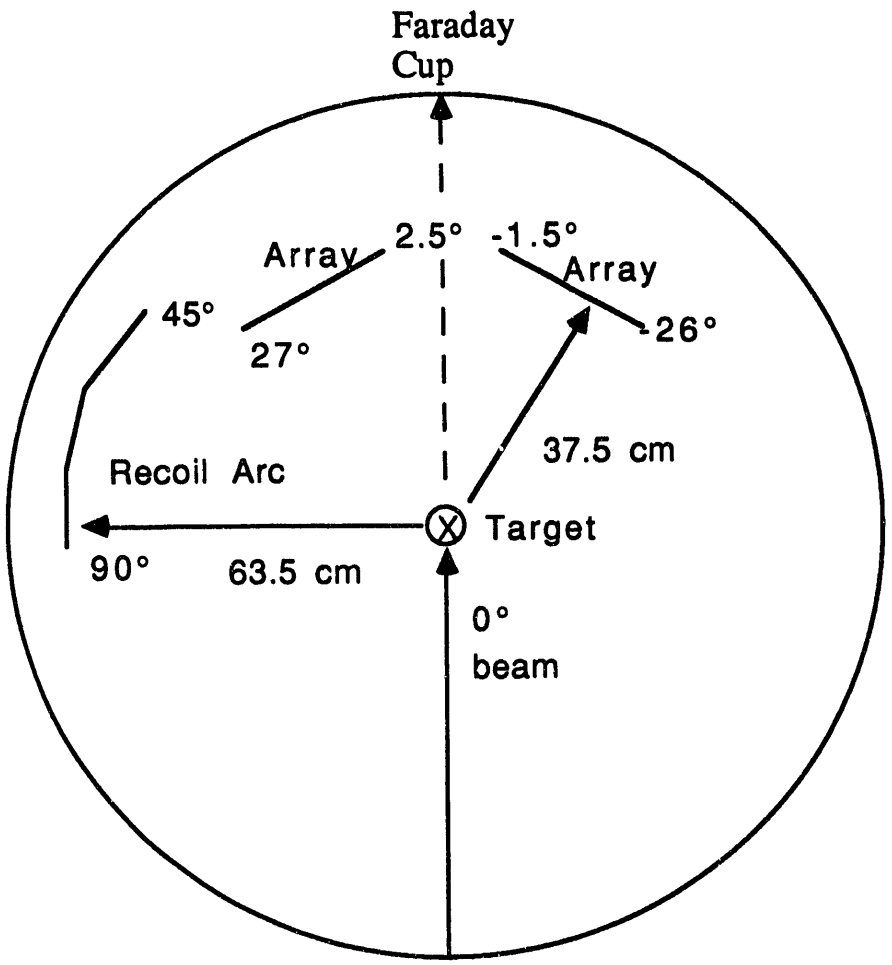
Faraday
Cup
2.5°
-1.5°
Array
Array
45°
27°
26°
37.5 cm
Recoil Arc
Target
90°
63.5 cm
0°
beam

II.C. DETECTOR SYSTEM

The detector system used in Experiment 941H consisted of a Si-Si(Li)-plastic array in the side-by-side configuration (KEH89, KEH92) to detect forward-focused intermediate mass fragments and 14 Si surface barrier detectors in an arc ranging from ~45° to ~90° as an attempt to detect target-like fragments. A diagram of the scattering chamber set-up as seen from above is shown in Figure II.3. The array and the recoil detectors are described in detail below.

II.C.1 The Si-Si(Li)-Plastic Array

The Si-Si(Li)-Plastic array, which has been described elsewhere in great detail (KEH89, KEH92) was designed for use in inverse kinematics reactions to detect particles ranging in charge from protons to beam particles. It is a modular array that can be reconfigured to meet the goals of the experiment. Each module (or telescope) consists of a 300-μm thick Si detector, a 5-mm thick Si(Li) detector, and a 7.5-cm thick Bicron BC400 plastic scintillator with attached photomultiplier tube. The active area of the Si detectors measured 46 by 46 mm. A drawing of one of the telescopes is shown in Figure II.4.

In this experiment, the array was mounted in the side-by-side configuration to maximize the angular coverage for intermediate mass fragments being emitted to relatively large angles. In this configuration, the modules are mounted in 3 telescope by 3 telescope square arrays on each side of the beam. The disadvantage of this mounting scheme is the lack of coverage at angles close to the beam, where the heavier reaction products are emitted.

Each array was placed on mounts that can be remotely controlled to

Figure II.4: Drawing of an individual telescope of the Si-Si(Li)-plastic array used in this experiment.

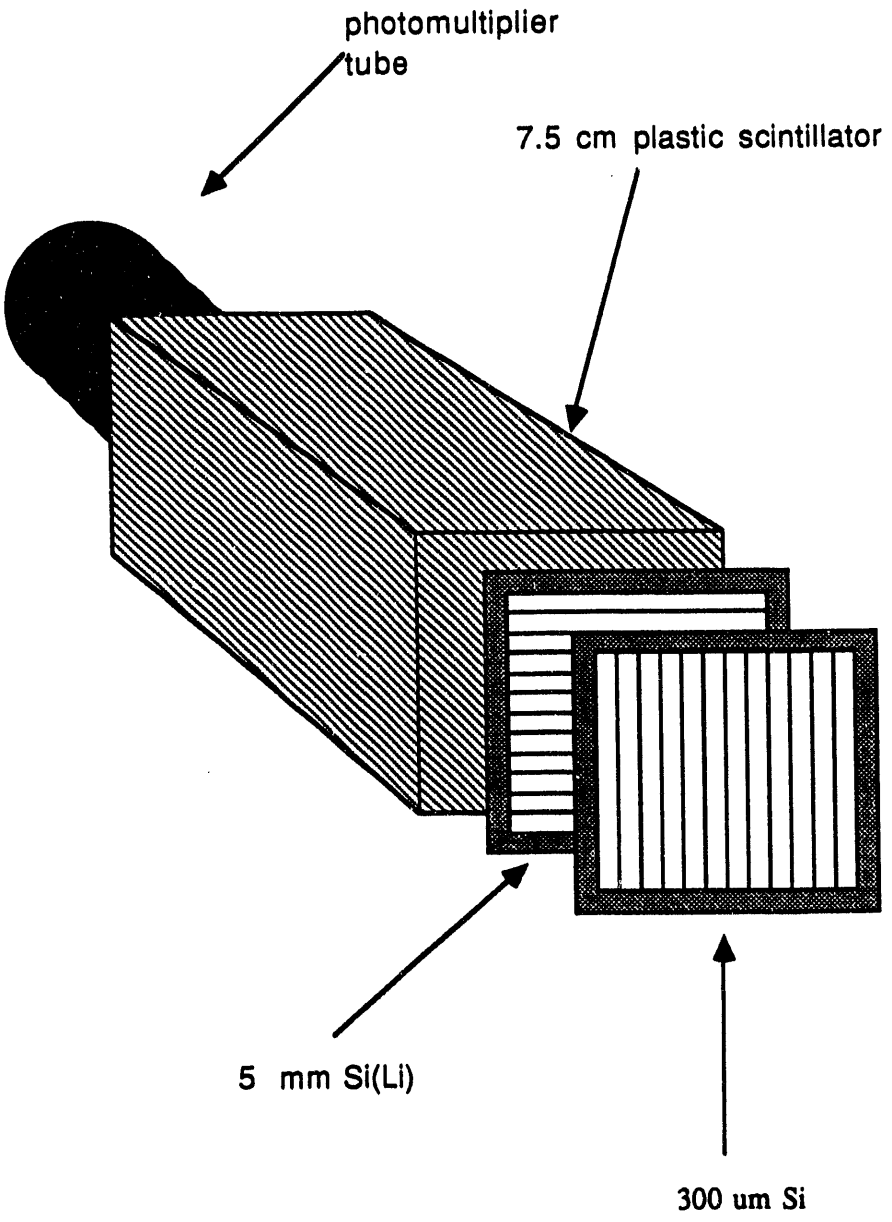
photomultiplier
tube
7.5 cm plastic scintillator
5 mm Si(Li)
300 um Si

Figure II.5: Schematic diagram of the arrays used in this experiment. The labels inside each telescope are the labeling scheme used. The angles show the positioning of the arrays with respect to the beam.

T1
T2
T3
S1
S2
S3
R1
R2
R3
26°
-14°
-1.5°
Beam ⊕
N1
N2
N3
M1
M2
M3
L1
L2
L3
2.5°
15°
27°

move up and down; and each of these motor mounts was placed on the arms inside the scattering chamber that rotate clockwise or counterclockwise. In this way, each

telescope can be placed directly into the beam during the calibration procedure, which is described in Section II.C.1.A. The arms were placed asymmetrically with respect to the beam, with the left array centered at 15° and the right array centered at -14°. This was done to increase the coverage of angles close to the beam for detection of heavy fragments. Each array was mounted so that the face of the 300-μm Si detector was 37.5 cm from the target, thus allowing an angular coverage (in the laboratory system) from 3° (-2°) to 27° (26°) in plane for the left (right) array and from -12 to 12 degrees out of plane. Additionally, each telescope was mounted so that its face was normal to the target, and a gold foil of either 1.5 or 3.0 mg/cm^2 was placed in front of each telescope for electron suppression. A schematic diagram of the array as it was mounted in this experiment (with the telescope labels) is shown in Figure II.5.

Each of the Si or Si(Li) detectors in the array was position sensitive in one direction; and they were mounted in such a way as to provide both the x and y position of a particle entering a telescope.

The position sensitivity for the Si detectors was achieved by the method of resistive charge division. A schematic diagram illustrating this process is shown in Figure II.6. The holes (formed in electron-hole pairs when the particle passes through the detector) migrate to one face of the detector to give the position signal, while the electrons migrate to the opposite face and provide the energy signal. Because there are two contacts to provide the position signal (one of which is grounded), the holes detected at one contact will be a fraction of the

Figure II.6: Schematic diagram illustrating the determination of the position of a particle entering a Si detector by resistive charge division.

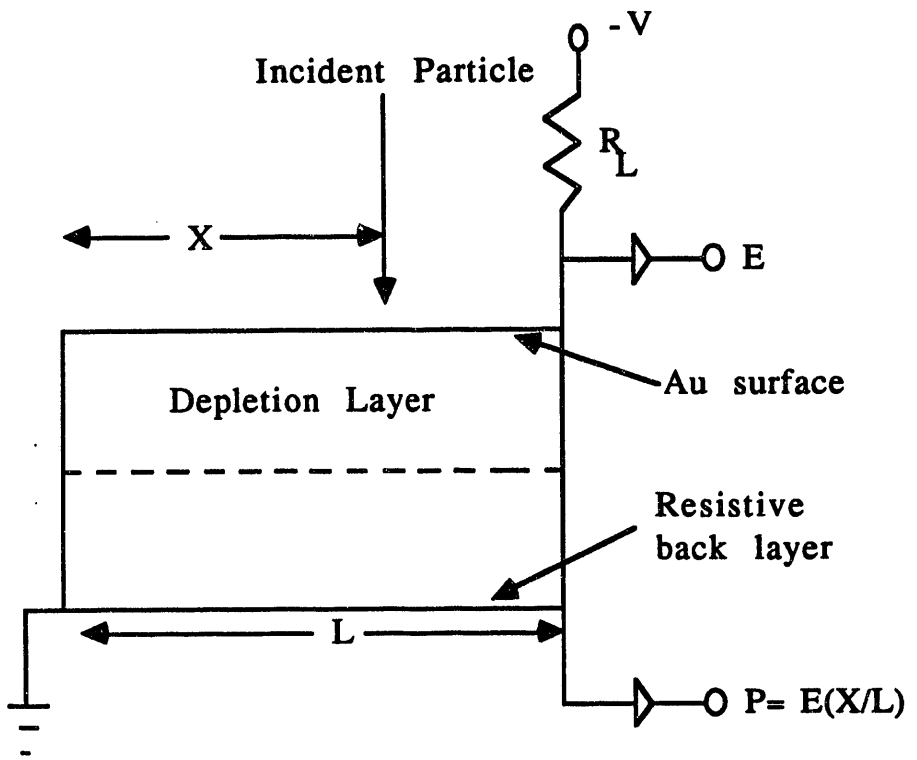
-V
Incident Particle
R_L
X
E
Depletion Layer
Au surface
Resistive
back layer
L
P= E(X/L)

energy signal proportional to the distance from the contact the particle traverse. In other words,

$$XE=E\ X/L \qquad (II.1)$$

in which XE is the position signal, E is the energy signal, X is the distance traversed by the holes, and L is the length of the resistive layer.

If the resistive layer is continuous, then at some time a mask must be placed in from of the detector to provide the information to calibrate the detector for position. However, the resistive layers for the Si detectors in the array are divided into strips and gaps of low and high resistivity, respectively. The detectors are thus self calibrating because the ratio of the position signal to the energy signal corresponds to discrete values. The face of each Si detector was divided into 15 low resistivity strips of 2.42-mm width and 14 high resistivity gaps of 0.607-mm width. The strips and gaps for the 300-μm detectors were fabricated by bombarding the detectors with 25 keV boron ions (WAL90). The low resistivity strips have a B concentration of ~2 x 10^{14} atoms/cm^2; the high resistivity gaps have a B concentration of ~3 x 10^{13} atoms/cm^2. For the 5-mm Si(Li) detectors, a thin layer of palladium was evaporated over the entire face of the detector; gold strips were then evaporated on top of the Pd layer, providing the low resistivity strips (WAL90).

II.C.1.A. Energy calibrations

Because the BEVALAC (and all electrostatic accelerators) accelerates ion species depending on the charge-to-mass ratio of the ion, it is possible to accelerate beams of multiple ion species. Figure III.5 shows the energy

Figure II.7: Energy spectrum of the "cocktail" calibration beam directed into one of the detector telescopes.

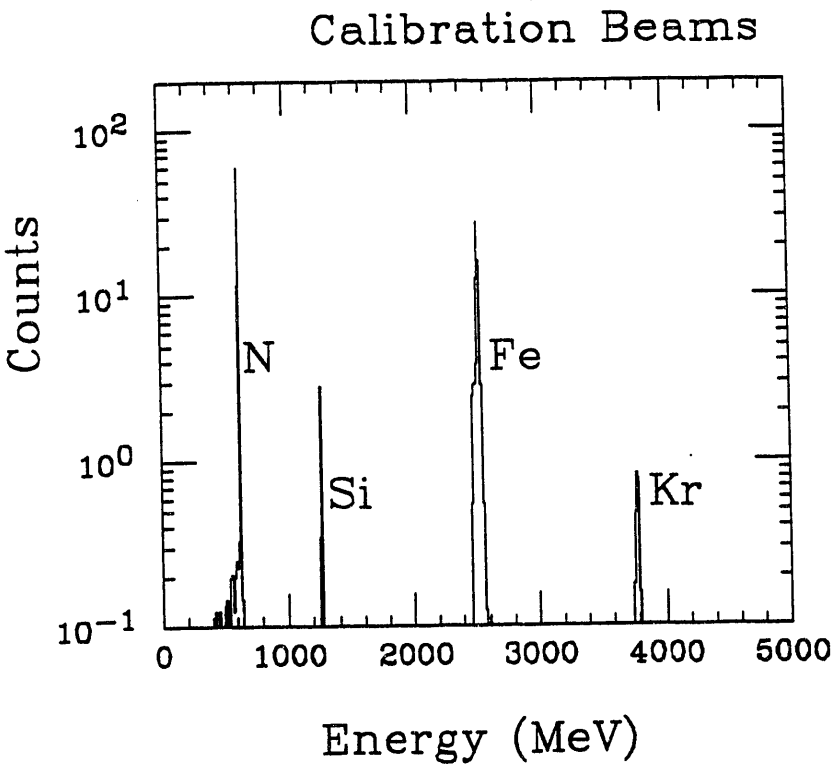
Calibration Beams
Counts
10^2
10^1
10^0
10^{-1}
N
Si
Fe
Kr
0
1000
2000
3000
4000
5000
Energy (MeV)

spectrum of $^{14}N^{2+}$, $^{28}Si^{4+}$, $^{56}Fe^{14+}$, and $^{84}Kr^{24+}$ accelerated to E/A=45 MeV and directed into one of the telescopes. Because the arrays were placed on mounts that moved up and down (and on arms that arced) it was possible to direct these "cocktail" beams into each telescope. In order to prevent radiation damage to the detectors, the beam was highly attenuated to approximately 100 particles per spill before it was directed into the detectors.

Silicon detectors have a non-linear energy response to heavy ions due to pulse-height defect (PHD), in which the pulse height produced for a heavy ion is lower than that for light ions of the same kinetic energy. This is caused by the high ionization density at the Bragg peak for heavy ions. Thus, electron-hole pairs can recombine before the electric field in the device separates them. This non-linearity is dependent on the energy, mass, and atomic number (Z) of the incident particle. The 5-mm Si(Li) detectors were calibrated to first order by directing the cocktail beam at E/A=35 MeV into the detector (with the 300-μm detectors removed) and then assuming a PHD of 0.6% for N and 0.9% for Si (BLU91). The PHD for heavier particles was determined empirically for each detector by fitting the deviation of the apparent energy of the calibration beams from the true energy with the proper function (COL90). For this experiment, the PHD was determined to have the form:

$$E_{real}=aZ^4E^{(0.8+4.7/\sqrt{Z})} \qquad \text{(II.2)}$$

in which E_{real} is the true energy of the particle, Z is the atomic number of the particle, E is the detected energy, and a is a constant adjusted to provide the best energy determination for the calibration beams. Typically an error of <1% in the energy determination was achieved.

The energy calibration for the 300-μm Si detectors was done in much the same way. The 300-μm detectors were remounted in front of the 5-mm detectors and the cocktail beams were directed into the telescopes. The energy deposited in the 300-μm detectors was then determined by the change in energy deposited into the 5-mm detectors. Because of the variable thickness of the 300-μm Si detectors, the energy calibration was corrected for both the x and y position of the particle in the telescope by the application of a linear function.

II.C.1.B Position Calibrations

The position, both in the x and y directions, of a particle passing through a telescope was determined by using the method of Kaufman (KAU70). After determination of the x and y position of a particle, a conversion was made to the polar angles Θ (in-plane angle) and Φ (out-of-plane angle). The position signal YE as a function of the energy of the particle is shown in Figure II.8. The 15 lines correspond to the 15 strips, and the intersection point is related to the electronic base-line offsets. As Figure II.8 stands, it is not useful for determining the position of the particle. The position signal must be divided by its energy signal, yielding a value called, for instance, POA. A plot of the energy of the particle as a function of POA yields curved lines for each strip, shown in Figure II.9. In order to straighten the lines at low energy, the following function is used:

$$POSX = A(XE+B)/(E+C) \qquad (II.3)$$

Figure II.8: Position signal YE (in channels) of particles entering a detector as a function of energy (in channels). Fifteen lines, corresponding to the fifteen strips, are clearly visible.

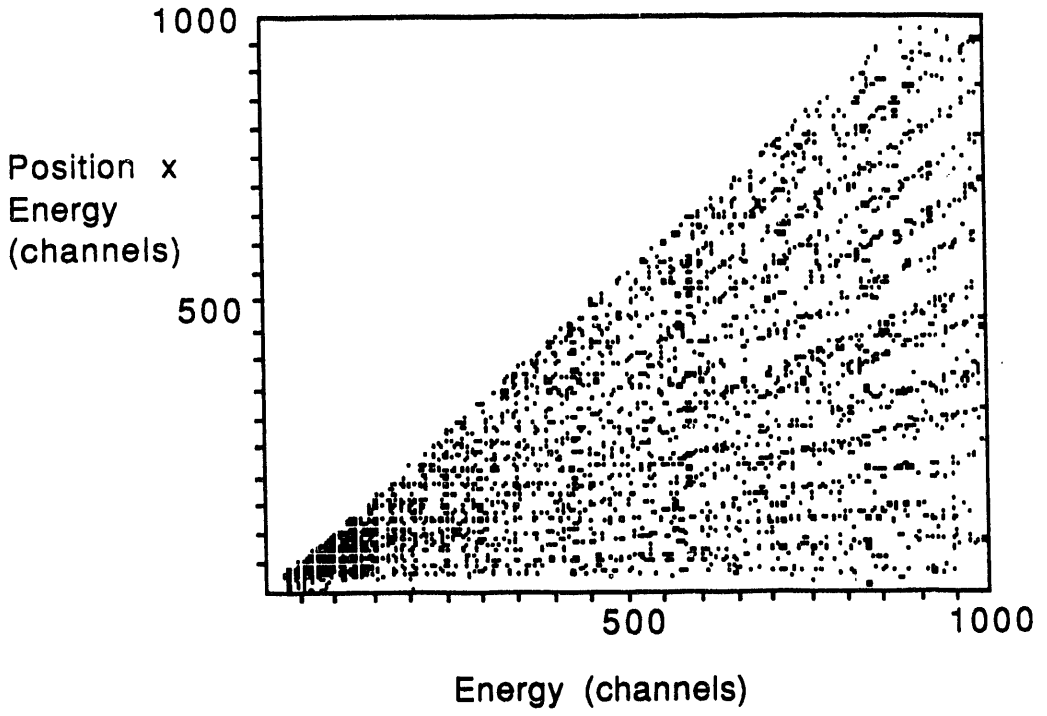
1000
Position x
Energy
(channels)
500
500
1000
Energy (channels)

Figure II.9: Energy signals (in channels) of particles entering a detector as a function of POA, the position-energy divided by the energy. Fifteen curves are clearly visible.

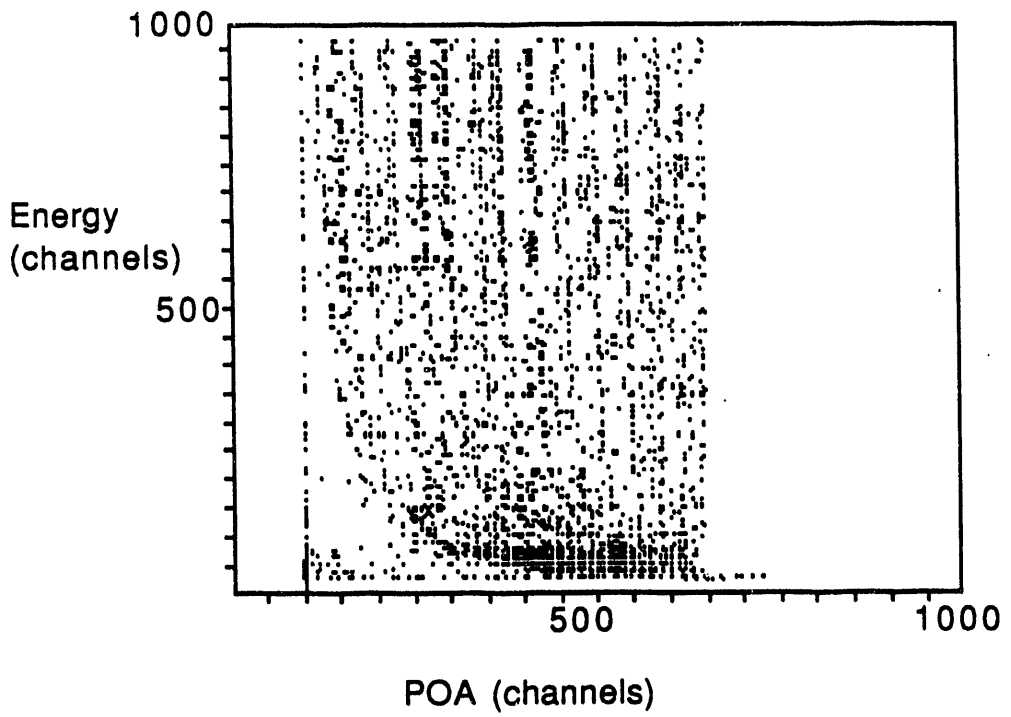
1000
Energy
(channels)
500
500
1000
POA (channels)

Figure II.10: Energy signals (in channels) of particles entering a detector as a function of POSX (POSX= A(YE+B)/(E+C), in which A is an expansion parameter, YE and E are the position-energy and energy signals, and B and C are related to the electronic baseline offsets). Fifteen lines are clearly visible.

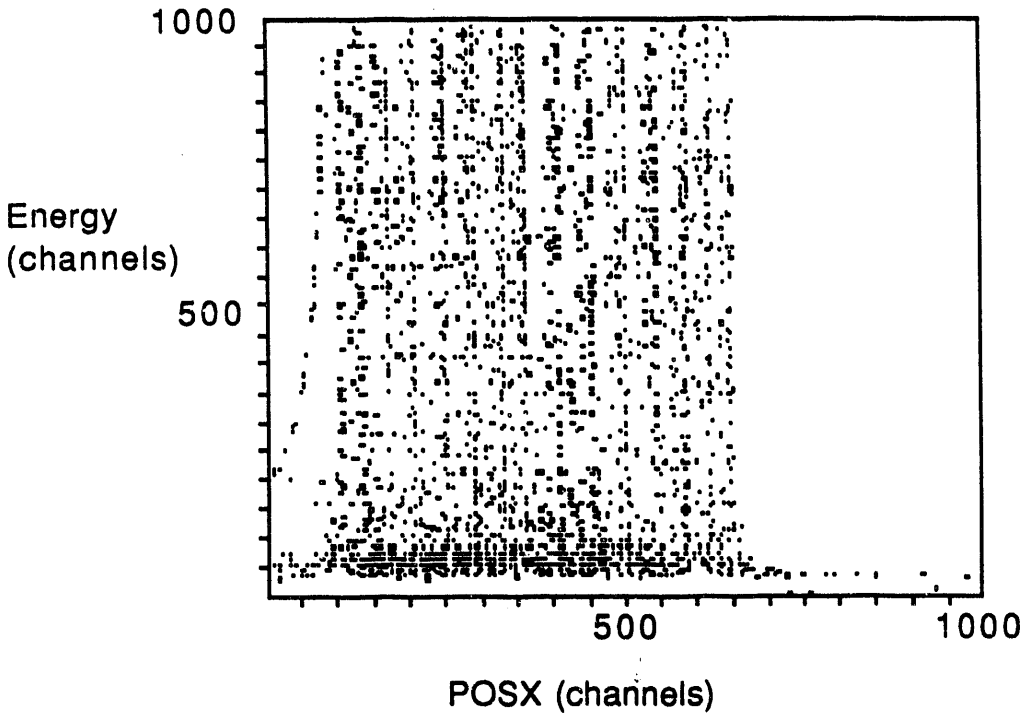
1000
Energy
(channels)
500
500
1000
POSX (channels)

Figure II.11: Projection of Figure II.10 onto the x-axis. The peaks correspond to individual strips on the face of the detector.

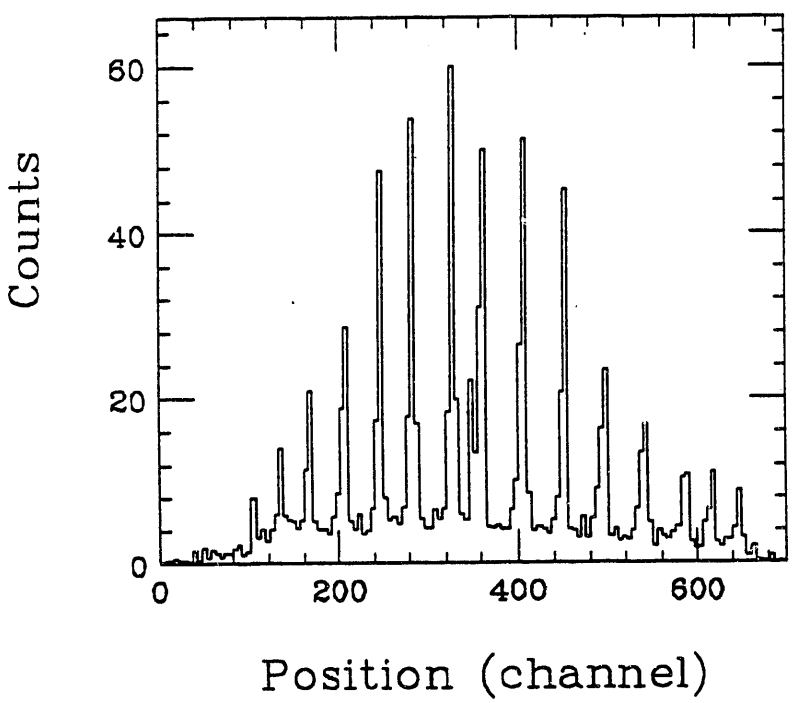
Counts
60
40
20
0
0
200
400
600
Position (channel)

in which A is a constant used to expand the data, XE and E are the position-energy signal and the energy signal, respectively, and the constants B and C are related to the electronic base-line offsets. A plot of energy as a function of POSX is shown in Figure II.10. By projecting Figure II.10 onto the x-axis, as shown in Figure II.11, the channel of each peak is determined. These peaks correspond to the position of each strip on the face of the detector. The position of the peak is then converted to the correct angle of its strip; and then the channels of the peaks are fit to a n-order polynomial (with n equal to 2 or 3) to provide a continuous function of the angles.

II.C.1.C Particle Identification and Z Calibrations

In order to identify the atomic number of a particle passing into a telescope, a plot of the total energy versus the energy deposited in the 300-μm detector can be examined for paraboli corresponding to each atomic number, as shown in Figure II.12. This plot shows curves for discrete atomic numbers, but is difficult to use to determine the atomic number of the particle.

In order to linearize the paraboli in Figure II.12, the Bohr equation for the energy lost by a charged particle passing through a medium is used:

$$-dE/dx = (4\pi e^4 k Z^2 \rho z / m_e v^2) \ln(m_e v^3 / 2Ze^2 \omega) \qquad \text{(II.4)}$$

in which e is the electron charge, m_e is the electron mass, z, ρ, and ω are the atomic number, number density of atoms, and the frequency of motion of the electron in the stopping medium, and Z and v are the charge and velocity of the charged particle and k is the degree of ionization of the charged particle. Because the logarithmic term varies slowly, Eq. II.4 can be simplified to:

$$-dE/dx \propto Z^2/v^2 \propto MZ^2/E \propto Z^3/E \qquad \text{(II.5)}$$

if one assumes that the effective charge is proportional to the mass of the charged particle. If one equates -dE/dx with the energy lost in the 300-μm detector (because dx is small), one has:

$$[(\Delta E)(E)] \propto Z^3 \qquad \text{(II.6)}$$

or

$$[(\Delta E)(E)]^{1/3} \propto Z \qquad \text{(II.7).}$$

The quantity on the left side of (II.7) is modified by the addition or subtraction of a fraction of the energy in the 300-μm detector to give the particle identification function (PID):

$$PID = M\{[(\Delta E)(E)]^{1/3} + N(\Delta E)\} \qquad \text{(II.8)}$$

The constant M is used to expand the data and N is a constant to straighten the lines in a plot of the ΔE as a function of the PID. After the straightening procedure the plot is then projected onto the PID-axis, as shown in Figure II.13. The peaks are then fit to the correct atomic number by matching the peaks to the known peaks of the cocktail calibration beams. These peaks are then fit to an n-order polynomial (with n equal to 2 or 3) using a least squares method. As can be readily seen from Figure II.13, peaks corresponding to atomic numbers up to Z_{beam}=57 can be distinguished.

Figure II.12: Energy of particles in the 300-μm device (in channels) as a function of energy in the 5-mm device (in channels). The paroboli are at discrete Z values.

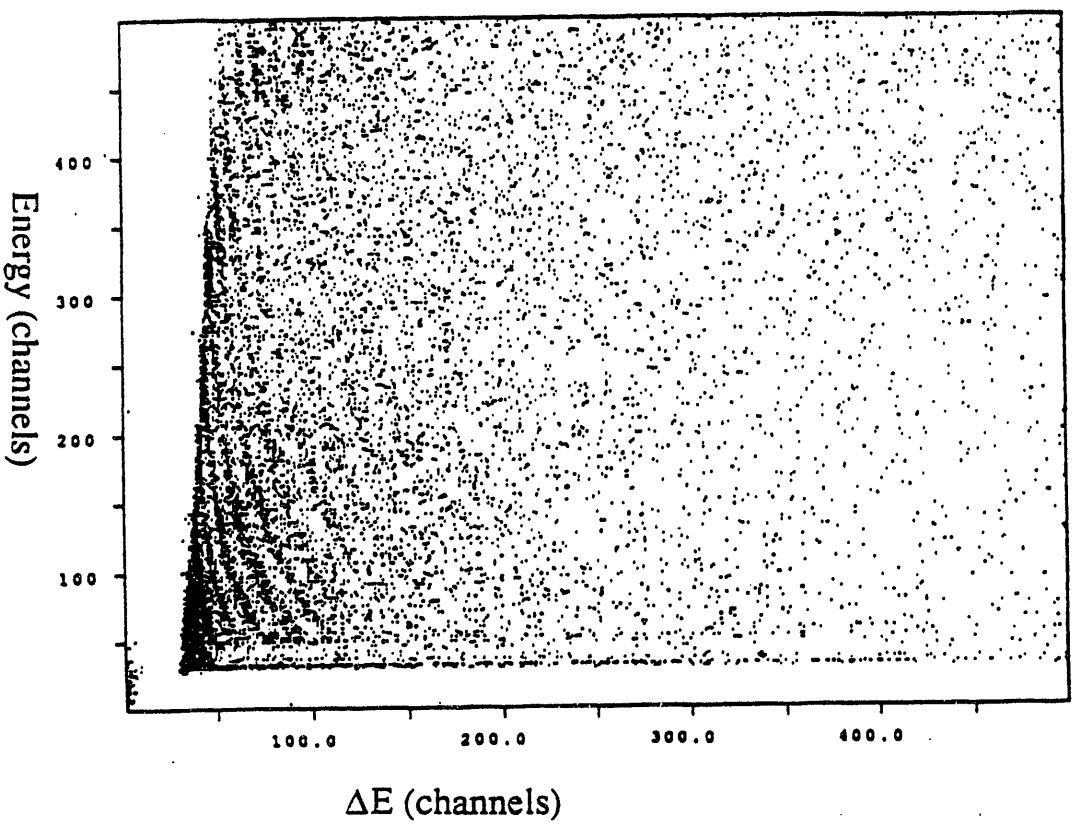
Energy (channels)
400
300
200
100
100.0
200.0
300.0
400.0
ΔE (channels)

Figure II.13: Projection of ΔE as a function of the PID onto the PID-axis. Peaks corresponding to individual Z's of fragments up to Z_{beam} (57) are clearly visible.

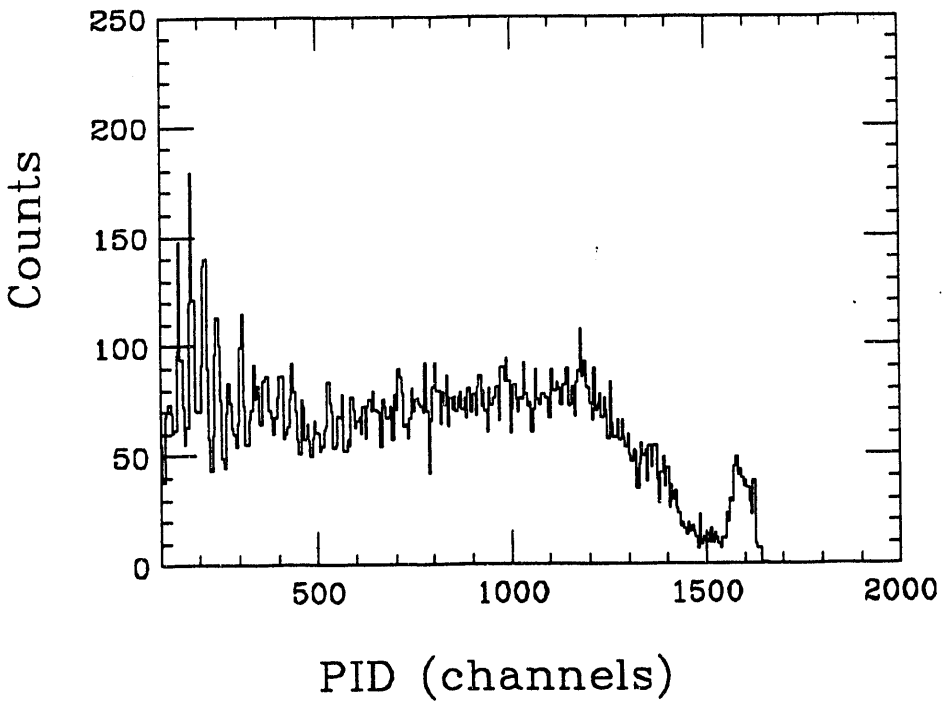
250
200
150
100
50
0
Counts
500
1000
1500
2000
PID (channels)

II.D. RECOIL DETECTORS

In an attempt to detect any target-like fragments (TLF's) recoiling from an incomplete fusion product or in a deep-inelastic reaction, an arc of 14 Si fission fragment detectors was placed 63.5 cm from the target at angles ranging from ~45 to ~90 degrees. The arc was made up of four 900-mm^2 and ten 450-mm^2 detectors, each with a thickness ranging from 200-300 μm. Each detector was mounted so that its face was normal to the target.

II.D.1. Energy Calibrations

The recoil detectors were calibrated for energy by using the known energies of the α particle and the two fission fragments from ^{252}Cf. The energy of the fission fragments (KAU74) was corrected for pulse-height defect (PHD) using the procedure of Moulton, et al. (MOU78) in an iterative process. For real particles, the energy lost in one half the target thickness was found to be almost independent of mass in this energy region (varying by only a few tenths of an MeV), so that the energy was corrected before mass and PHD determinations.

II.D.2. Time calibrations

The time of flight of particles between the target and the recoil detectors was determined by considering the detection of a gamma ray or a light charged particle in any of the array scintillators as a start signal and the detection of a particle in the recoil detectors as a stop signal. The stop signal was determined

by using a time pick-off preamplifier. In actuality, the start signal was delayed to ensure a coincidence between the start and the stop signal, so that the clock actually ran backwards. The zero point time (at which the clock was started) was determined by placing a $^{249}Cf(\alpha,\gamma)$ source directly between a recoil detector and a scintillator, with essentially no flight path. The time calibration was then determined by running a signal from an electronic time pulser with a time interval of 20 ns through the associated electronics.

II.D.3. Mass Determination

Because the energy of the target recoil from elastic scattering was below detector thresholds, an independent determination of the mass of any TLF detected was not possible. However, the mass could be calculated from the measured energy and time-of-flight of the recoil, according to the relationship

$$m=\frac{2Et^2}{x^2} \qquad \text{(II.9)}$$

in which x is the distance from the target to the detector, E is the corrected energy of the particle, and t is the measured TOF.

Because the energy of a particle entering the recoil detectors was determined fairly accurately, the error in the mass is associated almost entirely with errors in the determination of the TOF described in section II.D.2. However, it was possible to calculate (using scattering kinematics relationships) the mass of a particle using the experimental angle and energy of the particle. For this method, a range of reaction Q-values was used to determine if the calculated mass had a large dependence on the Q-value of the reaction. This calculated mass was then compared to the mass determined from the

experimental TOF, shown in Tables II.1and II.2 for reactions on the V and Cu targets, respectively. Because the calculated mass and the experimentally determined mass are close to each other, the experimental mass will be used as results. However, due to the various problems associated with the recoil detectors, no conclusions will be based on these results.

Table II.1 Experimental and calculated masses of recoil products at the indicated energy and angle over a range of reaction Q-values for the reaction La + V at E/A=45 MeV.

E=15 MeV, Θ=45°

Q (MeV)	M_{calc}	M_{expt}
0	58	55
-200	53	
-400	48	

E=18 MeV, Θ=60°

Q (MeV)	M_{calc}	M_{expt}
0	56	55
-200	51	
-400	46	

Table II.2 Same as Table II.2 for the reaction La + Cu at E/A=45 MeV

E=12 MeV, Θ=60°

Q (MeV)	M_{calc}	M_{expt}
0	68	55
-200	63	
-400	58	

E=20 MeV, Θ=60

Q (MeV)	M_{calc}	M_{expt}
0	69	70
-200	64	
-400	60	

CHAPTER III EXPERIMENTAL RESULTS

The results of the reactions La + Al, V, Cu, and La are presented in three sections. The first section presents the inclusive data, with which global features of the reactions can be described. The second section presents the results for array coincidence events. The third section discusses the inclusive results from the recoil detectors.

III.A. INCLUSIVE RESULTS

By studying the inclusive, or singles, results of fragments detected in the array, a broad understanding of the mechanism(s) responsible for complex fragment emission can be gained. This section will describe the fragment charge distributions, angular and velocity distributions, and angle integrated cross sections for the reactions on each target studied.

III.A.1. Charge Distributions

Shown in Figures III.1- III.8 are the fragment charge distributions in each telescope of the array for reactions on each target. Figures III.1 (III.2), III.3 (III.4), III.5 (III.6), and III.7 (III.8) are for the LMN (RST) array for the Al, V, Cu, and La targets, respectively. The results are presented relative to the actual telescope location, with the L and T columns farthest from the beam and the N and R columns closest to it, as shown in Figure II.5. It should be noted

Figure III.1: Distributions of the fragment charge detected in each telescope of the L-M-N array for the reaction La + Al.

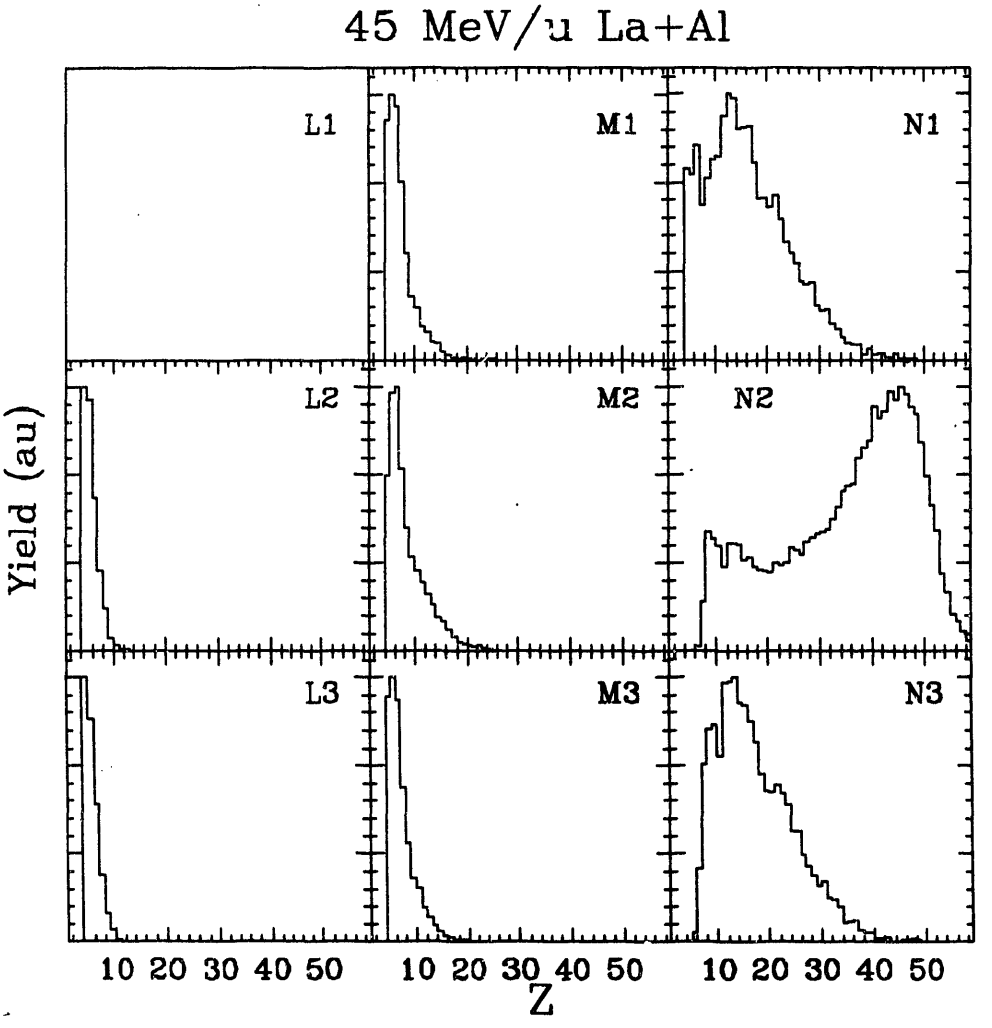
45 MeV/u La+Al
L1
M1
N1
L2
M2
N2
L3
M3
N3
Yield (au)
10 20 30 40 50
10 20 30 40 50
10 20 30 40 50
Z

Figure III.2: Distributions of the fragment charge detected in each telescope of the R-S-T array for the reaction La + Al.

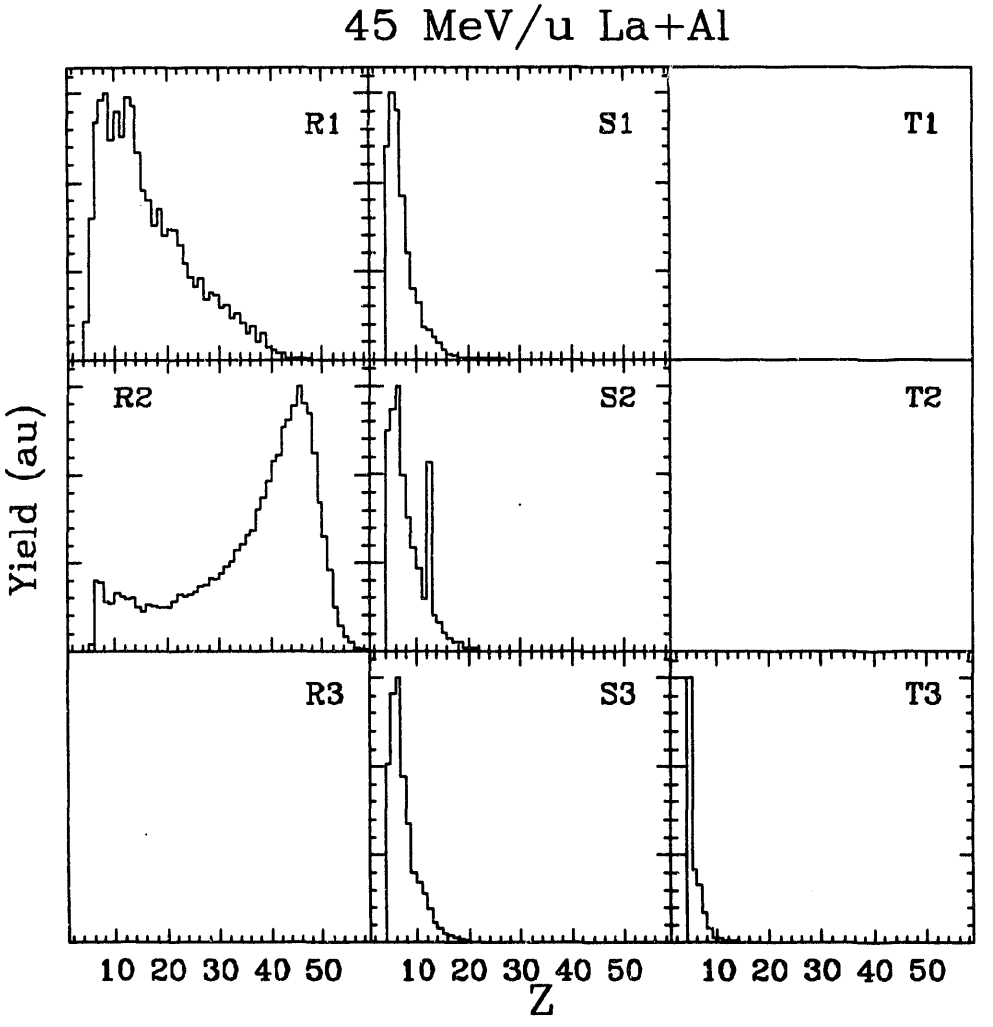
45 MeV/u La+Al
R1
S1
T1
R2
S2
T2
R3
S3
T3
Yield (au)
10 20 30 40 50
10 20 30 40 50
10 20 30 40 50
Z

Figure III.3: Same as Figure III.1 for the reaction La + V.

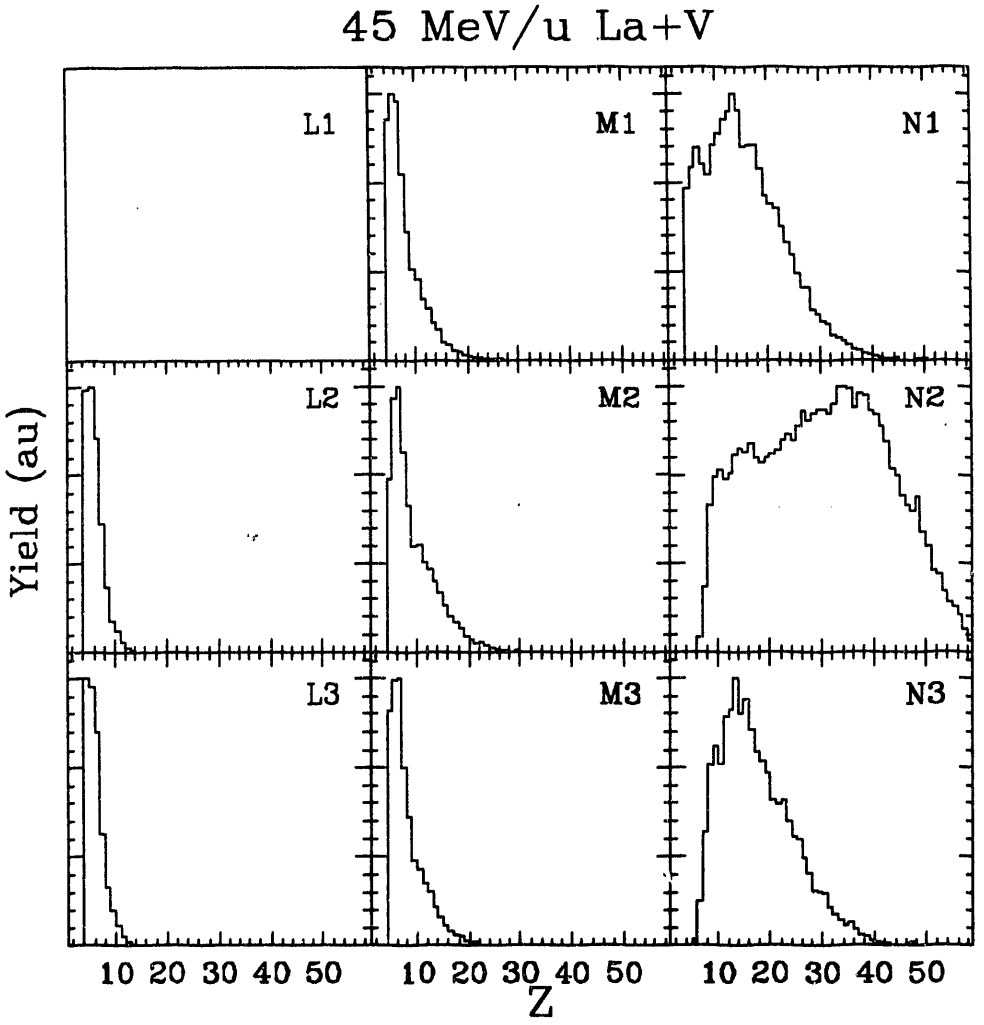
45 MeV/u La+V
L1
M1
N1
L2
M2
N2
L3
M3
N3
Yield (au)
10 20 30 40 50
10 20 30 40 50
10 20 30 40 50
Z

Figure III.4: Same as Figure III.2 for the reaction La + V.

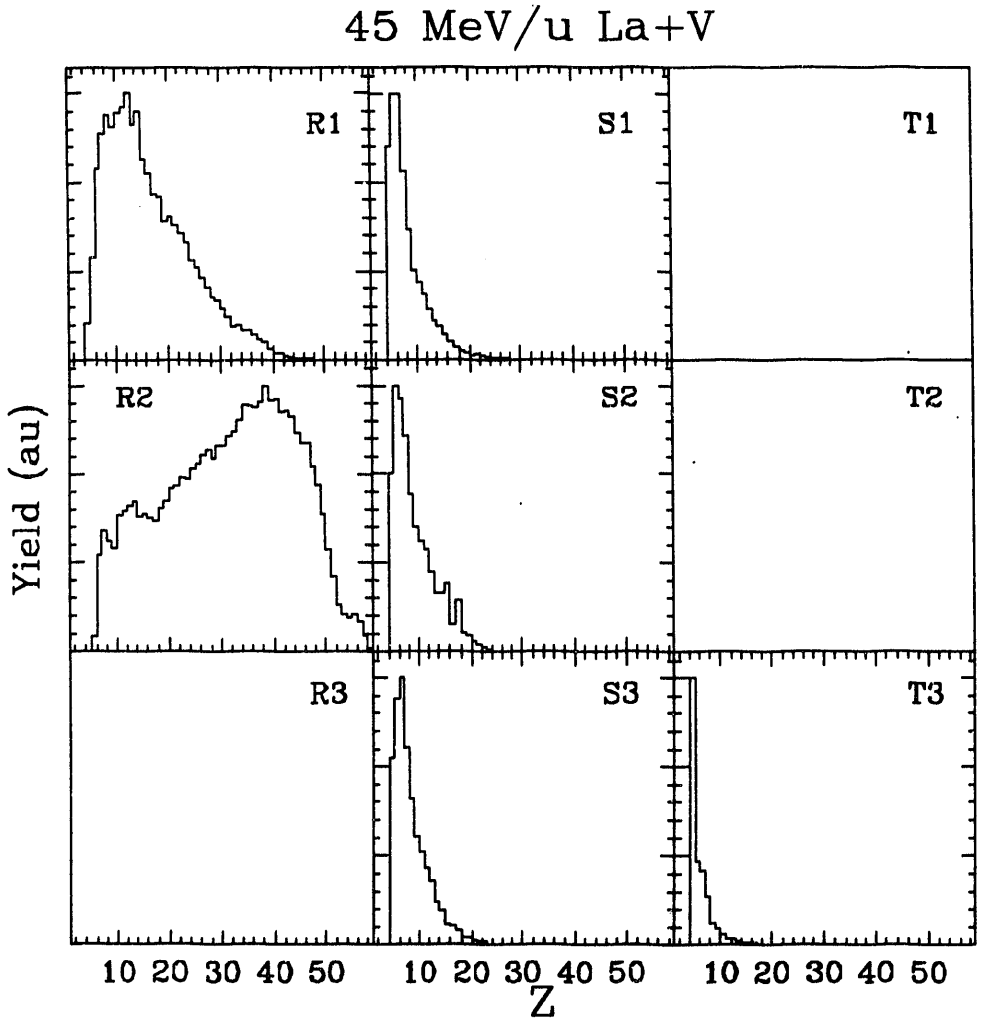
45 MeV/u La+V
R1
S1
T1
R2
S2
T2
R3
S3
T3
Yield (au)
10 20 30 40 50
10 20 30 40 50
10 20 30 40 50
Z

Figure III.5: Same as Figure III.1 for the reaction La + Cu.

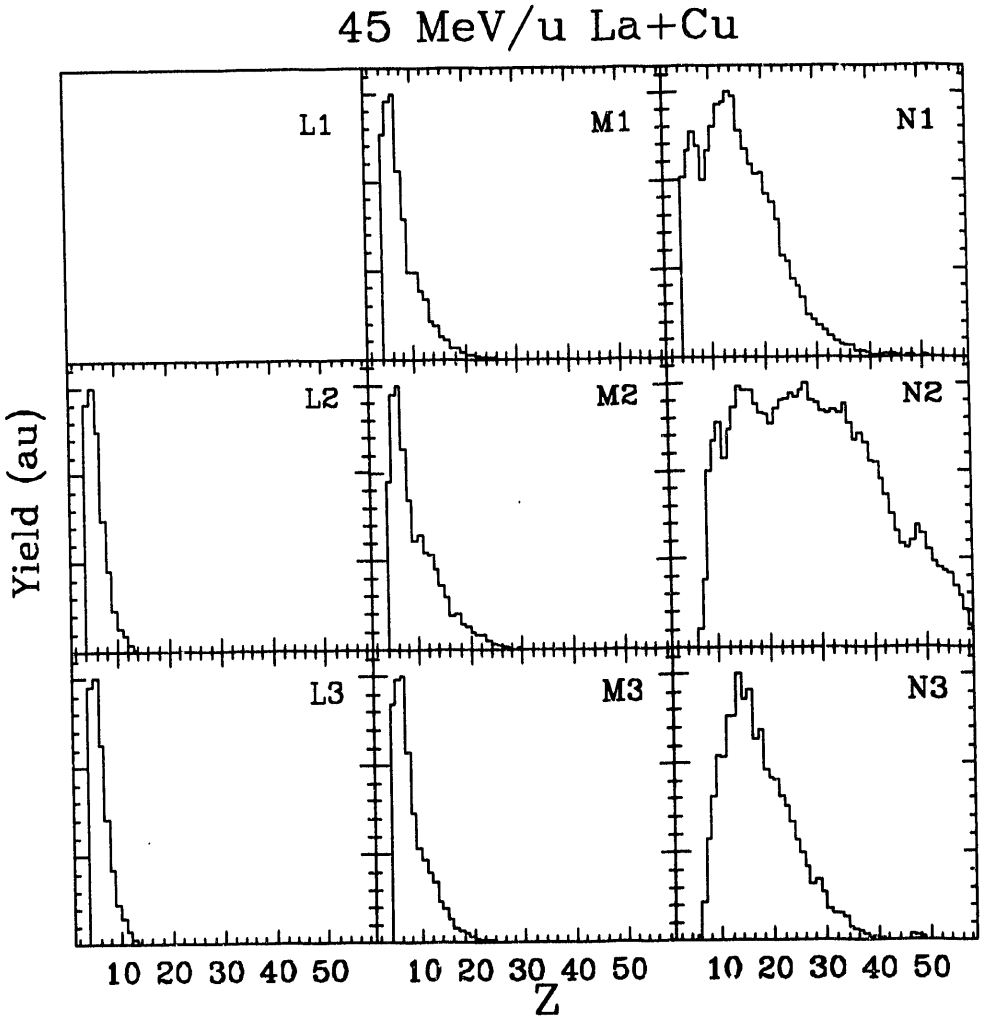
45 MeV/u La+Cu
L1
M1
N1
L2
M2
N2
L3
M3
N3
Yield (au)
10 20 30 40 50
10 20 30 40 50
10 20 30 40 50
Z

Figure III.6: Same as Figure III.2 for the reaction La + Cu.

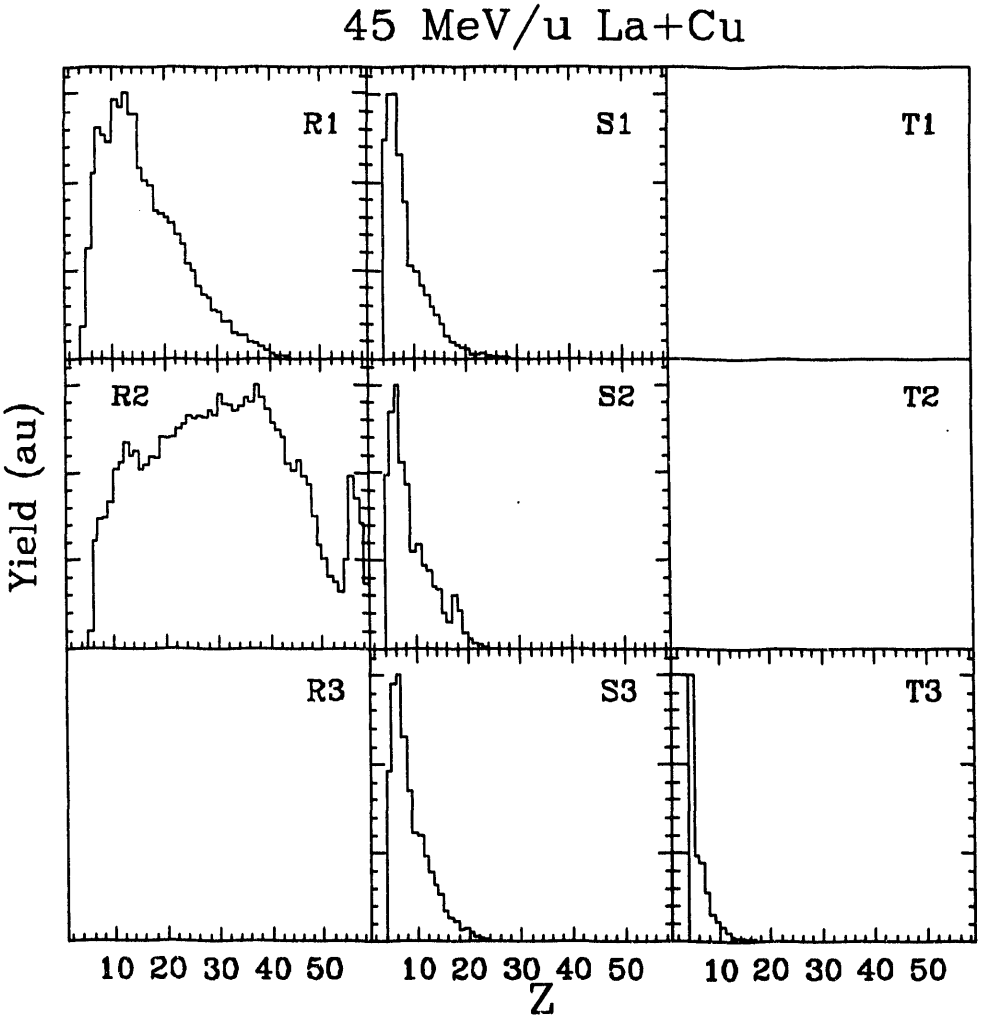
45 MeV/u La+Cu
R1
S1
T1
R2
S2
T2
R3
S3
T3
Yield (au)
10 20 30 40 50
10 20 30 40 50
10 20 30 40 50
Z

Figure III.7: Same as Figure III.1 for the reaction La + La.

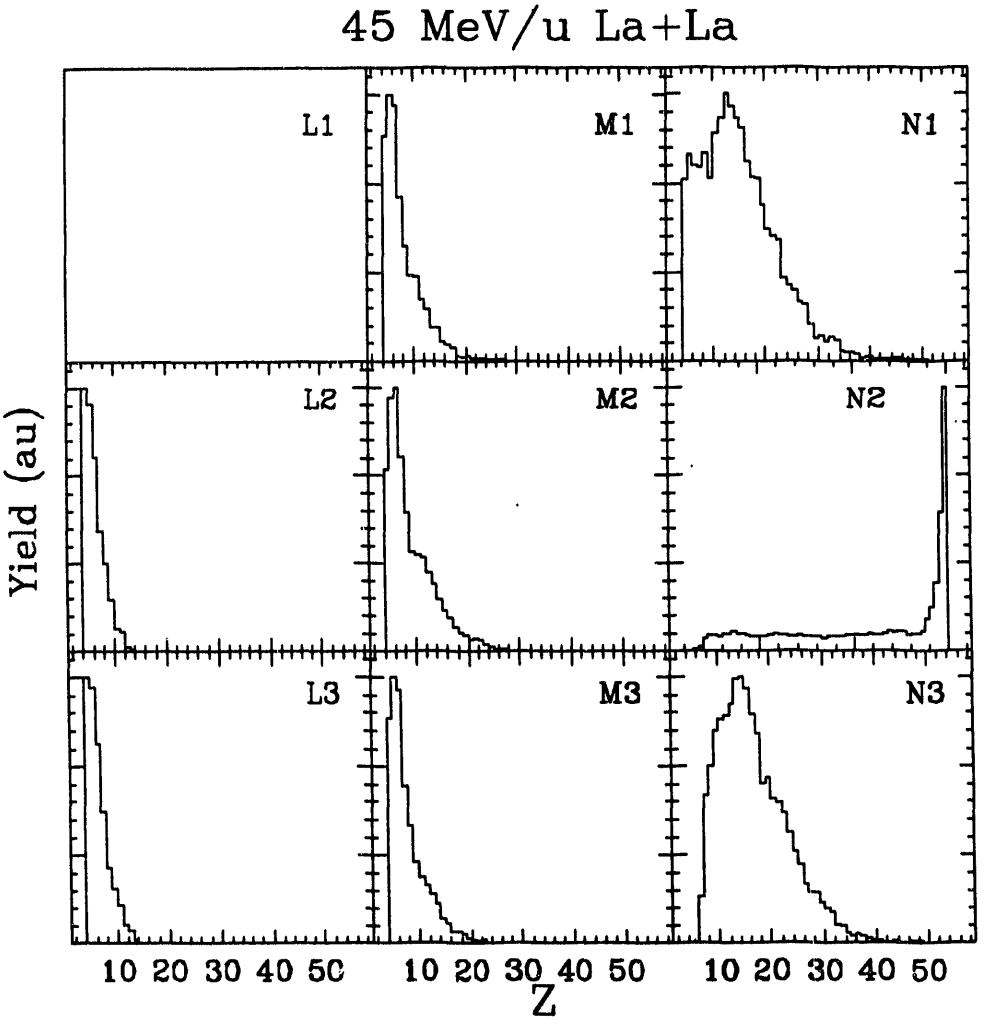
45 MeV/u La+La
L1
M1
N1
L2
M2
N2
L3
M3
N3
Yield (au)
10 20 30 40 50
10 20 30 40 50
10 20 30 40 50
Z

Figure III.8: Same as Figure III.2 for the reaction La + La.

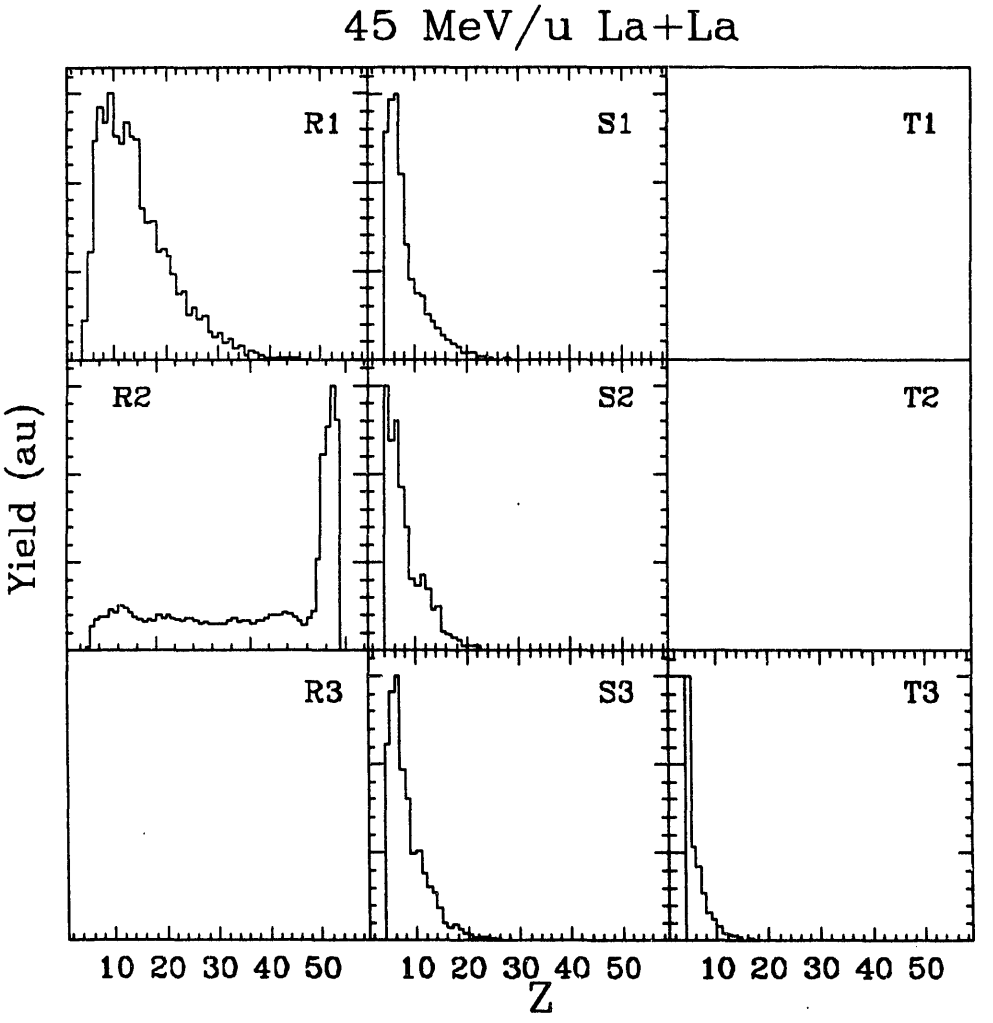
45 MeV/u La+La
R1
S1
T1
R2
S2
T2
R3
S3
T3
Yield (au)
10 20 30 40 50
10 20 30 40 50
10 20 30 40 50
Z

that the L1, R3, T1, and T2 telescopes malfunctioned at some time during the experiment, and were not included in any results.

For the reactions on Al, only those telescopes closest to the beam, N2 and R2, detect fragments with atomic numbers close to that of the projectile (Z_{proj}=57). The grazing angle for the La projectile in the reaction La + Al at this energy (0.85°) is too small for projectile-like-fragments (PLF's) and elastically scattered beam particles to be detected, even in the central telescopes. For fragments detected in telescopes farther from the beam, the distribution is heavily skewed toward the detection of lighter fragments. This can be attributed to the Coulombic origin (in the source frame) of the emission velocity, so that only light fragments will be emitted to large enough laboratory angles. (If one examines Figure II.1, it is clear that since the Coulomb circle for lighter fragments will have a larger radius than the circle for heavy fragments, the light fragments will be detected over a larger range of laboratory angles.) An important feature is that even the telescopes farthest from the beam detect fragments with Z up to 10 or more. This shows that the probability is high that complex fragments are being emitted at angles not covered by the array.

The Z distributions for the other targets show the same trend as for the Al target. An important difference arises for the Cu and La targets, in which beam particles are detected in the R2 telescope for the Cu target (grazing angle of 1.73°), as shown in Figure III.6, and for both central telescopes (N2 and R2) for the La target (grazing angle of 3.08°), shown in Figures III.7 and 8.

III.A.2. Coulomb Circles

As shown in Figure II.1, a source moving with a velocity V_s can emit fragments at any angle in its center of mass with a velocity due to the Coulomb repulsion between the fragment and the remaining fragment. If the distribution in the $V_{||}$-$V_{\perp}$ plane is actually a circle (there will be some broadening due to evaporation effects) then it can be deduced that the emission was statistical in nature because of the isotropic angular distribution. However, the lack of a well defined Coulomb circle does not necessarily mean that the emission was not statistical. It has been shown that emission from a continuum of isotropic sources will smear out the Coulomb circle for a given fragment. In such cases, only by gating on the source velocity to separate the different sources can one regain the circular feature of statistical emission (COL89).

In order to determine the velocity of a fragment, a parameterization of the mass M from the known charge Z of the fragment was used. This parameterization has the form:

$$M = 2.08(Z) + 0.0029(Z^2) \qquad \text{(III.1)}$$

and has been shown to adequately parameterize the mass in this region of excitation energy (BOW89, BOW91b).

Contour plots of $d^2\sigma/dV_{\perp}dV_{||}$ in the $V_{||}$-$V_{\perp}$ plane for representative Z-values are shown in Figures III.9-12 for each system studied. These plots are for the singles events. Similar results are obtained if only coincidence events are chosen. The Coulomb-like origins of the distribution in the $V_{||}$-$V_{\perp}$ plane is shown by the decrease in the radius of the distribution as the fragment charge increases.

For the reaction La + Al, the lightest fragments are emitted with a small parallel velocity, an indication of predominantly backwards emission in the

Figure III.9: Distributions in the $V_{||}$-$V_{\perp}$ space for representative fragments for the reaction La + Al.

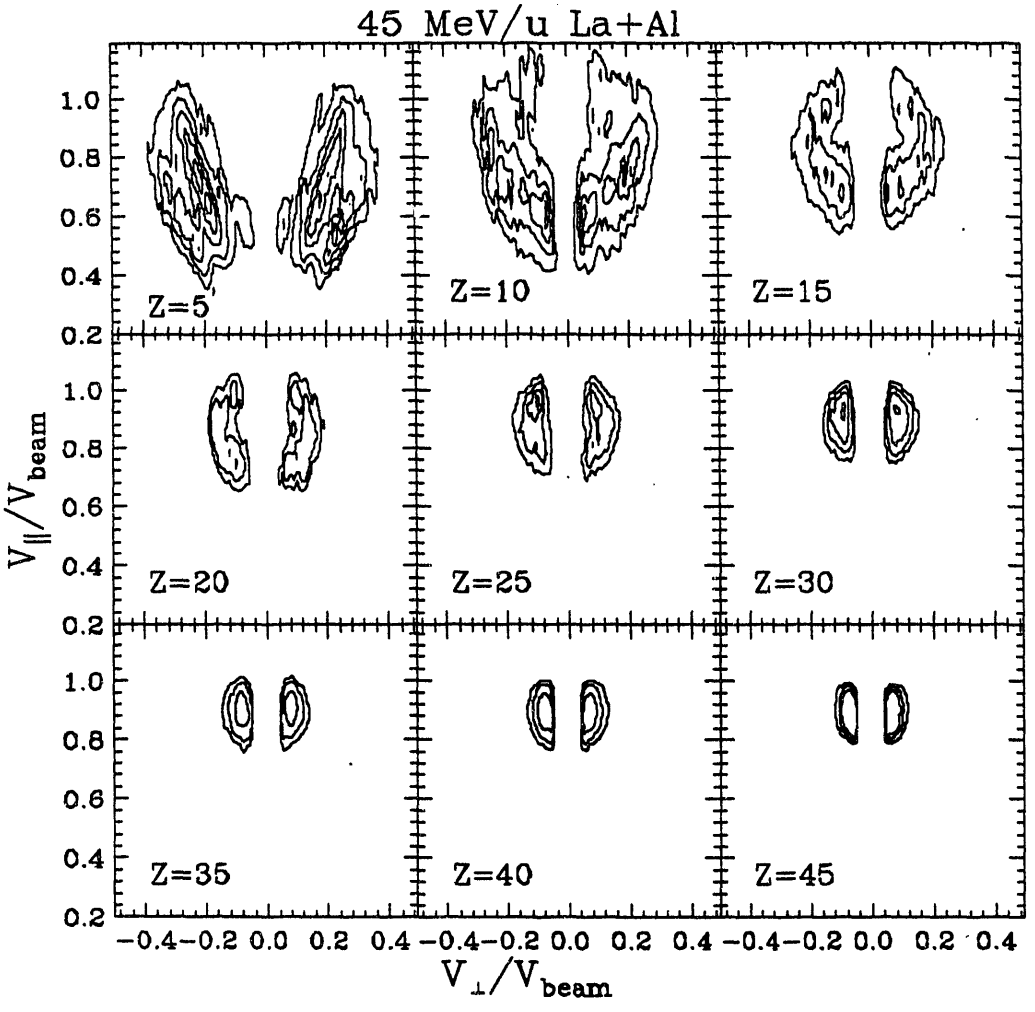
45 MeV/u La+Al
Z=5
Z=10
Z=15
Z=20
Z=25
Z=30
Z=35
Z=40
Z=45
1.0
0.8
0.6
0.4
0.2
−0.4 −0.2 0.0 0.2 0.4
$V_{\parallel}/V_{beam}$
$V_{\perp}/V_{beam}$

Figure III.10: Same as Figure III.9 for the reaction La + V.

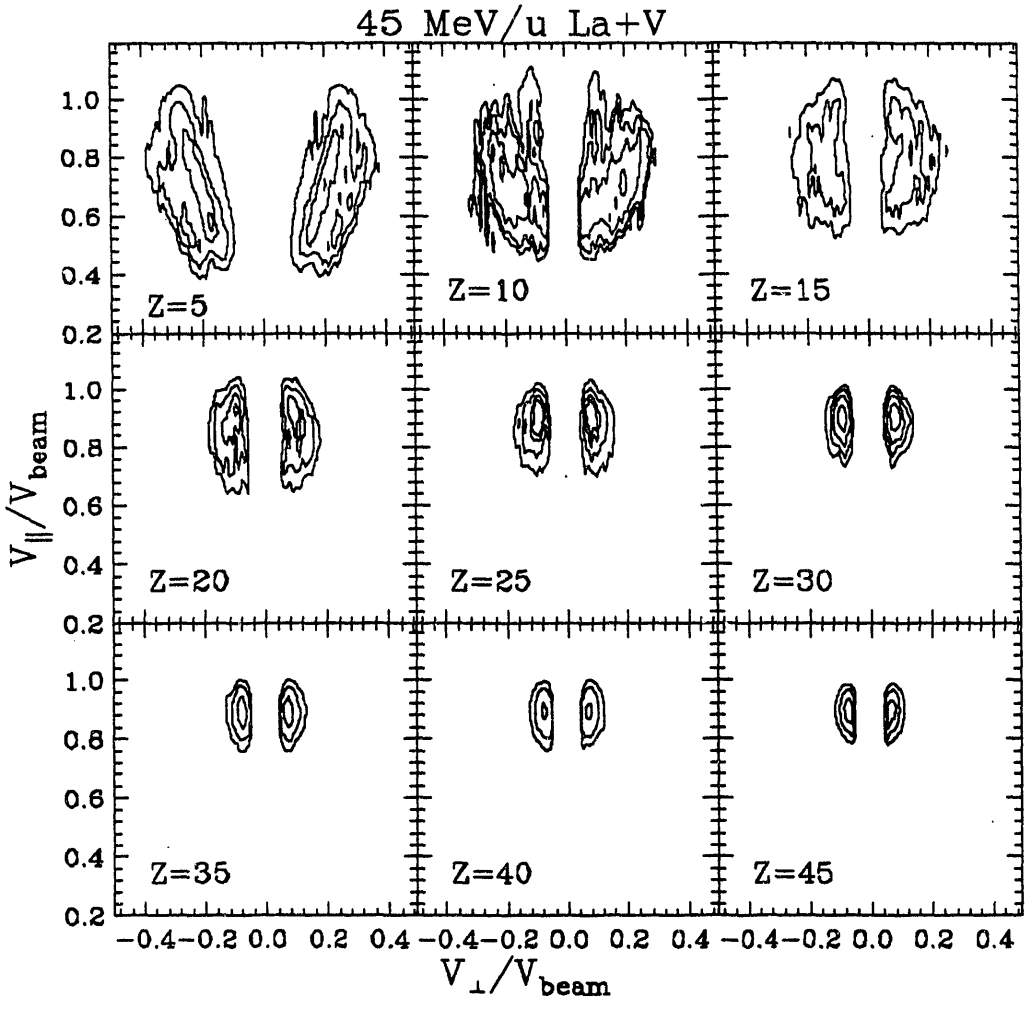
45 MeV/u La+V
Z=5
Z=10
Z=15
Z=20
Z=25
Z=30
Z=35
Z=40
Z=45
1.0
0.8
0.6
0.4
0.2
−0.4 −0.2 0.0 0.2 0.4
$V_{||}/V_{beam}$
$V_{\perp}/V_{beam}$

Figure III.11: Same as Figure III.9 for the reaction La + Cu.

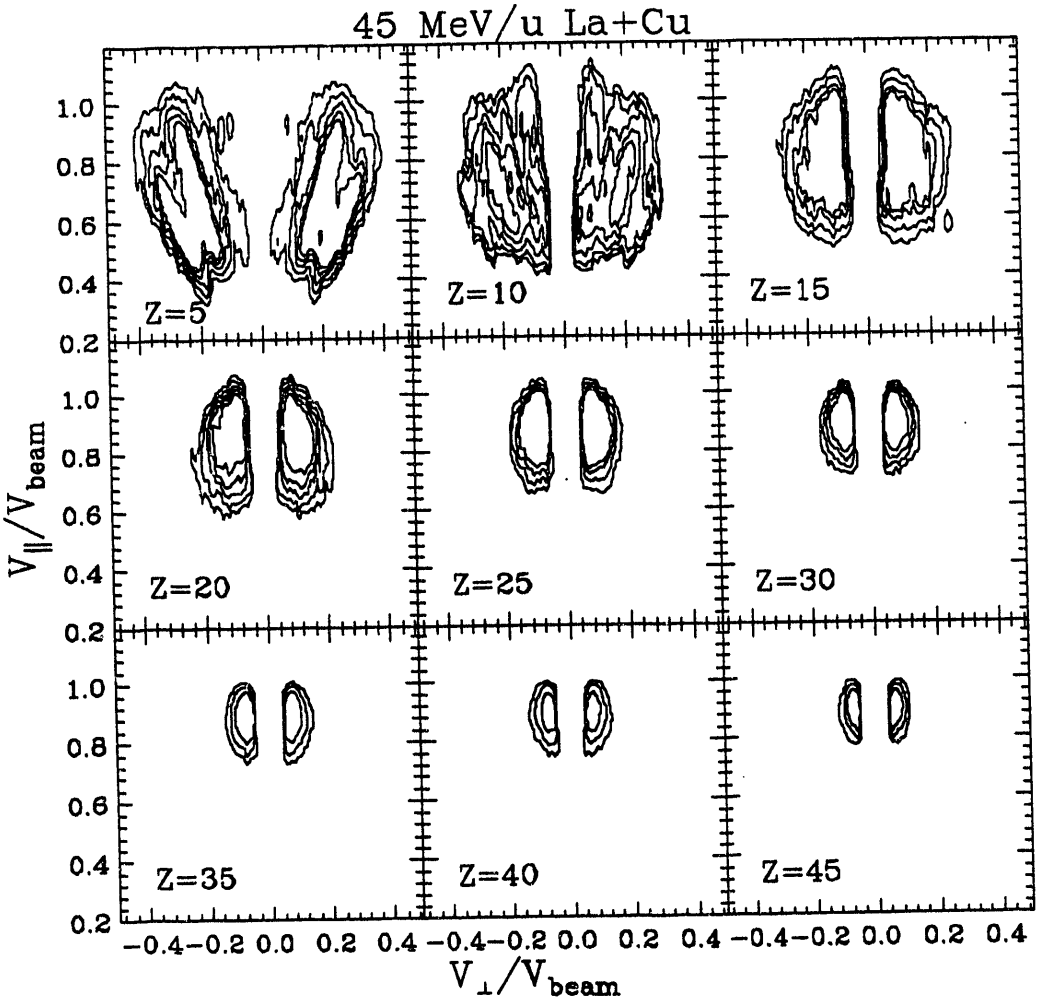
45 MeV/u La+Cu
Z=5
Z=10
Z=15
Z=20
Z=25
Z=30
Z=35
Z=40
Z=45
$V_{\parallel}/V_{beam}$
$V_{\perp}/V_{beam}$
1.0
0.8
0.6
0.4
0.2
−0.4 −0.2 0.0 0.2 0.4

Figure III.12: Same as Figure III.9 for the reaction La + La.

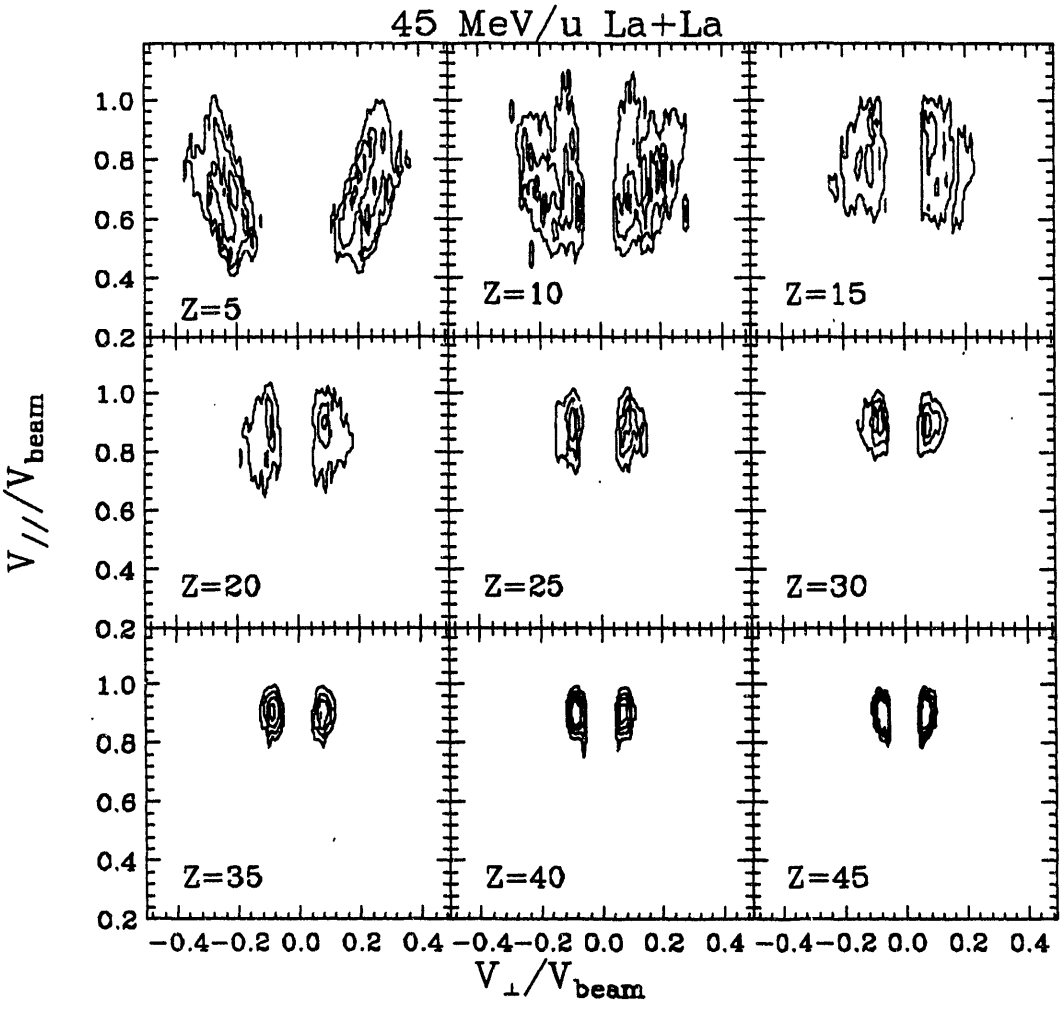
45 MeV/u La+La
Z=5
Z=10
Z=15
Z=20
Z=25
Z=30
Z=35
Z=40
Z=45
1.0
0.8
0.6
0.4
0.2
−0.4 −0.2 0.0 0.2 0.4
$V_{//}/V_{beam}$
$V_{\perp}/V_{beam}$

center of mass. At intermediate Z values, the emission becomes nearly isotropic (Z=20 for the Al and V targets, lower Z values for the Cu and La targets). For heavy fragments, the higher parallel velocity indicates forward peaking of the distribution.

The backward peaking of the distribution of light fragments in the $V_{||}$-$V_{\perp}$ indicates that there is some memory of the entrance channel (since the target is moving backward in the center-of-mass). This would arise if the fragment were emitted as the target-like partner in a deep inelastic reaction. Consequently, the heavy fragments are emitted forward in the center-of-mass in these types of reactions. The same type of angular distribution arises in non-equilibrium (or fast- or quasi-) fission. This type of fission occurs on a faster time scale than symmetric fission, so there is some memory of the entrance channel. Quasi-fission can be thought of as a link along the ℓ-wave coordinate between fusion-fission and deep inelastic reactions (HIN89).

III.A.3. Angular Distributions

The angular distribution in the center of mass for representative fragments for the reactions on each target are shown in Figure III.13 for the Al and V targets and Figure III.14 for the Cu and La targets. The angle was determined in the following manner:

$$\Theta_{cm}=\arctan\frac{V_{\perp}}{|V_s-V_{||}|} \qquad \text{(III.2)}$$

in which $V_{\perp}$ is the perpendicular velocity of the fragment, $V_{||}$ is the parallel velocity of the fragment, and V_s is the source velocity of that fragment determined from coincidence events. If $V_{||}$ is less than V_s, then Θ_{cm} is 180°-

Figure III.13: Angular distributions in the center of mass for representative fragments for the reactions La + Al, V. The solids lines are the results of a quadratic fit to the experimental points using a least-squares method.

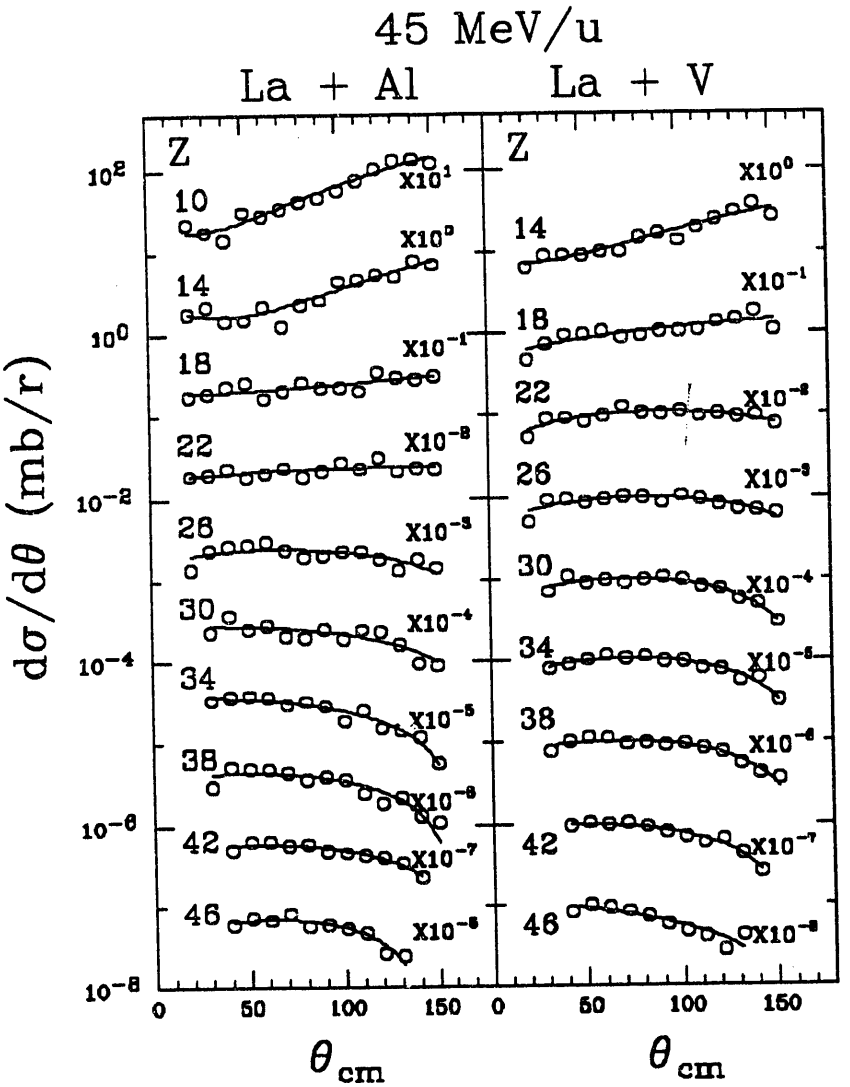
45 MeV/u
La + Al
La + V
Z
10
14
18
22
26
30
34
38
42
46
X10^1
X10^0
X10^-1
X10^-2
X10^-3
X10^-4
X10^-5
X10^-6
X10^-7
X10^-8
dσ/dθ (mb/r)
10^2
10^0
10^-2
10^-4
10^-6
10^-8
0
50
100
150
θ cm

Figure III.14: Same as Figure III.13 for the reactions La + Cu, La.

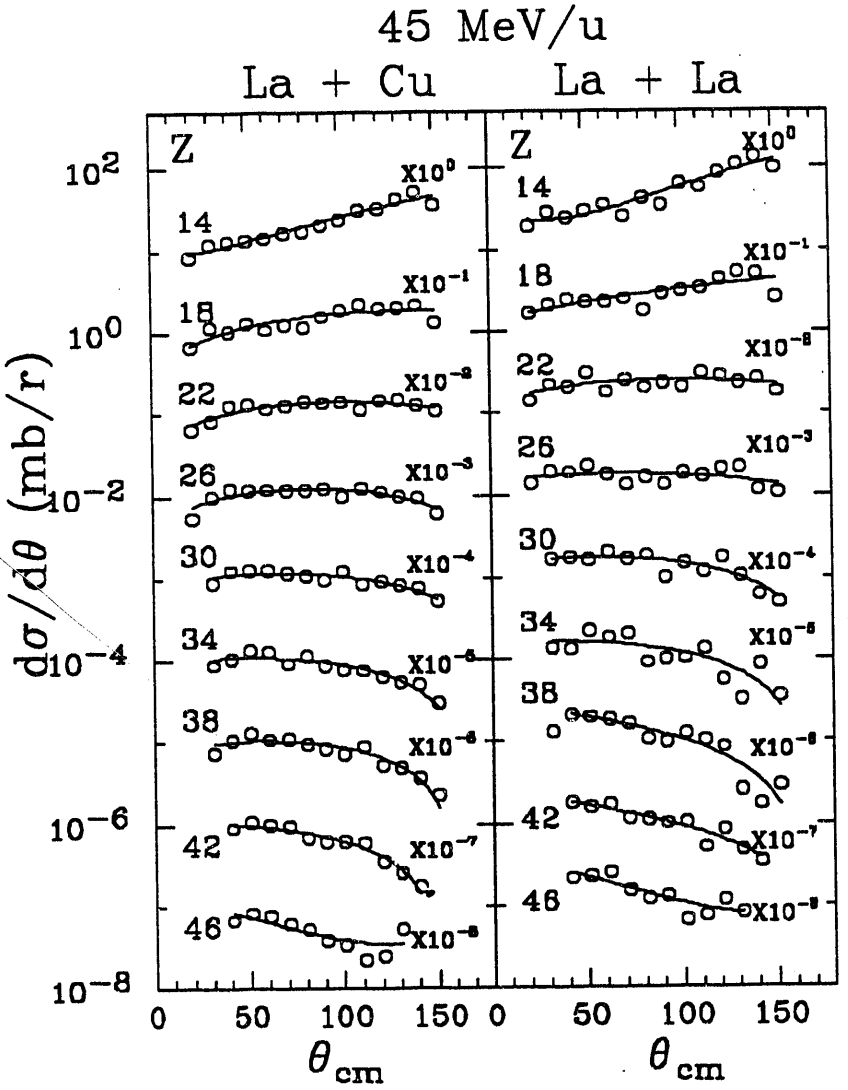
45 MeV/u
La + Cu
La + La
Z
14
18
22
26
30
34
38
42
46
X10^0
X10^-1
X10^-2
X10^-3
X10^-4
X10^-5
X10^-6
X10^-7
X10^-8
10^2
10^0
10^-2
10^-4
10^-6
10^-8
dσ/dθ (mb/r)
0
50
100
150
θ cm

Θ_{cm}. If the distribution in the $V_{||}$-$V_{\perp}$ plane is isotropic, then the source velocity can be determined from the centers of the Coulomb circles. However, this is not possible for this experiment as the fragment angular distributions go from being very backward to very forward peaked as the Z of the fragment increases. Only for a very narrow range of fragments is the yield isotropic. Because of this feature, the source velocity was determined from the coincidence events. The source velocity was calculated by the relation:

$$V_S = \Sigma p(i)/m(i) \qquad \text{(III.3)}$$

in which **p**(i) is the momentum vector of fragment i and m(i) is its mass determined from Equation III.1. This determination of the source velocity is almost model independent, relying on the constraint that the event was completely detected (which may not necessarily be true). The lines in Figures III.13 and 14 are the results of quadratic fits to the data for each fragment Z value, which was later used to determine the angle integrated cross sections.

The angular distributions show the same general trend as was seen in the Coulomb circles. The angular distributions range from very backward emission for light fragments to very forward emission for the heaviest fragments. A flat distribution is seen only for a limited range of fragment Z values. As stated above, this evolution of the angular distribution could be the result of deep inelastic or quasi-fission reactions. If this angular distribution is a result of asymmetric quasi-fission, then the nearly isotropic angular distributions for fragments with $Z \approx 20$ for the reactions on Al and V could arise from symmetric (equilibrium) fission. The decrease in the fragment Z for nearly isotropic emission as the target mass increases could be an indication of more pre-

equilibrium emission of light particles as the target mass increases. The anisotropy of the angular distribution could also be an indication of pre-equilibrium emission of complex fragments.

III.B.4. Integrated Cross Sections

The angular distributions for each fragment for reactions on each target were fit to a quadratic using a least squares method and then integrated from 0° to 180° to obtain the angle integrated cross section for each fragment charge, as shown in Figure III.15. For the lightest and heaviest fragments, which show the greatest anisotropies in the angular distributions, the integrated cross section can change by as much as a factor of two due to uncertainties in the yield of the fragments emitted at very forward (or backward) angles in the center of mass. This is because of the limited angular coverage of the array at forward laboratory angles (which correspond to either very forward or backward angles in the source frame). This uncertainty is reflected in the error bars in Figure III.15. The error bars were constructed by fitting the angular distribution for each fragment to a linear plus exponential fit in addition to the quadratic fit mentioned. (The error bars were also multiplied by the factor for each target shown in Figure III.15.) Only for the lightest and the heaviest fragments is there a significant difference between the integrated cross sections obtained by these two different fitting procedures.

The distributions of the total cross sections show a smoothly decreasing function for each target up to Z=30, and then increase slightly (for the Al target) or remains nearly constant (the heavier targets). This type of distribution could result from several different processes. The smoothly decreasing distribution

Figure III.15: Angle-integrated cross sections for fragments detected in the reactions La + Al, V, Cu, and La. For all fragments, the statistical error bars are smaller than the points. The error bars shown were determined by fitting the experimental angular distributions to a quadratic and to a linear plus exponential function. In all cases, the error bars have been multiplied by the same factor as the experimental data.

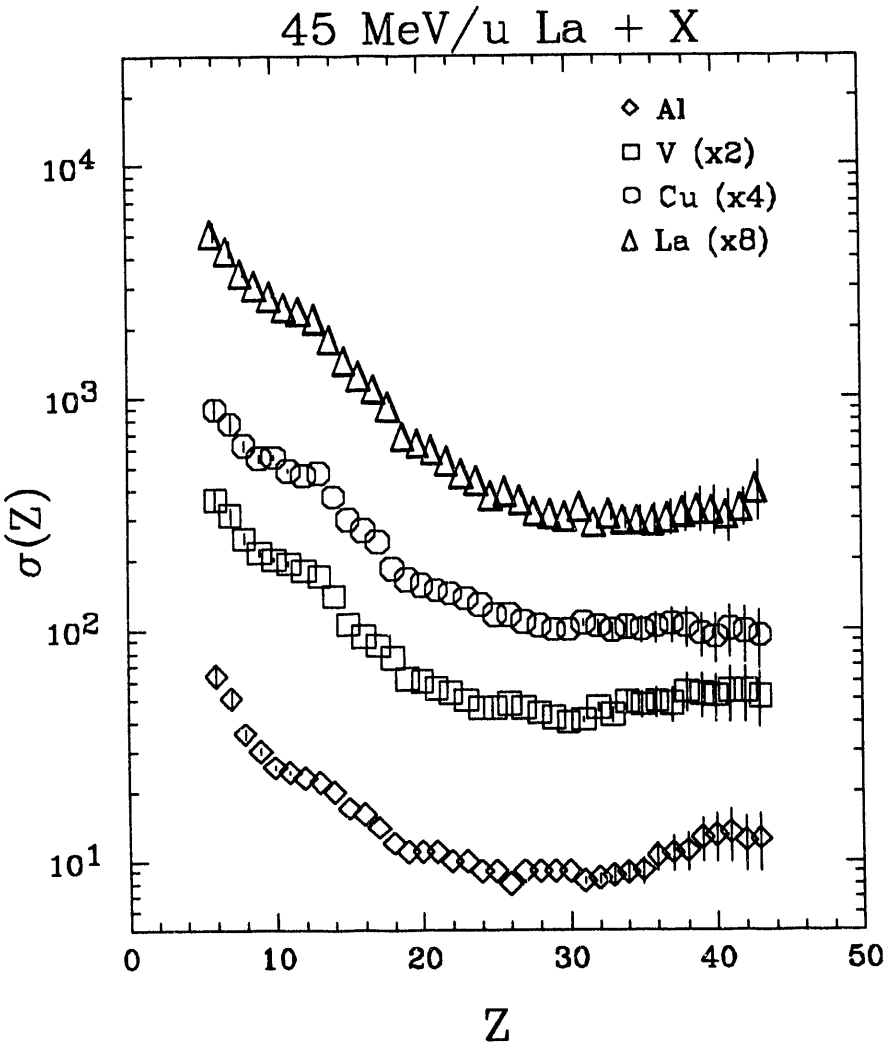
45 MeV/u La + X
◇ Al
□ V (x2)
○ Cu (x4)
Δ La (x8)
10^4
10^3
10^2
10^1
σ(Z)
0
10
20
30
40
50
Z

could be a result of some type of multifragmentation. This would lead to a depletion of the cross section for the heavier fragments and an increase for the lighter fragments. The flattening of the distribution for the heavier targets could be a result of an increase in the excitation energy of the system formed (compared to the Al target). This increase in excitation would then lead to an increase of fission and complex fragment emission from the source, again depleting the cross section at high Z values and increasing the yield at lower Z's.

III.B. COINCIDENCE RESULTS

As discussed in Section III.A.3, coincidence results can be used to determine features of the reaction that cannot be well determined by the inclusive data. Additionally, fragment-fragment correlations can further clarify reaction mechanisms that may be occurring.

III.B.1. Total Charge Distributions

The total charge detected for all coincidence events, and also for events in which the multiplicity of complex fragments n is equal to 2, 3, and 4, is shown in Figure III.16. Several features are readily apparent by examining Figure III.16. One of the most striking features is the peak at Z_{tot}=52 for n=2 for the reaction on La. This peak is most likely the result of an oxide coating on the target due to poor vacuum. For the higher multiplicity events for the La target, this peak disappears, showing that there is little contamination in the n=3 and 4 events. As the event multiplicity increases, the tail at low Z_{tot} for each multiplicity and target decreases. This tail arises from the incomplete detection

Figure III.16: Total charge distributions for multiple fragment events for the reactions La + Al, V, Cu, and La. The top row of histograms are the distributions for all events; the lower rows are for events with a multiplicity of complex fragments n equal to 2, 3, and 4.

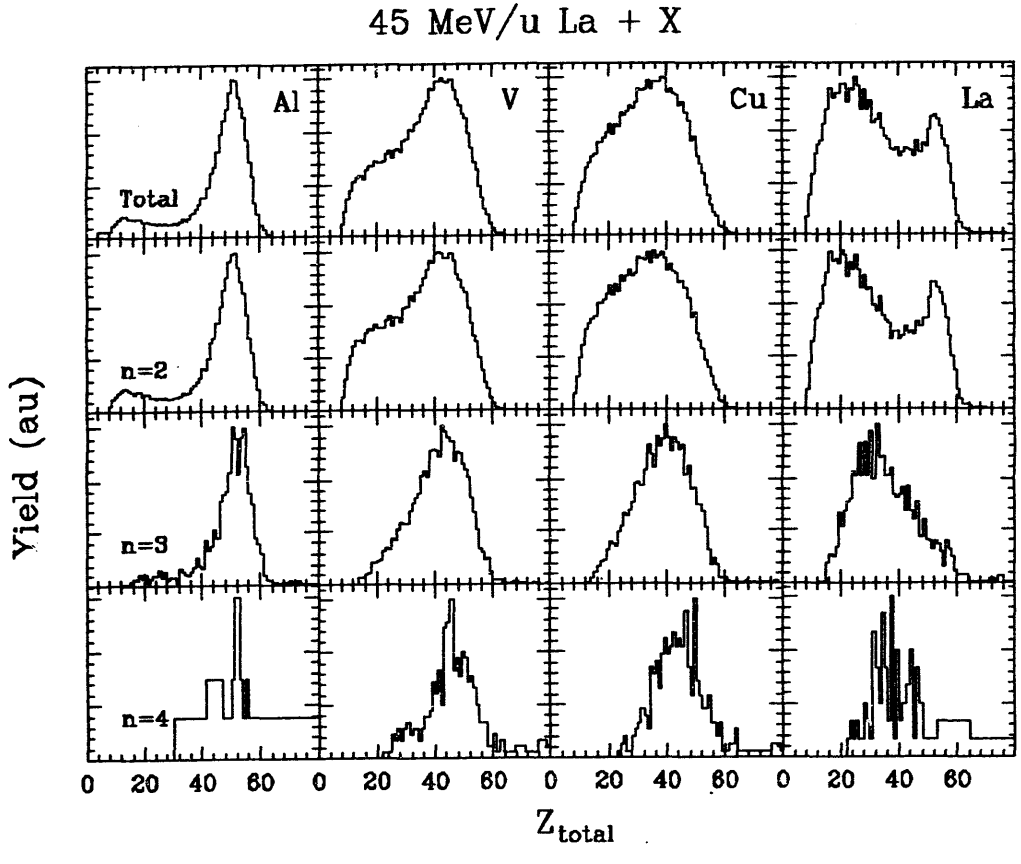
45 MeV/u La + X
Al
V
Cu
La
Total
n=2
n=3
n=4
Yield (au)
0
20
40
60
Z_{total}

of a higher multiplicity event (i.e. for an n=3 or 4 event, only 2 complex fragments were detected).

The values of the centroids of the distributions for each target and multiplicity are shown in Table III.1. For the Al target, the centroid remains nearly constant independent of the multiplicity. The missing charge ($Z_p+Z_t - Z_{tot}$) in this reaction can easily be accounted for by light particle emission (both pre- and post-equilibrium) and by any target-like-fragment remaining after an incomplete fusion reaction.

This is not the case for the reactions La + V, Cu, and La. For these reactions, the centroid increases as the multiplicity increases. The most likely reason for this missing charge is the lack of detection of complex fragments emitted to large angles. This is especially true for the reaction La + La, in which the total charge detected in n=4 events is still less than half the total charge of the system. One can easily see by examining Figures III.1-8 that the yield of heavier complex fragments decreases at large angles. However, the light IMF's ($4<Z<10$) can still be emitted to angles greater than that covered by the array. The values of the centroids are also lower for the heavier targets as compared to the Al target. This can be caused by the missing of fragments, but also by the increased evaporation and pre-equilibrium emission of light particles from the heavier targets, due to the increase in available energy (in the center of mass) as the target mass increases.

III.B.2. Z1-Z2 Correlations

Shown in Figure III.17 are contour plots in the Z1-Z2 plane for the reactions with each target. In order to remove any possible experimental bias for

the detection of light or heavy fragments, the identification of the fragment as Z1 or Z2 has been randomized.

Table III.1 Centroids of the Z_{tot} distributions as a function of complex fragment multiplicity. The * for the n=2 centroid for La indicates that the peak at Z_{tot}=54 from the reaction La + O has been ignored.

Multiplicity	Al	V	Cu	La
2	50.44± 5.26	40.12± 12.0	33.12± 14.4	23.51±10.4*
3	51.99± 5.06	42.39± 9.30	39.31± 9.92	33.37± 10.9
4	52.24± 3.18	46.15± 7.04	43.51± 8.10	36.70± 7.42

The Z1-Z2 plot for the reaction on Al shows a ridge at constant Z1+Z2, with only a small amount of yield below this ridge line. This ridge is an indication that the decay of hot nuclei formed in this reaction is essentially binary and from a well defined source. Along this ridge line the yield is mostly due to asymmetric combinations of the two fragments (one fragment heavy, the other light), but there is some yield at more symmetric splits.

For the V and Cu targets, the Z1-Z2 plots lack the binary ridge of the Al reaction. This shows that the decay of the composite system formed in these reactions is not well characterized by the identification of 2 fragments. By examining the total Z detected for these two targets for n=2 events, one can see that the tail extending to low total Z makes up a large portion of the distribution, which shows up as contours filling in the entire space available in the Z1-Z2 plane.

Figure III.17: Contour plots of yield in the Z1-Z2 plane for the reactions La + Al, V, Cu, and La.

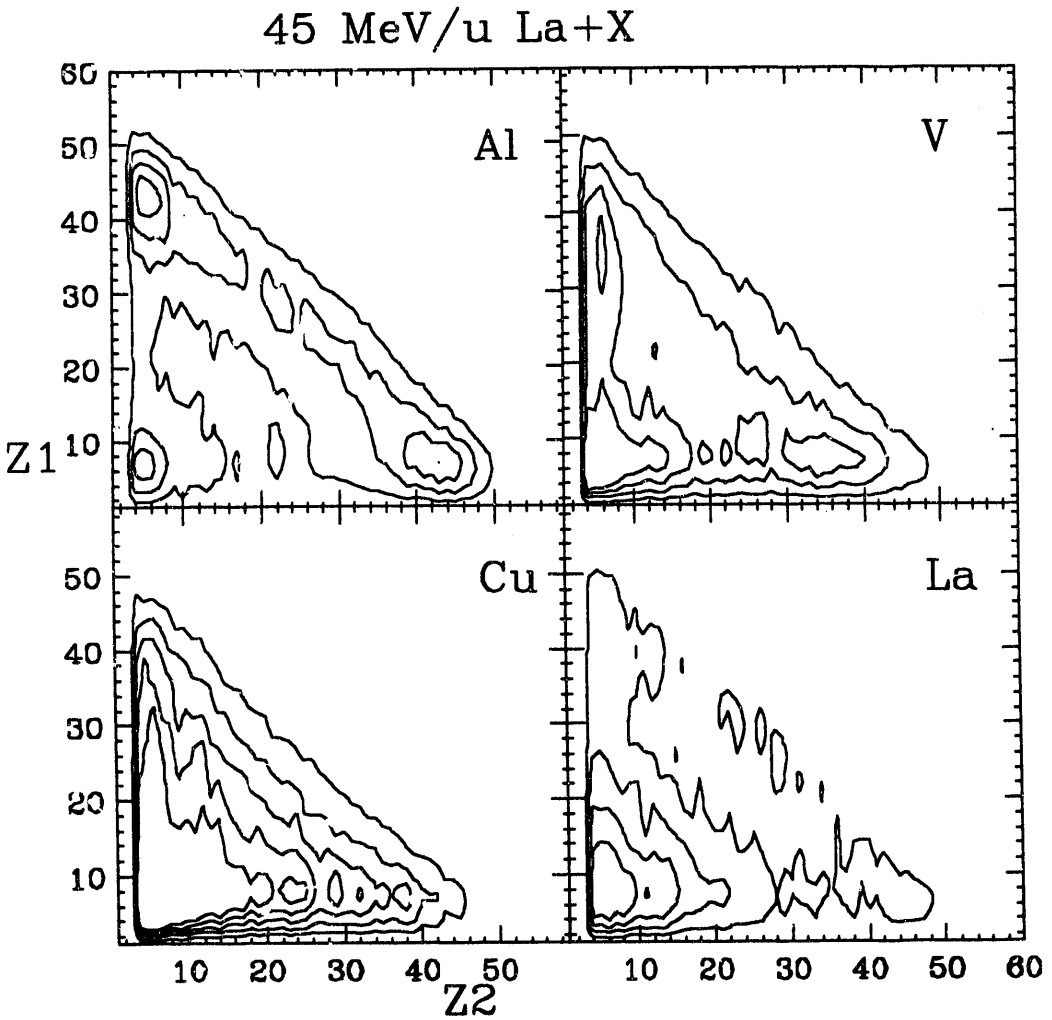
45 MeV/u La+X
Al
V
Cu
La
Z1
Z2
10
20
30
40
50
60

For the reaction on the La target, the yield at the constant Z1+Z2 ridge line is due to the oxygen contamination. Although the statistics for this target are poor, the asymmetric and symmetric fission events are visible along this line. There is appreciable yield at lower Z1-Z2 correlation due to the reactions on the La target. For each target there is yield at low values of Z1-Z2 correlation. This is due to complex decays in which more than two fragments are produced. Although this effect is not large for the reaction La + Al, its importance increases as the mass of the target increases, so that for the reactions La + Cu and La + La multiple fragment events dominate the distributions.

III.B.3. Source Velocity Distributions

As discussed in Section III.A.3, if a hot nucleus undergoes statistical decay, then the source velocity of a fragment can be extracted from the center of a Coulomb circle, and is independent of the fragment charge. However, for the experiment studied, the plots in the $V_{\perp}$-$V_{||}$ space do not exhibit well defined circles, so this method fails. The source velocity for the reactions studied was determined event-by-event by use of Eq. III.3. The source velocity distributions for reactions on each target are shown in Figure III.18. To ensure that the kinematic reconstruction was adequate, the source velocity was determined only for those events in which the total charge detected was greater than 30. The top row of histograms is the total distribution; the lower histograms are gated on multiplicity of complex fragments equal to 2, 3, and 4. The arrows above each column refer to the source velocity for complete fusion for each target. The centroids of the distributions for each multiplicity and target are given in Table III.2.

Figure III.18: Source velocity distributions for multiple fragment events for the reactions La + Al, V, Cu, and La. The arrows above each column refer to the source velocity for complete fusion for each reaction. The rows of histograms refer to the total distribution and the distribution for events with a multiplicity of complex fragments n equal to 2, 3, and 4.

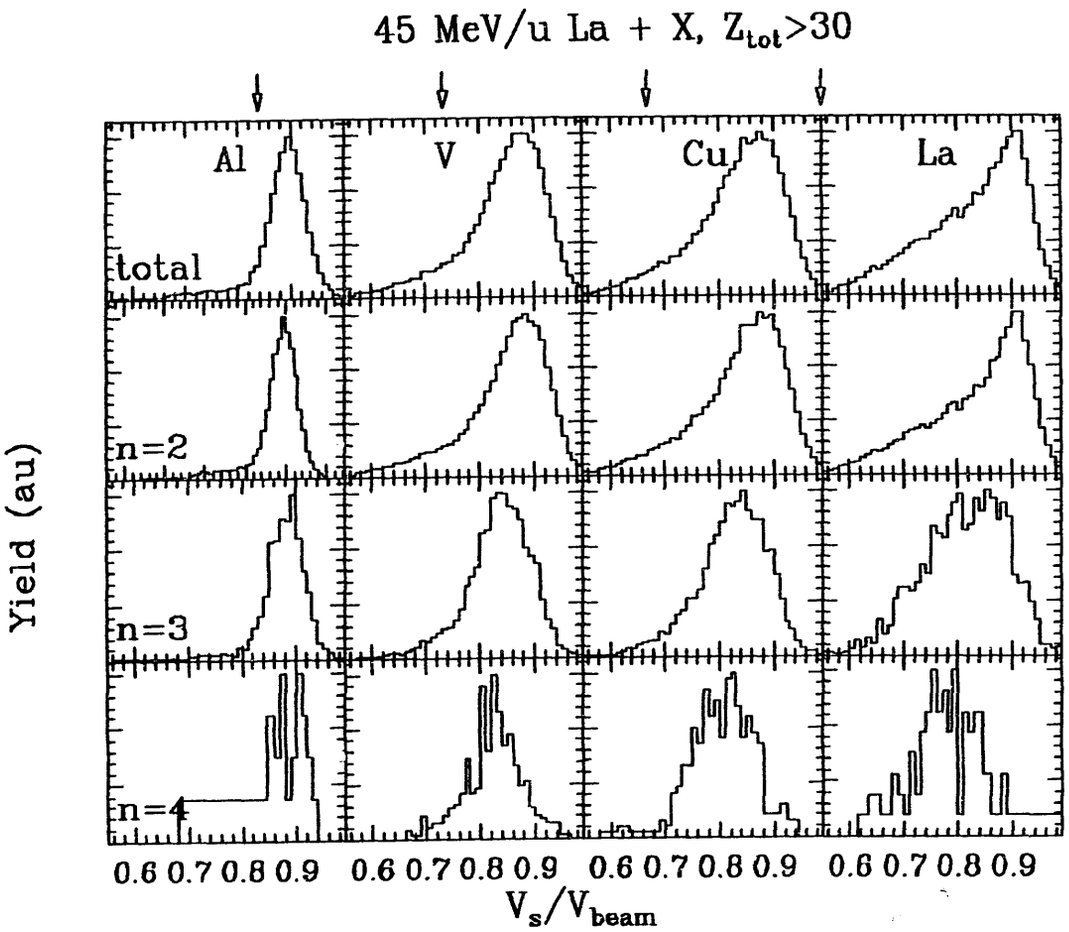
45 MeV/u La + X, Z_{tot}>30
Al
V
Cu
La
total
n=2
n=3
n=4
Yield (au)
0.6 0.7 0.8 0.9 0.6 0.7 0.8 0.9 0.6 0.7 0.8 0.9 0.6 0.7 0.8 0.9
V_s/V_{beam}

Figure III.19: Distributions in the V_S-Z_{tot} plane for n=2 and 3 events for the reactions La + Al, V, and Cu.

45 MeV/u La+X

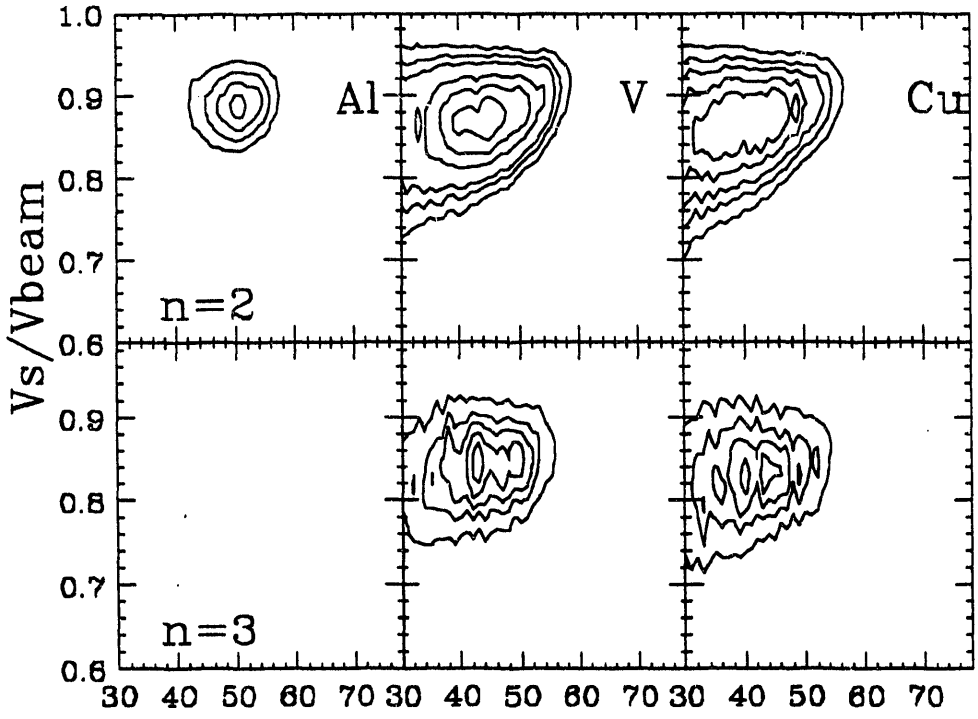

Ztot

As the multiplicity n increases, the tail at low source velocity decreases. This is similar to what is seen with the total Z distributions and gives further indication that the tail arises from incompletely detected events. For each target and multiplicity (except for n=4 for the reaction La + Al), the source velocity decreases as the multiplicity of complex fragments increases. For the Al target, the total Z remains constant for the n=3 and 4 events. This is not the case for the heavier targets, where the Z_{tot} increases with multiplicity. Because source velocity and impact parameter are correlated (central collisions have a lower source velocity) this could indicate that a more central collision is needed to produce the higher multiplicity events.

Table III.2 Centroids of the source velocity distributions (as a fraction of beam velocity) as a function of complex fragment multiplicity for each target studied.

Multiplicity	Al	V	Cu	La
2	.896±.032	.875±.056	.865±.076	.890±.056
3	.884±.030	.844±.052	.836±.058	.824±.080
4	.887±.036	.826±.044	.808±.056	.777±.056

For each target and multiplicity, the source velocity is between that of the beam and the complete fusion product (compound nucleus). This indicates that the hot nuclei in these reactions are formed by some kind of incomplete fusion reaction, in which only a portion of the target is incorporated into the projectile. The fate of the target spectator matter is unknown.

The decay characteristics of these excited nuclei can be further examined by comparing contour plots in the Z_{tot} -V_s space for the n= 2 and 3 events for

each target, as shown in Figure III.19. For the n=2 events, only the reactions on the Al target are well characterized by the detection of two fragments. The distribution is centered at a well determined source velocity and total charge. This is another good indication that the decay of hot nuclei formed in these reactions is essentially binary.

For the heavier targets, the decay is not well characterized in the Z_{tot} - V_S plane by the detection of either two or three fragments. Instead, the distribution is over a much broader range on both the Z_{tot} and V_S axes. Low Z_{tot} is correlated with a low source velocity, showing that these events have not been well determined, even by the detection of three fragments.

As the multiplicity increases to n=3, the distribution in the Z_{tot}-V_S space narrows slightly compared to that for n=2, but is still very broad. This is an example that, at these energies, hot nuclei are formed over a range of impact parameters, and it is difficult to focus on a specific source of complex fragments.

III. B. 4. Decay Probabilities

The width of the source velocity distribution arises from two different sources - the evaporation of light particles and the formation of sources at different impact parameters. It has been estimated that about half of the width of the source velocity distribution for the reaction La + Al is due to light particle evaporation, and that this fraction decreases as either the target mass or the bombarding energy increases (BLU91). In other words, it is possible to focus on an impact parameter range of a reaction by gating the data on different source velocities.

The probability of decaying by an n-multiplicity event can be calculated for different gates of the source velocity distribution. This probability is simply:

$$P(n)=\frac{Y(n)}{Y(2)+Y(3)+Y(4)} \qquad \text{(III.4)}$$

in which P(n) is the probability, Y(n) is the yield of multiplicity n events at a certain source velocity. Thus, Y(2), Y(3), and Y(4) are the yields of n=2, 3, and 4 events at that source velocity.

A plot of the decay probability P(n) as a function of source velocity is shown in Figure III.20 for each target studied. This figure shows that the decay probability is nearly independent of the target mass over the entire range of source velocities. One can further examine the results from Figure III.20 by converting source velocity to excitation energy to remove the beam velocity term from Figure III.20. First, the mass of the source must be determined. It can be inferred from the source velocity by assuming conservation of momentum in an incomplete fusion reaction where the excitation energy (and the laboratory velocity) of the unfused fragment is zero. The mass of the source is then:

$$A_S=A_p\frac{V_b}{V_s} \qquad \text{(III.5)}$$

in which A_p is the projectile mass, and V_b and V_s are the beam and source velocities, respectively. The total excitation energy of the incomplete fusion product is:

$$E^*=\frac{A_S-A_p}{A_S}E_b \qquad \text{(III.6)}$$

in which E_b is the beam energy in MeV. Equation III.6 also neglects reaction Q-values, which are quite small compared to the total excitation energy of the system. This total excitation energy is then divided by the source mass to give the excitation energy per nucleon of the source.

The conversion from source velocity to excitation energy has several assumptions that may not be valid. The first is that any target remnant left after the incomplete fusion reaction remains at zero laboratory velocity and excitation, which is probably not true. However, the velocity and excitation are most likely very small. The second is that the event has been completely characterized by the detection of 2, 3, or 4 fragments, which is probably valid for the Al target (in which Z_{tot} remains fairly constant independent of the multiplicity). For the other targets, however, Z_{tot} increases with multiplicity, indicating that some fragments are not detected. The third assumption is that no excitation energy is lost from pre-equilibrium emission of light particles, which also is not valid for these reactions. However, the net effect of the second two assumptions would only be to contract the distribution to lower excitation energies. The same general trend in the P(n) distributions would still be present.

A plot of the decay probability P(n) as a function of excitation energy per nucleon of the source is shown in Figure III.21. To first order, this decay probability is shown to be dependent only on the excitation energy of the system, not on how that system was formed. Another feature is that the decay probability for higher fold events does not show a rapid increase as the excitation energy increases past 5 MeV/A. This is at odds with many multifragmentation models (as stated in Chapter I), which predict an increased probability of multifragmentation as the excitation energy passes 5 MeV/nucleon.

Figure III.20: Decay probability P(n) as a function of source velocity for multiple fragments events for all reactions studied.

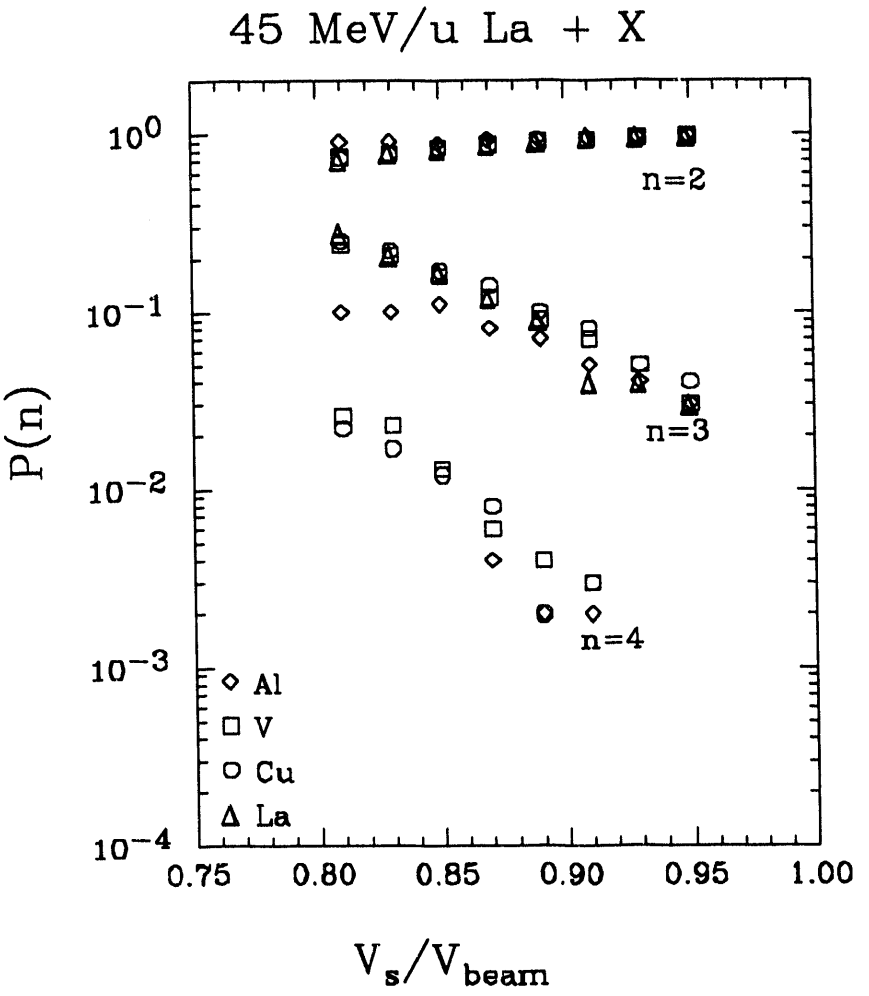
45 MeV/u La + X
P(n)
10^0
10^{-1}
10^{-2}
10^{-3}
10^{-4}
n=2
n=3
n=4
◇ Al
□ V
○ Cu
Δ La
0.75
0.80
0.85
0.90
0.95
1.00
V_s/V_{beam}

Figure III.21: Decay probability P(n) as a function of maximum excitation energy per nucleon of the source for multiple fragment events for all reactions studied.

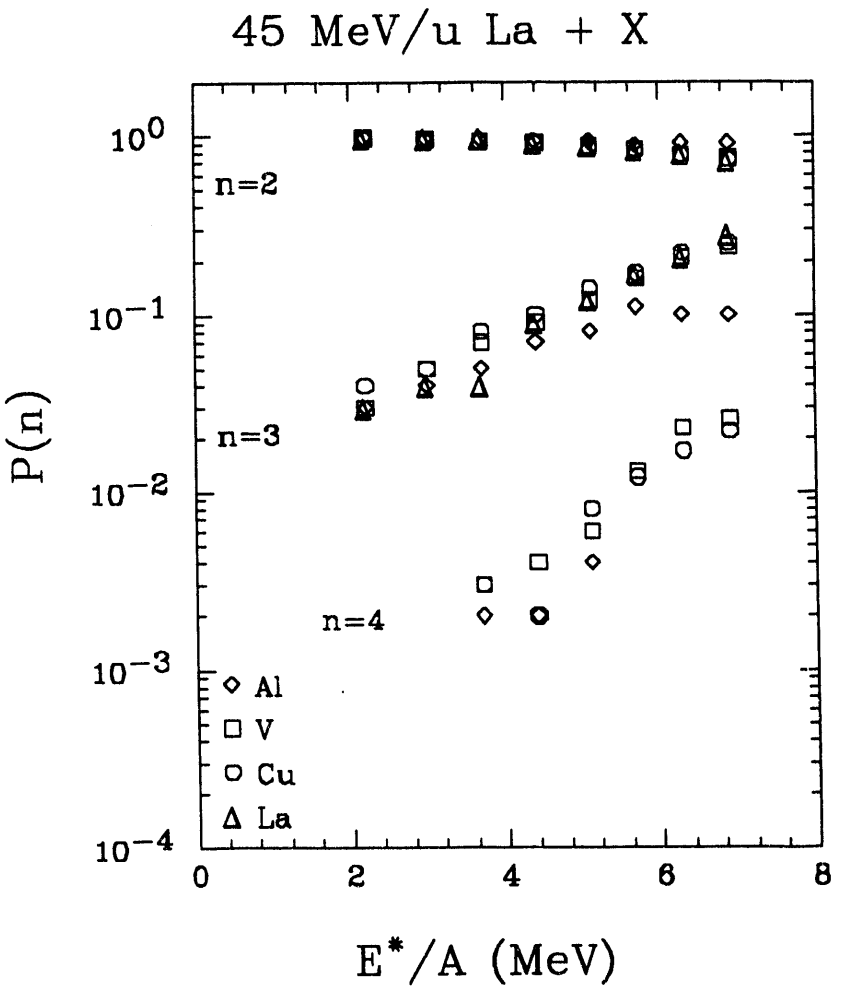
45 MeV/u La + X
P(n)
10^0
10^{-1}
10^{-2}
10^{-3}
10^{-4}
n=2
n=3
n=4
Al
V
Cu
La
0
2
4
6
8
E*/A (MeV)

III.B.5. Charge-Dalitz Plots

Another way of characterizing reactions in which three complex fragments are detected is to construct a charge-Dalitz plot of the Z's of the three fragments. A schematic of a Dalitz plot is shown in Figure III.22. The scales in the figure run from the edges of the triangle to the opposite vertex and have a value of Z_i/Z_{tot} in which Z_i is the charge of the fragment i (i =1, 2, or 3)and Z_{tot} is the total charge detected in the event. The fragments are randomized as to which is 1, 2, or 3; and the minimum Z_{tot} for which an event was characterized in this way was taken to be 30 in order to guarantee good kinematic characterization of the event. In a Dalitz plot, if the yield is concentrated at the vertices, then the event has one large fragment and two small ones. Yield along the edges corresponds to 2 medium and one small fragment; yield in the center is due to nearly symmetric 3-body splits.

Contour plots in the Dalitz space for the reactions on the Al, V, and Cu targets are shown in Figure III.23. The La target was not included due to poor statistics. For the most part, the yield in the Dalitz plots for each target is concentrated at the vertices. For the Al target, the contour in the center of the plot is actually due to a hole. As the mass of the target increases, the yield along the edges and in the center increases. As this occurs, the peaks at the vertices decrease. This shows the increasing importance of more symmetric decay as the target mass increases.

As with the decay probability distributions, it is possible to see how the charge-Dalitz plots change as a function of source velocity (excitation energy). The source velocity distributions for the n=3 events showing the limits of the gates of the source velocity are shown in Figure III.24. Contours of the

Figure III.22: Schematic diagram of a charge-Dalitz plot.

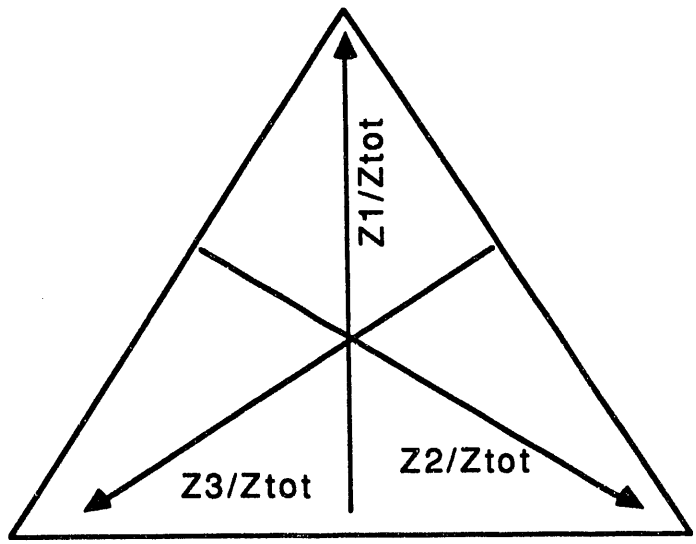
Z1/Ztot
Z3/Ztot
Z2/Ztot

Figure III.23: Charge-Dalitz plots for the reactions La + Al, V, and Cu.

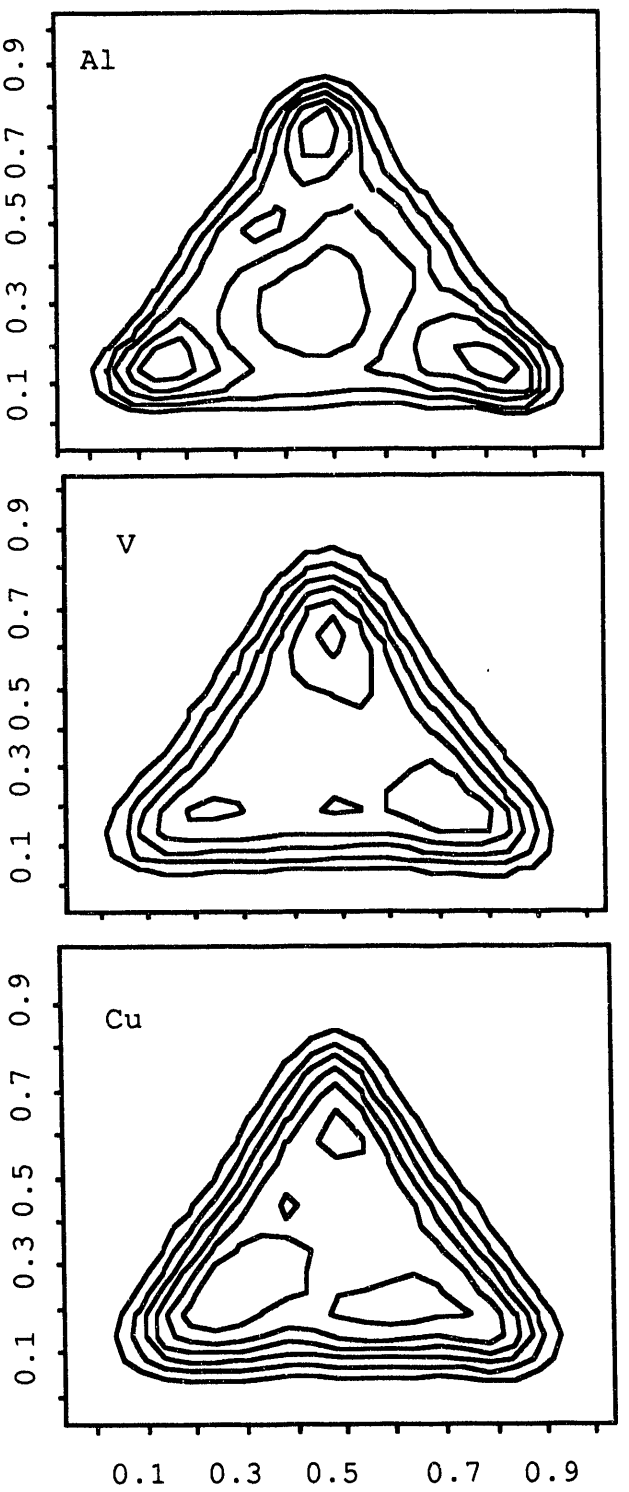
Al
V
Cu
0.1
0.3
0.5
0.7
0.9

Figure III.24: Source velocity distributions for n=3 events for the reactions La + Al, V, and Cu. The dashed lines correspond to the limits of the low and high source velocity used as gates for the charge-Dalitz plots.

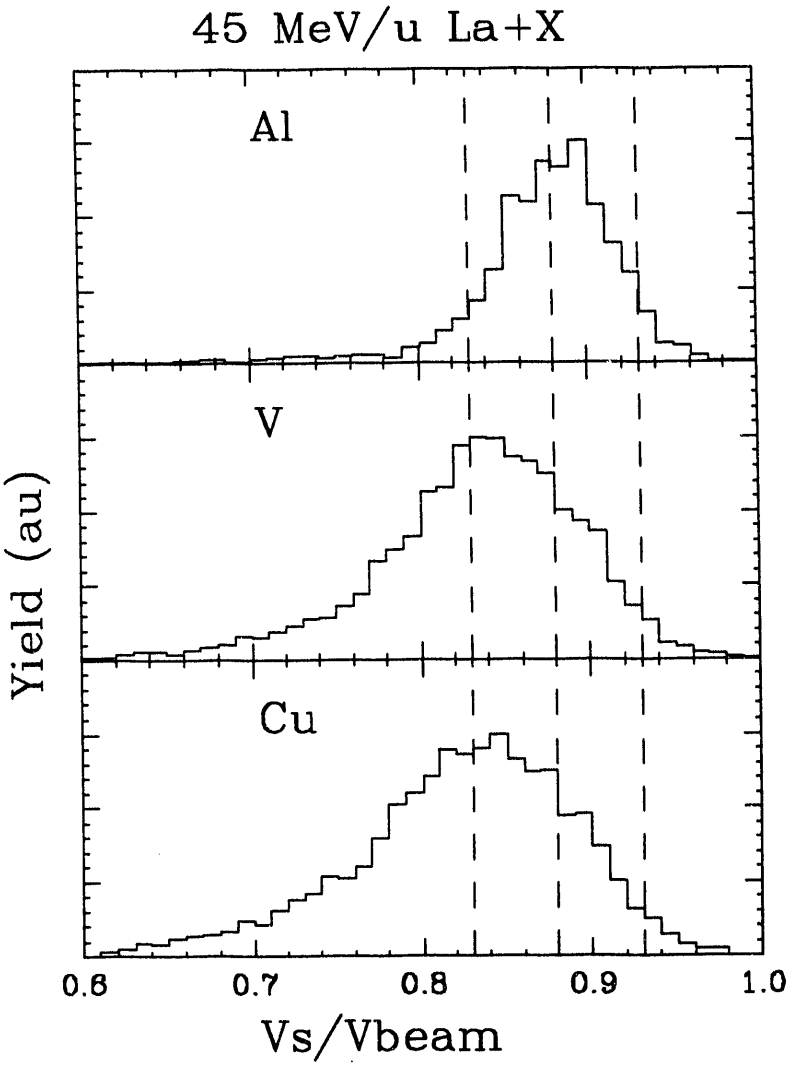
45 MeV/u La+X
Al
V
Cu
Yield (au)
0.6
0.7
0.8
0.9
1.0
Vs/Vbeam

Figure III.25: Charge-Dalitz plots for the reactions La + Al, V, and Cu gated on low source velocity.

.83< (Vs/Vbeam) < .88

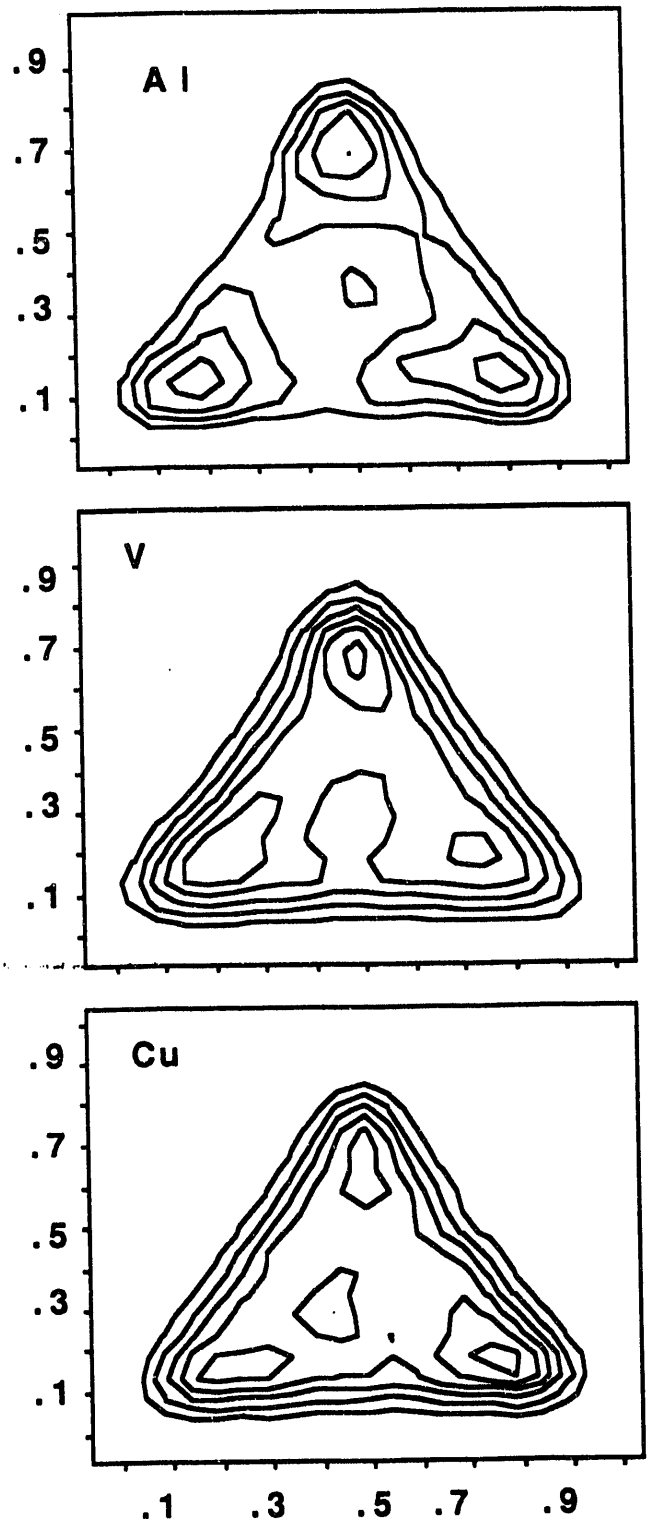

Figure III.26: Charge-Dalitz plots for the reactions La + Al, V, and Cu gated on high source velocity.

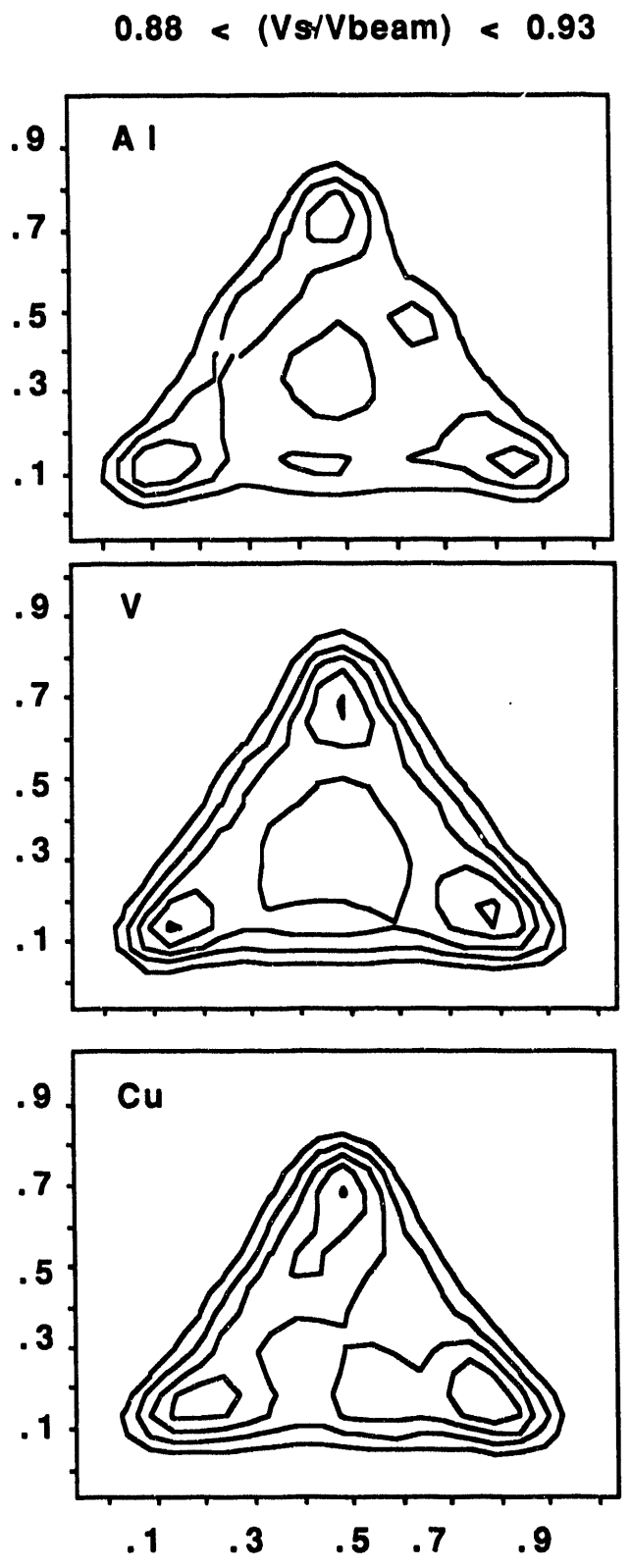
0.88 < (Vs/Vbeam) < 0.93
Al
V
Cu
.9
.7
.5
.3
.1
.1
.3
.5
.7
.9

distribution in Dalitz-space are shown in Figures III.25 and III.26 for two bins of source velocity .83<(V_S/V_{beam})<.88 and .88<(V_S/V_{beam})<.93. Important differences are seen between the charge Dalitz plots gated on source velocity. For the high source velocity bin (which corresponds to low excitation energy), the bulk of the distribution is at the vertices, meaning that the preferred decay at low excitation is to one heavy and two light fragments. There are holes in the centers of the space for the reactions La + Al and V, indicating that the probability of symmetric decay is low. For the Cu target, there is more distribution in the center of the Dalitz-space, which is most likely due to the contouring process. At higher excitation energy (lower source velocity) the yield in the center and along the edges increases for each target, indicating there more central collisions are needed to produce more symmetric decays.

III.B.6 Relative Velocity and Angle Measurements

In order to determine whether the reaction mechanism that produces three complex fragments is sequential or simultaneous, the relative angles and velocities between pairs of fragments in n=3 events were calculated. The shapes of these distributions are sensitive to the mechanism of the breakup. For a simultaneous breakup, the relative velocities and angles between pairs of fragments are similar. On the other hand, in a sequential breakup, the first scission defines two directions, so that one fragment is detected approximately 180° from the other two.

Histograms of the relative velocities and angles between pairs of fragments in n=3 events for the reactions on the Al, V, and Cu targets are shown in Figures III.27-29, respectively. The La target was not included in this

analysis due to poor statistics. In these plots, HI refers to the relative velocity or angle between the heaviest and the middle-sized fragments, HL to the heaviest and the lightest fragments, and IL to the middle and lightest fragments.

One of the most striking features in Figures III.27-29 is the fact that the relative velocities and angles between pairs of fragments are quite insensitive to the target mass and dependent only on which pair of fragments is examined. The sharp peaks in the relative velocity spectra at 2 cm/ns is what is expected if the relative velocity is Coulomb-like in origin. However, the fact that these velocities can extend to greater than 4 cm/ns could indicate that there is some kind of interaction among the three fragments, boosting the velocities of each.

Within each target, important differences are seen in the relative angles between pairs of fragments (independent of the identity of the target). One of the most important features is the strong peak at θ_{rel}=160° - 170° for the HI and HL pairs. This is a good indication that these two fragments could arise from the fission of a heavy residue. The backward peaking is not as strong for the HL pair, but could still indicate a fission-like origin for this fragment pair also. The relative angle distribution for the IL pair shows no peak.

The average relative velocity between pairs of fragments in n=3 events has been used to judge the centrality of the collision (BOU88). If the relative velocities between the three pairs of fragments show a large difference, the production of the three fragments could be due to the fissioning of the target in a peripheral collision (in normal kinematics). On the other hand, similar relative velocities can only arise from symmetric divisions of the nucleus. As shown in the charge-Dalitz plots gated on source velocity (Figures III.25 and 26), symmetric decays preferentially occur for central collisions. The centrality can be expressed by calculating a quantity Y, which is related to the divergence of

Figure III.27: Relative velocity and angle distributions between pairs of fragments in n=3 events for the reaction La + Al. HI refers to the heavy-medium fragment pair, HL to the heavy-light pair, and IL to the medium-light pair.

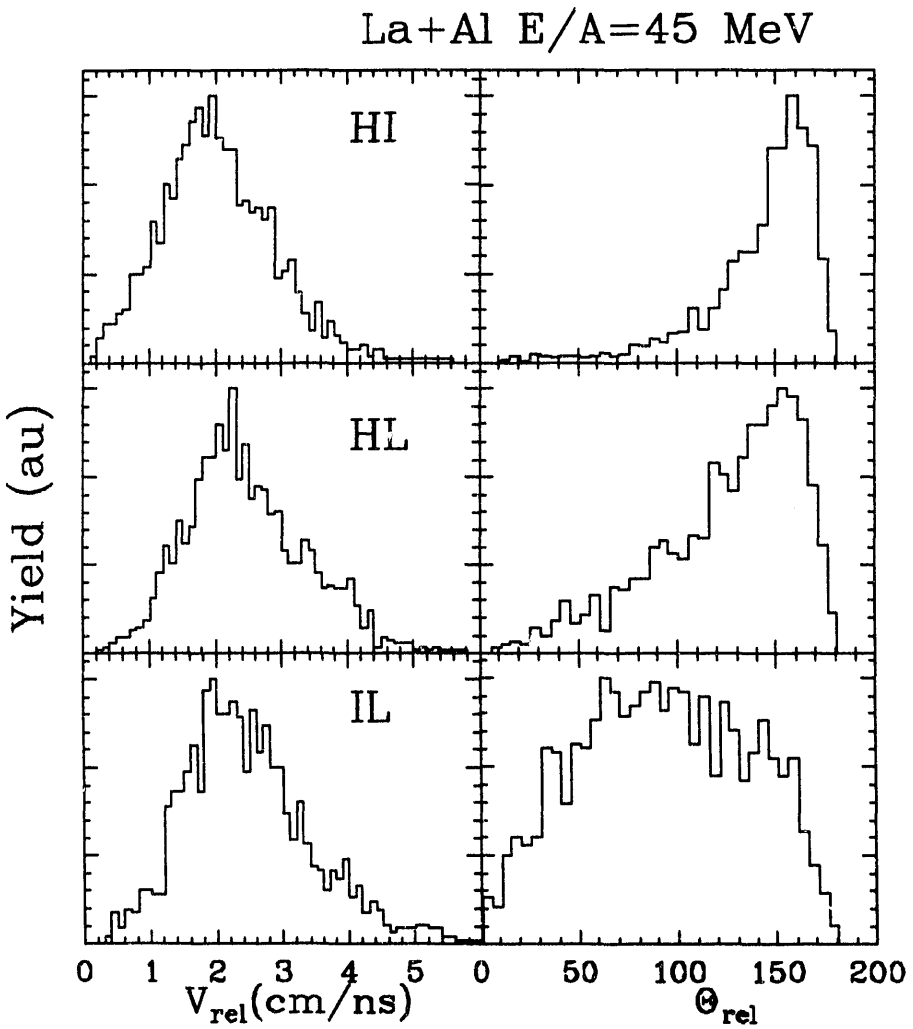
La+Al E/A=45 MeV
HI
HL
IL
Yield (au)
0 1 2 3 4 5
V_{rel}(cm/ns)
0 50 100 150 200
Θ_{rel}

Figure III.28: Same as Figure III.26 for the reaction La + V.

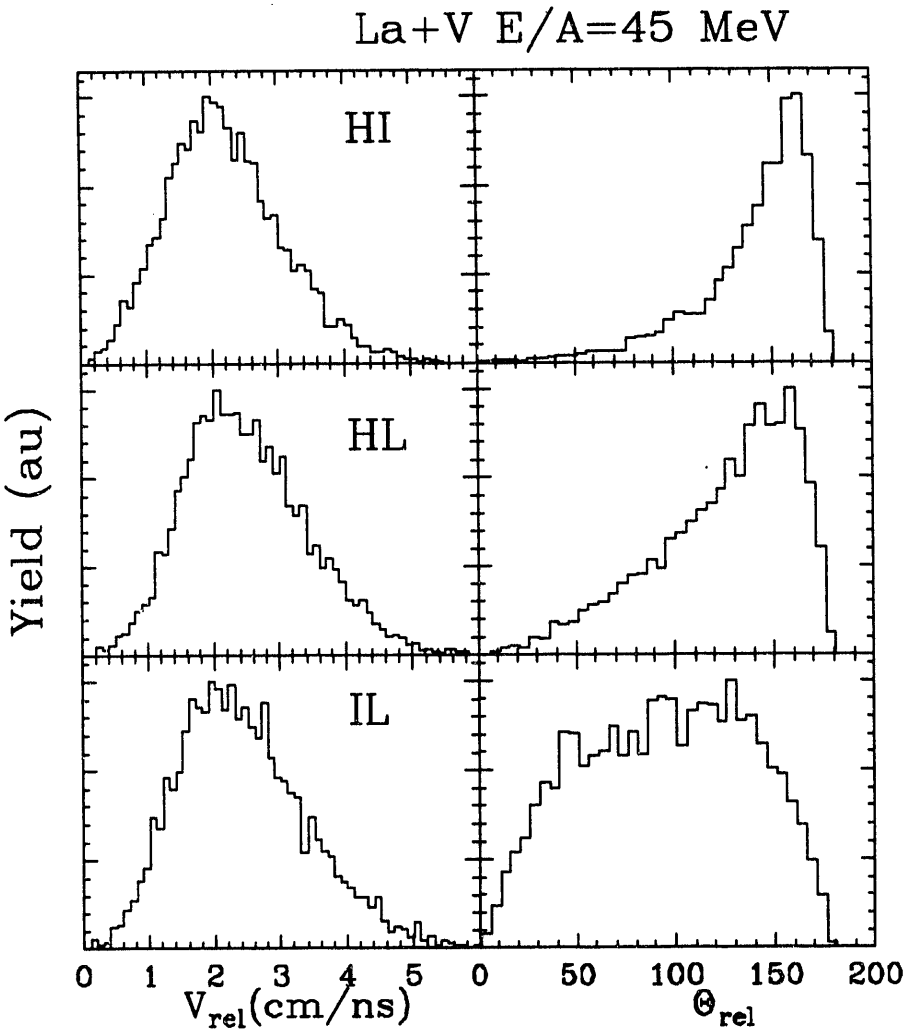
La+V E/A=45 MeV
HI
HL
IL
Yield (au)
0 1 2 3 4 5
V_{rel}(cm/ns)
0 50 100 150 200
Θ_{rel}

Figure III.29: Same as Figure III.26 for the reaction La + Cu.

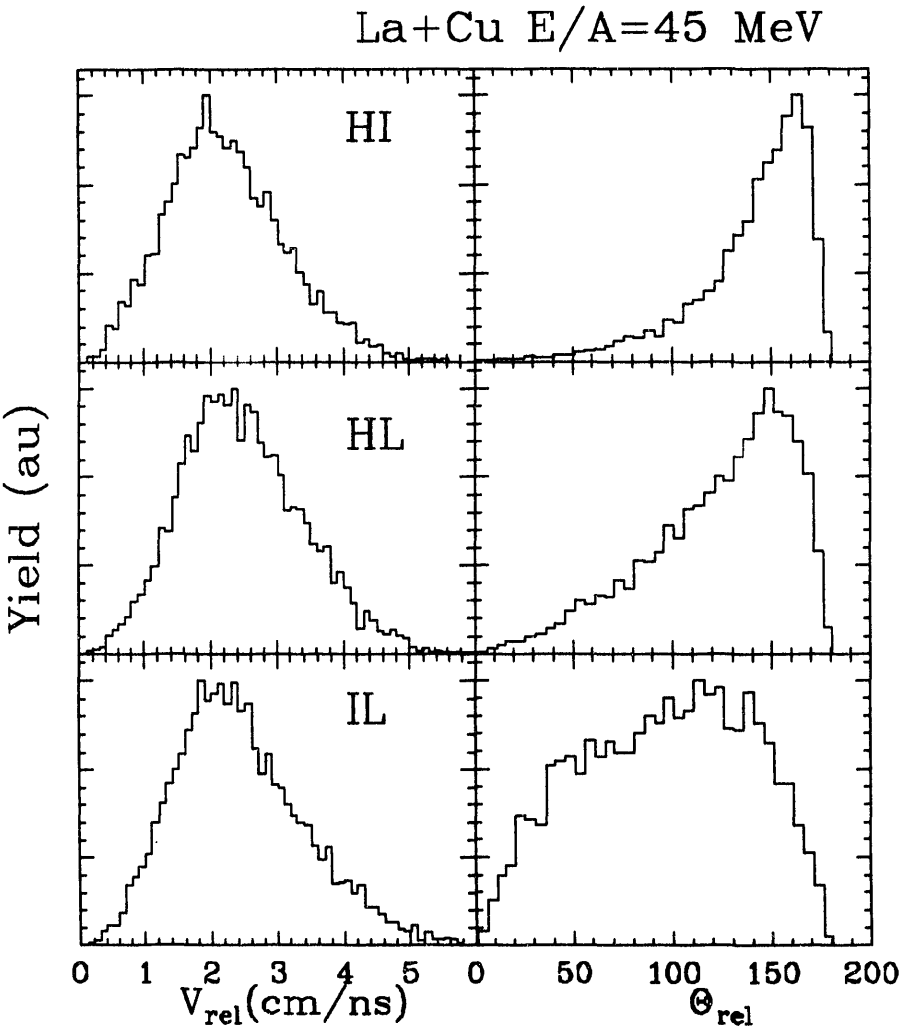
La+Cu E/A=45 MeV
HI
HL
IL
Yield (au)
0 1 2 3 4 5
V_{rel}(cm/ns)
0 50 100 150 200
Θ_{rel}

Figure III.30: Distributions in the Y-<v_{rel}> plane for the reactions La + Al, V, and Cu.

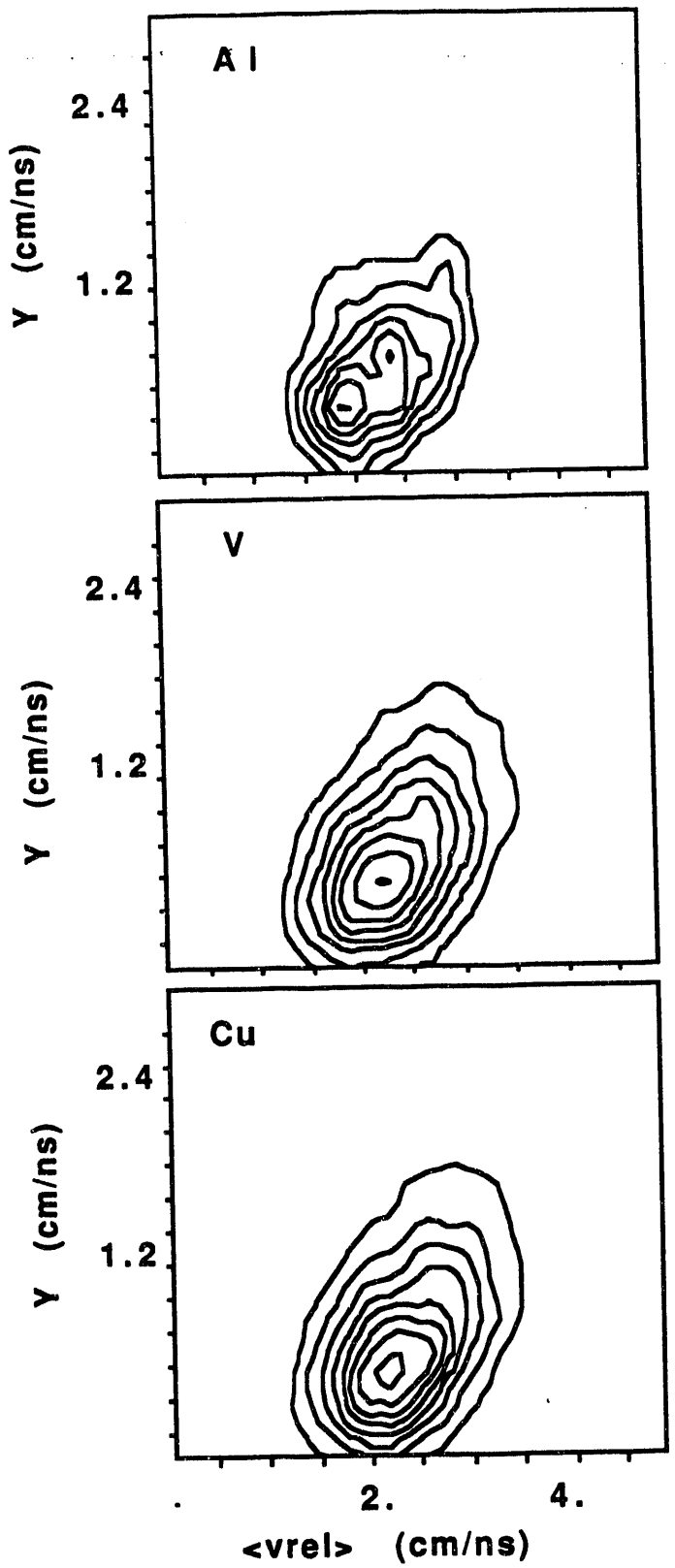
Al
V
Cu
2.4
1.2
Y (cm/ns)
2.
4.
<vrel> (cm/ns)

the relative velocities between the three pairs of fragments in the n=3 events, and is defined as:

$$Y = \langle v_{rel} \rangle - v_{rel,min} \qquad \text{(III.6)}$$

in which $\langle v_{rel} \rangle$ is the average relative velocity between the three pairs of fragments and $v_{rel,min}$ is the minimum relative velocity. This expression has been used to gate on event centrality for the reaction Kr + Au at E/A= 43 MeV (BOU88). In that reaction, two sources of n=3 events were found, corresponding to peripheral (Y>2 cm/ns) and central (Y<2 cm/ns) collisions. Contour plots of the value of Y as a function of $\langle v_{rel} \rangle$ are shown in Figure III.30 for the reactions La + Al, V, and Cu. Only one source of n=3 events is apparent for these reactions, and the distributions are almost identical for each target studied. The values of Y for these reactions are similar to those used to identify the central collisions in the reaction Kr + Au at E/A = 43 MeV, indicating that the n=3 events in this study probably arise from central collision.

III.C. RECOIL DETECTORS

The results for the recoil detectors will only be described in the most general terms. The results will not be used to attempt to characterize any specific mechanism, due to the problems described in Chapter II. However, one can use these results to give a general picture of what may be occurring. Even though it is possible, in principle, for events in the recoil arc to be detected in coincidence with multifragment events in the array, the coincidence rate was too low, so that events could not be kinematically reconstructed.

As discussed in Chapter II, there were many experimental difficulties involving the recoil detectors. Because the time-of-flight and the energy of the "fragments" were observed for events in which no target was in the beam, it was necessary to determine which range of time-of-flight and mass of fragments corresponded to real events. In order to determine whether a signal in any of the recoil detectors corresponded to actual detection of a fragment, correlation functions were constructed for the time-of-flight and the mass for "fragments" detected in the recoil arc. The correlation function has the form:

$$R_{12}=\frac{t-b}{t+b} \qquad \text{(III.7)}$$

in which t is the yield with a target in place and b is the yield with no target. The sum of the yields over all times was normalized so that the function has a value between -1 and 1. The time-of-flight correlation function is shown in Figure III.31 for the Al, V, and Cu targets. It is clear that times measured to be less than 50 ns or greater than 100 ns do not correspond to real events in the detectors.

With a window on the time-of-flight of 50 to 100 ns, the correlation functions were then constructed for the mass of the particles, the results of which are shown in Figure III.32. The condition on the mass of the fragment being a real mass is 50 to 100 amu. This condition is a result only from the correlation function, not from an actual physical limit of the detector system. Therefore only those fragments with a time-of-flight between 50 and 100 ns and a mass between 50 and 100 amu were further analyzed.

Histograms of the energy distributions of recoil fragments for reactions on the V, Cu, and La targets are shown in Figure III.33. The Al target was not

Figure III.31: Correlation function as a function of time-of-flight of the fragments detected in the recoil arc for the reactions La + Al, V, and Cu.

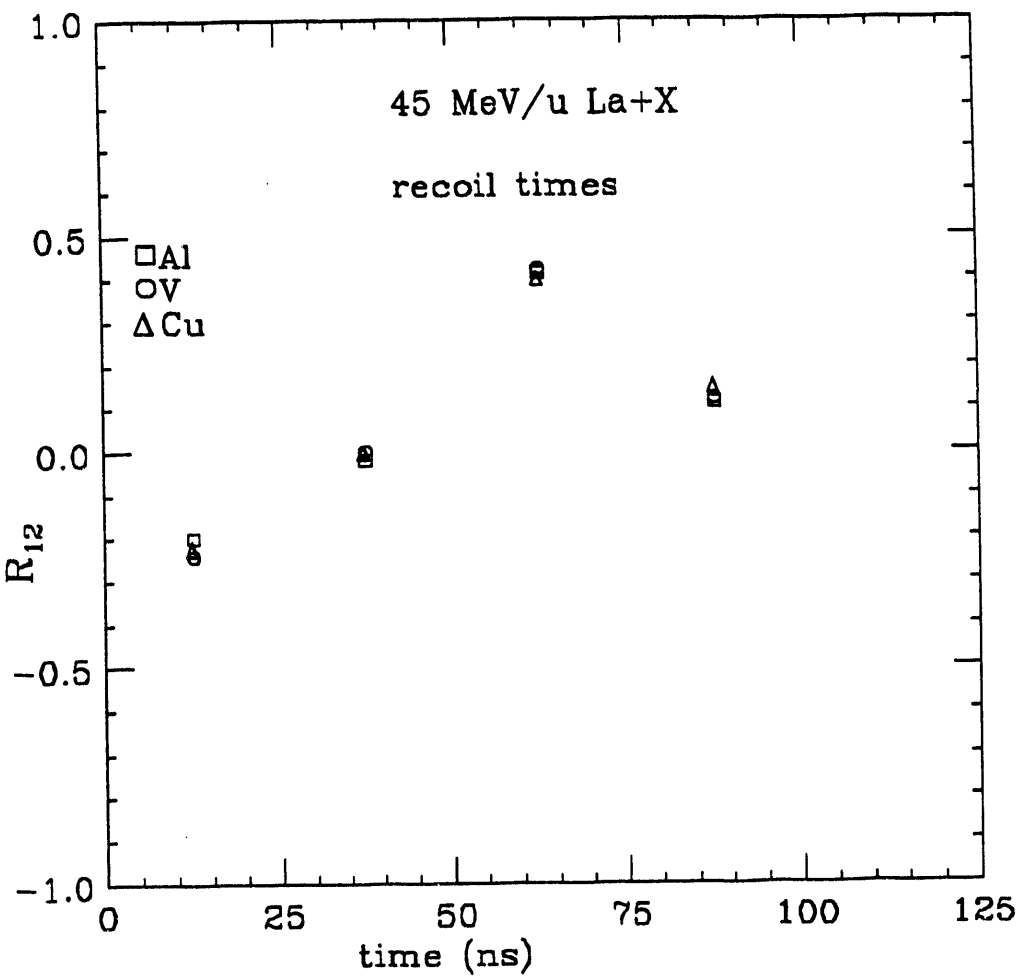
45 MeV/u La+X
recoil times
□Al
○V
ΔCu
1.0
0.5
0.0
−0.5
−1.0
R_{12}
0
25
50
75
100
125
time (ns)

Figure III.32: Correlation function as a function of mass for fragments detected in the recoil arc for the reactions La + Al, V, and Cu. A window on the time-of-flight of 50-100 ns was used.

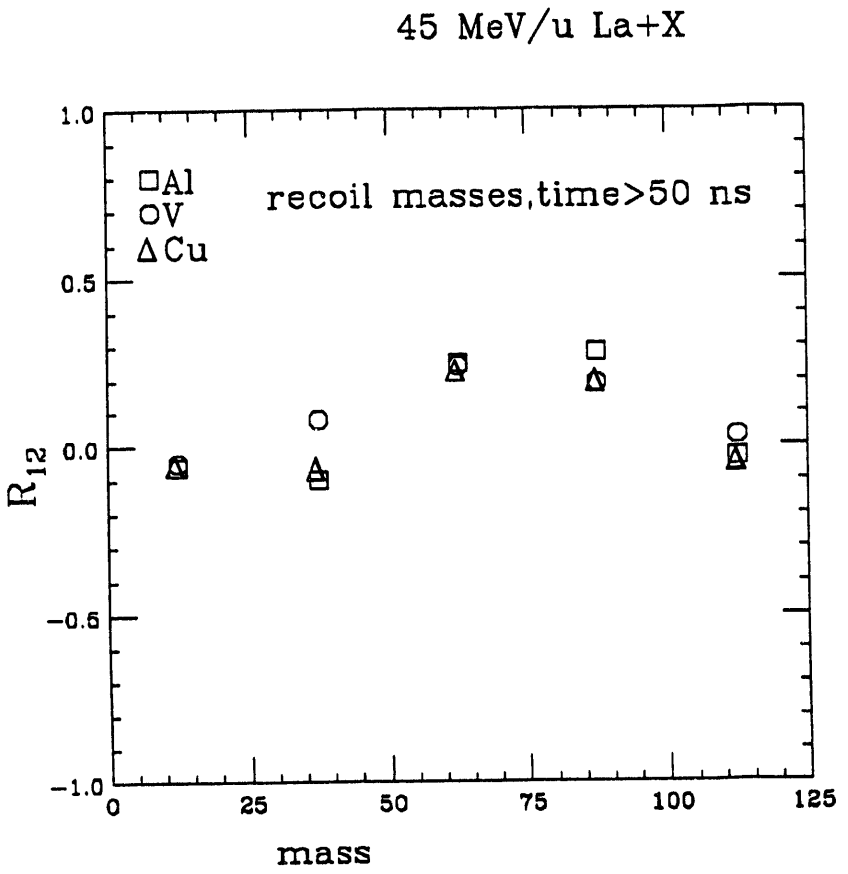
45 MeV/u La+X
recoil masses,time>50 ns
□Al
○V
ΔCu
R_{12}
1.0
0.5
0.0
−0.5
−1.0
0
25
50
75
100
125
mass

included due to poor statistics and the fact that the window of the mass of the recoil does not allow target-like fragments for the reaction La + Al. As expected, the energy distributions are skewed heavily toward low energies, with almost no fragments having energies greater than 25 MeV.

Histograms of the recoil mass distributions are shown in Figure III.34. For the V target, most of the distribution is at mass less than 75. The yield in the mass distribution below mass 60 is most likely due to quasi-elastic scattering. The same is also true for the peak in the mass distribution at mass 60 for the reaction La + Cu. The peak at mass 70 for the reaction La + V most likely involves some type of pick-up mechanism, in which mass is stripped away form the La projectile. For the reaction Nb + Be, it is possible for this type of stripping to occur at these energies for intermediate and large (b>5 fm) impact parameters (CHA88b). For the recoil mass distribution for the La target, the TLF is at mass that is outside of the window allowed by the correlation function (Figure III.25). However, the peak in the mass distribution is in the region of about one-half the target mass. This could be an indication that the collision might be central enough to cause the TLF to fission.

The angular distributions of these recoil fragments are shown in Figure III.35. The distribution is skewed towards lower angles, with no yield near the grazing angle of approximately 90°. This is because those fragments emitted to larger angles are not energetic enough to make it out of the target and be above the detector thresholds. The yield at forward is most likely due to the dissipative nature of the reactions producing these fragments, with an appreciable amount of energy loss. Because of the lack of coincidence measurements between the recoil events and array events, it is not possible to determine Q-values for these reactions.

Figure III.33: Histograms of the energy of fragments detected in the recoil arc for the reactions La + V, Cu, and La.

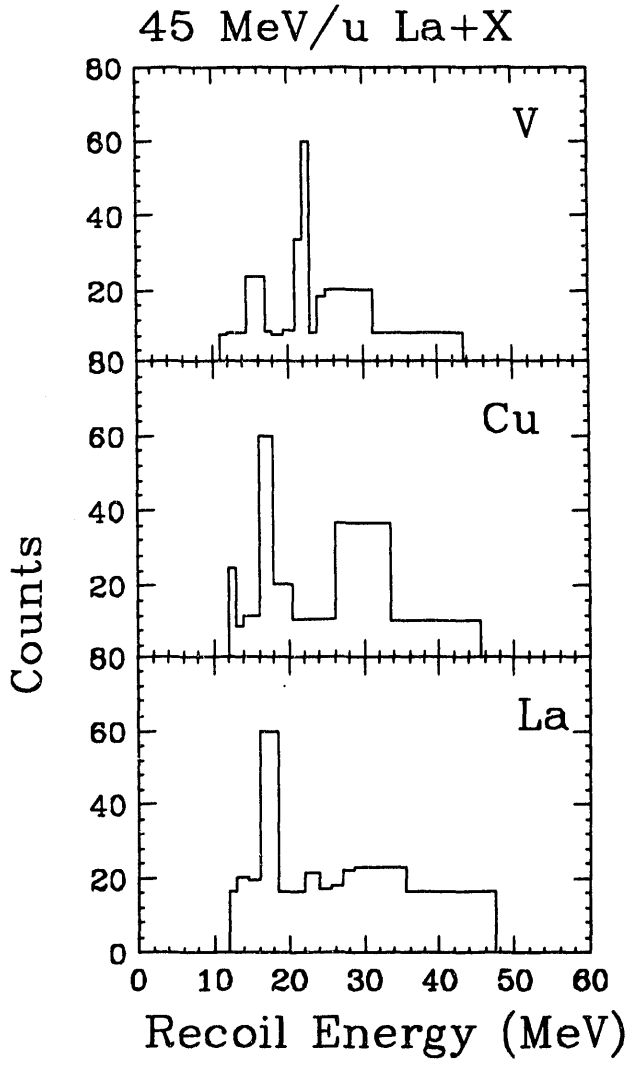
45 MeV/u La+X
V
Cu
La
Counts
Recoil Energy (MeV)
0
20
40
60
80
0
10
20
30
40
50
60

Figure III.34: Histograms of the mass of fragments detected in the recoil arc for the reactions La + V, Cu, and La.

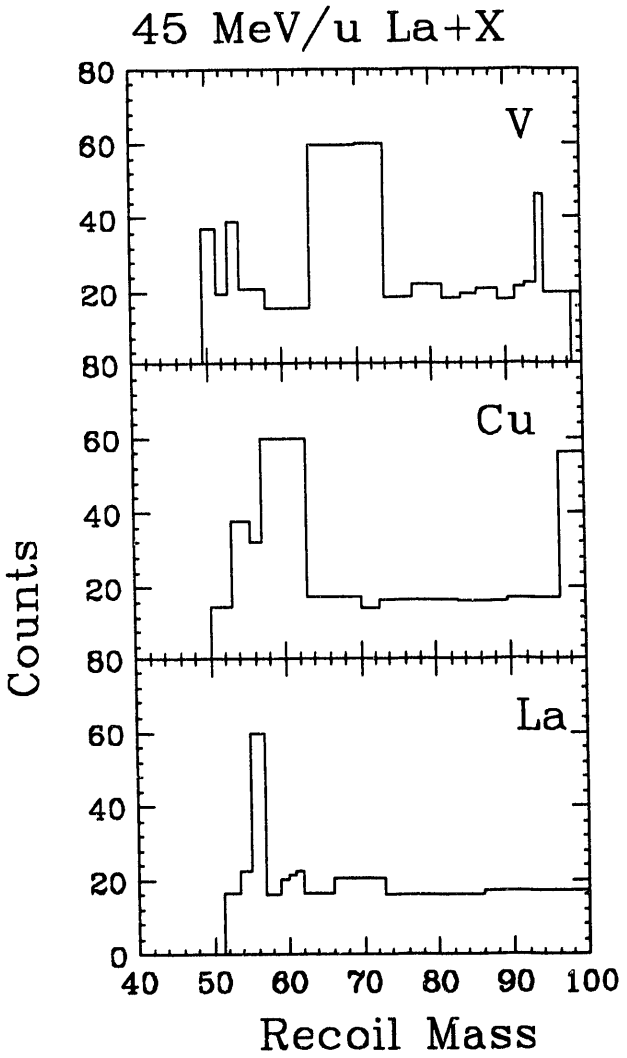
45 MeV/u La+X
V
Cu
La
Counts
Recoil Mass
0
20
40
60
80
40
50
60
70
80
90
100

Figure III.35: Histograms of the angular distributions of fragments detected in the recoil arc for the reactions La + V, Cu, and La.

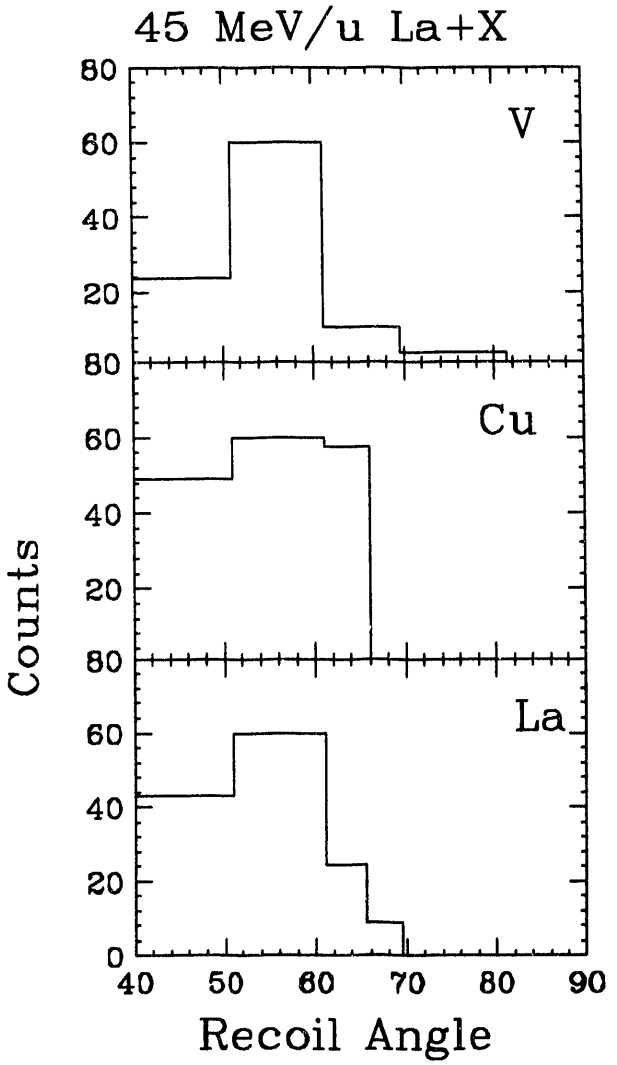
45 MeV/u La+X
V
Cu
La
Counts
Recoil Angle
80
60
40
20
0
40
50
60
70
80
90

CHAPTER IV REACTION MODEL CALCULATIONS

Except for a very narrow range of projectile-target combinations in which the available energy (in the center of mass) is fairly small, the statistical model of compound nucleus decay (incorporating incomplete fusion and the full range of decay asymmetries), as discussed in Chapter I, fails to reproduce experimental observables in intermediate energy heavy-ion reactions. These observables include fragment cross sections, angular distributions and fragment-fragment correlations. Additionally, even systems whose decay can be well characterized by the statistical model (BOW87) can also be described by other models (GRO88, PI91). Because the statistical model does not take into account pre-equilibrium emission, fast-fission, and other dynamical effects, a more realistic way of describing the early stages of a reaction is needed.

Within the past 10 years, a plethora of dynamical models have been used in an attempt to characterize reactions at intermediate energies. These models, which go under the names Boltzmann-Uehling-Uhlenbeck (BUU), Vlasov-Uehling-Uhlenbeck (VUU), Boltzmann-Nordheim-Vlasov (BNV) and Landau-Vlasov (LV) are all essentially semi-classical versions of time-dependent Hartree-Fock calculations. All of these models include a term for the mean fields of the colliding nuclei and a collision term for individual nucleon-nucleon collisions. While the BUU (or VUU) and LV (or BNV) models are based on the same theory, differences are found in some of the results that can be calculated, such as collective flow effects in heavy ion reactions (HAR88). Although these models

provide a characterization of the dynamical processes occurring during the early stages of reactions, they cannot account for the statistical emission of complex fragments once equilibrium is reached (ADO91). However, these calculations can be coupled to statistical decay models. This can then provide a description of the reaction from the earliest moments (which are governed by dynamical considerations) until equilibrium is reached and fragments are emitted statistically.

This chapter describes the use of dynamical and statistical reaction models to characterize the reactions studied. The first section describes the dynamical calculations. The second discusses the statistical decay model. The third section compares the calculated results to those from the experiment.

IV.A THE LANDAU-VLASOV EQUATION

IV.A.1 The Vlasov Equation

The Vlasov equation (VE) was originally used to describe the behavior of particles in a stellar gas (NEU84), but it can be applied to the study of collisions between quantum particle systems where individual collisions are either inhibited by the Pauli principle or negligible due to the diluteness of the system (REM85b). The VE can be considered to be the projection of the exact phase space onto the class of solutions given by a group of coherent states (pseudo-particles) moving in a mean field (REM85a). For a dynamical system governed by a time dependent Hamiltonian H(**r**,**p**;t), in which **r** and **p** are the position and momentum vectors, the VE gives the time evolution of the phase-space .

probability distribution. If f(r,p;t) is the one-body phase-space density distribution, the VE has the form:

$$D_t f = \frac{df}{dt} + \{f,H\} = 0 \qquad \text{(IV.1)}$$

(GRE87, REM85a), in which D_t is the differential operator which describes the conservative forces on the particles (REM85b) and

$$\{f,H\} = \frac{p}{m}\nabla_r f - \nabla_p f \nabla_r U \qquad \text{(IV.2)}$$

(GRE85b) in which U is the potential of the mean field and m is the mass. The potential U(r) can have the form of a density dependent Skyrme interaction (GRE87, SEB89) or a Gogny force, which takes into account the non-locality of nuclear forces (SEB89). The Skyrme interaction has the form:

$$U(r,p) = a\frac{\rho}{\rho_o} + b(\rho/\rho_o)^{1+\nu} \qquad \text{(IV.3)}$$

(SEB89). The parameters a, b, and ν are fit to the density, binding energy, and compressibility of the nucleus, respectively, and ρ and ρ_o are the actual and equilibrium nuclear densities. The time dependence of the Hamiltonian can arise from the action of an external field or from the average field in the case of a self-interacting many particle system. The VE conserves mass, charge, energy, and momentum and is Galilean invariant. The coherent state distributions succeed in reproducing bulk nuclear properties (nuclear matter saturation density, exponential fall off at the surface) as compared with other approaches (REM85b).

Solution of the VE is accomplished by use of a pseudo-particle method, in which each nucleon corresponds to be a finite number of pseudo-particles. If $f(\mathbf{r},\mathbf{p};t_o)$ is a solution at time t_o, and

$$\frac{d\mathbf{r}}{dt} = \frac{\mathbf{p}}{m} \qquad \text{(IV.4)}$$

and

$$\frac{d\mathbf{p}}{dt} = \frac{-dU}{d\mathbf{r}} \qquad \text{(IV.5)}$$

then the solution at time t is (GRE87):

$$f(\mathbf{r},\mathbf{p},t) = \int d\mathbf{r}_o d\mathbf{p}_o \delta[\mathbf{r}-\mathbf{R}(\mathbf{r}_o,\mathbf{p}_o;t)]\delta[\mathbf{p}-\mathbf{P}(\mathbf{x}_o,\mathbf{p}_o;t)]f(\mathbf{r}_o,\mathbf{p}_o;t) \qquad \text{(IV.6)}\ .$$

These are the bases of numerical solutions of the VE if the phase space distribution is considered as an ensemble of phase-space cells (pseudo-particles) which behave like classical particles. Because a finite set of point-like particles cannot describe a continuous phase-space function, numerical solutions based on pseudo-particle trajectories amount to a course graining of the phase-space, followed by a random sampling of the grains (GRE87).

This method can only be used for static studies of the nucleus, such as the preparation of the nucleus before studying nuclear reactions. For dynamical studies of heavy-ion reactions, the function $f(\mathbf{r},\mathbf{p};t)$ can be decomposed into a static distribution folded with a dynamical function that plays the role of the moving basis for the distribution. This decomposition then has the form:

$$f(\mathbf{r},\mathbf{p};t) = w(\mathbf{r},\mathbf{p}) * d_\alpha(\mathbf{r},\mathbf{p};t) \qquad \text{(IV.7)}$$

(GRE87) in which w is the static distribution and d_α is a dynamical function. The function d_α can be considered to be a collection of gaussian wave packets. This reduces to the pseudo-particle method if d_α is a delta function (GRE87). The function w(r,p) has the form:

$$w(r,p) = \Theta(E_F - \langle H \rangle_d) \qquad \text{(IV.8)}$$

(GRE85a) in which E_F is the Fermi energy and $\langle H \rangle_d$ is the energy of the coherent state centered at (r,p).

For use in actual calculations,

$$f(r,p;t) = \sum_{n=1}^{N} w(r,p)\, d_\alpha(r-r_o, p-p_o; t) \qquad \text{(IV.9)}$$

(GRE87) in which N is the total number of coherent states (pseudo-particles, gaussians). The variable N is chosen by requiring the stability of the solutions against variations in the results, and $r-r_o$ and $p-p_o$ are the widths of the gaussians in space and momentum, respectively (GRE87).

The widths are chosen to reproduce nuclear radii and binding energies. Because of the finite number of coherent states, there will be some numerical fluctuations in the solutions of f(r,p;t). However, because the actual solution of the VE is done by a Monte-Carlo method, the fluctuations should be averaged out. Any information that relies on the observation of dynamical fluctuations can be lost because of this. Fortunately, most observables are quantities averaged over the phase-space (REM85b).

The solution of the VE is useful as an approach to studying nuclear reactions for several reasons:

1) Since it is positive, it can be interpreted as a probability distribution of an assembly of pseudo-particles.

2) Because it is semi-classical, the interpretation of its properties is easier.

3) It can be coupled to a collision term to account for individual nucleon-nucleon collisions (REM85a).

IV.A.2 The Landau-Vlasov Equation

The Landau-Vlasov equation (LVE), also known as the Boltzmann-Nordheim-Vlasov (BNV) equation, arises from the coupling of the VE to a collision term. This allows for the study of the interplay between one- and two-body interactions in heavy-ion reactions (REM85a). For the most part, the collision term used is the Uehling-Uhlenbeck collision term (REM88, REM85b, GRE85, PI91, LER90). For applications using the collision term, Equation IV.1 is modified so that it has the form:

$$D_t f = \frac{df}{dt} + \{f,H\} = I_{coll} \qquad \text{(IV.10)}$$

in which I_{coll} is the collision integral. The resultant LVE is a dynamical approach which describes the time evolution of the one-body phase-space density under the influence of the self consistent mean field and nucleon-nucleon collisions (LER90).

The collision integral I_{coll} has the form :

$$I_{coll} = \frac{g}{4m^2\pi^3\hbar^3}\int dp_2 dp_3 dp_4 \frac{d\sigma}{d\Omega}[A]\delta(b)\delta(c) \qquad \text{(IV.11)}$$

with

$$A = [(1-f_1')(1-f_2')f_3f_4 - (1-f_3')(1-f_4')f_1f_2] \qquad \text{(IV.12)}$$

$$b = (p_1 + p_2 - p_3 - p_4) \qquad \text{(IV.13)}$$

and

$$c = (\varepsilon_1 + \varepsilon_2 - \varepsilon_3 - \varepsilon_4) \qquad \text{(IV.14)}$$

in which g is the degeneracy, f_i is the distribution function, f_i' is the occupation number, p_i is the momentum, ε_i is the energy of pseudo-particle i (i=1,2 before the collision and 3, 4 after) and $\frac{d\sigma}{d\Omega}$ is the nucleon-nucleon cross section (REM85b, PI91).

The cross section term $\frac{d\sigma}{d\Omega}$ is the effective (in-medium) nucleon-nucleon cross section:

$$\left(\frac{d\sigma}{d\Omega}\right)_{eff} = \left(\frac{d\sigma(E)}{d\Omega}\right)_{free} (1-Y(\rho)) \qquad \text{(IV.15)}$$

(GRE87) in which $Y(\rho)$ is a density scaling factor which accounts for the reduction of the cross section as the density increases. Since collisions at E/A < 100 MeV occur essentially at the surface, this in-medium correction is of little importance (<10 %) at the energies studied in this experiment (GRE87).

The collision term described above is only valid for application to a dilute quantum gas, but the strongly interacting system of a nucleus can be considered

as such as long as the Pauli principle is effective (the mean free paths and times between collisions are large compared to spatial extensions and duration of the collisions) (GRE85b).

For actual solution of the LVE, the reaction is considered over a series of time steps. At each time step, a collision between two test particles occurs if the following conditions are met:

1) During the time step, the test-particles must pass the point of closest approach.

2) The distance of closest approach must be smaller than $\sqrt{\sigma_{nn}/\pi}$, in which σ_{nn} is the nucleon-nucleon cross section.

3) The collision is not Pauli-blocked (BON89).

Because the phase space is sampled using a Monte-Carlo method, the following procedure is used to determine whether two test-particles interact:

1) Two test-particles are randomly chosen in the occupied momentum space.

2) The quantity λ is calculated as

$$\lambda = \frac{1}{(\sigma_{nn,ave})(\rho)} \qquad \text{(IV.16)}$$

in which $\sigma_{nn,ave}$ is the average nucleon-nucleon cross section and ρ is the test-particle density.

3) A collision probability is introduced:

$$\Pi_{ij} = \Delta t/\Delta t_{collision} \qquad \text{(IV.17)}$$

$$\Delta t_{collision} = \lambda/v_{rel\ i,j} \qquad \text{(IV.18)}$$

$$\Delta t \leq \Delta t_{collision} \qquad \text{(IV.19)}$$

in which $v_{rel\ i,j}$ is the relative velocity between two test-particles and Δt is the time step.

4) A random number x ($0<x<1$) is calculated.

If x is less than Π_{ij}, then a collision occurs (BON89).

The main drawback of the use of the LVE is that it is an equation for the average one-body distribution function; it neglects fluctuations and correlations apart from incoherent two-body scatterings and Pauli principle correlations (BON90).

IV.B STATISTICAL DECAY MODEL CALCULATIONS

The statistical decay of a compound nucleus (an excited nucleus in thermal equilibrium) was originally described as occurring by two separate mechanisms- either the emission of light particles (protons, neutrons, and α particles) or by symmetric fission if the system is heavy enough or has a high enough angular momentum. (It should be noted that particle emission or fission can only occur if the system is above the Yrast line. Once the system reaches the Yrast line, it can only decay by the emission of γ rays.) The division between the two separate compound nucleus decay mechanisms was more of an illusion than an actual fact. As heavy ions were accelerated to higher energies, compound nuclei were produced with excitation energies and angular momenta high enough for complex fragments to be emitted with a large enough cross section to be easily detected. A theory arose (MOR75) that extended the statistical model to the mass asymmetry

coordinate. In other words, symmetric fission and light particle emission could be considered to be extremes of a single decay mechanism.

The statistical decay computer code GEMINI (CHA88a, CHA88b) is based on this formulation. In GEMINI, all decay channels are considered, from the emission of light particles, through complex fragment emission, to symmetric fission. For the emission of light particles, the formalism of Hauser and Feshbach is used. In this formalism, the decay width to go from the nucleus (Z_0, A_0, J_0) at an excitation energy E* to the residual nucleus (Z_2, A_2, J_2) with excitation energy U_2 through the emission of a particle (Z_1, A_1, J_1) has the form:

$$\Gamma_{J2}(Z_1, A_1, Z_2, A_2)=\frac{2J+1}{2\pi\rho_0}\sum_{\ell=|J_0-J_2|}^{J_0+J_2}\int_0^{E^*-B-E_{rot}(J_2)} T_\ell(\varepsilon)\rho_2(U_2,J_2)d\varepsilon \quad \text{(IV.20)}$$

in which ℓ and ε are the orbital angular momentum and kinetic energy of the emitted particle, $\rho_2(U_2,J_2)$ is the level density of the residual system with a thermal excitation energy U_2 and ρ_0 is the level density of the original system. The value of U_2 is determined by:

$$U_2 = E^* - B - E_{rot}(J_2) - \varepsilon \quad \text{(IV.21)}$$

in which B is the nuclear binding energy and $E_{rot}(J_2)$ is the rotation plus deformation energy of the residual nucleus. The transmission coefficients $T_\ell(\varepsilon)$ are calculated with the sharp cut-off approximation, in which:

$$T_\ell(\varepsilon) = 0 \text{ if } \quad \varepsilon < E_{coul} + \frac{\hbar^2 \ell(\ell+1)}{2\mu R^2} \tag{IV.22}$$

and

$$T_\ell(\varepsilon) = 1 \text{ if } \quad \varepsilon \geq E_{coul} + \frac{\hbar^2 \ell(\ell+1)}{2\mu R^2} \tag{IV.23}$$

in which μ is the reduced mass, E_{coul} is the Coulomb barrier (calculated using a diffuseness of the nuclear radius), and R is the absorptive radius. The absorptive radius R has the values:

$R = 1.16\, A_2^{1/3} + 2.6$ fm for proton and neutron emission

$R = 1.16\, A_2^{1/3} + 3.7$ fm for α emission.

For the emission of heavy fragments, the transition state formalism of Moretto (MOR75) is used:

$$\Gamma(Z_1, A_1, Z_2, A_2) = \frac{1}{2\pi\rho_o} \int_0^{E^*-E_{sad}(J_o)} \rho_{sad}(U_{sad}, J_o)\, d\varepsilon \tag{IV.25}$$

in which U_{sad} and ρ_{sad} are the thermal energy and level density of the saddle point configuration, and

$$U_{sad} = E^* - E_{sad}(J_o) - \varepsilon \tag{IV.26}$$

in which $E_{sad}(J_o)$ is the deformation plus rotational energy of the saddle point configuration and ε is the energy of the translational degree of freedom.

To determine the level densities, the Fermi gas expression is used:

$$\rho(U,J) = 2(J+1)(\hbar^2/2\mathcal{J}))^{(3/2)} \frac{\sqrt{a}}{12} \frac{\exp(2(aU)^{1/2})}{U^2} \qquad \text{(IV.27)}$$

in which $\mathcal{J}$ is the moment of inertia of the residual nucleus (or the saddle-point configuration) and a is the level density parameter. The level density parameter is taken as a= A/8.5.

For actual calculations, the integral in the Hauser-Feshbach and Moretto formalisms are treated as a summation, and Eq. IV.20 has the form:

$$\Gamma(Z_1, A_1, Z_2, A_2) = \frac{2J_1+1}{2\pi\rho_o} \sum_{J_2=0}^{\infty} \sum_{|J_0-J_2|}^{J_0+J_2} t_2\rho_2(U_2,J_2) \qquad \text{(IV.28)}$$

with

$$U_2 = E^* - B - E_{rot}(J_2) - E_{coul} - \frac{\hbar^2 \ell(\ell+1)}{2\mu R^2} \qquad \text{(IV.29)}$$

and

$$t_2 = \sqrt{\frac{U_2}{a}} \qquad \text{(IV.30)}$$

where t_2 is the nuclear temperature.

For heavy fragment emission (including symmetric fission), the decay width has the form:

$$\Gamma(Z_1, A_1, Z_2, A_2) = \frac{1}{2\pi\rho_o} t_{sad}\rho_{sad}(U_{sad},J_o) \qquad \text{(IV.31)}$$

with

$$U_{sad} = E^* - E_{sad}(J_o) \qquad \text{(IV.32)}$$

and

$$t_{sad}=\sqrt{\frac{U_{sad}}{a}} \qquad \text{(IV.33).}$$

Secondary products formed in the binary decay of the initial system are allowed to continue to decay, using the same formalism as above. The spin of the residual system is chosen by a Monte-Carlo calculation from the partial decay widths $\Gamma_{J_2}(Z_1, A_1, Z_2, A_2)$. For emission of complex fragments, the spin of the fragment was calculated in the sticking limit:

$$J_1=\frac{\mathcal{J}_1}{\mathcal{J}}J_o \qquad \text{(IV.34)}$$

in which J_1 is the spin of the emitted fragment, $\mathcal{J}_1$ is the moment of inertia of the fragment, and $\mathcal{J}$ is the total moment of inertia of the system. The excitation energy of the emitted fragment was determined assuming equal temperatures of the emitted fragment and the residual nucleus.

IV.C REACTION MODEL CALCULATIONS

Performance of the dynamical model calculations requires the use of several variables- the number of gaussians (test-particles) per nucleon, their widths in space and momentum, and the compressibility of the nucleus. Use of the Skyrme interaction yields a compressibility constant of 200 MeV. Widths in space and momentum are chosen to be 1.444 fm and 0.346 MeV/c, respectively, which reproduce the binding energy and radii of the target and projectile within 20%. Stability of the system at non-reacting (very large) impact parameters was achieved by using 40 gaussians/nucleon.

The calculations were performed for the systems La + Al, V, and Cu over a range of impact parameters and times up to 210 fm/c. The La target only studied in the case of a central collision in which multifragmentation may occur. In some cases, the dynamics were followed until longer times to attempt to verify certain features of the calculations. For the V target, the calculation needed to be performed several times for larger impact parameters (b = 5, 6, and 7 fm) due to variations in the results because of the Monte-Carlo sampling of the phase-space. These numerical fluctuations are not necessarily related to dynamcal fluctuations in the reaction being studied.

Once the dynamical calculations have been performed, a clusterization routine (BON90) is used to determine the properties of any fragment(s) present in the calculated results. These properties include the Z, A, E*, angular momentum, angles, and source velocity of the fragment(s). It should be noted that these calculations can account for fast-fission, deep-inelastic reactions, participant-spectator-like reactions, and (possibly) multifragmentation, so there may be several fragments present at some (though not all) impact parameters. In the clusterization routine, two test-particles are considered to be in the same cluster if the following criteria are met:

$$|r_i - r_j| < D \qquad \text{(IV. 35)}$$

and

$$|p_i - \langle p \rangle_c| < \sqrt{p_F^2 + 2mBE} \qquad \text{(IV. 36)}$$

in which i and j are two particles in the same cluster, r_i and r_j are their positions, D is a parameter that gives the range of the nuclear force, $\langle p \rangle_c$ is the momentum of the center-of-mass of the cluster, p_F is the Fermi momentum and BE is the

nucleon binding energy (approximately 8 MeV). The clusterization routine also determines the energies and angles of particles (protons and neutrons) not included in the cluster.

In order to combine the dynamical and statistical models discussed in Sections IV.A and B, it is necessary to determine the time at which to end the dynamical calculations and begin the statistical decay calculations. In other words, at what time does the reacting system reach equilibrium? Because the dynamical model calculations include light particle emission at all stages of the reaction, the determination of this time is very important. If it is too early in the reaction, then equilibrium has not been reached and the statistical model is not applicable. If it is too late, then the pre-equilibrium stage will also include some statistical emission of light particles, and the properties of the fragment(s) will not be correctly determined for application of the statistical decay model.

In order to determine at which time to "freeze-out" the properties of the clusters and start the GEMINI calculations, the mean energy of the light particles emitted as a function of time in the reactions La + Al, V, and Cu at E/A=45 MeV and b=1 fm is shown in Figure IV.1. The lines are included to guide the eye. For the reaction La + Al, the mean energy of the light particles decreases until time = 90 fm/c, after which the energy is constant. This change in the mean energy indicates the time at which equilibrium emission of the light particles starts, and is thus called the freeze-out time. For the reaction La + V, the freeze-out time is slightly longer, approximately 100 to 110 fm/c. This is most likely due to the increase in the available energy for the reaction on the V target. It then takes more nucleon-nucleon collisions (more time) to thermalize the energy. The fluctuations in the mean energy of the light particles at longer times in the reaction La + V are due to oscillations in the density of the fusion residue. The same is

true for the reaction La + Cu. The density of the composite system formed in the reactions La + V and Cu at b = 1 fm as a function of time is shown in Figure IV.2. The composite system undergoes an expansion-compression stage, with the fluctuations in the density at large times leading to fluctuations in the energies of the emitted light particles.

The results of the dynamical calculations are also sensitive to the choice of the value of the compressibility constant. For the reaction La + Cu at an impact parameter of 1 fm, the density of the composite system as a function of time for three values of the compressibility constant is shown in Figure IV.3. While the lowest compressibility constant yields the familiar compression-expansion oscillations of density, the stiffer constants do not yield this result. This shows the calculations are sensitive to the input parameters. For the results presented below, a constant of 200 MeV is used because of evidence of a soft equation of state at intermediate energies (COL91).

In the case of reactions in which more than one fragment may be present, the fragments may not be well separated at the freeze-out time, so it is difficult to determine their properties for application to GEMINI. In such instances, the reactions are followed to larger times and the properties are extrapolated back to the freeze-out time.

For each system studied, the properties of the fragments were parameterized over a range of impact parameters (converted to ℓ-waves) for use in GEMINI calculations. Additionally, the results of GEMINI were placed through a detector angle and velocity filter before fragment-fragment correlations, source velocity distributions, and other observables were compared to the experimental results.

Figure IV.1: Mean energy of light particles emitted in the reactions La + Al (diamonds), V (squares), and Cu (triangles) as a function of time. The lines are to guide the eye.

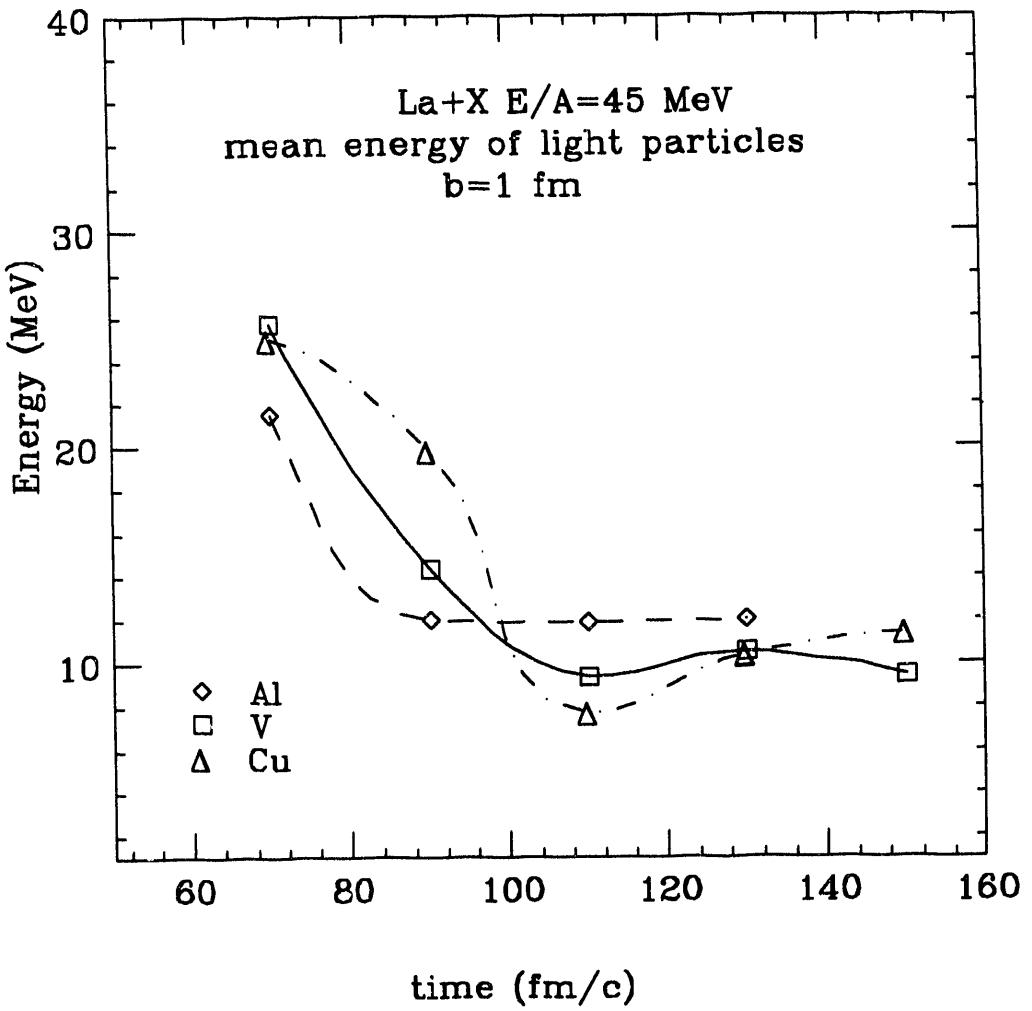
La+X E/A=45 MeV
mean energy of light particles
b=1 fm
Energy (MeV)
time (fm/c)
40
30
20
10
60
80
100
120
140
160
Al
V
Cu

Figure IV.2: Density of the composite system (in fm^{-3}) as a function of time for the reactions La + V (squares) and La + Cu (triangles) at b=1 fm. The lines are to guide the eye.

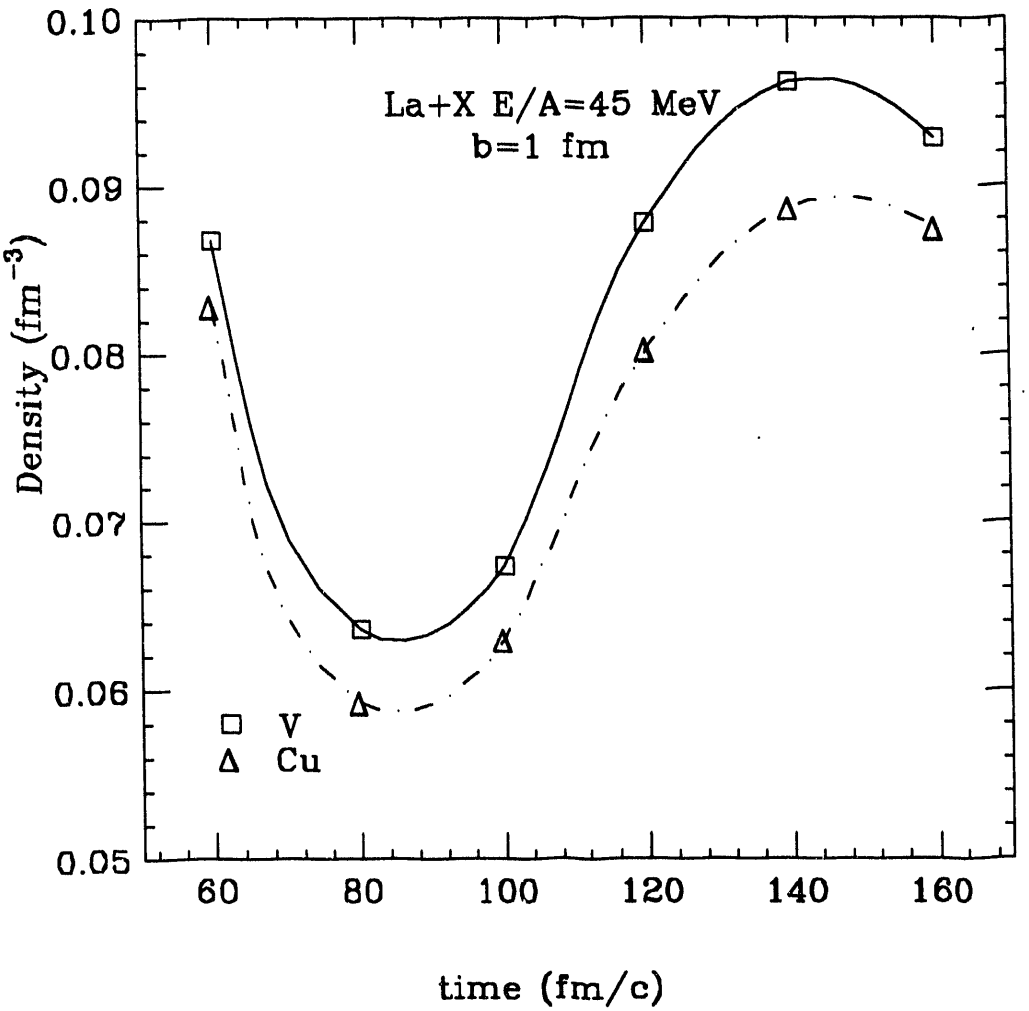
La+X E/A=45 MeV
b=1 fm
Density (fm^{-3})
0.10
0.09
0.08
0.07
0.06
0.05
60
80
100
120
140
160
V
Cu
time (fm/c)

Figure IV.3: Density of the composite system (in fm^{-3}) as a function of time for the reaction La + Cu at b=1 fm for different values of the compressibility constant K. The lines are to guide the eye.

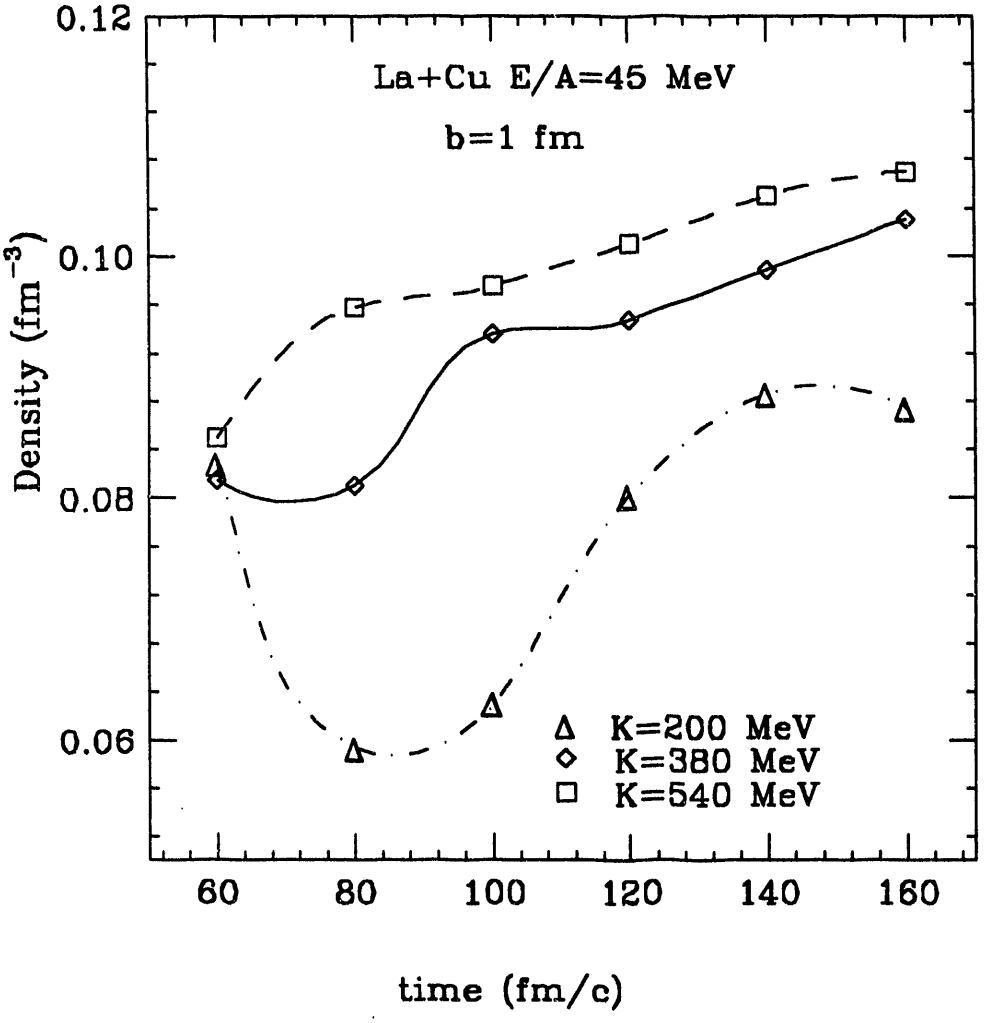
La+Cu E/A=45 MeV
b=1 fm
Density (fm^{-3})
0.12
0.10
0.08
0.06
60
80
100
120
140
160
time (fm/c)
K=200 MeV
K=380 MeV
K=540 MeV

IV.C.1 The Reaction La + Al

Contour plots of the time evolution of the distribution of nucleons in space for the reaction La + Al at E/A = 45 MeV for a range of impact parameters are shown in Figure IV.4. For the most central collisions a hot fused system is formed. At more peripheral impact parameters the reaction is more reminiscent of deep-inelastic collisions, in which a rotating dinuclear system forms and then the projectile and target reseparate. The picture is less clear for the intermediate (b = 3 and 4 fm) impact parameters. While at first glance these reactions seem to be similar to the more central collisions, this may not be the case. The possibility of a fast-fission reaction mechanism at these impact parameters warrants a closer look at the distribution of nucleons in space for these reactions. (Calculations indicate that the fission barrier for a system formed with a charge and mass similar to the system studied disappears at incoming ℓ-waves corresponding to an impact parameter between b= 2 and 3 fm.)

To further study the possibility of fast-fission in the dynamical calculations in this reaction, contour plots of the density of nucleons in space for various times at b=3 fm are shown in Figure IV.5. Two centers of density are clearly present at a time scale that is not inconsistent with asymmetric fast-fission for systems at similar masses and energies (HIN89). This division is still present at times of up to 300 fm/c.

In order to determine whether this effect is reflected in the experimental data or not, the properties of the system were determined at b= 3 and 4 fm both by considering the product to be a single hot nucleus and by dividing in space between the two centers of density. The properties were then parameterized, including the information from the other impact parameters, and GEMINI

Figure IV.4: Contour plots of the distribution of nucleons in space as a function of time for the reaction La + Al over a range of impact parameters. The time steps are in units of fm/c.

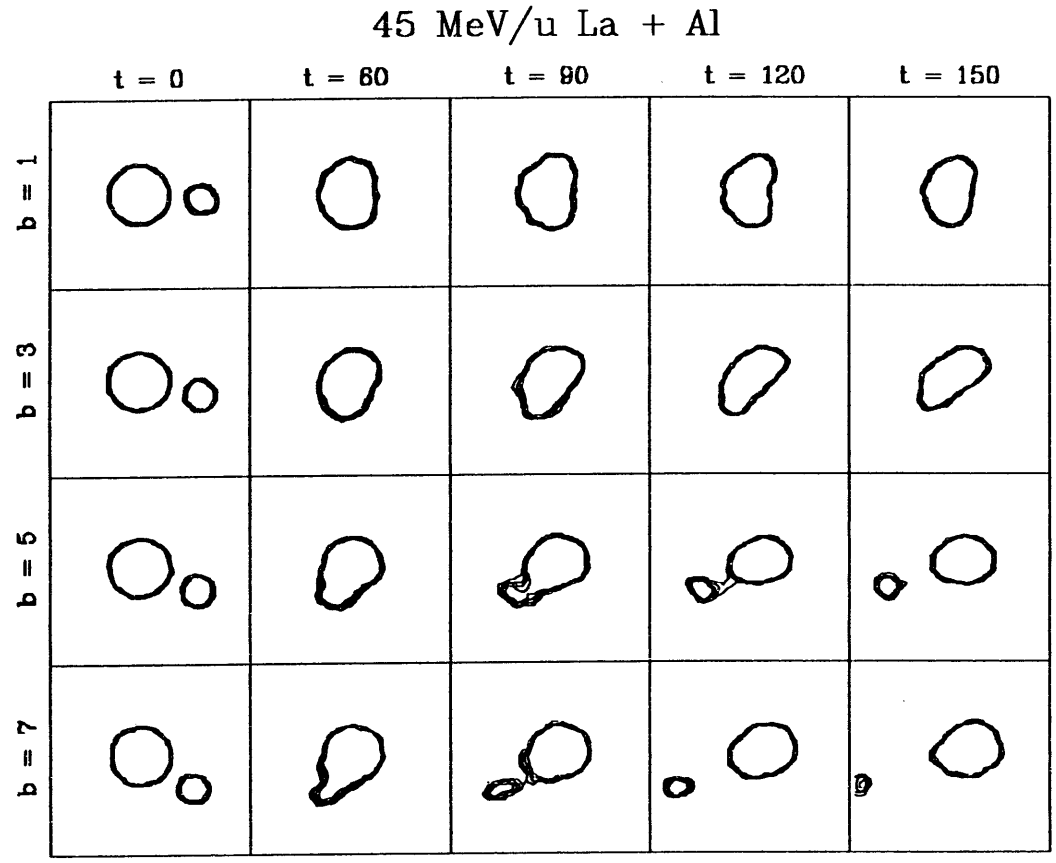
45 MeV/u La + Al
t = 0
t = 60
t = 90
t = 120
t = 150
b = 1
b = 3
b = 5
b = 7

Figure IV.5: Contour plots of the distribution of nucleons in space for the reaction La + Al at b=3 fm and times of 120, 140, 160 and 180 fm/c. Z is the beam direction; Y is the out-of-plane axis.

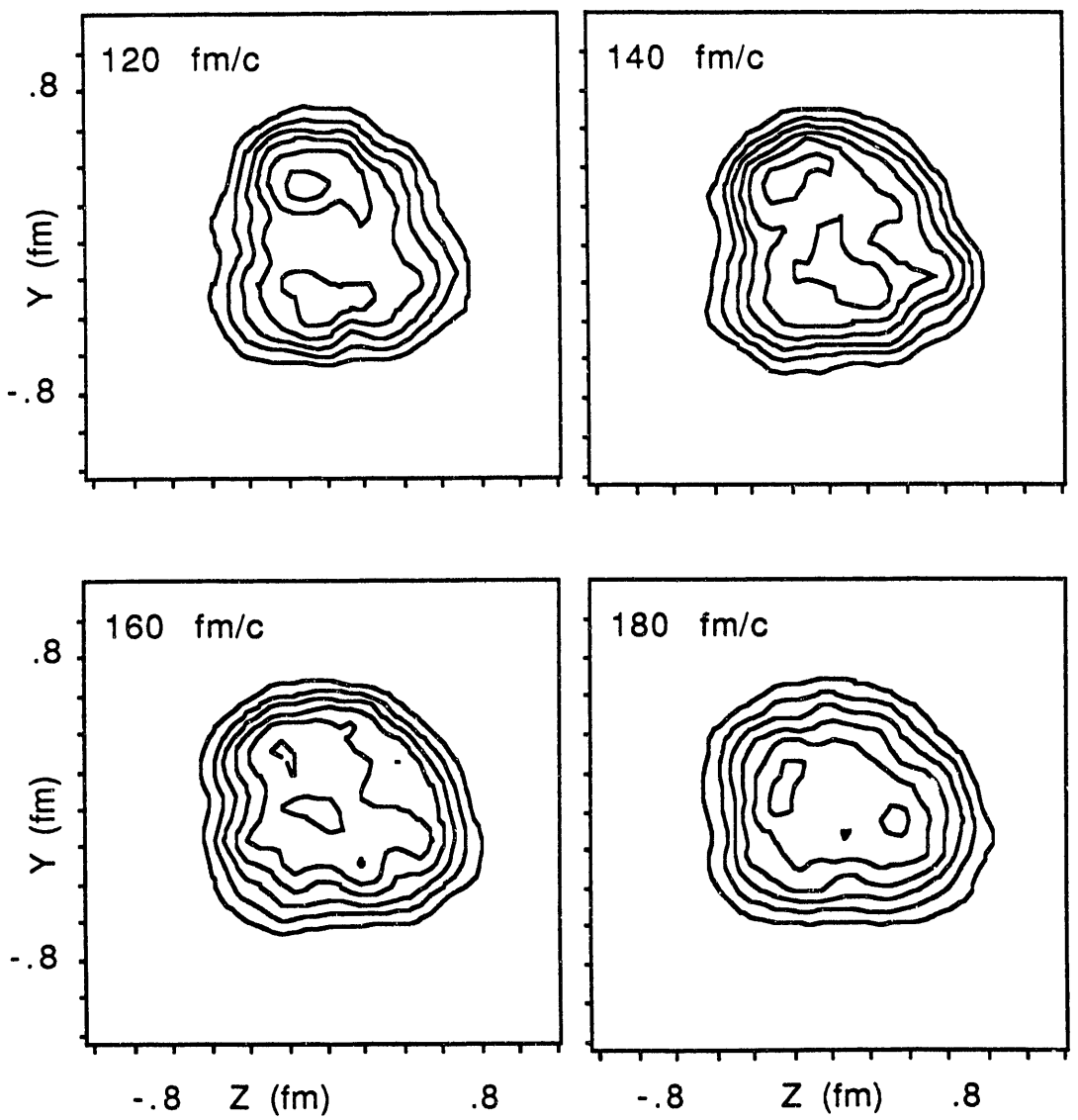
120 fm/c
140 fm/c
160 fm/c
180 fm/c
.8
-.8
Y (fm)
-.8
Z (fm)
.8

calculations were performed.

The experimental fragment cross sections $\sigma(Z)$, and the cross sections calculated both with and without the fast fission scenario are shown in Figure IV.6 . The error bars shown for the experimental cross section are the same as shown in Figure III.15. It is clear that it is necessary to include fast-fission to reproduce the cross section for fragments with $Z < 20$. Although the absolute magnitude of the distribution is not reproduced except for $20 < Z < 30$, the general shape over the entire range of fragments studied is. For the rest of the results concerning this reaction, the fast fission scenario will be used.

Figure IV.7 shows the total charge and source velocity distributions for the experimental data (solid line) and the calculation (dashed line) for n = 2 and 3 events. For the n=2 events, the peak in the Z_{tot} distribution is well reproduced by the calculation, but the tail at low Z_{tot} is vastly underpredicted. This effect is most likely due to the underestimation of the number of n=3 events. The low Z_{tot} tail is due to n=3 events for which only 2 fragments were detected. For n= 3 events, the model overpredicts the peak of the distribution and underestimates both the width and the tail. For the calculation, virtually no n=4 events were produced. The production of four fragments would tend to widen the total charge distribution of the n=3 events. The model reproduces the peaks in the V_s distribution within a few percent, but underestimates the tail of the distribution for the n=3 events. The double peak in the n=2 V_s distribution is most likely due to the abrupt change in the reaction mechanism between b=2 and 3. This leads to a discontinuity in the GEMINI parameters at the ℓ-wave of the transition.

Experimental and calculated charge-Dalitz plots are shown in Figure IV.8. Although the general trend in the data is reproduced (yield predominantly at the vertices), the model underpredicts the more symmetric splits, which show up as

Figure IV.6: Experimental (diamond) and calculated (circles and squares) fragment cross sections for the reaction La + Al. The circles are for the scenario not including fast-fission; the squares include fast-fission. The error bars are the same as presented in Figure III.15.

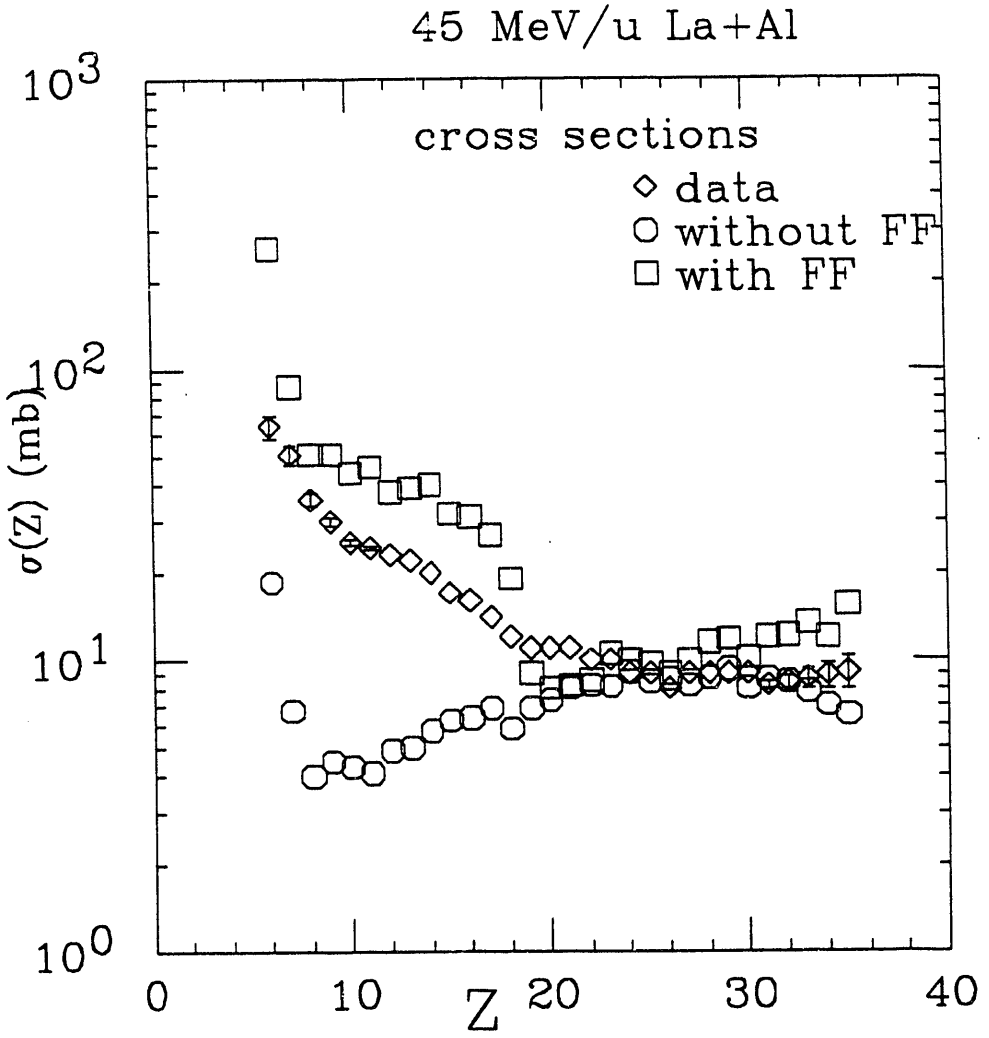
45 MeV/u La+Al
cross sections
data
without FF
with FF
10^3
10^2
10^1
10^0
σ(Z) (mb)
0
10
Z
20
30
40

Figure IV.7: Experimental (solid line) and model (dashed line) total charge and source velocity distributions for n=2 and 3 events for the reaction La + Al. The arrow is at the complete fusion source velocity.

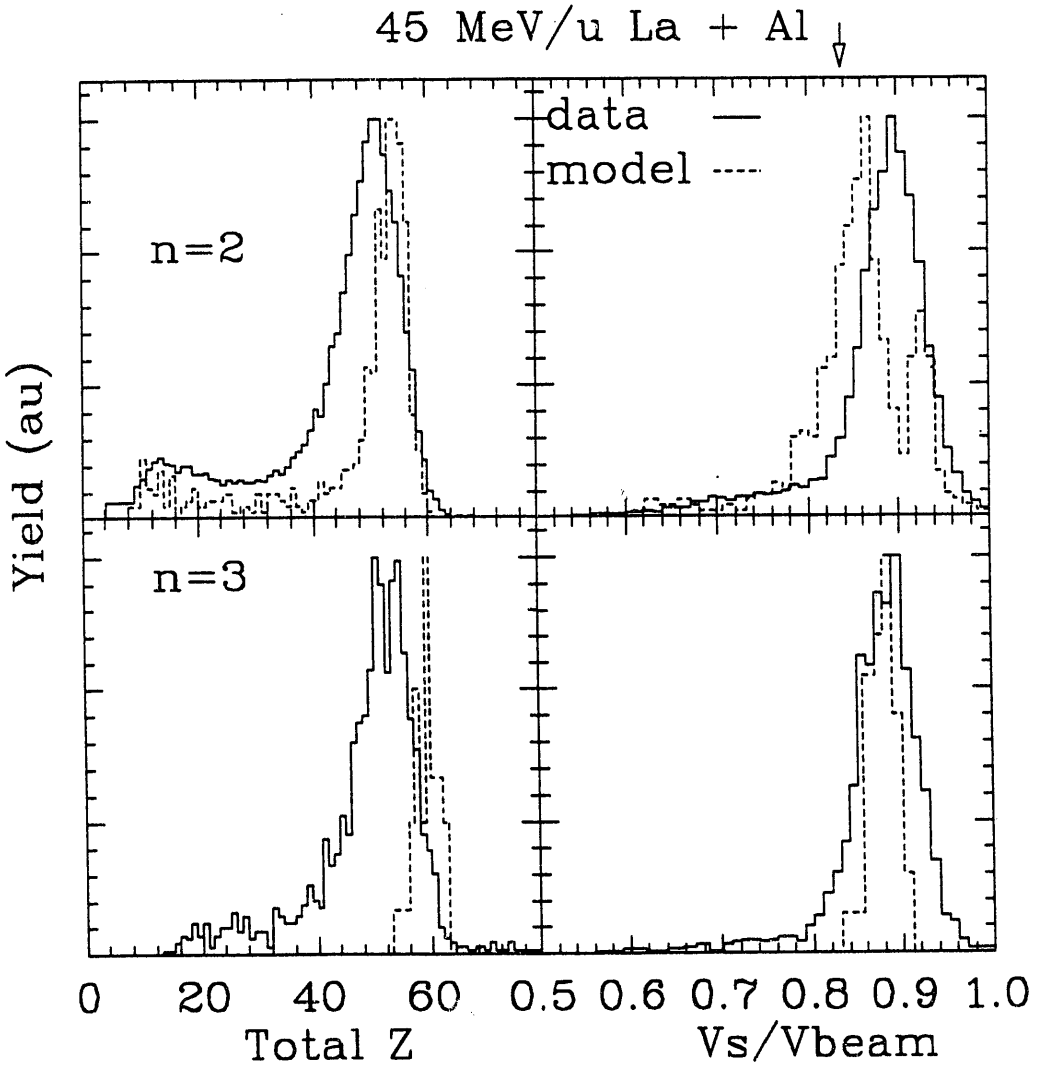
45 MeV/u La + Al
data
model
n=2
n=3
Yield (au)
0
20
40
60
Total Z
0.5
0.6
0.7
0.8
0.9
1.0
Vs/Vbeam

Figure IV.8: Experimental (top) and model (bottom) charge-Dalitz plots for the reaction La + Al.

La + Al E/A= 45 MeV

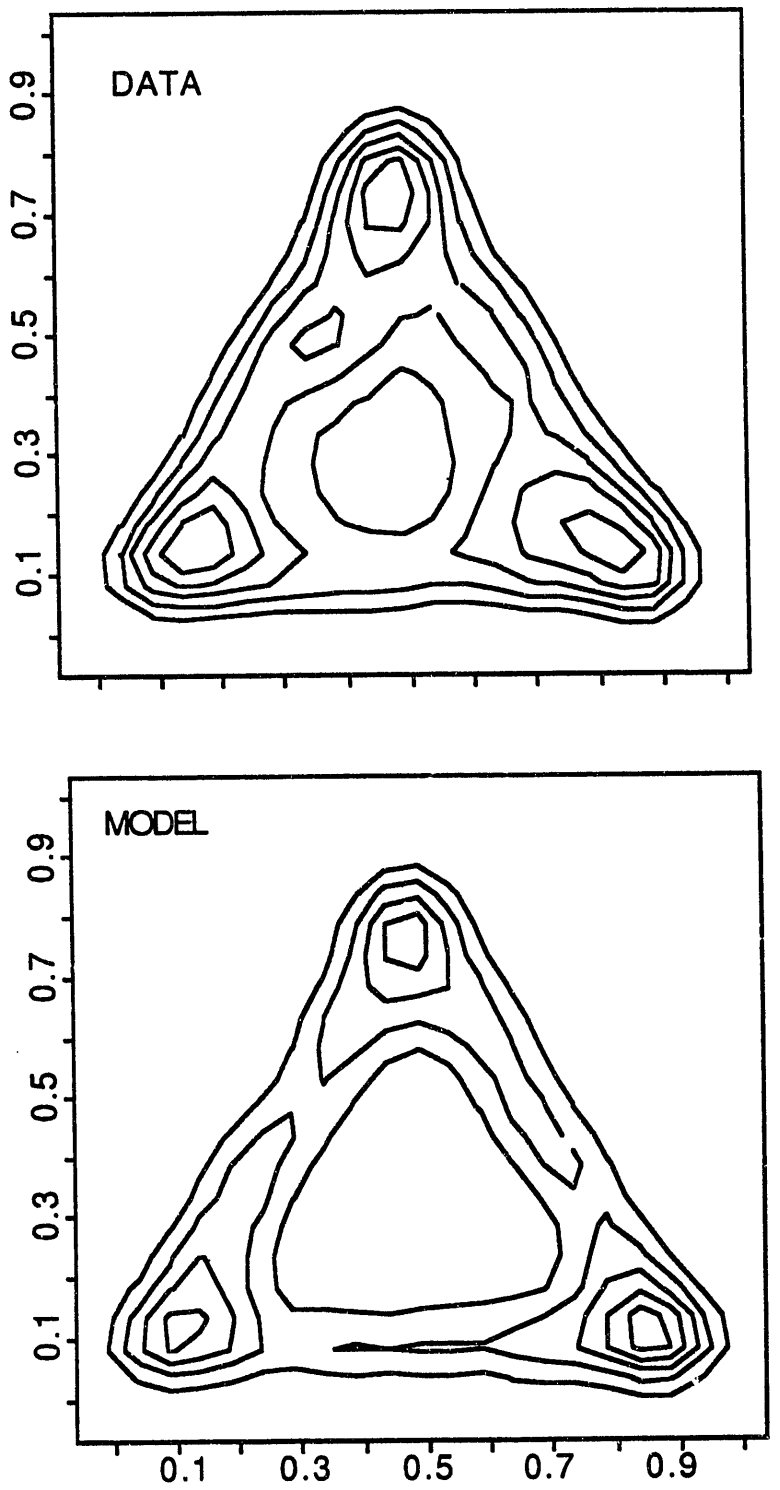

yield along the edges and in the center of the Dalitz plot. The contours in the center of the charge-Dalitz plots are due to holes in the distribution.

Another way of examining how well the model reproduces the experimental data is to determine the branching ratios for n = 2, 3, and 4 events, as shown in Table IV.1. It is apparent that the model vastly underpredicts the amount of n= 3 and 4 events. So, although global reaction features (fragment cross sections, Z_{tot} and V_s distributions) are reproduced by the model, the finer features are not being calculated correctly for this reaction.

Table IV.1 Experimental and calculated proportions of multiple fragment events for the reaction La + Al E/A =45 MeV.

multiplicity	data	calculation
2	.909	.938
3	.086	.042
4	.005	.00025

Figure III.26 showed the relative velocities and angles between pairs of fragments for n=3 events in the reaction La + Al. A comparison between the experimental and calculated relative velocities and angles for this reaction is shown in Figure IV.9. It is clear that there are many features in the V_{rel} and θ_{rel} distributions that are different between the calculation and the experimental data. While the experimental and the calculated peaks in the V_{rel} spectra match closely, the model V_{rel} distributions extend to lower velocities. The IL relative angle distribution is peaked at low and high θ_{rel} for the calculation, while the experimental distribution if fairly flat. The most likely cause of these differences

Figure IV.9: Experimental (solid line) and calculated (dashed line) relative velocities and angles between pairs of fragments for the reaction La + Al. HI refers to the heavy-medium fragment pair, HL to the heavy-light pair, and IL to the medium-light pair.

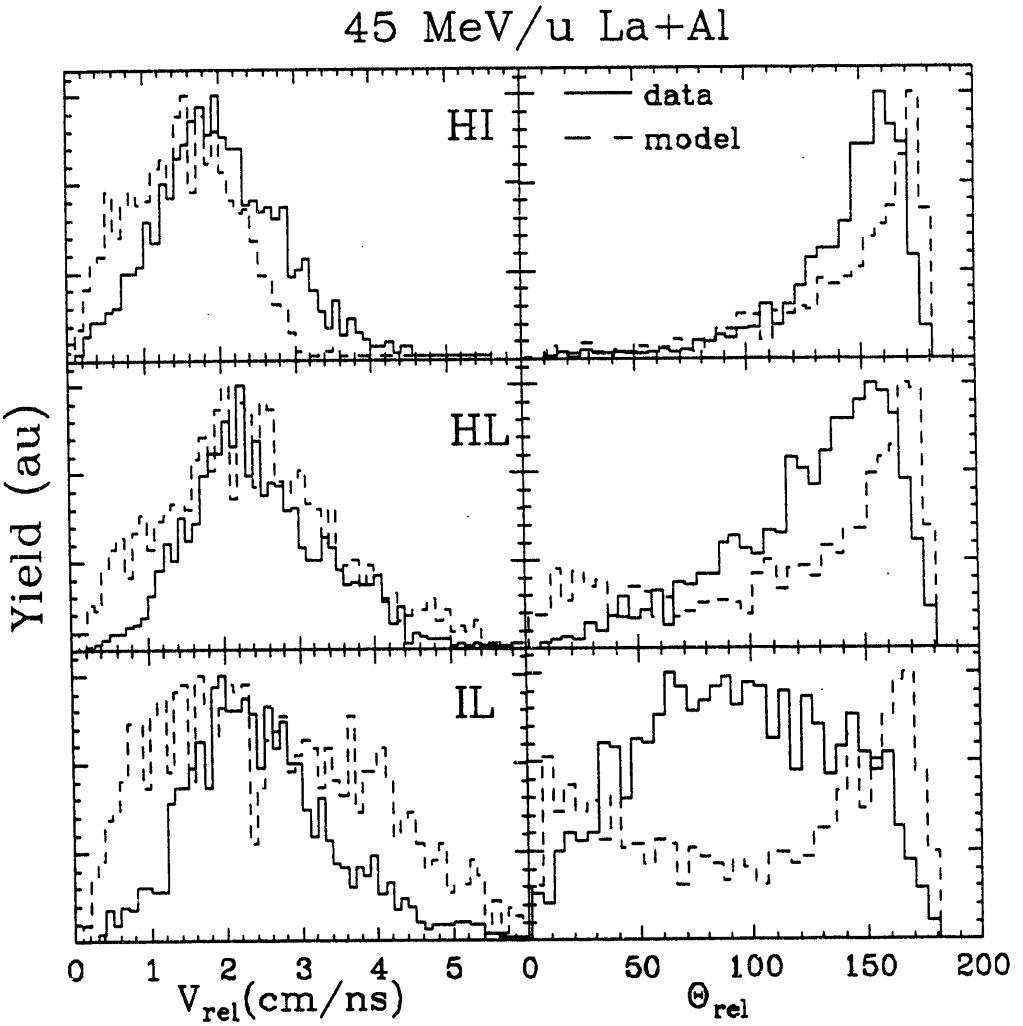
45 MeV/u La+Al
data
model
HI
HL
IL
Yield (au)
0
1
2
3
4
5
V_{rel}(cm/ns)
0
50
100
150
200
Θ_{rel}

is that, although the global experimental observables ($\sigma(Z)$, total charge and source velocity distributions) are reproduced by the model, the finer features, such as the branching ratios and the charge-Dalitz plots are not. The V_{rel} and θ_{rel} distributions are very

sensitive to changes in the charge and angular distributions of the three fragments. Because these are not being correctly calculated by the model, the V_{rel} and θ_{rel} distributions differ when compared to the experimental data.

IV.C.2 The Reaction La + V

Density plots of the time evolution of the distributions of nucleons in space for the reaction La + V at E/A = 45 MeV over a range of impact parameters are shown in Figure IV.10. For this reaction, calculations show that the fission barrier disappears (fast-fission starts) at impact parameters between b = 1 and 3 fm. The density plots at larger impact parameters show that the fast-fission channel is readily apparent (b=3 fm, t=150 fm/c) and at larger impact parameters the reaction seems to become more deep-inelastic-like. As the impact parameter is further increased, the results of the dynamics vary because of the Monte-Carlo sampling of the phase-space as was pointed out in Section IV.C. This is shown in Figure IV.11 for reactions at b= 5 fm and t=180 fm/c and Figure IV.12 at b= 6 fm and times of 180 fm/c. At b = 5 fm, the first run through the dynamics yields a result that could be interpreted as being a participant-spectator scenario, but other calculated results are more deep-inelastic-like. At b = 6 fm, the dynamics show the same variation.

One way of examining the calculated reaction mechanisms is to determine the transfer of nucleons between the projectile and target. The percent of

Figure IV.10: Same as Figure IV.4 for the reaction La + V.

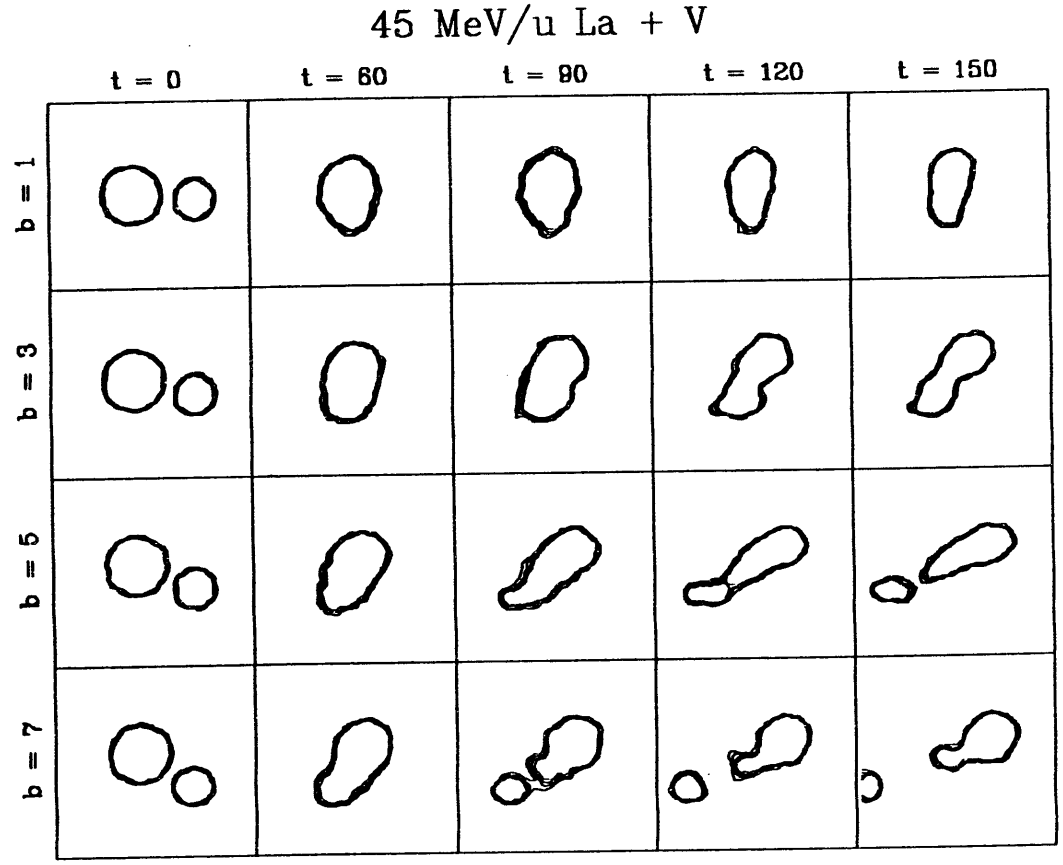
45 MeV/u La + V
t = 0
t = 60
t = 90
t = 120
t = 150
b = 1
b = 3
b = 5
b = 7

Figure IV.11: Distribution of nucleons in space for the reaction La + V at b=5 fm and t=180 fm/c for four runs through the dynamical calculations. Z is the beam axis; X is the in-plane axis.

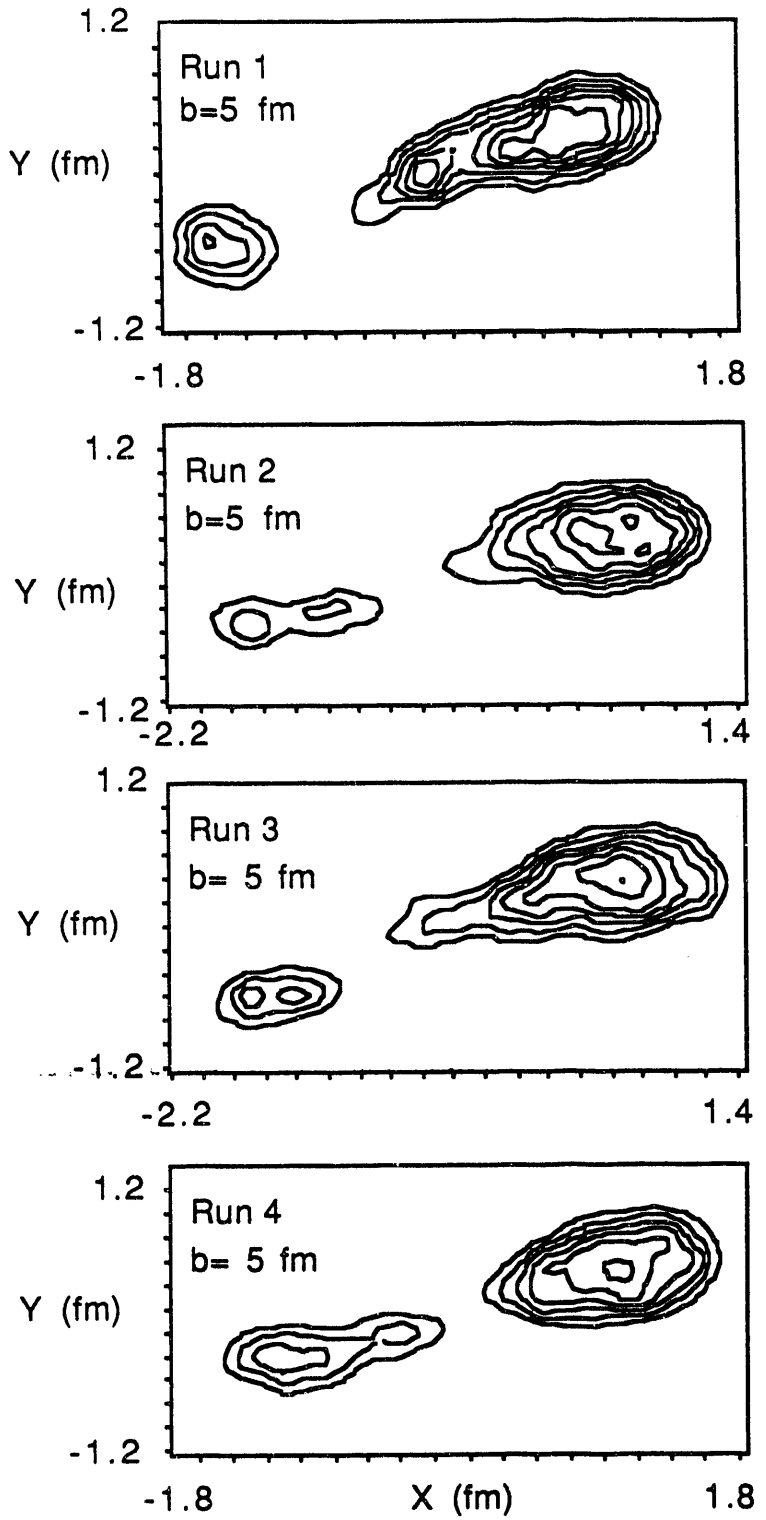
Run 1
b=5 fm
Y (fm)
1.2
-1.2
-1.8
1.8
Run 2
b=5 fm
Y (fm)
1.2
-1.2
-2.2
1.4
Run 3
b= 5 fm
Y (fm)
1.2
-1.2
-2.2
1.4
Run 4
b= 5 fm
Y (fm)
1.2
-1.2
-1.8
X (fm)
1.8

Figure IV.12: Same as Figure IV.11 for b=6 fm.

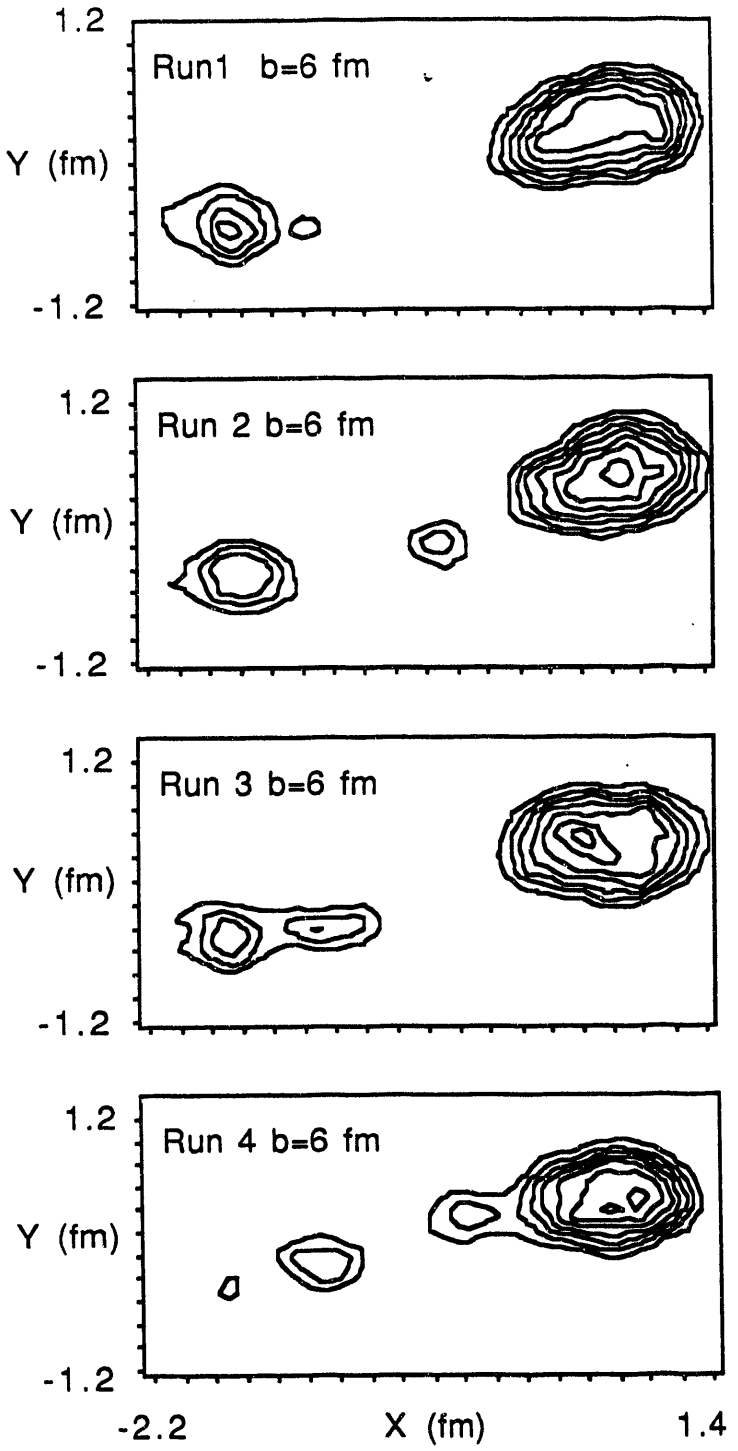
Run1 b=6 fm
Run 2 b=6 fm
Run 3 b=6 fm
Run 4 b=6 fm
1.2
-1.2
Y (fm)
-2.2
X (fm)
1.4

Figure IV.13: Percent of projectile nucleons in each fragment as a function of impact parameter for the reaction La + V. Diamonds represent the projectile-like fragment (PLF), squares the target-like fragment (TLF) and circles the participant zone. The multiple points for some impact parameters reflect the variations in the results for different runs through the dynamics.

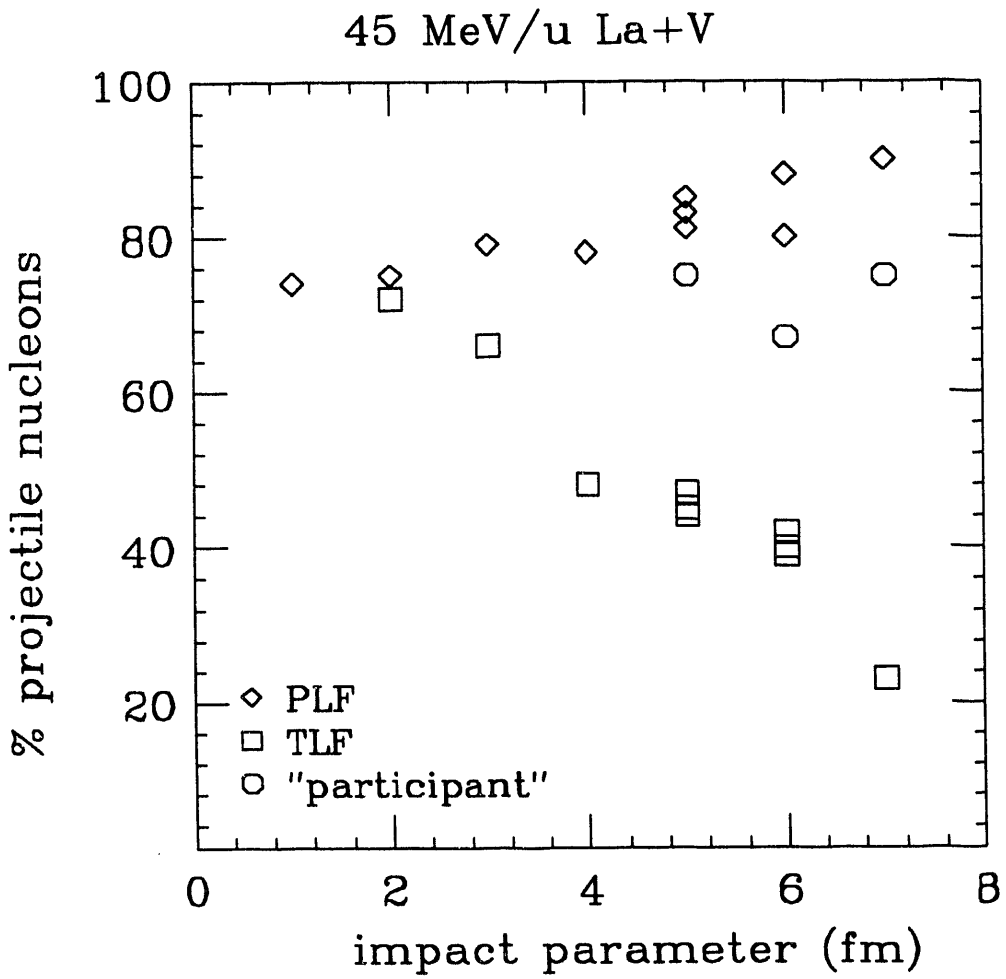
45 MeV/u La+V
100
80
60
40
20
% projectile nucleons
PLF
TLF
"participant"
0
2
4
6
8
impact parameter (fm)

projectile nucleons in the calculated fragments as a function of impact parameter is shown in Figure IV.13. At larger impact parameters, less and less of the projectile is being incorporated into the target-like fragment (and vice-versa). This shows that the asymptotic behavior of the reaction is being reproduced. As the reaction becomes more central, a larger portion of the target is incorporated into the projectile, so that for b=2 (the beginning of the fast-fission behavior) an equilibration is reached.

Moreover, central collisions show that complete fusion takes place, with the product at the same projectile-nucleon percentage as the initial reacting system.

Because of the variation in results for different runs at large impact parameters, the properties of the fragments were parameterized for each run through the dynamics and then used as the inputs for GEMINI. The parameterization was also done using different values of the freeze-out time due to the uncertainty in its determination, as shown in Figure IV.1 The calculated cross sections were then averaged over several runs. This is shown in Figure IV.14 for the calculation at two different freeze-out times (100 and 105 fm/c) and the experimental data. At t=100 fm/c, the shape of the distribution matches that of the data, except at low fragment Z values. This is most likely due to the discrete nature of the dynamics, in which a change of one ℓ-wave results in a change of the reaction mechanism.

The overprediction of the cross section by the calculation arises from the choice of the freeze-out time. By using a larger freeze-out time, the magnitude of the distribution becomes more similar to that of the experimental data (between Z = 14 and 25), but the overall shape of the distribution is much different. This change in magnitude, especially for fragments around Z = 30, is probably due to the lower excitation energy and angular momentum of the fusion product. This

Figure IV.14: Experimental (diamonds) and calculated (squares and stars) fragment cross sections for the reaction La + V. The model cross sections were calculated using two different freeze-out times. The error bars are the same as in Figure III.15.

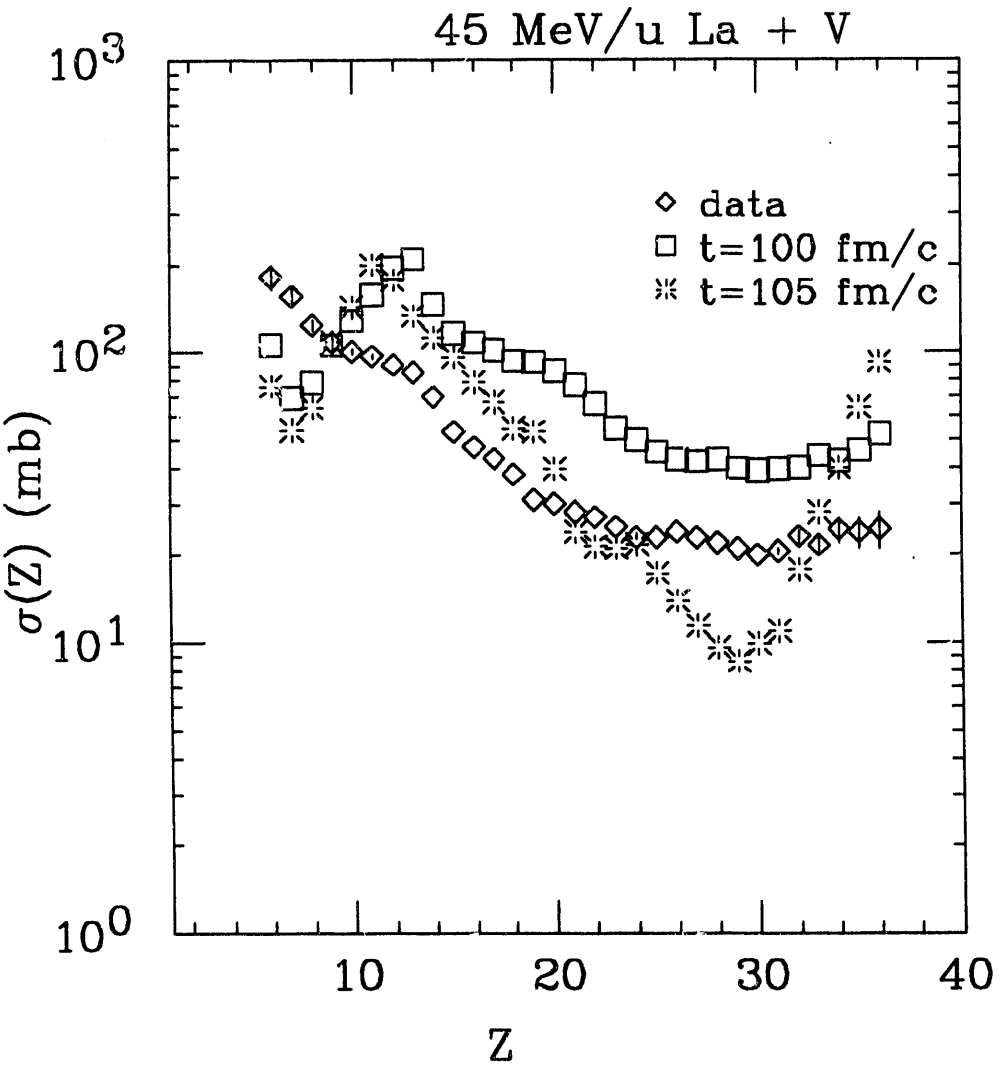
45 MeV/u La + V
data
t=100 fm/c
t=105 fm/c
10^3
10^2
10^1
10^0
σ(Z) (mb)
10
20
30
40
Z

product can either evaporate light particles or undergo fission. Fission is a function of both excitation energy and angular momentum of the nucleus. Because the angular momentum is decreased , this leads to a decrease in the fission of the fusion product, depleting the cross section near symmetry. Another problem with the calculation of the fragment cross section arises from the transformation of the dynamical results into parameterized inputs to GEMINI. As shown in Figures IV.11 and 12, the resulting fragments from the dynamics can be highly deformed nuclei. However, GEMINI treats all fragments as spherical nuclei. The surface energy of these distorted shapes is much higher than for the equivalently sized spherical nuclei. At this time, GEMINI has no way to easily treat the relaxation of these highly distorted nuclei to spherical nuclei or the decay directly from these distorted shapes. This relaxation would involve the conversion of surface energy to excitation energy of the nucleus.

The total charge and source velocity distributions for the experimental data and the calculations for the reaction La + V are shown in Figure IV.15. A freeze-out time of 100 fm/c was used because this time reproduced the shape of the cross section distribution. The peak of the Z_{tot} distribution for n=2 does not match the data as closely as for the reaction La + Al. However, the difference is about 4 Z units, which could easily be accounted for by the emission of two alpha particles or 4 H isotopes. The magnitude of the differences in the Z_{tot} distributions for n=3 between experiment and model is similar for both the Al and V targets. This could indicate that there is not enough light particle emission from both the primary and secondary fragments. The source velocity distributions are well reproduced by the model, differing only by a few percent. This is similar to the modeling of the reaction La + Al.

The charge-Dalitz plots for the data and for the model calculations are

Figure IV.15: Experimental (solid line) and calculated (dashed line) total charge and source velocity distributions for n=2 and 3 events for the reaction La + V. The arrow is at the source velocity for complete fusion.

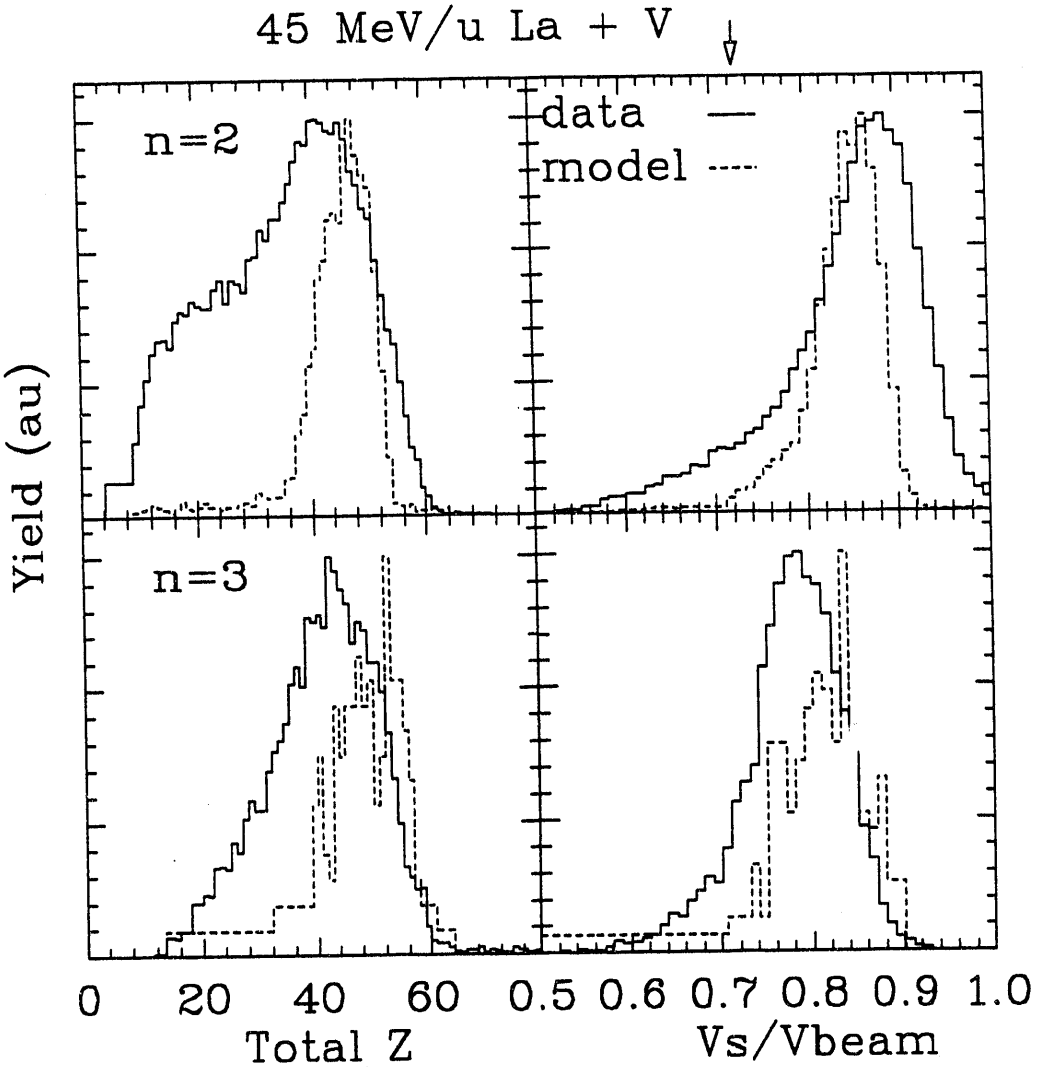
45 MeV/u La + V
n=2
data
model
n=3
Yield (au)
0
20
40
60
Total Z
0.5
0.6
0.7
0.8
0.9
1.0
Vs/Vbeam

Figure IV.16: Experimental (top) and model (bottom) charge-Dalitz plots for the reaction La + V.

La + V E/A = 45 MeV

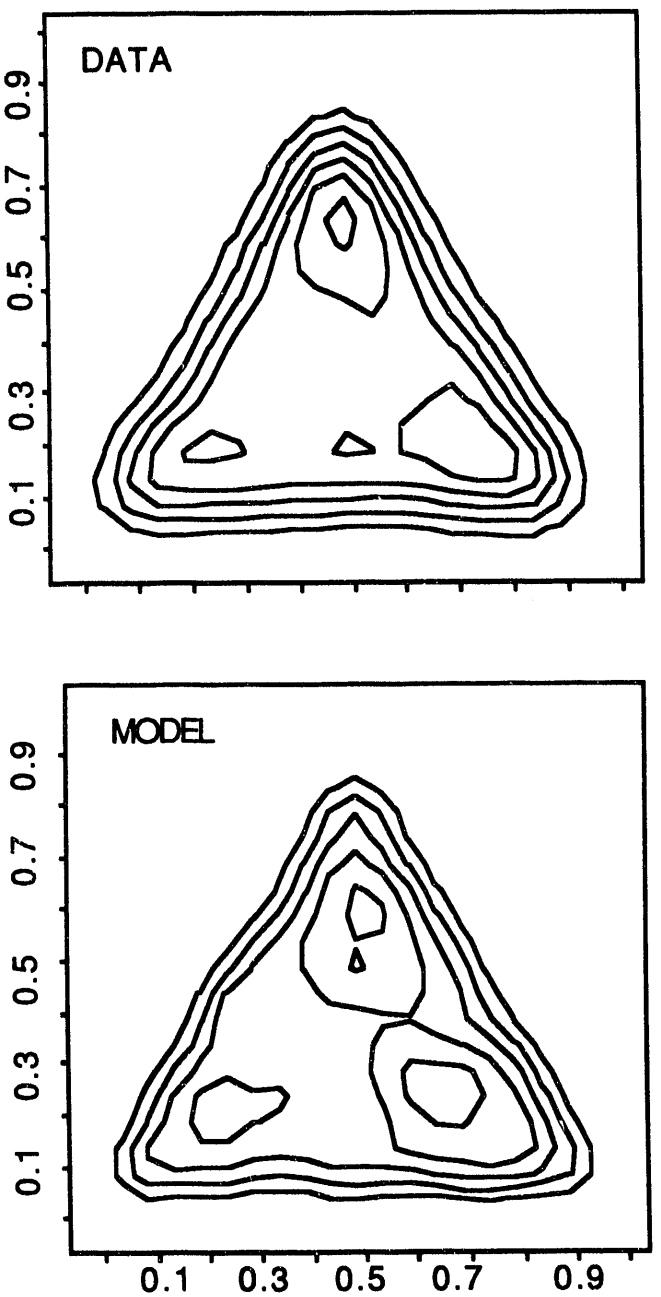

shown in Figure IV.16. The match between the data and the model in this reaction is much better than for the Al reaction. In both the experimental data and the calculation, the bulk of the yield is at the vertices (one large and two small fragments) but there is appreciable yield along the edges and in the center, which correspond to more symmetric splits of the system.

As with the modeling of the La + Al reaction, the branching ratios can be examined to see how well the calculation reproduces the data. The branching ratios of the multifragment events for the reaction La + V are shown in Table IV.2. The calculation vastly underpredicts the n =3 and 4 multiplicity events, and predicts an even smaller fraction of n=3 events than the calculation of the La + Al reaction.

The n= 4 proportion is still much smaller than that of the experimental data, but is of the same order of magnitude, unlike the Al calculation.

Table IV.2 Same as Table II.1 for the reaction La + V

multiplicity	data	calculation
2	.891	.970
3	.102	.029
4	.0076	.0011

IV.C.3 The Reaction La + Cu

The dynamical evolution of the reaction La + Cu is shown in Figure IV.17

Figure IV.17: Same as Figure IV.4 for the reaction La + Cu.

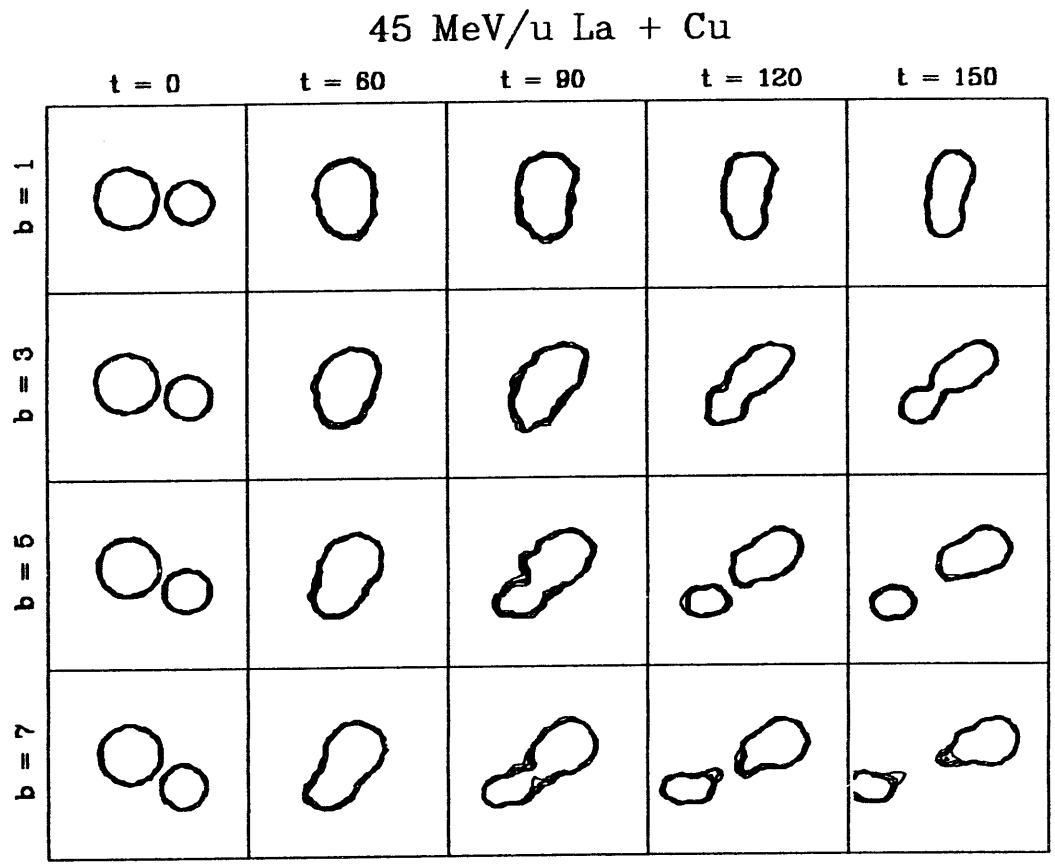
45 MeV/u La + Cu
t = 0
t = 60
t = 90
t = 120
t = 150
b = 1
b = 3
b = 5
b = 7

Figure IV.18: Distribution of nucleons in space for the reaction La + Cu at b=1 fm and times of 60, 100, 140, and 300 fm/c. X is the in-plane axis, Y is the out-of-plane axis.

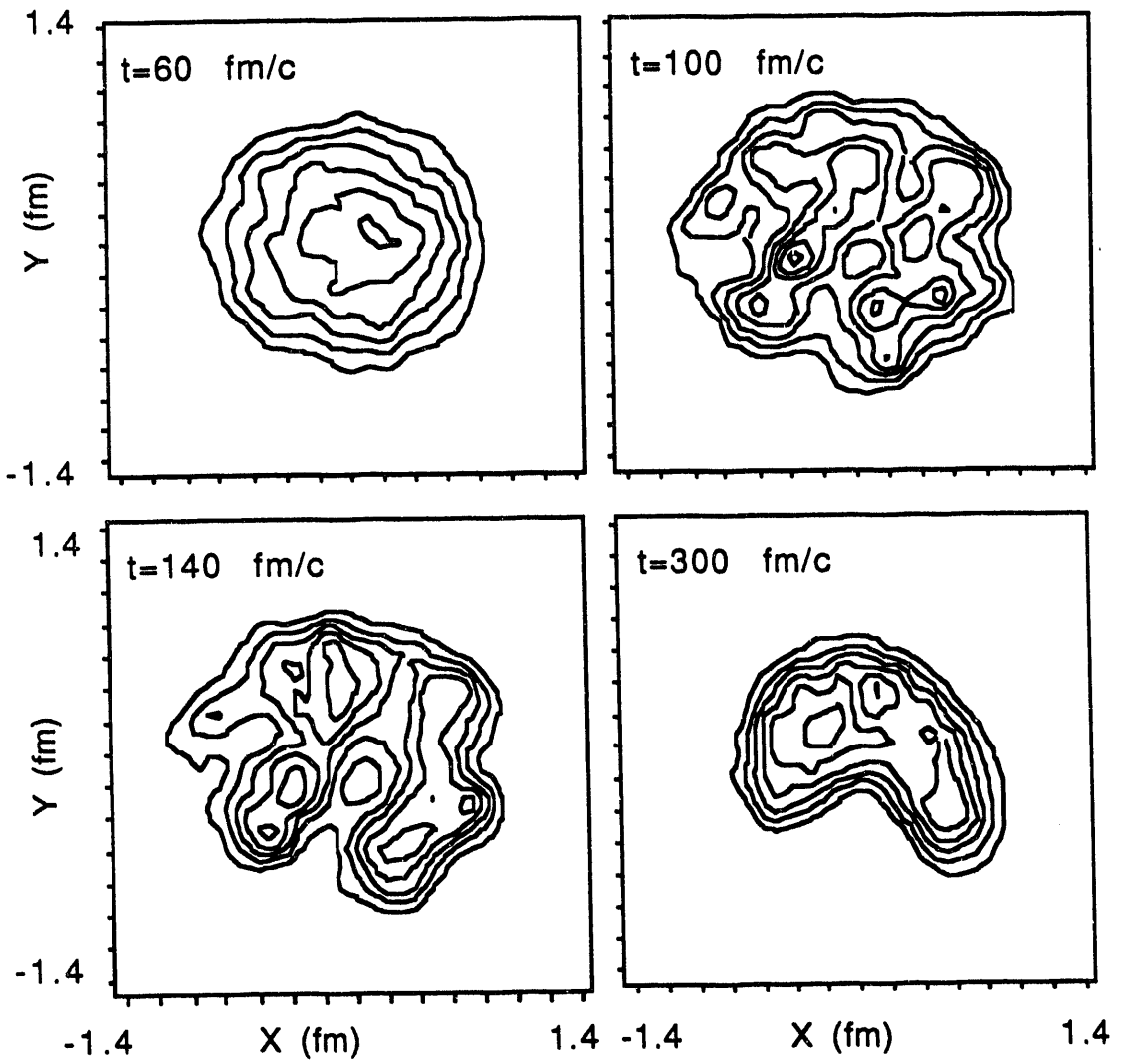
t=60 fm/c
t=100 fm/c
t=140 fm/c
t=300 fm/c
1.4
-1.4
Y (fm)
X (fm)

for a series of impact parameters. The evolution of the mechanism with increasing impact parameter is similar to that of the other targets. However, for the most central collisions (b = 1 fm), a new mechanism may be occurring that is not seen for the more asymmetric systems studied.

The density distributions of nucleons in space for this reaction at various times are shown in Figure IV.18. At t=60 fm/c, the system is a hot and very compressed system. As the system expands (t=100 fm/c), fluctuations in the density distribution start to form. The fluctuations seem to produce clusters of nucleons in space (t=140 fm/c). This might be the onset of some type of multifragmentation. However, these clusters never separate but condense back into a highly distorted system by t=300 fm/c.

The formation of a disk of nucleons and the subsequent multifragmentation has been linked to Rayleigh-Taylor-like surface instabilities (MOR92). In these instabilities , multifragmentation occurs because of interactions between the two surfaces of the disk. The disk breaks into spherical fragments with a lower total surface energy than that of the disk. Other dynamical model calculations for reactions of similar systems and energies show the formation of bubbles, rings, or even donuts of nucleons in space (BAU92, GRO92). The formation of fragments in this reaction could also be related to spinodal decomposition of the system. This means that the initial compression-expansion process leads to a region of negative compressibility, in which the system is then unstable (SUR89).

It is very difficult to determine the properties of the fragments (Z, A, velocity, and angles) in the multifragmentation scenario. Therefore, the central collisions were considered to be a hot, fused system and the GEMINI inputs were parameterized. The fragment cross sections were then determined and

Figure IV.19: Experimental (diamonds) and calculated (squares and stars) fragment cross sections for the reaction La + Cu. The calculated cross sections are for two different freeze-out times. The error bars shown are the same as in Figure III.15.

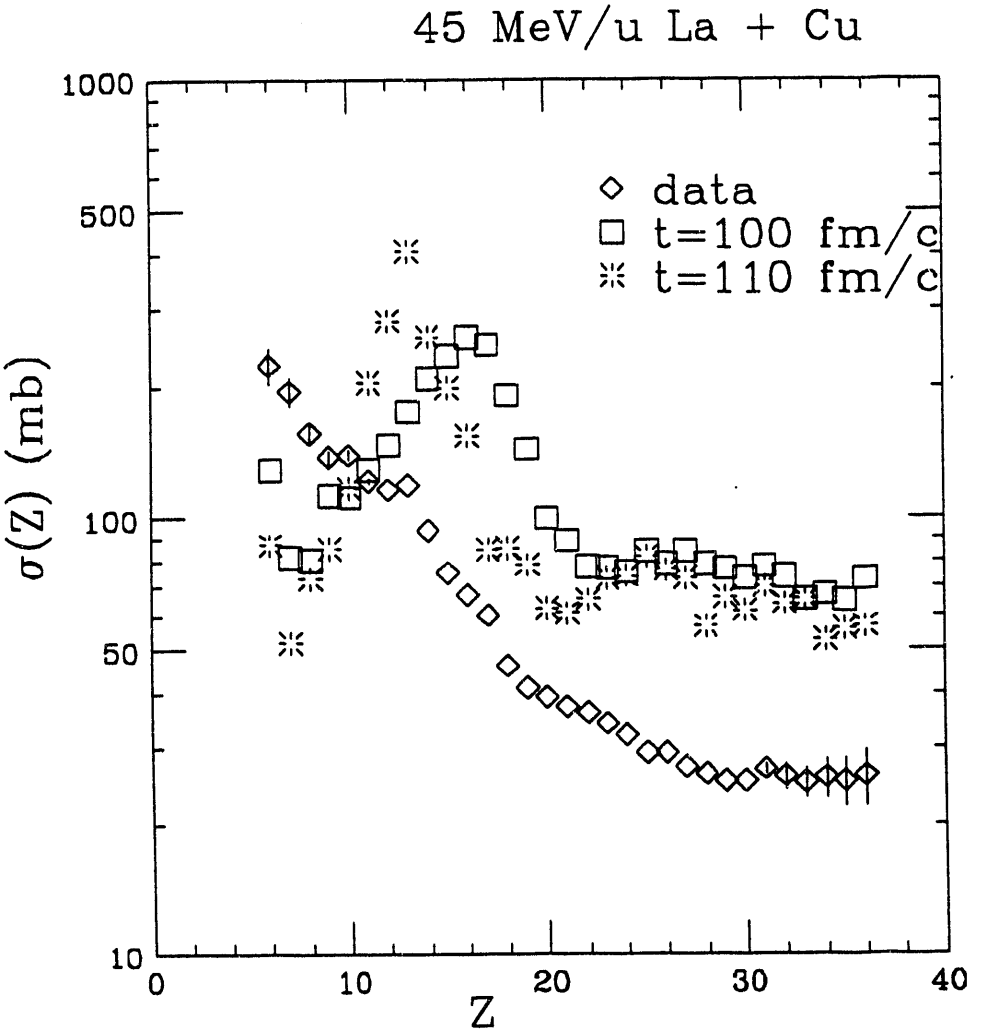
45 MeV/u La + Cu
data
t=100 fm/c
t=110 fm/c
σ(Z) (mb)
Z
1000
500
100
50
10
0
10
20
30
40

Figure IV.20: Experimental (solid line) and calculated (dashed line) total charge and source velocity distributions for n=2 and 3 events for the reaction La + Cu.

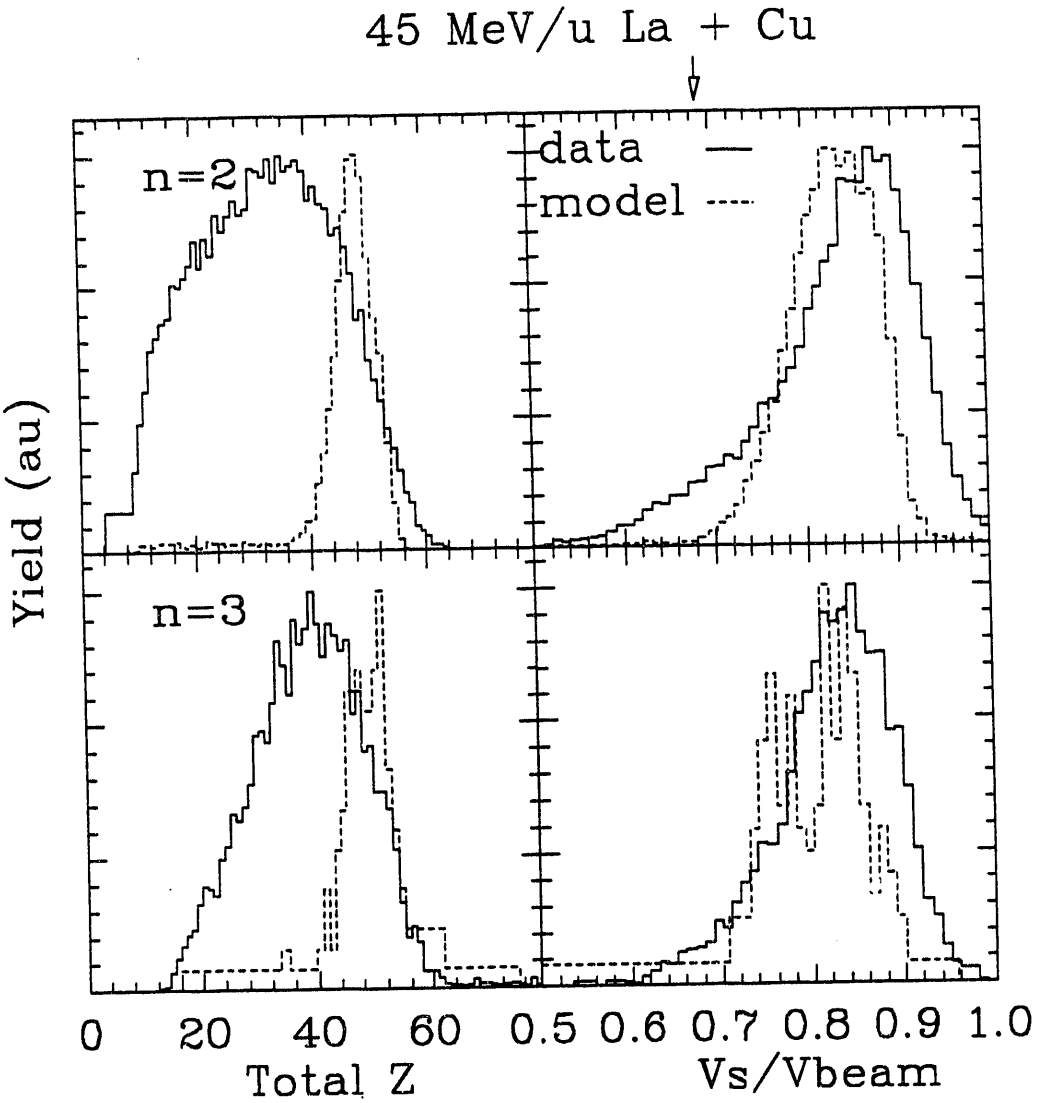
45 MeV/u La + Cu
data
model
n=2
n=3
Yield (au)
0
20
40
60
Total Z
0.5
0.6
0.7
0.8
0.9
1.0
Vs/Vbeam

compared to the actual experimental cross sections. Shown in Figure IV.19 are the experimental and calculated fragment cross sections for two freeze-out times, 100 and 110 fm/c. (Two freeze-out times were used for the same reason as for the reaction La + V.) As with the calculation of the La + V reaction, there is a dip in the cross section distribution at low fragment Z values most likely caused by the discrete nature of the calculation. However, there is a large peak in the distribution at Z = 16 for this reaction. This shows that the GEMINI calculation is not treating the breakup of the source correctly. In the calculation the cross section is fairly flat between Z=20 and 36. Changing the value of the freeze-out time does not tend to change the overall distribution. On the other hand, the experimental cross section distribution decreases smoothly until Z = 30, where it flattens out. Additionally, the magnitude of the distribution is much higher than that of the experimental data (roughly a factor of 3 between Z=20 and 36). This is a much different result than for the study of the La + Al system, in which both the magnitude and shape of the distribution were reproduced. Even the calculation involving the reaction La + V reproduced the shape of the distribution over the entire range of fragments and was within a factor of two in magnitude. This could be an indication that some type of multifragmentation is occurring for this reaction.

To get a better understanding of where the calculation may be failing in this reaction, the total charge and source velocity distributions of multiple fragment events were determined using a freeze-out time of 110 fm/c.. The longer freeze-out time was used because the magnitude of the cross section distribution was more in line with that determined experimentally (even though only the shape was reproduced for a limited range of fragments and the magnitude was still much too high). The total charge and source velocity distributions for the experimental data

and the calculation are shown in Figure IV.20. Surprisingly, the source velocity distributions for the n=2 and 3 events are well reproduced by the calculation, differing by only a few percent. This is very similar to the results of the calculations for the other reactions studied. Because the source velocity is a characteristic of the early stages of the reaction, this shows that use of the dynamics does an excellent job of preparing the system that will further decay. However, neither the peaks nor the tails of the Z_{tot} distribution are reproduced by the calculation. For the n=2 events, the experimental distribution is peaked at a much lower value than the calculation. Recall that the modeling of this reaction did not use a possible multifragmentation that may be occurring for central collisions. The lack of agreement between the calculation and the experiment could be evidence that some type of multifragmentation is occurring for this reaction. The mechanism of this multifragmentation is still an important question that has not been answered by these calculations.

IV.C.4 The Reaction La + La

In order to further clarify the possible multifragmentation that may be occurring in the reaction La + Cu for central collisions, the LV calculations were also performed for the reaction La + La at an impact parameter of 1 fm. Contour plots of the distribution of nucleons in space for this reaction at different times are shown in Figure IV.21. It is clear that for this reaction the dynamics predict the occurrence of multifragmentation. Because it is difficult to determine the properities of the fragments for this reaction, the results of the LV calculation are not combined with statistical decay calculations for this reaction. A better method of treating multifragmentation is needed to study this reaction.

Figure IV.21: Density of nucleons in space for the reaction La + La at E/A = 45 MeV and b=1 fm at t = 60, 100, and 140 fm/c.

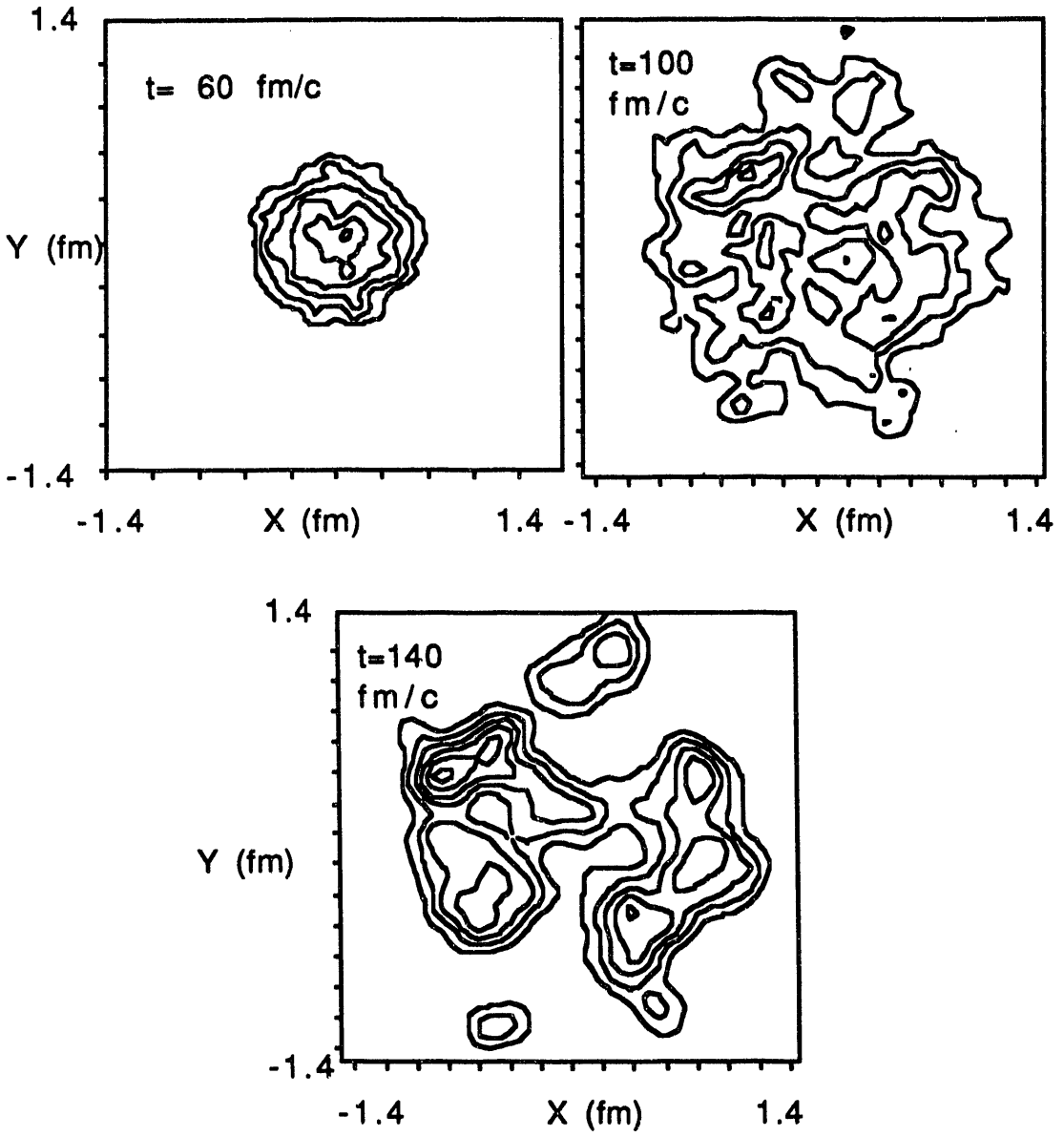
1.4
t= 60 fm/c
Y (fm)
-1.4
-1.4
X (fm)
1.4
t=100
fm/c
-1.4
X (fm)
1.4
1.4
t=140
fm/c
Y (fm)
-1.4
-1.4
X (fm)
1.4

CHAPTER V SYSTEMATICS AND DISCUSSION

By comparing the results presented in Chapter III and modeled in Chapter IV to similar reacting systems at intermediate energies, it may be possible to gain further insight into the mechanism of complex fragment emission. The bulk of the experimental work of the Maryland-LBL collaboration over the past several years has been the systematics of complex fragment emission in La-induced reactions from E/A= 35 to 55 MeV. In Section V.A these results, including modeling of the reaction La + Al at E/A=55 MeV, will be compared and contrasted to the data in this study. Section V.B includes a further discussion of the relative velocity and angle measurements presented in Chapter III. Comparison of the data presented in Chapter III and Section V.A to other studies at intermediate energy is made in Section V.C. Systematics of the fast-fission mechanism, and how this mechanism may be applicable in this study, are discussed in Section V.D. Finally, a summary of the discussion is presented in Section V.E.

V.A LA-INDUCED REACTIONS AT E/A= 35-55 MeV

The systematics of complex fragment emission have been studied over a range of bombarding energies in order to examine how the mechanism(s) responsible for fragment production evolve as both the mass of the target and bombarding energy are changed. This produces systems with an overlapping range of excitation energies, allowing comparison between different systems and energies.

The Z1-Z2 coincidence plots are shown in Figure V.1 for the reactions La + C, Al, V or Ti, and Cu or Ni at E/A=35, 40, 45, and 55 MeV (ROU92). In this plot,

the data from the Ti and V targets and Cu and Ni targets are presented in the same columns because their atomic numbers differ only by one.

For the reactions on the C target at E/A=35 and 40 MeV, the decay of the system is essentially binary. The Z1-Z2 plane is populated along a ridge line at constant total Z. However, there seem to be two different mechanisms involved in these reactions - asymmetric and symmetric fission. As either the target mass or the bombarding energy increases, the symmetric fission channel decreases, so that for the reaction La + Ti at E/A=35 MeV only asymmetric fission occurs. The ridge line of constant total Z is an important feature of the Z1-Z2 plots up to the reaction La+Al at E/A=45 MeV. The asymmetric binary decay is present in this reaction at E/A=55 MeV and for the reaction La +Ti or V at the lower energies. The increasing importance of multiple fragment decay (not to be confused with true multifragmentation) is shown by the increase in the yield below this ridge line, so that for the heavier systems at the highest energies the reaction cannot be well characterized by detection of two fragments.

As shown in Figures III.13 and 14, the angular distribution of a fragment in the center-of-mass shows an evolution from backward to forward peaking as the fragment charge is increased. This is true for all systems and energies studied. Only for a narrow range of Z values is the isotropic distribution characteristic of statistical emission processes observed. The binary ridge line in the Z1-Z2 plots shown in Figure V.1 for the C and Al targets is due to both asymmetric and symmetric fission. The angular distributions and the Z1-Z2 plots indicate that the symmetric fission is due to normal, equilibrium fission of a compound nucleus. This type of fission is seen in the system La + C at E/A=50 MeV (BOW87, BOW89a, BOW89b). The asymmetric events could be caused by a type of fission called fast-fission, in which the system is formed at entrance ℓ-waves above the fission barrier. Fast-fission

Figure V.1: Linear contour plots of yield in the Z1-Z2 plane for the reactions La + C, Al, Ti or V, and Cu or Ni at E/A=35, 40, 45, and 55 MeV (ROU92).

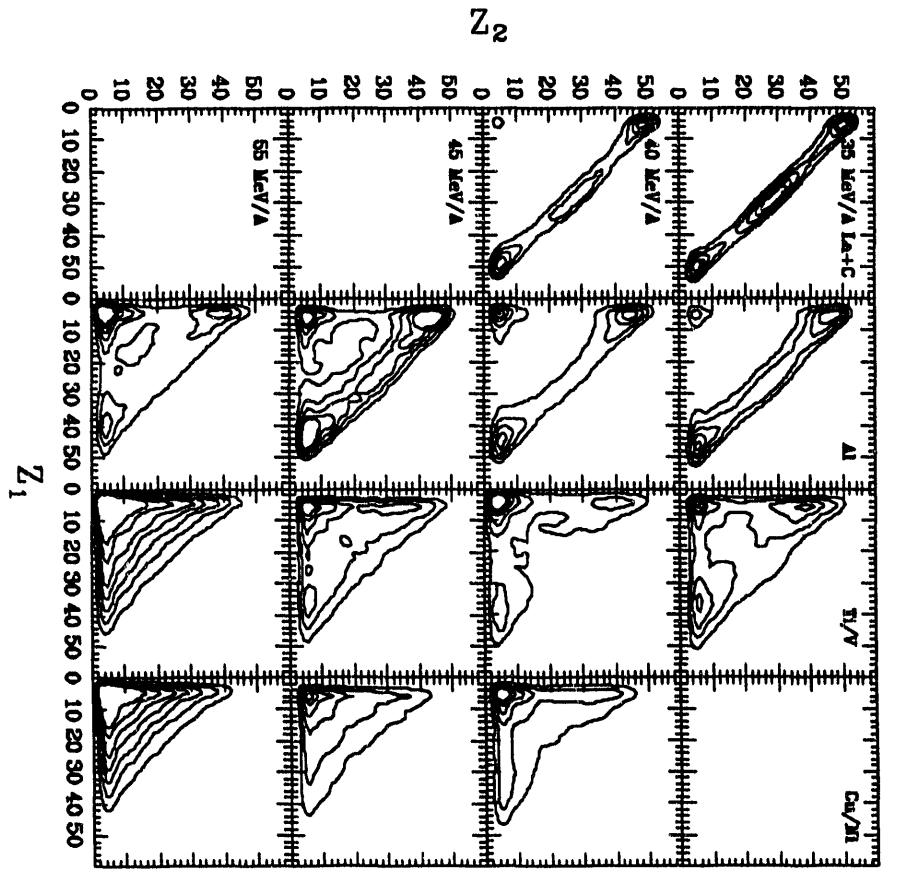
Z_2
Z_1
35 MeV/A La+C
40 MeV/A
45 MeV/A
55 MeV/A
Al
Ti/V
Cu/Ni

reactions will be discussed in detail in Section V.D.

Contour plots in the Z_{tot} - V_S plane for n=2 events for all systems and energies studied are shown in Figure V.2 (ROU92). The lines in Figure V.2 correspond to the complete fusion source velocity, the arrows are at the projectile charge (57) and the numbers refer to the available energy in the center of mass assuming complete fusion. For the reaction La + C at E/A= 35 and 40 MeV, the distribution is centered at a well determined source velocity and total charge. The source velocity is between that of the projectile and complete fusion, showing that some type of incomplete fusion reaction occurs. This is consistent with the Z1-Z2 plots presented in Figure V.1. As the target mass or bombarding energy increases, the distribution spreads throughout the Z_{tot} - V_S plane. This shows the increasing importance of reactions over a wider range of impact parameters for these reactions. This also shows the increasing need of examining the results at high multiplicity for heavier systems and higher bombarding energies, because the decaying system is not well defined by the detection of two complex fragments.

The charge-Dalitz plots for the reactions La + Al, V or Ti, and Cu or Ni at E/A=35, 40, and 55 MeV are shown in Figure V.3 (ROU92). At E/A=55 MeV, the central contour is due to a hole in the distribution. For the reaction La+C at E/A=35 and 40 MeV, the number of n=3 events was too low to prepare the charge-Dalitz plots. For the lighter systems at the lower bombarding energies, the charge-Dalitz plots show yield only at the vertices, meaning that the preferred decay mechanism for these systems is one large fragment and two small ones. As either the mass of the target or the bombarding energy is increased (which increases the available energy in the center-of-mass), the more symmetric decay modes become possible, filling in the charge-Dalitz space along the edges (2 medium-mass and one light fragment) and the center (three equal-sized fragments). Even for the La + Cu system at E/A=55 MeV,

Figure V.2: Linear contour plots in the Z_{tot} - V_s plane for the reactions La + C, Al, Ti or V, and Cu or Ni at E/A=35, 40, 45, and 55 MeV. The lines indicate the complete fusion source velocity, the arrows are at the charge of the projectile (57) and each number is the available energy in the center of mass for each reaction, assuming complete fusion (ROU92).

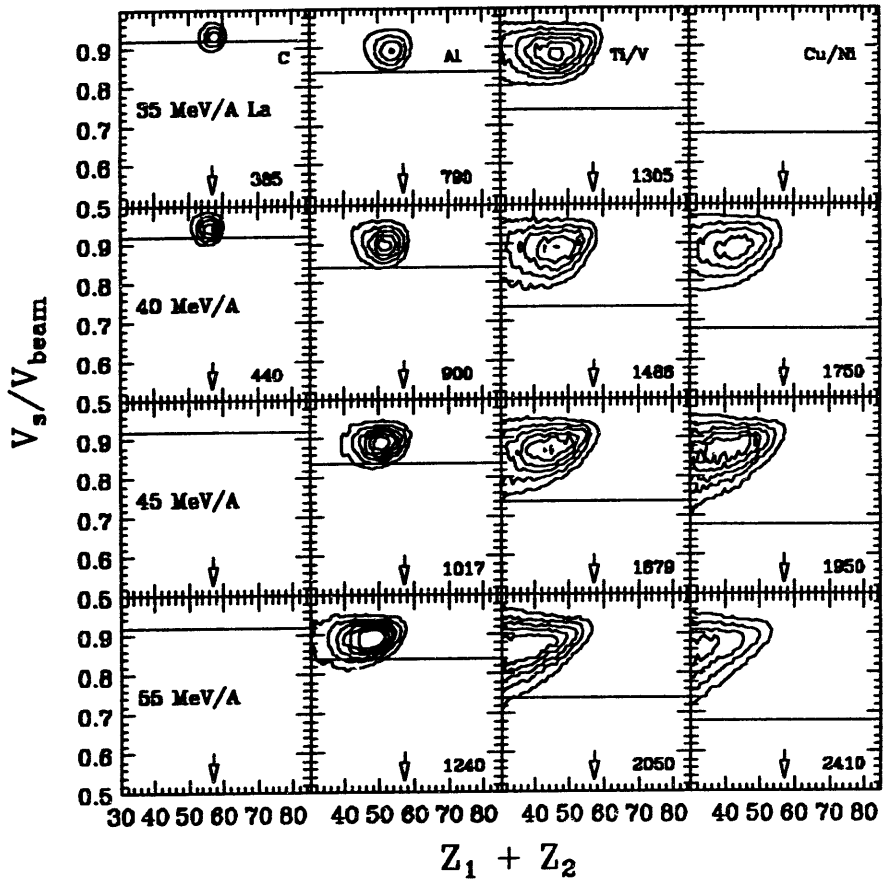
C
Al
Ti/V
Cu/Ni
35 MeV/A La
40 MeV/A
45 MeV/A
55 MeV/A
385
780
1305
440
900
1488
1750
1017
1679
1950
1240
2050
2410
V_s/V_{beam}
$Z_1 + Z_2$

Figure V.3: Charge-Dalitz plots for the reactions La + Al, Ti or V, and Cu or Ni at E/A=35, 40, and 55 MeV (ROU92).

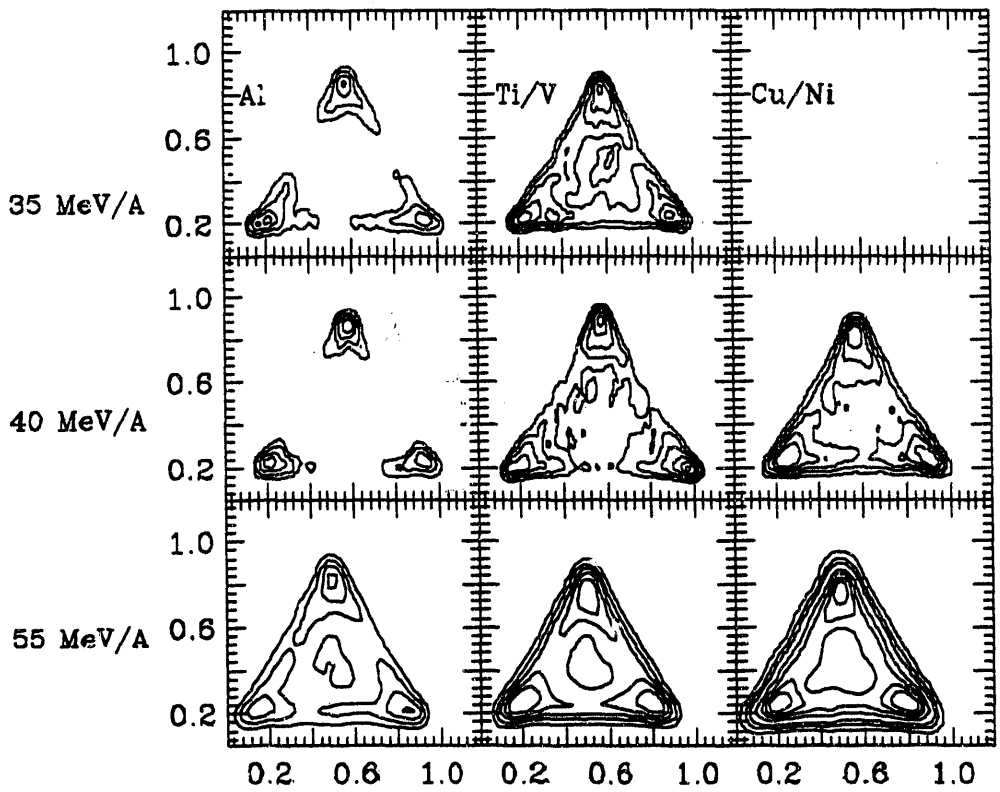
Al
Ti/V
Cu/Ni
35 MeV/A
40 MeV/A
55 MeV/A
1.0
0.6
0.2
0.2
0.6
1.0

the yield at the vertices is higher than in the center, showing that the preferred decay channel is still to decay into one heavy and two light fragments.

For the reactions La + C, Al, V or Ti, Cu or Ni, and La at E/A=35, 40, 45, and 55 MeV, the decay probabilities for multiple fragment events were determined as a function of source velocity. The source velocity was then converted to excitation energy using the prescription of equations III.5 and III.6. The decay probabilities as a function of source velocity are shown in Figure V.4 (ROU92) It should be noted that the excitation energy scale is the maximum excitation energy available, and could be 20-30% lower due to pre-equilibrium emission of light particles, recoil of any target residue, and incompletely detected events. That said, there are many remarkable features in Figure V.4.

The first is that over the entire range of energies and targets studied, the probability of decay into n fragments is independent of the system being studied, except for the reaction La + C. The probability of multiple fragment decay in the La + C reactions is systematically lower than for the other targets because the width of the source velocity distribution is due almost entirely to light particle evaporation (BLU91, ROU92). Due to this effect, using cuts in the source velocity (excitation energy) to select an impact parameter may not be applicable for this system. At high excitation energies, the probability of higher fold events for the Al target is lower than for other targets. This may be because these excitation energies correspond to the tail of the source velocity distribution, which could be due to incompletely detected events.

Another important feature arises if the excitation functions for each energy are superimposed. The excitation functions for the different bombarding energies correspond very closely. This shows that the decay probability is also independent of the bombarding energy, and dependent only on the excitation energy of the system.

Figure V.4: Decay probabilities as a function of excitation energy per nucleon of the source for the reactions La + C, Al, V or Ti, Cu or Ni, and La at E/A = 35, 40, 45, and 55 MeV (ROU92).

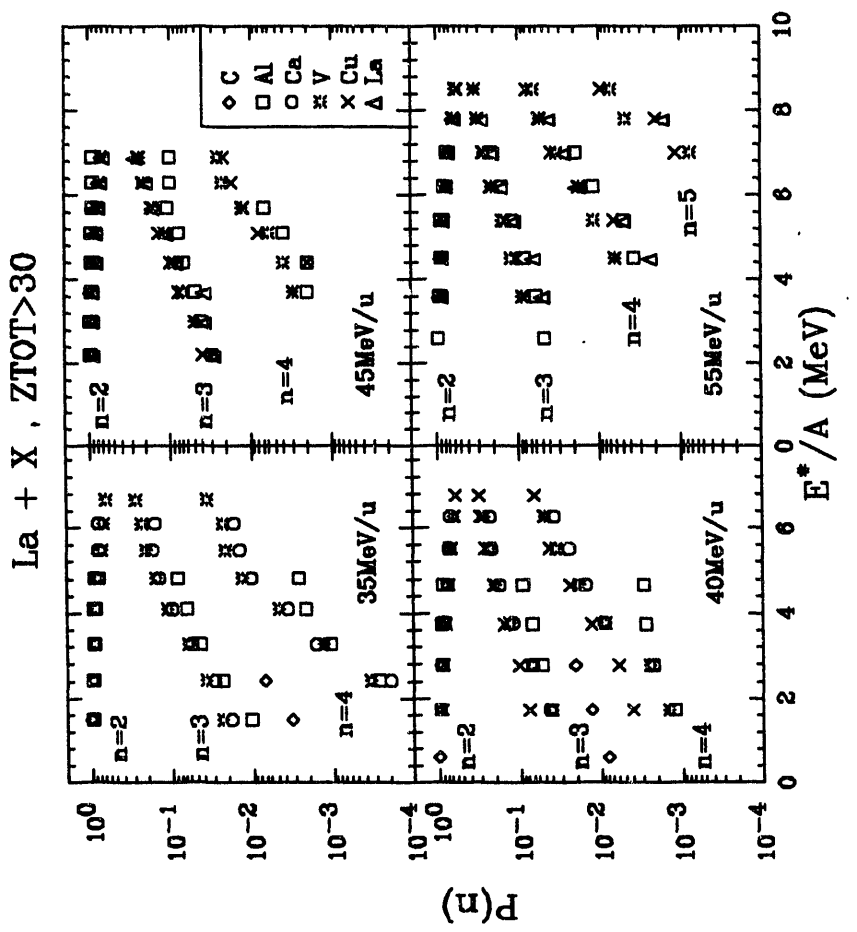
La + X , ZTOT>30
P(n)
E*/A (MeV)
C
Al
Ca
V
Cu
La
n=2
n=3
n=4
n=5
35MeV/u
40MeV/u
45MeV/u
55MeV/u

In other words, statistics seems to play an important role in multiple fragment emission from highly excited systems formed in these reactions.

The excitation functions also show a smooth increase in the probability of the higher multiplicity events as the available excitation energy increases. This is at odds with many multifragmentation models which predict a sharp increase in the probability of multifragmentation as the excitation energy increases beyond 5 MeV/A. Maximum excitation energies of greater than 8 MeV/A have been reached in these studies, with no discontinuity in the excitation functions, within the caveats of the incomplete fusion mechanism. Even decreasing the excitation energy by 20-30 % still leaves greater than 5 MeV/A of excitation energy, beyond the supposed multifragmentation limit.

Another feature shown in the excitation functions is the limiting excitation energy for the onset of the higher multiplicity events. This limit is 2-3 MeV/A for n=4 events at E/A= 35 and 40 MeV and about 4 MeV/A at the higher bombarding energies. Lower excitation energy corresponds to a higher source velocity. At higher bombarding energies, this source velocity is at the very limit of the distribution. For example, an excitation energy of 2 MeV/A corresponds to a source velocity of 0.95 beam velocity at E/A = 45 MeV. Events with this high of a source velocity are not detected at E/A = 45 MeV (see Figure III.18). Almost no n=5 events were detected until the bombarding energy reached E/A= 55 MeV, with an excitation energy for the onset of production of five fragments of about 7 MeV/A.

The calculations performed in Chapter IV to model the reactions at E/A=45 MeV have also been performed for the reaction La + Al at E/A=55 MeV (COL91). As with the results at E/A=45 MeV, the results at E/A=55 MeV have been filtered through the detector geometry and velocity acceptance. The experimental and calculated fragment cross sections are shown in Figure V.5. This figure is very

Figure V.5: Experimental (open points) and calculated (filled points) fragment cross sections for the reaction La + Al at E/A=55 MeV (COL91).

La + Al E/A = 55 MeV

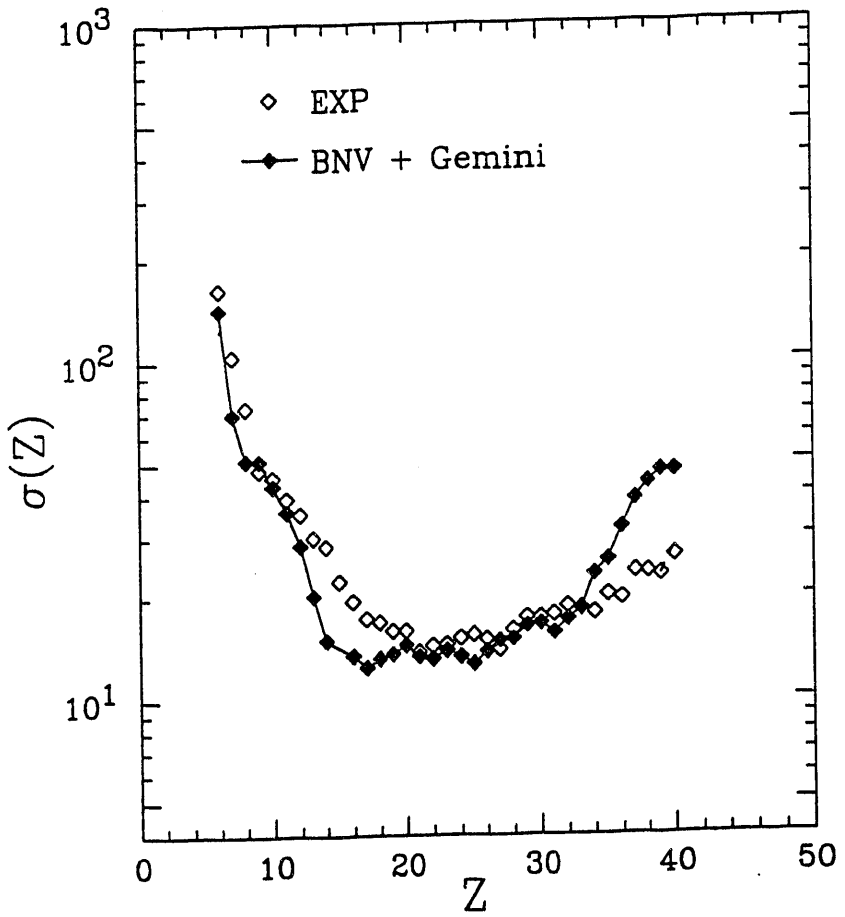

similar to Figure IV.4. The overprediction of the cross section for heavy fragments is most likely due to the experimental uncertainties in the determination of the cross sections for theses fragments. The total charge and source velocity distributions for the multiple fragment events (n = 2, 3, and 4) are shown in Figure V.6 (COL91). The peak of the total charge distributions for the n = 2 events for the model closely matches that of the data. However, the tail of the distribution is not reproduced. The discrepancy for the total charge distributions for n=3 between the data and the calculation are similar to that for the reaction La + Al at E/A = 45 MeV. The calculation reproduces the peak of the source velocity distributions, but the widths of the distributions are not reproduced for either the n = 3 or 4 events. The experimental and calculated branching ratios for this reaction are shown in Table V.1 (COL91). The simulation at E/A = 55 MeV does a much better job of reproducing the experimental branching ratios than at E/A=45 MeV, but still underestimates the yield of n=4 events.

Table V.1 Experimental and calculated proportions of multiple fragment events for the reaction La + Al E/A = 55 MeV.

multiplicity	data	calculation
2	.869	.855
3	.122	.144
4	.0088	.0017

The experimental and model charge-Dalitz plots for this reaction are shown in Figure V.7 (COL91). The calculated data is shown both before and after filtering through the detector acceptance. Although, for the most part, the calculated results

Figure V.6: Experimental (solid lines) and calculated (dashed lines) total charge and source velocity distributions for multiple fragment events for the reaction La + Al at E/A=55 MeV (COL91).

La + Al E/A = 55 MeV

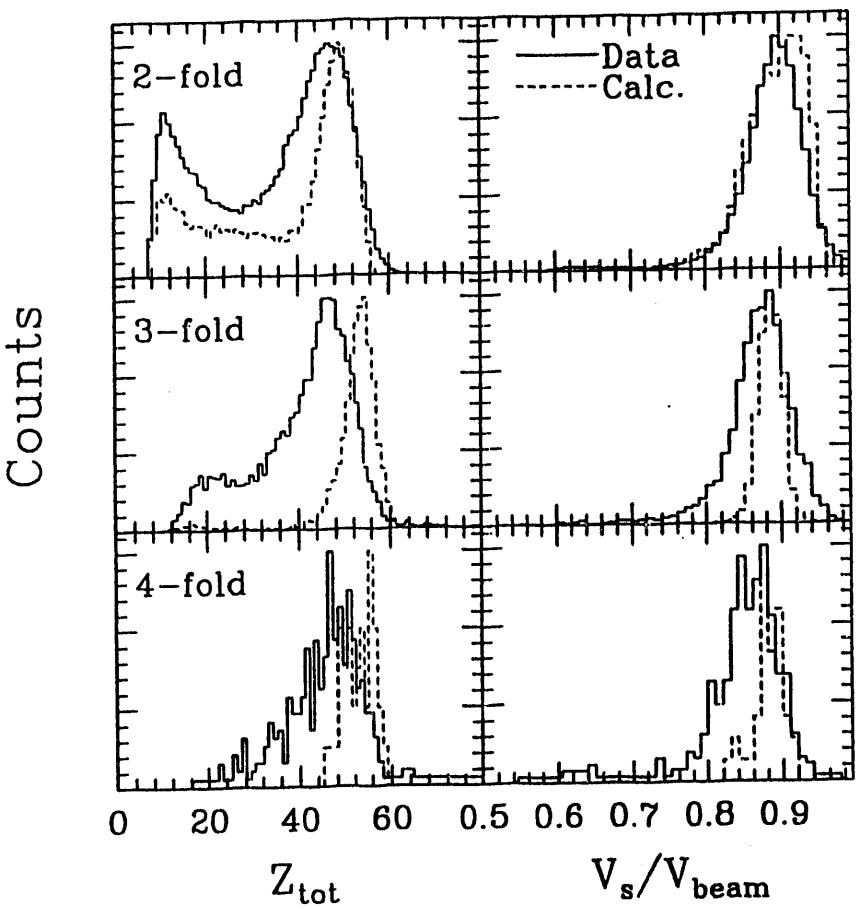

Figure V.7: Experimental and calculated charge-Dalitz plots for the reaction La + Al at E/A=55 MeV (COL91).

La + Al E/A = 55 MeV

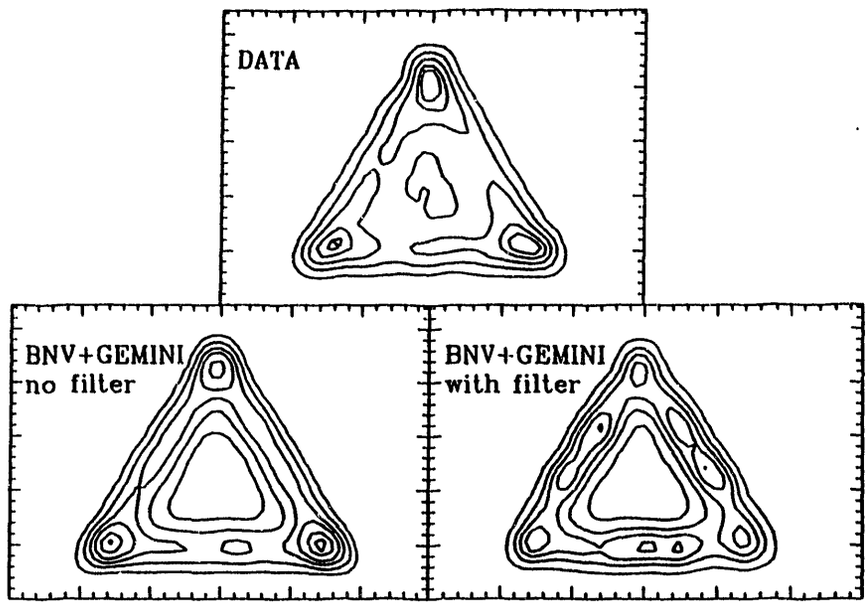

reproduce the experimental data, there seems to be a lack of population in the center of the charge-Dalitz space (symmetric splits), similar to the result of the simulation at E/A=45 MeV.

V.B CORRELATION FUNCTION ANALYSIS

In Section III.C, correlation functions were used to determine which features of the recoil fragment energy and mass spectra actually corresponded to beam on target. They can also be used to determine whether features in the experimental data are correlated in time and space or arise from random processes. For the n=3 events in the reactions La + Al, V, and Cu at E/A=45 MeV, they have been used to determine whether the features in the V_{rel} and θ_{rel} spectra are real or random. Once this has been accomplished, the correlation functions can be compared to those calculated for reactions of similar systems and also for simulations of different scenarios of the breakup mechanism.

The correlation function has the form:

$$R_{12} = \frac{R-F}{R+F} \qquad (V.1)$$

in which R and F are the yields at constant V_{rel} or θ_{rel} for real and uncorrelated events, respectively. The uncorrelated events were constructed by taking the properties of one fragment from each of three different n=3 events. The total yields are normalized to each other so that the correlation function has the values $-1 \leq R_{12} \leq 1$.

Correlation functions of the V_{rel} and θ_{rel} were constructed for each pair of fragments in n=3 events for the Al, V, and Cu targets, and are shown in Figure V.8.

Figure V.8: Correlation functions for the relative velocities and angles between pairs of fragments for the n=3 events for the reactions La + Al, V, and Cu at E/A=45 MeV. HI refers to the heavy-medium fragment pair, HL to the heavy-light pair, and IL to the medium-light pair.

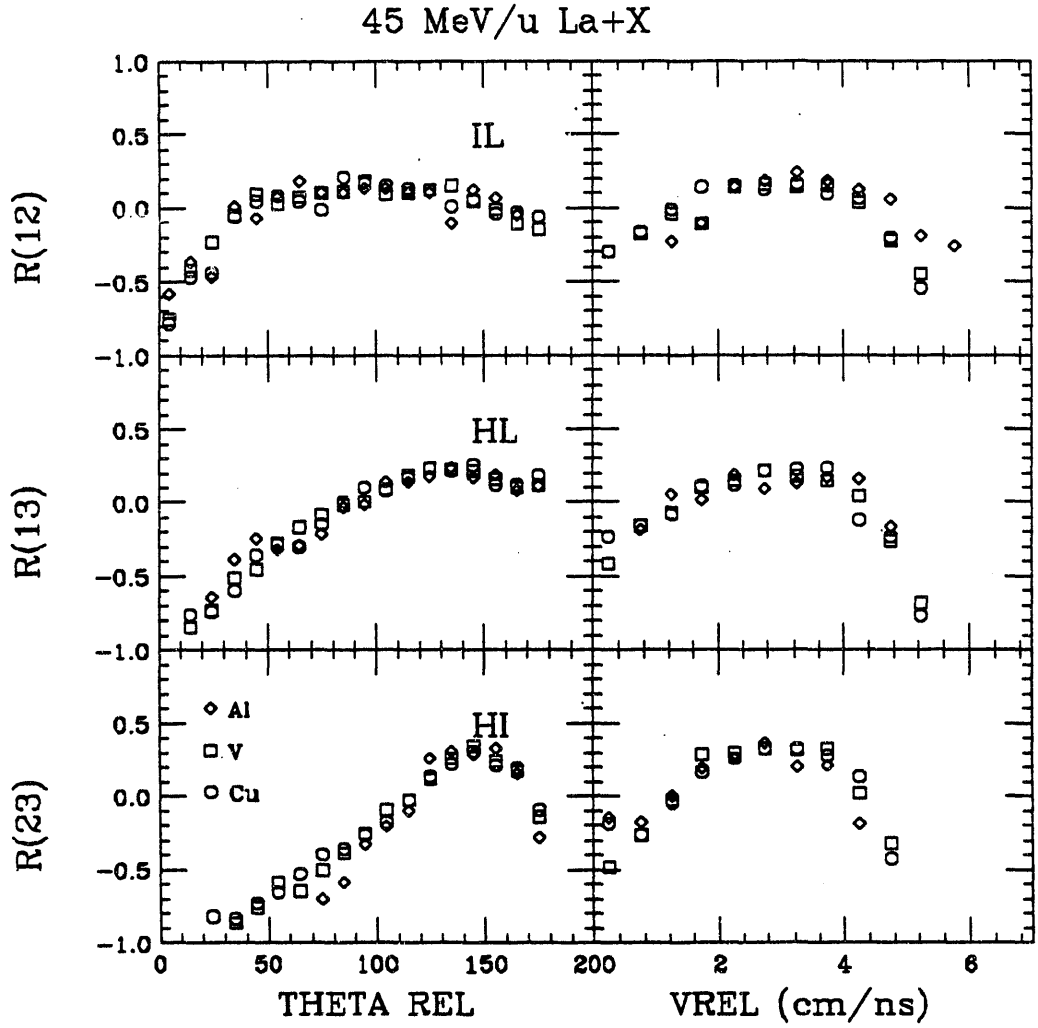
45 MeV/u La+X
R(12)
R(13)
R(23)
IL
HL
HI
Al
V
Cu
1.0
0.5
0.0
-0.5
-1.0
0
50
100
150
200
2
4
6
THETA REL
VREL (cm/ns)

The labels HI, HL, and IL refer to the heavy-intermediate, heavy-light, and intermediate-light fragments pairs, respectively. There are several important features in Figure V.8. The first is that the shape of the correlation function for each fragment pair is independent of the system studied. This is another indication, along with the excitation functions, that the decay mechanism(s) which are being studied are nearly independent of the target mass. The Coulomb-like peak in the V_{rel} distribution at ~2-4 cm/ns is a real effect. An indication of the Coulombic origin of this peak is the dip to negative values of the correlation function at low V_{rel}. This dip is largest for the HI pair and smallest for the IL fragment pair. This is exactly what would be expected if the V_{rel} is due to Coulomb repulsion between the fragments, because the HI pair is the heaviest system, and would not be expected to have a small V_{rel}.

Examination of the θ_{rel} correlation functions for each pair of fragments, shows that the peak at θ_{rel} = 140°-150° for the HI fragment pair is also real. This peak is less pronounced for the HL pair, and the flat distribution for the IL pair indicates that there is no feature in the θ_{rel} distribution of the IL pair that can be linked to correlation in time and space. The dip in the correlation function at low θ_{rel} is also largest for the HI fragment pair. This is another indication of the Coulomb-like origin of the relative velocities and angles, because Coulomb repulsion will deflect the HI fragment pair to large relative angles.

In Chapter III, different cuts in the V_s distribution were used to select an excitation energy (impact parameter range). In this way, changes in the charge-Dalitz plots, for example, could be linked to changes in the excitation energy of the system. The same can be done with the correlation functions. The same gates on the excitation energy, 3-5 MeV/A and 5-7 MeV/A, were used for the correlation functions as were used for the charge-Dalitz plots shown in Figures III.24 and 25. This covers

the range of excitation energy before and after which multifragmentation has been predicted to occur.

The correlation functions for the low and high E* bins are shown in Figures V.9 and V.10. Although the relative angle correlation functions do not seem to change with excitation energy, there seems to be an increase in the yield at higher relative velocity (>3 cm/ns) and high excitation energy compared to low excitation energy for the HI fragment pair. This increase in the yield at high relative velocities can be explained as an increase in the more symmetric decays at higher excitation energy. If the relative velocity is due to Coulombic repulsion, then the maximum velocity would occur for a symmetric decay. The charge-Dalitz plots gated on excitation energy, shown in Figures III.24 and III.25, indicate an increase in the more symmetric decays (increased yield at the edges and center) at higher excitation.

Correlation functions of this type have also been constructed to study the reaction Au + Al at E/A = 50 MeV (PEA90) and Ne + Au at E/A = 60 MeV (BOU89). These correlation functions are shown in Figures V.11 and V.12, respectively. These correlation functions are very similar to those in this study, showing a similarity in the reaction mechanism over a range of systems and energies. The excitation energies inferred in these reactions are also quite similar to those in the reaction La + Al at E/A=45 MeV.

The correlation functions in Figure V.12 have been simulated by three different scenarios (shown in the figure): simultaneous break-up (dotted line), sequential break-up with a long time between the emissions (dashed line) and sequential break-up with a short time between emissions (solid line). It is clear that the simultaneous mechanism (multifragmentation) fails to reproduce the experimental correlation functions. On the other hand, both sequential mechanisms reproduce major features of the experimental correlation functions. The sequential mechanism with a short time between decay processes allows mutual Coulomb interaction among

Figure V.9: Same as Figure V.8 at low excitation energy (high source velocity).

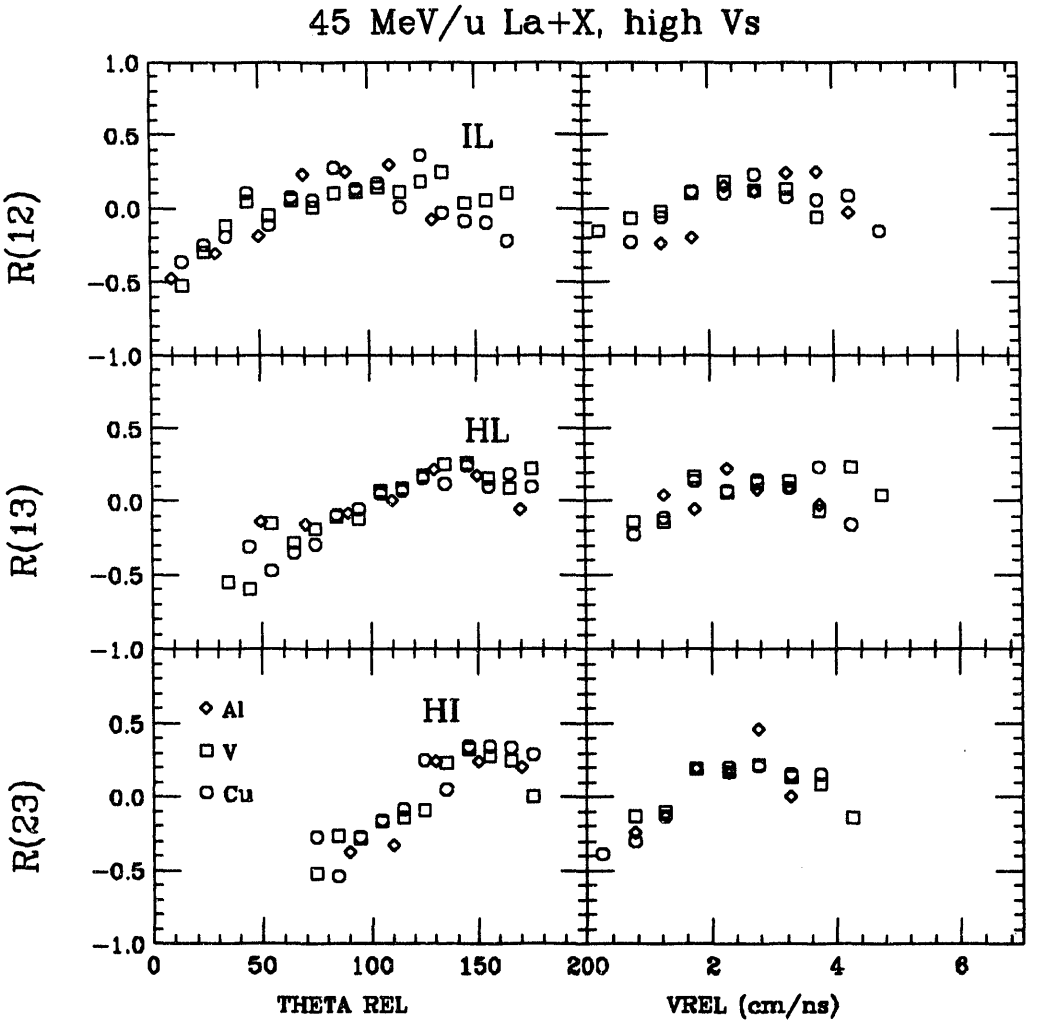
45 MeV/u La+X, high Vs
IL
HL
HI
Al
V
Cu
R(12)
R(13)
R(23)
THETA REL
VREL (cm/ns)

Figure V.10: Same as Figure V.8 at high excitation energy (low source velocity).

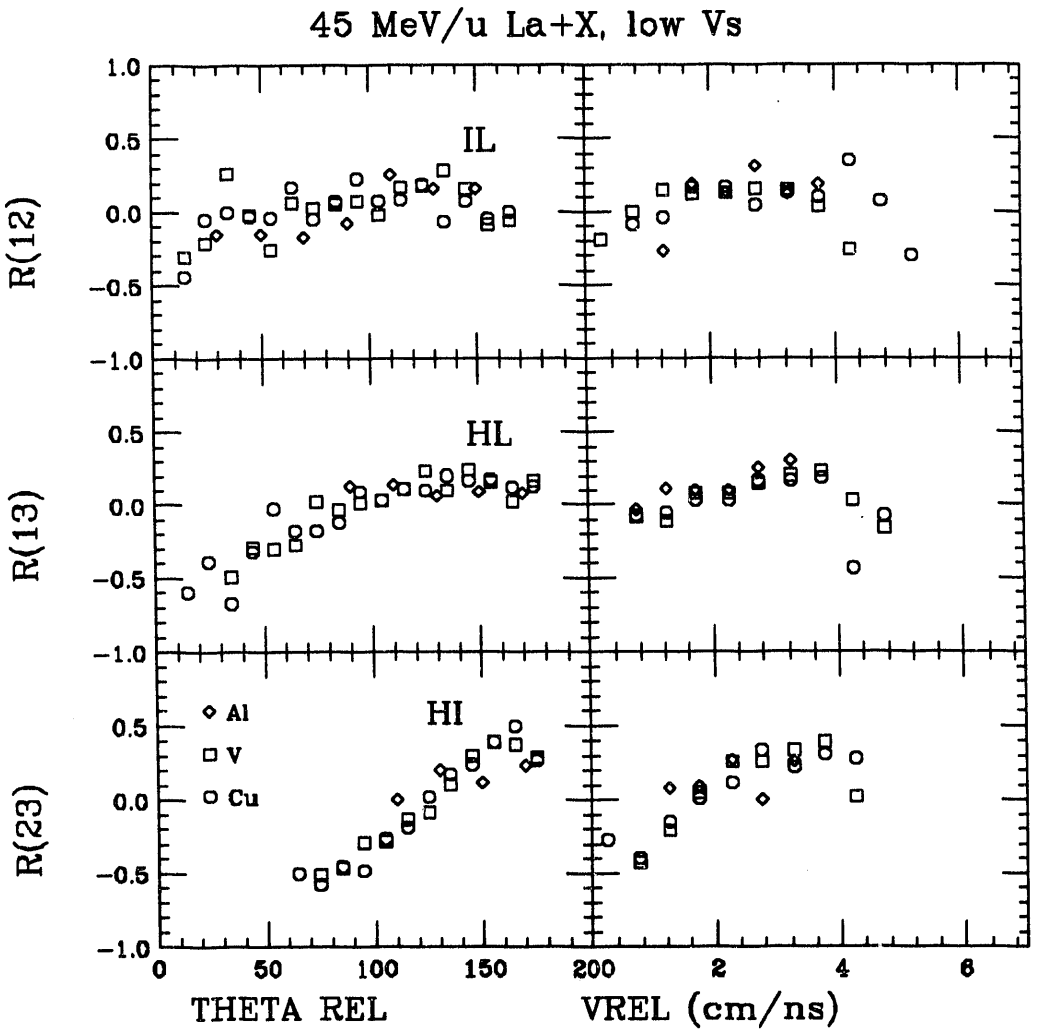
45 MeV/u La+X, low Vs
IL
HL
HI
Al
V
Cu
R(12)
R(13)
R(23)
THETA REL
VREL (cm/ns)

Figure V.11: Correlation function of the relative velocities and angles between pairs of fragments in n=3 events for the reaction Au + Al at E/A=50 MeV. The subscript 23 refers to the heavy-medium fragment pair, 13 to the heavy-light pair, and 12 to the medium-light pair (PEA90).

50 MeV/A ^{197}Au + ^{27}Al

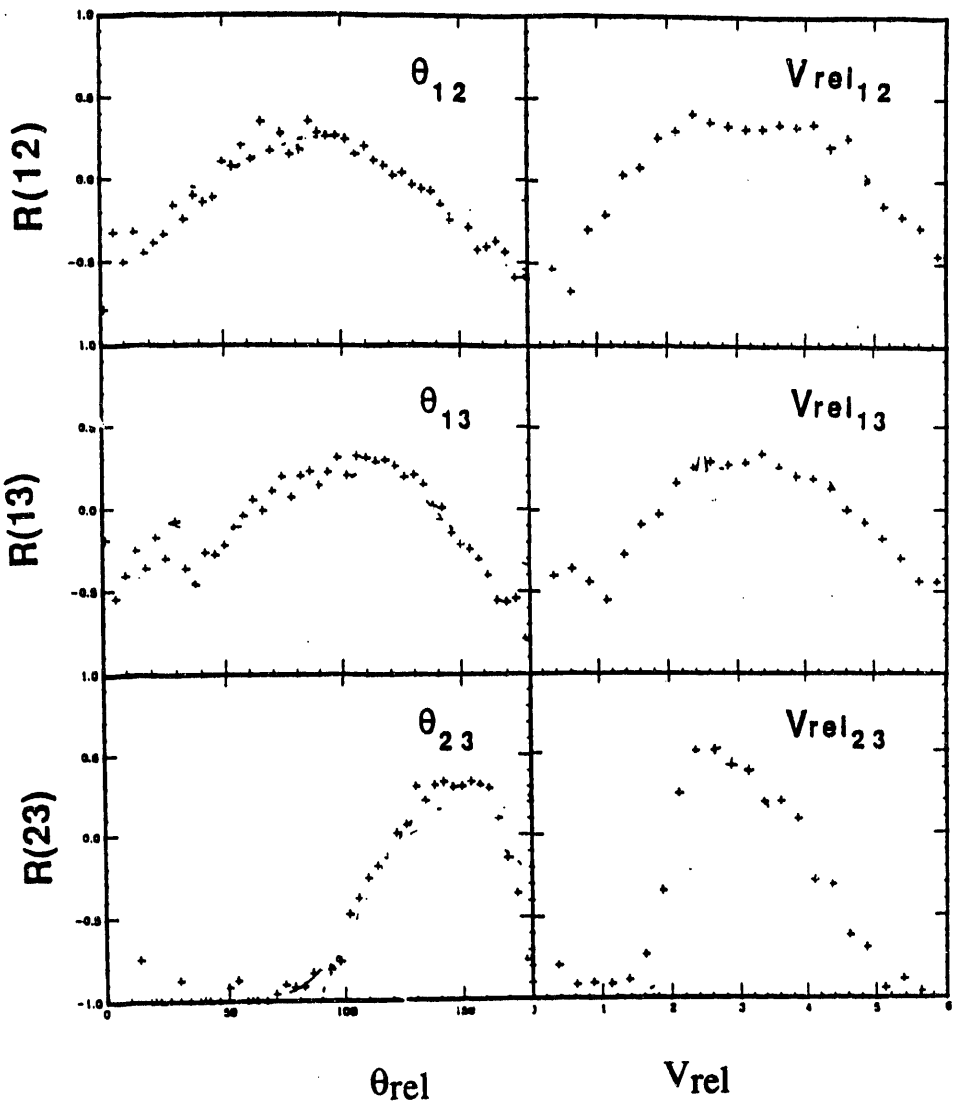

Figure V.12: Correlation functions of the relative velocities and angles between pairs of fragments in n=3 events for the reaction Ar + Au at E/A=60 MeV. The subscripts refer to the same fragment pairs as Figure V.11. The points are the experimental data. The dotted line is for a simulation of a prompt multifragmentation. The dashed line is for a pure sequential mechanism, and the solid line is for a sequential mechanism with a short time between decay steps (BOU89).

Ar + Au E/A = 60 MeV

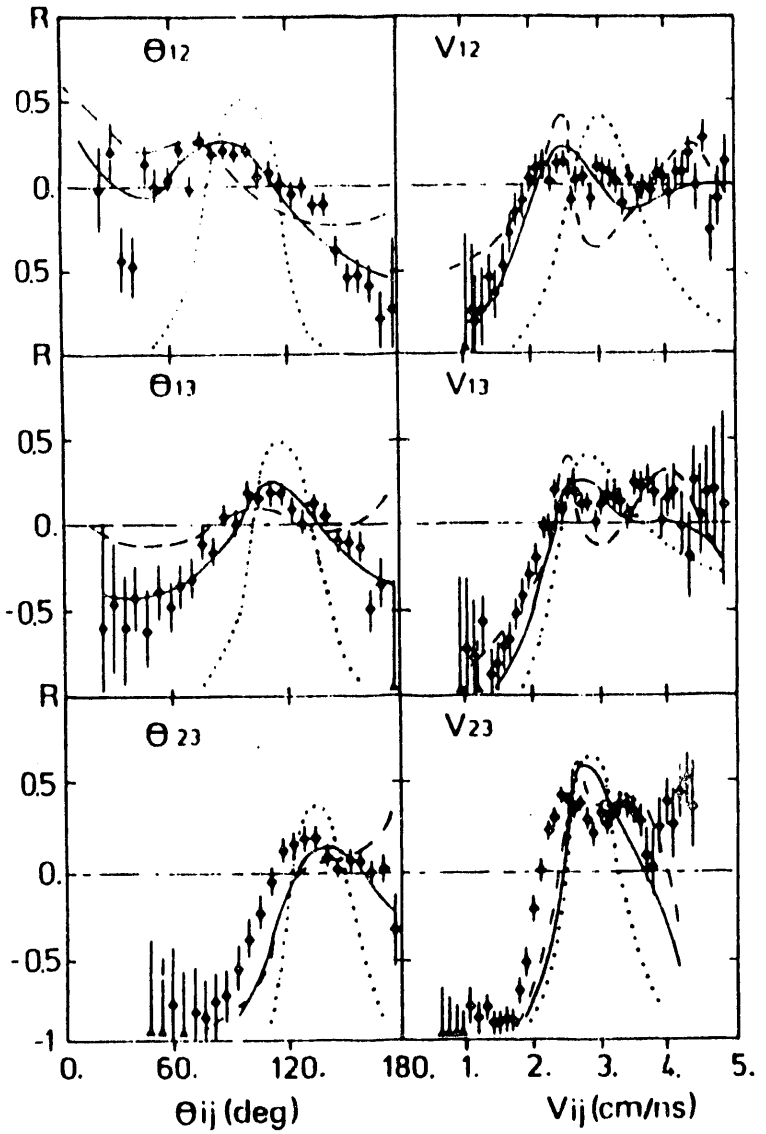

the three fragments, and seems to reproduce the experimental data better than the pure sequential mechanism.

V.C OTHER REACTIONS AT INTERMEDIATE ENERGIES

As stated in Chapter I, nuclear reactions at intermediate energies have been extensively studied over the past decade. A new generation of 4π detectors has allowed the study of complex fragment emission in coincidence with charged particle and neutron multiplicity measurements. This section presents results from these different detector systems with an eye towards clarifying the systematics discussed previously in this chapter and in Chapters III and IV.

Two of the most interesting aspects of nuclear reactions at intermediate energy have been the persistence of lower energy mechanisms, such as deep-inelastic reactions and compound nucleus formation, to fairly high bombarding energies (BOW87, BOR88) and the production of a high multiplicity of complex fragments in reactions at intermediate energies. The observation of many fragments in the final state of nuclear reactions in this energy region is now a common occurrence (BOW91b, HAG92, KIM89, KIM91, TRO89). Less clear is the mechanism for their emission. The production of many fragments has been called generically "multifragmentation", without discerning between prompt and sequential mechanisms. Deep-inelastic reactions can also produce intermediate mass fragments (IMF's) leading to a many body final state (BOR88). By examining certain features of the experimental data (and comparing features over a range of systems and energies), it may be possible to determine which features are consistent with true multifragmentation.

V.C.1. Velocity Plots

Plots in the parallel velocity and perpendicular velocity space ($V_{||}$-$V_{\perp}$) were used in Section III.A to determine whether the emission of complex fragments was due to a statistical mechanism. These plots can also be used to identify different sources of particles or complex fragments emitted in nuclear reactions.

For the reaction $^{136}Xe + ^{209}Bi$ at E/A=28.2 MeV, the $V_{||}$-$V_{\perp}$ distribution of protons detected in coincidence with 6 complex fragments is shown in Figure V.13 (LOT92). There are clearly two sources of the protons, one centered at the center-of-mass velocity of the target, the other at that of the projectile. This shows that a high multiplicity of complex fragments can arise in deep-inelastic-like reactions.

This is at odds with the study of the reaction Xe + Au at E/A=50 MeV. Velocity plots of alpha particles (top) and C fragments (bottom) are shown in Figure V.14 (BOW92a). The left (right) side of each figure are the velocity plots of the representative fragment in coincidence with low (high) charged particle multiplicity. This is used to gate on peripheral and central reactions. It is clear that the velocity spectrum of the alpha particles for peripheral collisions shows two sources. This is consistent with Figure V.13. However, central collisions in this reaction yield a source with a velocity in between that of the projectile and target, and it is only for the central collisions that a high multiplicity of complex fragments detected. A similar results is seen for the C fragments. This figure shows that the reaction mechanism changes as the multiplicity of charged particles changes. Figures V.13 and V.14 show the evolution of the reaction mechanism producing IMF's as the bombarding energy is increased.

Velocity plots can also be constructed for all IMF's detected in a heavy-ion experiment. Figure V.15 shows just such a plot for events in which 5 complex

Figure V.13: Contour plot of the distribution of protons in coincidence with 6 IMF's in $V_{||}$-$V_{\perp}$ space for the reaction Xe + Bi at E/A = 28.2 MeV (LOT92).

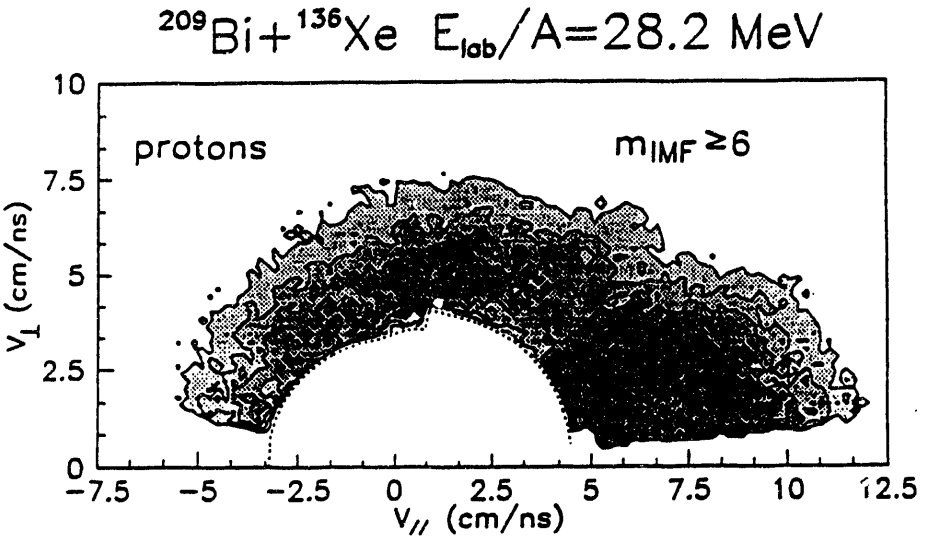
$^{209}Bi+^{136}Xe$ $E_{lab}/A=28.2$ MeV
protons
$m_{IMF} \geq 6$
$V_\perp$ (cm/ns)
$V_{//}$ (cm/ns)
10
7.5
5
2.5
0
−7.5
−5
−2.5
0
2.5
5
7.5
10
12.5

Figure V.14: Contour plots of the distribution of alpha particles (top) and C fragments (bottom) in $V_{||}$-$V_{\perp}$ space for the reaction Xe + Au at E/A = 50 MeV. The left half of the figure is for low charged particle multiplicity (peripheral reactions); the right half of the figure is for high charged particle multiplicity (central collisions) (BOW92a).

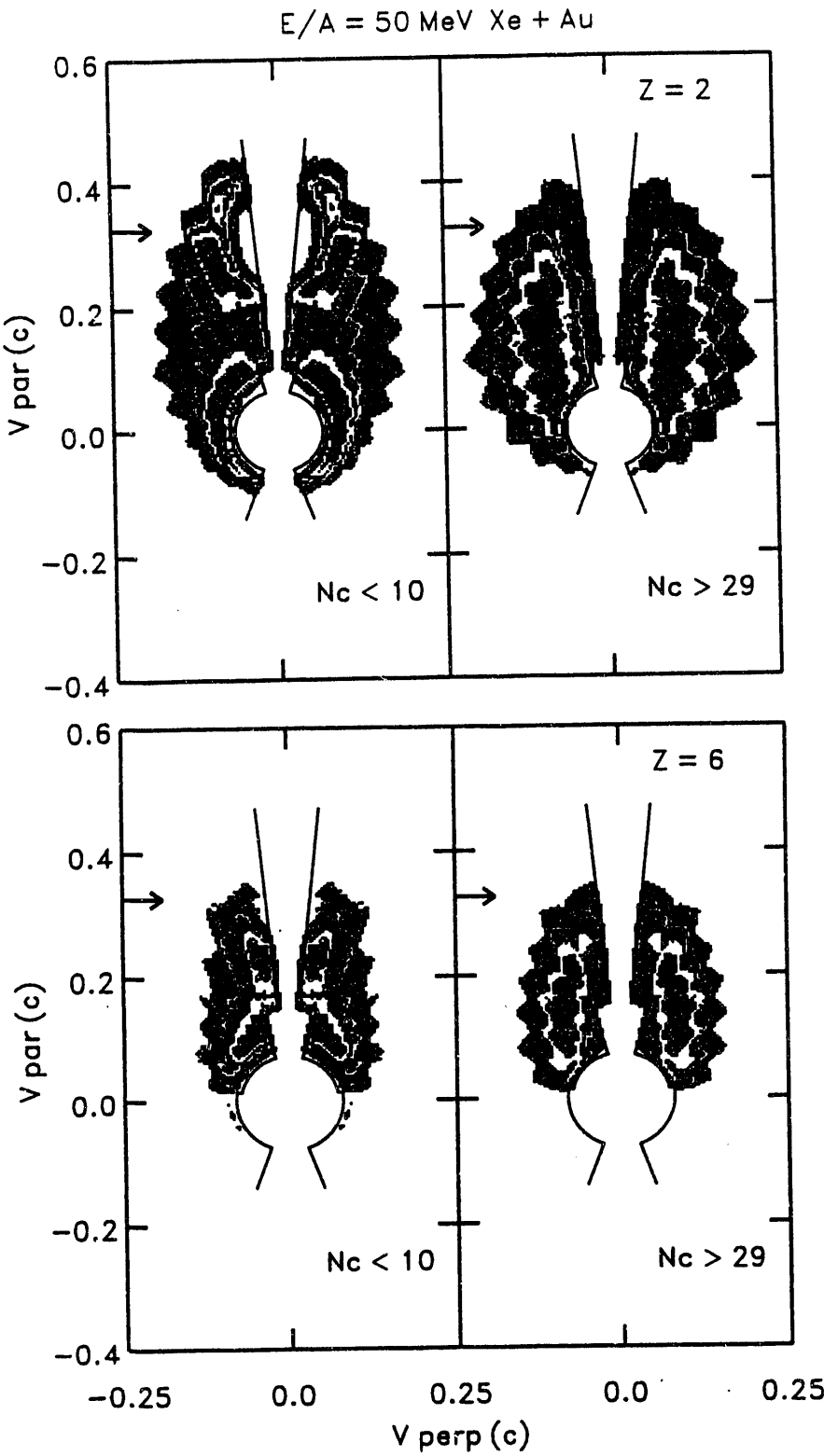
E/A = 50 MeV Xe + Au
Z = 2
Nc < 10
Nc > 29
Z = 6
Nc < 10
Nc > 29
V par (c)
V perp (c)
0.6
0.4
0.2
0.0
−0.2
−0.4
−0.25
0.0
0.25

Figure V.15: Contour plots in $V_{||}$-$V_{\perp}$ space of IMF's for n=5 events for the reaction Kr + Au at E/A=43 MeV (BOU88).

Kr + Au E/A = 43 MeV

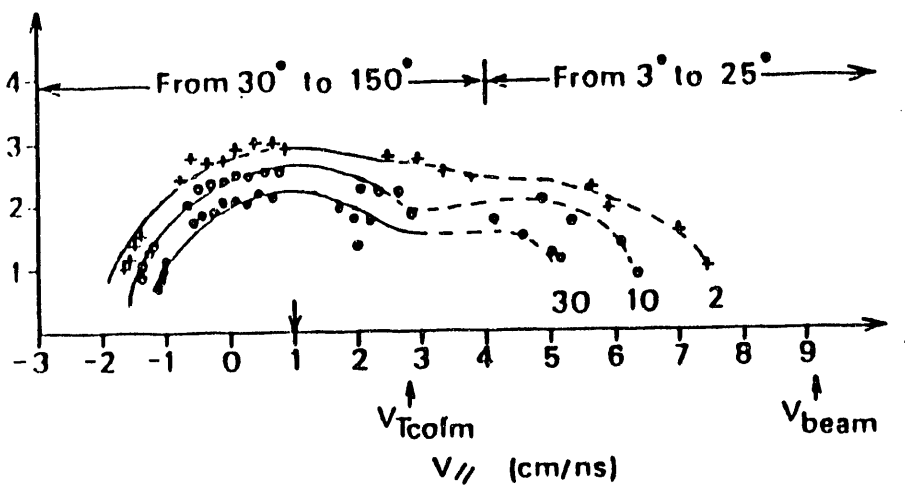

Figure V.16: Contour plots in $V_{\|}$-$V_{\perp}$ space for C fragments emitted in the reaction ^{3}He + Ag at E/A=1.2 GeV. The top half is for fragments detected in coincidence with one IMF, the bottom half for coincidences with 3 IMF's. The letters in the top half of the figure correspond to the arrows (from left to right) indicating the source velocity of the contour (YEN91).

$^{3}He + ^{nat}Ag$ E/A = 1.2 GeV

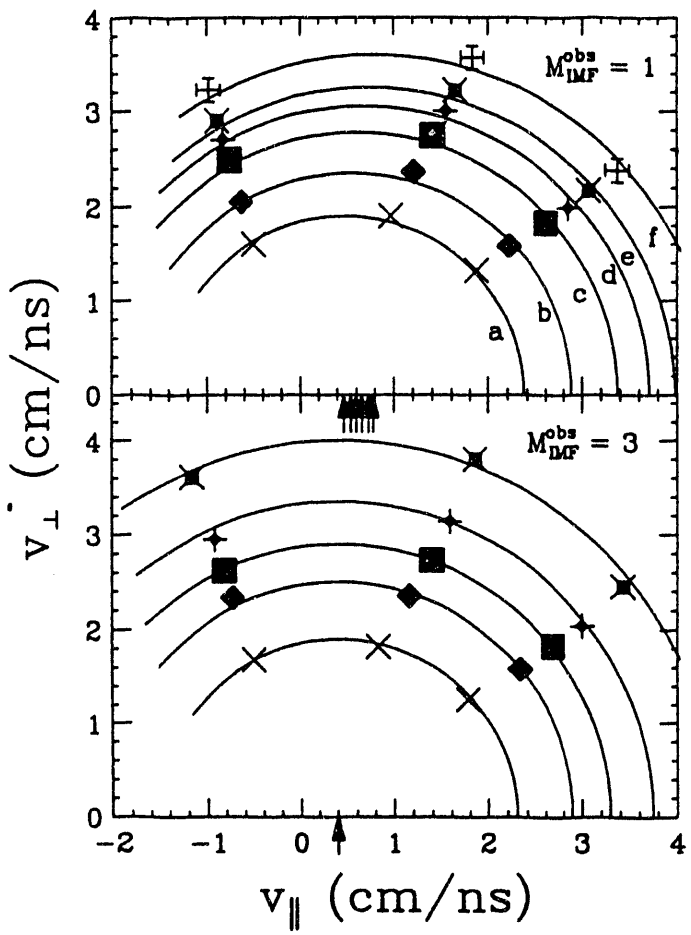

fragments were detected for the reaction Kr + Au at E/A=43 MeV (BOU88). The angular ranges in Figure V.15 are the ranges of angles at which complex fragments were detected. For the n=5 events, 92% of the events had a majority of the fragments detected between 30° and 150°. These fragments have a common origin, shown as a single center for the contours. On the other hand, events with a majority of fragments detected at forward angles do not show a common origin.

Velocity plots have also been constructed for C fragments detected in the reaction $^{3}He + ^{nat}Ag$ at E/A=1.2 GeV, shown in Figure V.16 (YEN91). The top half of this figure shows contours for those fragments in coincidence with only one other IMF; the bottom half is for a coincidence with three other IMF's. In the top half of the figure, the source velocity (arrows on the $V_{||}$ axis) seems to increase with an increase in the velocity of the fragment. The letters for each contour indicate the arrow (from left to right) corresponding to the centroid of the contour (source velocity). This shows that C fragments are being emitted by many different sources. On the other hand, the contours in the bottom half of the figure show a common source velocity. This figure helps to show that the reaction mechanism can also change as the IMF multiplicity changes. Additionally, other features of the reaction are consistent with the emission of fragments from an expanded source (YEN91).

V.C.2 Multiple Fragment Emission

The Xe-induced reaction shown in Figure V.14 is part of a systematic study of IMF emission at E/A=50 MeV ranging from the reaction Xe + C to Xe + Au (BOW92b). The multiplicity of IMF's as a function of charged particle multiplicity is shown in Figure V.17. Because charged particle multiplicity is correlated with excitation energy, the figure shows that, in these reactions, the IMF multiplicity is a

Figure V.17: Mean multiplicity of IMF's as a function of charged particle multiplicity for Xe-induced reactions At E/A = 50 MeV (BOW92b).

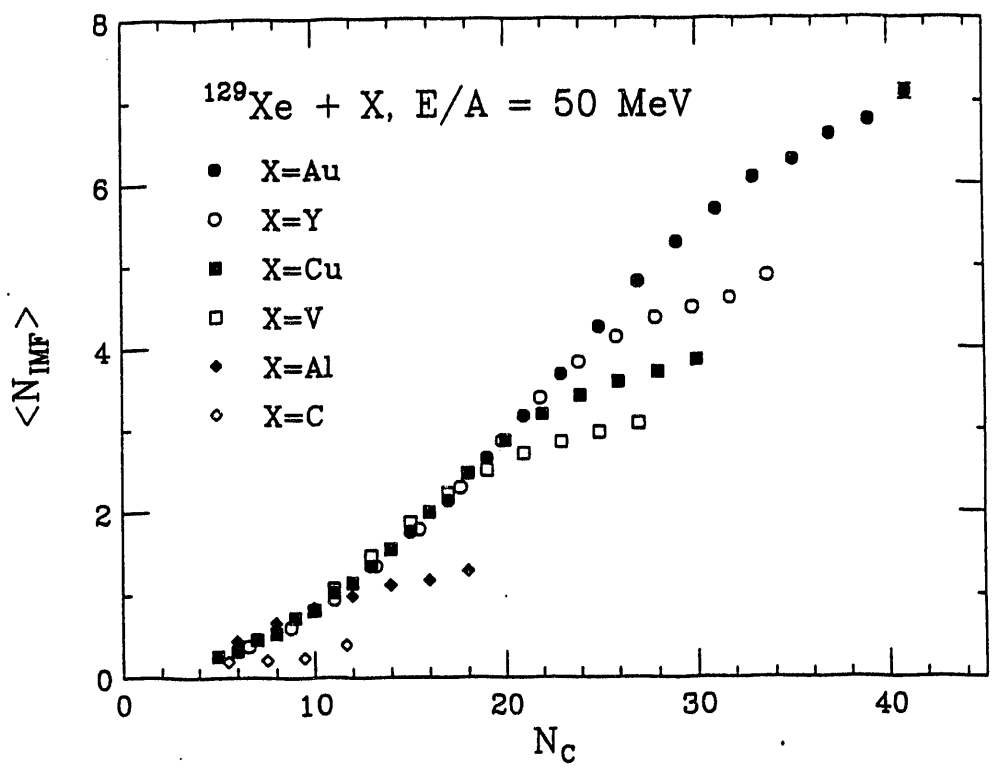
^{129}Xe + X, E/A = 50 MeV
X=Au
X=Y
X=Cu
X=V
X=Al
X=C
$\langle N_{IMF} \rangle$
N_C
0
2
4
6
8
0
10
20
30
40

Figure V.18: Mean multiplicity of IMF's as a function of charged particle multiplicity for the reaction Xe + Au at E/A = 50 MeV. The solid points are the experimental data, the lines, crosses and open points are predictions of different reaction models (BOW91b).

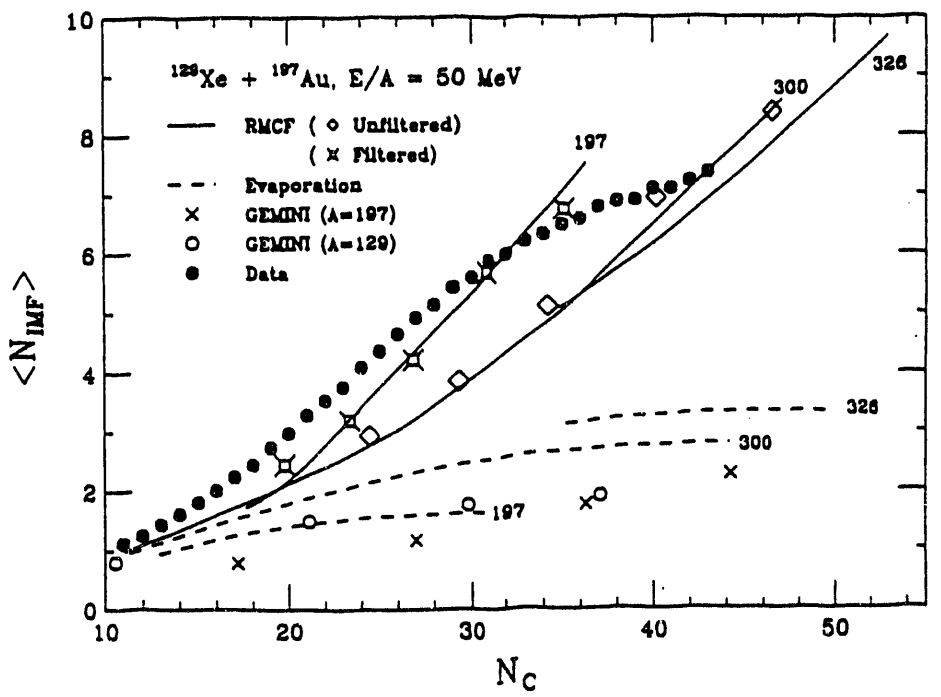
^{129}Xe + ^{197}Au, E/A = 50 MeV
RMCF (◇ Unfiltered)
(✕ Filtered)
Evaporation
GEMINI (A=197)
GEMINI (A=129)
Data
197
300
326
$<N_{IMF}>$
N_C

function of excitation energy and not of the reacting system. This is similar to the results presented in Figure V.4 for the La-induced reactions from E/A=35-55 MeV.

For the reaction Xe+ Au at E/A=50 MeV, the IMF multiplicity as a function ofcharged particle multiplicity is shown as the solid points in Figure V.18. The dashed lines, crosses and circles in Figure V.18 are the predictions of standard statistical decay models for this reaction which have been filtered through the detector acceptance. It is clear that these calculations do not reproduce the observed multiplicities. The diamonds and stars in Figure V.18 are the predicted multiplicities for an expanding compound nucleus decay model. The stars have been filtered through the detector acceptance to show the distortion of the distribution due to the limitations of the detector system. This model does a much better job at reproducing the experimental IMF multiplicities than standard statistical models.

This is different conclusion than from the study of the reactions ^{12}C, ^{18}O, ^{20}Ne, $^{40}Ar + ^{nat}Ag$, ^{197}Au at E/A=30 to 84 MeV (TRO89). The mean multiplicity of IMF's as a function of excitation energy is shown in Figure V.19. The dashed line is a sequential calculation (CHA88a, CHA88b); the solid is the result of a multifragmentation model (BON85b). It is clear that the multifragmentation model overpredicts the IMF multiplicity for reactions on each target. The sequential calculation reproduces the IMF multiplicity for the reactions on the Au target.. However, the reactions in this study are of very asymmetric projectile-target combinations, leading to fairly low excitation energies. It is not surprising, then, that the sequential model fairly well reproduces the experimental data. It is only when reactions produce a high multiplicity of IMF's that statistical sequential models fail to reproduce the experimental data, such as in the reaction Xe + Au at E/A = 50 MeV previously discussed.

The reaction $^{40}Ca + ^{40}Ca$ at E/A=45 MeV was studied using a 4π detector

Figure V.19: Mean multiplicity of IMF's as a function of excitation energy in the reactions ^{12}C, ^{18}O, ^{20}Ne, and ^{40}Ar + Ag, Au at E/A = 30-84 MeV. The solid lines are the prediction of a multifragmentation model, the dashed line is for a sequential decay calculation (TRO89).

^{12}C, ^{18}O, ^{20}Ne, ^{40}Ar + ^{nat}Ag, ^{197}Au
E/A = 30 to 84 MeV

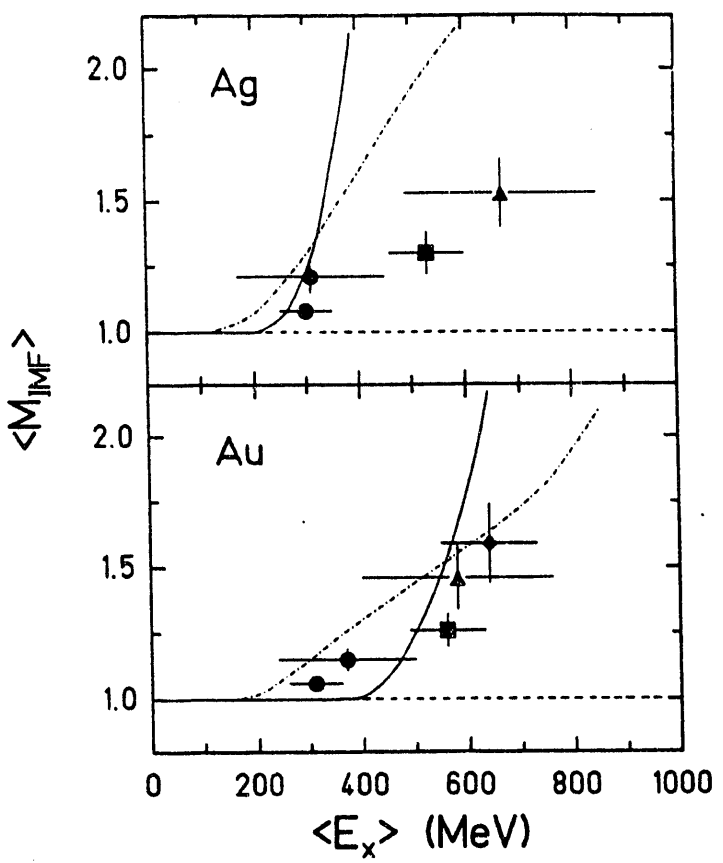

Figure V.20: Fragment Z distributions (points) for the reaction $^{40}Ca + ^{40}Ca$ at E/A = 35 MeV. The solid line is the prediction of a multifragmentation model. The dashed and dotted lines are the predictions of sequential decay models (HAG92).

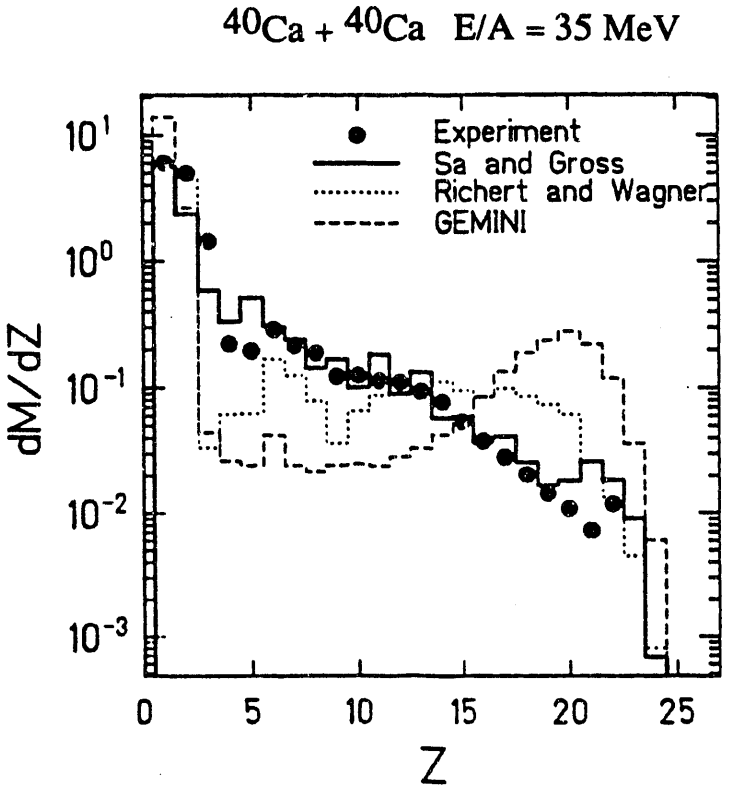
$^{40}Ca + ^{40}Ca$ E/A = 35 MeV
Experiment
Sa and Gross
Richert and Wagner
GEMINI
dM/dZ
Z
10^{1}
10^{0}
10^{-1}
10^{-2}
10^{-3}
0
5
10
15
20
25

system (HAG92). In order to concentrate on central collisions, only events with a large charged particle multiplicity were analyzed. Experimental and model charge distributions for this reaction are shown in Figure V.20. The solid line is the result of a multifragmentation model (SA85), the two dashed lines are sequential decay models (CHA88a, CHA88b, RIC90). It is clear that standard sequential mechanisms fail to reproduce the charge distributions. However, use of the expanding emitting source model (FRI90) (used in the study of the reaction Xe + Au at E/A=50 MeV) does reproduce experimental observables.

The expanding compound source model (FRI90) has been successfully used to treat the complex fragment emission in which the IMF multiplicity is very high (BOW91a, HAG92). Is the consideration of fragment emission from an expanding source a realistic assumption? In Chapter IV, Figure IV.16 showed that highly compressed nuclei can undergo some type of expansion. Fragments can then form, whether due to Rayleigh-Taylor surface instabilities or by spinodal decomposition or by some other mechanism (MOR92, GRO92, BAU92). Use of BUU and LV calculations in the reaction Ca + Ca at E/A=35 MeV show that the initial compression is followed by an expansion (until t=70 fm/c) (HAG92). Use of the expanding compound nucleus model has also been successfully applied to other reactions. (FRI90)

There are many different models that have been used to study multiple fragment emission in heavy-ion reactions. These models can be classified as dynamical, statistical or hybrid (a combination of two or more models, each for a different stage of the reaction), and prompt or sequential. Table V.2 lists some of the models that have been used to interpret experimental results.

While at first it may seem that these models are not compatible, the statistical and hybrid models assume that at some stage of the reaction, the decay of fragments

is due to equilibrium emission of particles or fragments. Additionally, the purely statistical models do not describe the early stages of the reaction, which are governed by dynamcal considerations. However, the fact that several of the models can be used to interpret the same experimental results shows the difficulty in attempting to define new reaction processes in the intermediate energy region.

Table V.2: Theoretical models used at intermediate energies.

Model	Statistical (S), dynamical (D), or Hybrid (H)	Sequential (S) or Prompt (P)	Experiments Studied
Gross (GRO88)	S	P	50 MeV/u La + C 35 MeV/u Ca + Ca
GEMINI (CHA88a)	S	S	50 MeV/u La + C 25+30 MeV/u Nb +Be, Al
EES (FRI90)	H	S	50 MeV/u Xe + Au 35 MeV/u Ca+ Ca
RAM (LER90)	H	P	25-65 MeV/u Ar + Al
QMD(AIC88)	D	P	1.05 GeV/u Ne + Au

V.D. FAST-FISSION SYSTEMATICS

Fast-fission (or quasi-fission) is a reaction mechanism that occurs in heavy-ion reactions and can be considered to be the connection along the ℓ-wave coordinate between compound nucleus (CN) and deep-inelastic (DI) reactions. Originally, the boundary between the CN and DI reactions was assumed to occur at some ℓ-wave (called ℓ_{crit}) which is the maximum angular momentum for fusion. However, there are cases in which ℓ_{crit} is at values greater than the ℓ-wave at which the fission barrier disappears (ℓ_{Bf}). These reactions occurring between ℓ_{crit} and ℓ_{Bf} are called fast-fission reactions. In other words, fast-fission occurs when the compound nucleus is formed at such a high angular momentum that the symmetric fission barrier is zero. The nucleus is trapped behind the barrier at the entrance channel asymmetry, but once mass equilibration occurs the nucleus can then fission (HIN89). A schematic diagram of the cross section along the ℓ-wave coordinate illustrating this process is shown in Figure V.21 (GRE82). A visual picture of the fast-fission process is shown in Figure V.22 (TOK85).

One of the main features of fast-fission type reactions is fission-like mass (or charge) distributions but a lack of isotropy in the angular distributions of the emitted fragments. (Recall that isotropic angular distributions of fragments is one of the features of the statistical decay of hot nuclei.) The study of fast-fission reactions has usually been associated with lower energy reactions, in which a distinction is sought between fusion-fission and deep-inelastic reactions. For example, study of the reactions ^{50}Ti, ^{56}Fe + ^{208}Pb at E/A from 5-8 MeV showed fragments with an anisotropic angular distributions in the center-of-mass (except for symmetric fission fragments). For fragments with Z less than $Z_{symmetry}$, the angular distribution showed forward peaking, while heavy fragments showed backward peaking

Figure V.21: Schematic diagram of the differential cross section $d\sigma/d\ell$ as a function of ℓ-wave for reactions in which ℓ_{cr} is below (a) and above (b) the fission barrier. ℓ_{cr} is the critical ℓ-wave for compound nucleus formation and ℓ_{Bf} is the ℓ-wave at which the symmetric fission barrier disappears (GRE82).

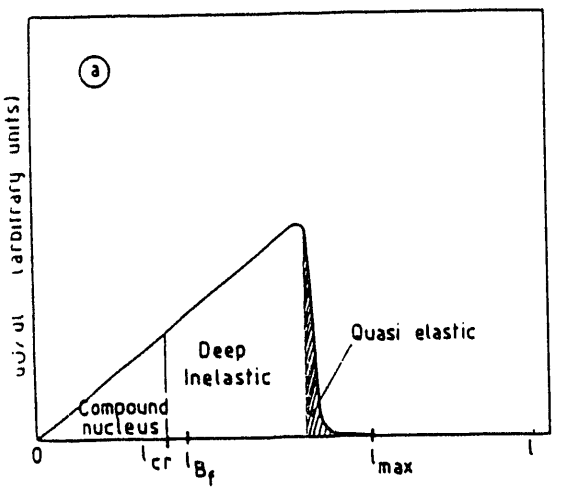
a
Deep
Inelastic
Quasi elastic
Compound
nucleus
0
l_{cr}
l_{B_f}
l_{max}
l

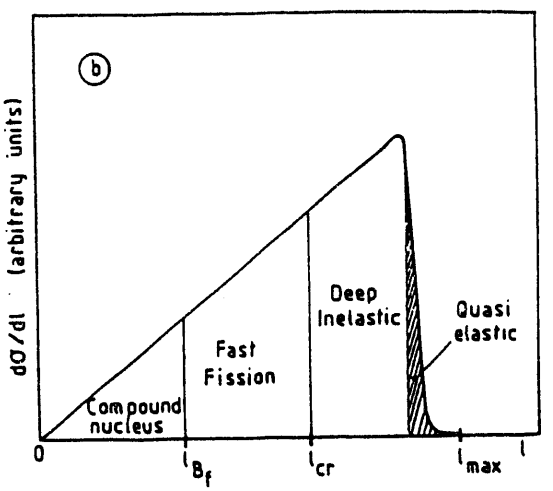
b
dσ/dl (arbitrary units)
Deep
Inelastic
Quasi
elastic
Fast
Fission
Compound
nucleus
0
l_{B_f}
l_{cr}
l_{max}
l

Figure V.22: Schematic diagram illustrating the differences between compound nucleus, fast-fission, and deep-inelastic reactions (TOK85).

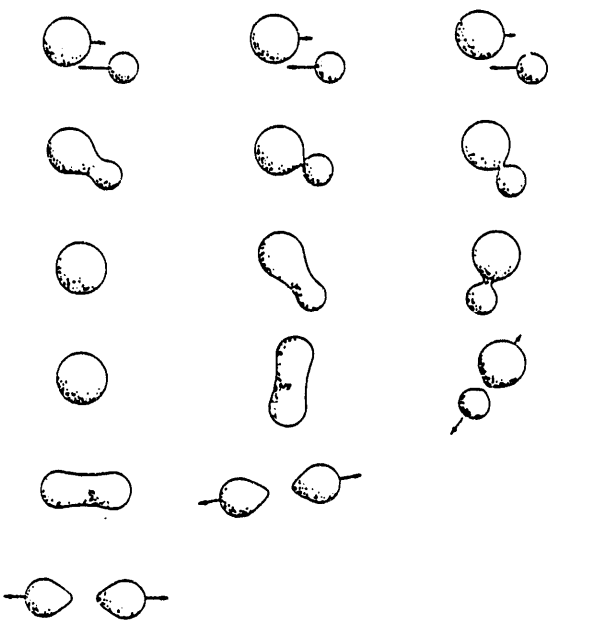
COMPOUND NUCL. FISSION
QUASI-FISSION
DEEP INELASTIC SCATTERING

Figure V.23: Contour plots in the θ_{cm}-mass plane for fragments emitted in U-induced reactions at E/A = 6 MeV (TOK84).

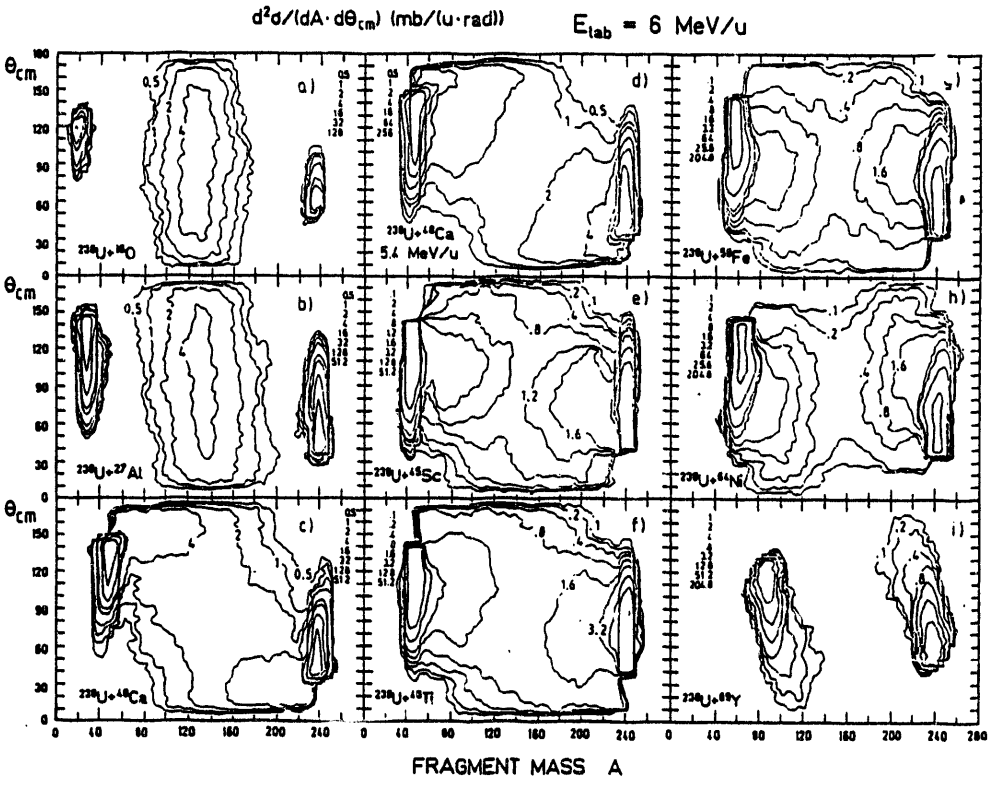
$d^2\sigma/(dA \cdot d\theta_{cm})$ (mb/(u·rad))
E_{lab} = 6 MeV/u
θ_{cm}
a) $^{238}U+^{16}O$
b) $^{238}U+^{27}Al$
c) $^{238}U+^{48}Ca$
d) $^{238}U+^{48}Ca$ 5.4 MeV/u
e) $^{238}U+^{45}Sc$
f) $^{238}U+^{49}Ti$
g) $^{238}U+^{58}Fe$
h) $^{238}U+^{64}Ni$
i) $^{238}U+^{89}Y$
FRAGMENT MASS A

(LUT86). It should be noted that the reactions in this study were in normal kinematics. Use of inverse kinematics reactions, such as in U-induced reactions at E/A=5.4 and 6.0 MeV, showed heavy fragments with a forward-peaked distribution and light fragments with a backward-peaked angular distribution (TOK84). The angular distributions as a function of fragment mass for these reactions is shown in Figure V.23. The reactions U + O and Al show isotropic angular distributions with a yield at the mass due to symmetric fission. However, increasing the target mass eliminates the yield at symmetry and increases the drift in the masses of the target -like and projectile-like fragments. The drift in the mass correlates with drift in the center-of-mass angles at which fragments are detected. This drift in mass and angle is due to fast-fission type reactions. The angular distributions shown in Figure V.23 are similar to those presented in Figures III.13 and 14.

There is evidence that fast fission reactions can occur at bombarding energies of up to E/A=100 MeV. The Z1-Z2 plots for the reaction La + C at four bombarding energies are shown in Figure V.24 (BOW91b). The ratios of the forward-focused cross section to the backward-focused cross section for the reactions at E/A=50, 80, and 100 MeV are shown in Figure V.25 (BOW91b). At E/A= 18 and 50 MeV, the yield is due to symmetric fission and fragments are emitted isotropically, indicative of a fusion-fission reaction. However at E/A= 80 and 100 MeV, there are both symmetric and asymmetric fission events. The symmetric fragments still have isotropic angular distributions, but the light (heavy) fragments are emitted backward (forward) in the source frame. The yield at higher energies is substantially lower than the dotted line corresponding to Z_P+Z_T due to the increased emission of light particles at higher energies. Other experiments at similar energies (CAS89) have also shown a fast-fission component.

The angular distributions of the fragments emitted in the reaction La + C at

Figure V.24: Z1-Z2 coincidence plots for the reaction La + C at E/A=18, 50, 80, and 100 MeV. The dashed line is at Z_{tot}=63, the sum of Z_P+Z_T (BOW89b).

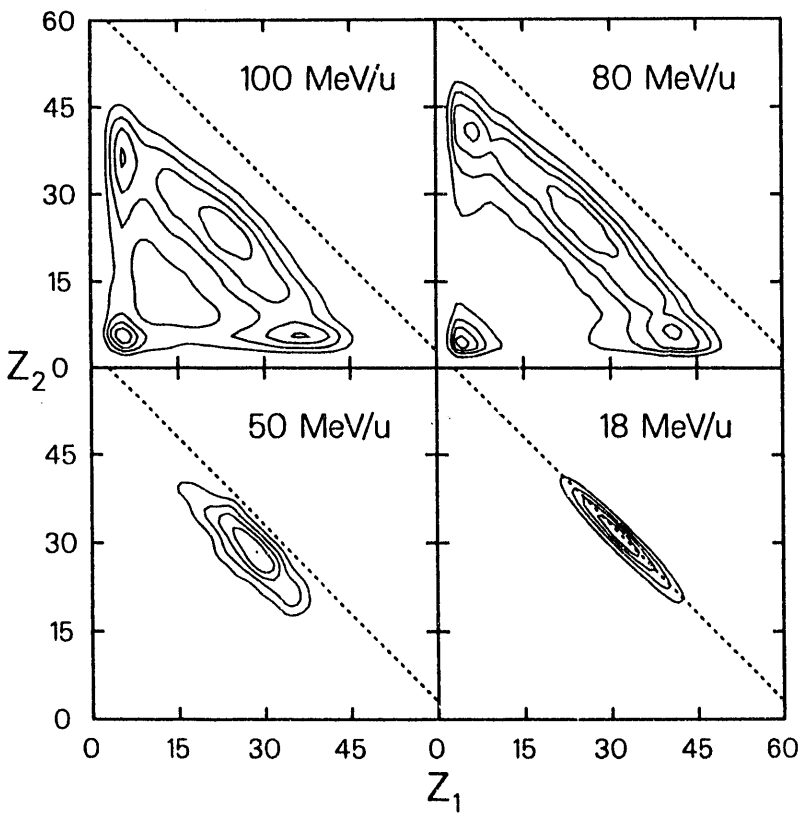
100 MeV/u
80 MeV/u
50 MeV/u
18 MeV/u
60
45
30
15
0
Z_2
0
15
30
45
60
Z_1

Figure V.25: Forward to backward ratio of the cross section for fragments emitted in the reaction La + C at E/A=50, 80, and 100 MeV. The dashed line indicates isotropic emission (BOW89b).

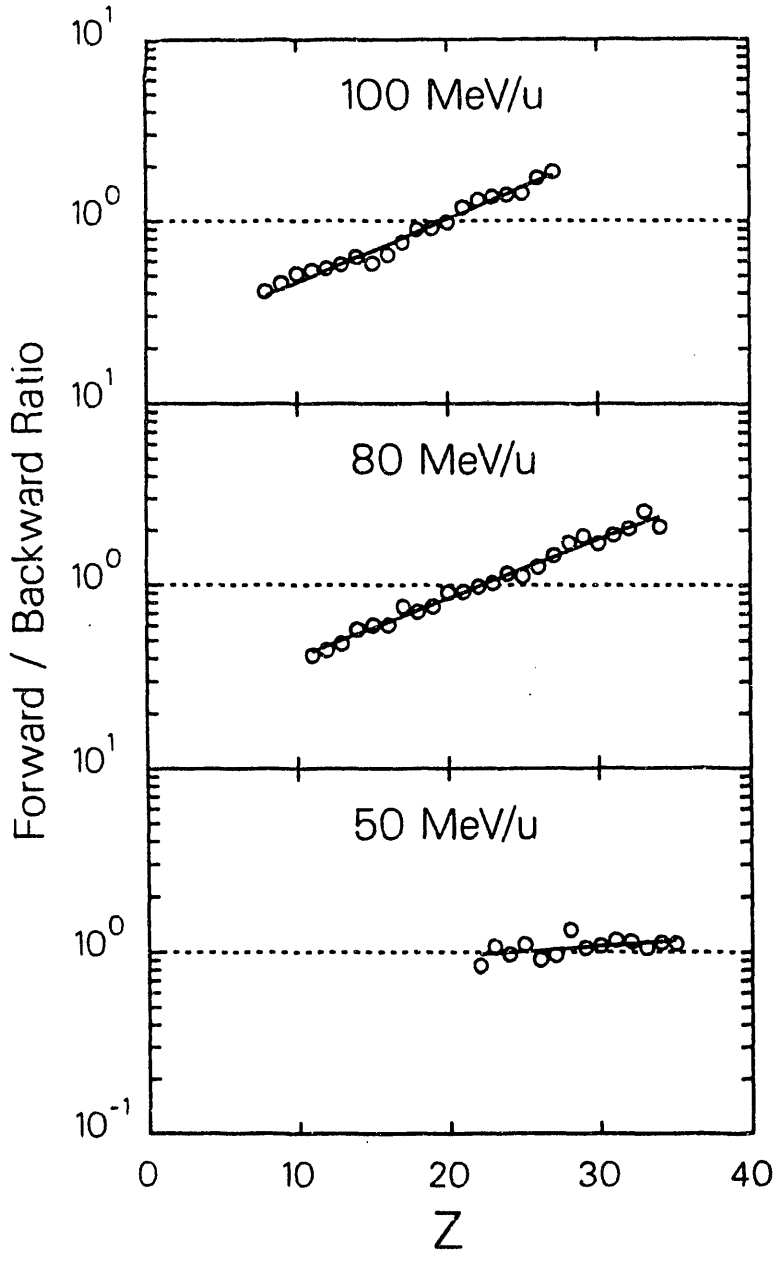
100 MeV/u
80 MeV/u
50 MeV/u
Forward / Backward Ratio
Z
10^{1}
10^{0}
10^{-1}
0
10
20
30
40

E/A = 80 and 100 MeV have also been interpreted as due to the formation of the composite system at an energy just below the onset of a participant-spectator mechanism (BOW91b). This system can then emit fragments before it fully relaxes from an extended geometry (such as in Figure IV.11), leading to the anisotropic angular distributions of emitted fragments.

The time scale associated with fission (both fast-fission and equilibrium fission) has been studied by use of neutron multiplicity measurements. The mean lifetime can be calculated from the decay width Γ_n, with the lifetime equal to $\hbar/\Gamma_n$. The lifetime is very sensitive to the excitation energy of the nucleus, decreasing by a factor of 20 as the excitation energy is increased from 75 to 150 MeV (HIN89). The time-scales associated with fusion-fission and fast-fission for a variety of reactions leading to the formation of Z = 77 and 78 nuclei at bombarding energies up to E/A=26 MeV are shown in Figure V.26 (HIN89). Asymmetric fast-fission is found to occur on a time scale of several 10^{-21} s, and the time decreases as the excitation energy of the system increases. This time scale for fast-fission is slightly slower than that associated with the dynamical calculations performed in Chapter IV. However, the excitation energies of the systems studied in Chapter IV were higher than those of the systems presented in Figure V.26. Extrapolation of the time scale to the excitation energy of the composite system formed in the dynamical studies brings the time for fast-fission to the same order of magnitude.

V.E SUMMARY

The reactions La + Al, V, Cu, and La at E/A=45 MeV have been studied as part of a series of experiments that have examined the mechanism of complex fragment emission at intermediate energy. The results from this study are very

Figure V.26: Extracted lifetimes of a Z=77 or 78 nucleus before fission as a function of excitation energy. The points are for various experiments performed (HIN89).

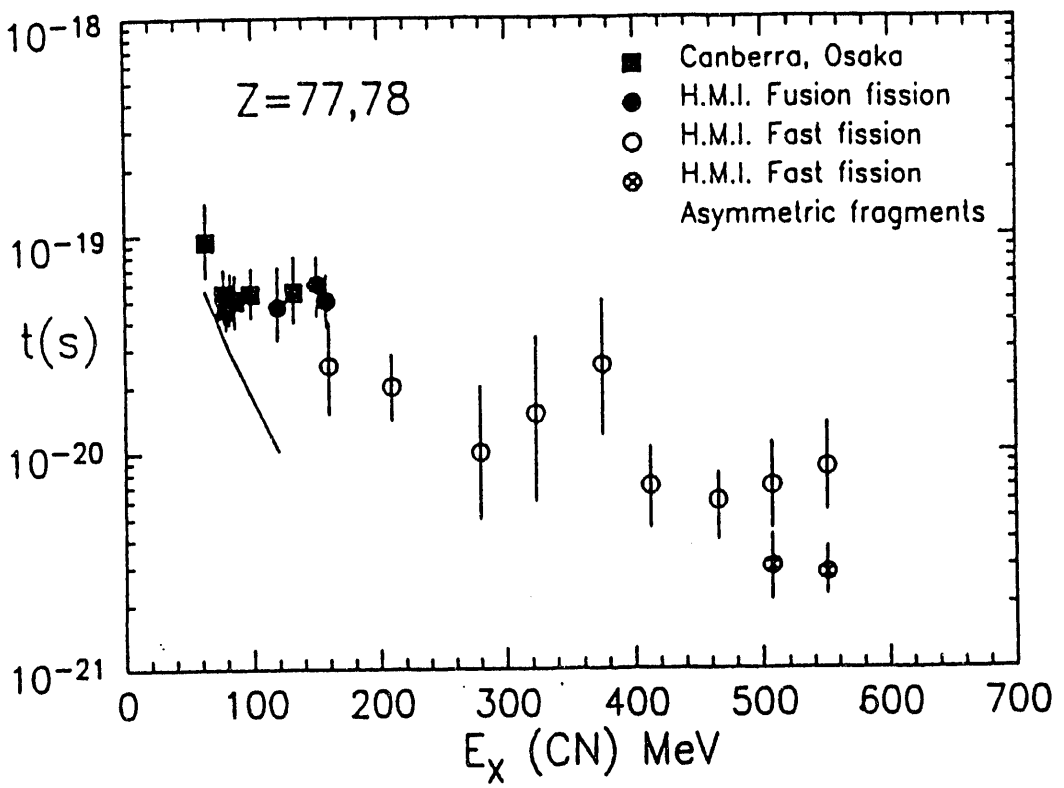
Z=77,78
Canberra, Osaka
H.M.I. Fusion fission
H.M.I. Fast fission
H.M.I. Fast fission
Asymmetric fragments
t(s)
10^{-18}
10^{-19}
10^{-20}
10^{-21}
0
100
200
300
400
500
600
700
E_x (CN) MeV

similar to those of the same systems at different bombarding energies. The probability of decay by the emission of multiple fragments has been shown to be nearly independent of the system and bombarding energy and dependent only on the excitation energy of the system. Similar results have been obtained in the study of Xe-induced reactions at E/A=50 MeV (BOW92b).

Correlation functions of the relative velocities and angles between pairs of fragments in the n=3 events are also quite similar to other systems at comparable excitation energies. These have been interpreted as being consistent with the sequential emission of complex fragments from some source, with a short decay time between emission stages.

Many other reactions have been studied at intermediate energies. Although many models have been used to describe experimental features, none show any exclusivity. The same reaction can be explained by several different models, showing that the differentiation between prompt and sequential mechanisms of IMF emission may not be something easily accomplished. It is clear, however, that lower energy mechanisms, such as deep-inelastic scattering and fast-fission, continue to play a role in nuclear reactions at intermediate energies.

CHAPTER VI CONCLUSIONS

The reactions La + Al, V, Cu, and La have been extensively studied both experimentally and theoretically. The results of this study have been compared to similar reactions at intermediate energy in order to discern the mechanism of the decay of highly excited nuclei formed in these reactions. The conclusions from the study of the reactions of the Al, V, and Cu targets are contained in separate sections, along with a section to provide an overview of the entire range of reactions studied. No definitive conclusions can be based on the study of the reaction La + La due to the target contamination and the lack of well characterized events. (Recall that the missing charge is greater than the detected charge for this reaction.) Finally, a section will be devoted to new research directions for the study of intermediate energy reactions.

VI.A. THE REACTION La + Al

The study of the reaction La + Al provides a baseline of a well understood nuclear reaction to which other reactions can be compared. The experimental and theoretical study of this reaction complement each other, leading to some fairly strong conclusions about the decay of hot nuclei formed in this reaction.

In the reaction La + Al, the majority of the data are consistent with the conclusion that hot nuclei are formed by means of an incomplete fusion mechanism with a source velocity and mass between those of the beam and the complete fusion product. The hot nuclei then decay by either fast-fission or equilibrium fission mechanisms. Experimental features, such as anisotropic angular distributions and a constant ridge line in the Z1-Z2 plane point toward

these competing mechanisms. The use of dynamical calculations coupled to a statistical decay code also show that these competing mechanisms are present for this reaction. This further clarifies the conclusion of Kehoe (KEH89), who could attribute only part of the experimental cross section to statistical decay processes in the reaction La + Al at E/A=47 MeV. The present study has shown that dynamical effects leading to two and three body final states are an important part of this reaction, and are the main cause of the production of fragments with an atomic number less than 20. These dynamical effects combine with statistical decay of resultant fragments to produce a sequential mechanism for the multiple fragment events. Further evidence of the sequential nature of the decay is shown by the analysis of the relative angles and velocities between pairs of fragments in n=3 events.

VI.B THE REACTION La + V

Most of the results for the reaction on the V target are similar to those for the reaction La + Al. Even though there is no ridge line at constant total Z in the Z1-Z2 plane, yield can be seen corresponding to asymmetric fission. The spread of the yield in the Z1-Z2 plane shows the increasing presence of multibody final states. The yield in charge-Dalitz space shows that the symmetric decays become more likely as the target mass increases, probably due to the increase in the available energy.

Use of the model calculations for the La + V reaction shows that the many-body (more than two fragments) events in this reaction can be attributed to a sequential decay mechanism. This result is in agreement with the analysis of the relative velocities and angles between pairs of fragments in the n=3 events. The model calculations reproduce bulk properties of the reaction, such as the shape of

the fragment cross section distribution, the total charge and source velocity distributions, and the major features of the charge-Dalitz plots. Discrepancies between the experimental and calculated total charge distributions can be explained by the emission of a few more H isotopes. However, the calculations fail to reproduce the magnitude of the fragment cross sections and finer reaction features, such as the branching ratios of multiple fragment events and the symmetric decays shown in the charge-Dalitz plots.

VI.C THE REACTION La + Cu

The results of the study of the reaction La + Cu are less clear than those for the lighter targets. Certain experimental features are almost identical to those of the reactions La + Al and V, such as the relative velocity and angle measurements and the decay probabilities of the multiple fragment events. However, other experimental features are strikingly different. There is no yield in the Z1-Z2 plane for asymmetric fission events, unlike the Al and V targets. Dynamical and statistical model calculations reproduce the source velocity of the n=2 and 3 events, but no other features. The source velocity is a function of what is happening in the early stages of the reaction, before the fragmentation stage. This indicates that the decaying system is being reproduced by the model, but not the mechanism of the decay.

There is an indication that some type of multifragmentation is occurring in this reaction. The dynamical calculations for central collisions show a hot compressed system which undergoes expansion and then possibly fragments. The mechanism of the fragmentation has been linked to Rayleigh-Taylor surface instabilities, spinodal decomposition, or even the formation of rings, bubbles, or donuts of nucleons.

It would be interesting to study these more symmetric reactions at intermediate energies with 4π detector systems, as further discussed in Section VI.E.

VI.D OVERVIEW OF THE REACTIONS STUDIED

The study of reactions of asymmetric systems at intermediate energy using inverse kinematics has proven to be a useful method of preparing nuclei under extreme conditions, at which they are expected to undergo some type of fragmentation. Certain experimental features, such as the relative velocities and angles between fragments in multiple fragment events, point to a sequential mechanism for the decay of these highly excited nuclei. The decay probabilities of multiple fragment events show a similarity over a range of systems and bombarding energies. These probabilities are nearly independent of the reacting system and dependent only on the excitation energy of the decaying source.

Modeling of these reactions by the combination of dynamical and statistical reaction models has proven useful in the understanding of the mechanism of the decay of hot nuclei formed in these reactions. The calculations are successful in reproducing certain global features (such as fragment cross sections, source velocity distributions and total charge distributions for multiple fragment events) of the experimental results for the reactions La + Al and V, but fail to reproduce the finer features (branching ratios, charge-Dalitz plots) for these reactions. The calculation can only reproduce the source velocity distributions for the reaction La + Cu, showing that the failure of the model is not due to the dynamical calculations (which are performed for the early stage of the reaction) but due to a failure to reproduce the latter stages of the reaction.

VI.D THE FUTURE

The reactions studied in this experiment have shown that a fairly clear understanding of nuclear decay mechanisms can be gained by using a reasonably inexpensive modular detector system. The future, however, is the construction of full 4π detector systems that can be used for either normal or inverse kinematics experiments. The MSU 4π array consists of 160 elements, each containing a low pressure proportional counter, a Bragg curve counter, and a plastic scintillator phoswich detector (WES85). It is in the process of being modified by the addition of a Si-phoswich array at forward angles (MIG92). This will allow a larger dynamic range for the detection of fragments at forward angles, while keeping the low thresholds at large angles (because of gas detectors) for the detection of low energy intermediate mass fragments, target-like fragments, and light particles. Other 4π detector systems have been or are in the process of being built at Indiana University, Washington University, and GANIL in France, among others.

The experiments presented in this study have been complemented by the use of dynamical calculations to simulate the early stages of the reactions. Other models, such as the Expanding Emitting Source by Friedman, have also shown their usefulness in interpreting experimental data (FRI90). The dynamical calculations in this study have shown that highly distorted and non-spherical nuclei can be produced at intermediate energies. Statistical decay models have proven useful for studying nuclear reactions when dynamical effects are no longer present. In order to further explore this effect, a model that can follow the decay of non-spherical nuclei should be developed.

The Bevalac facility at Berkeley has shown the usefulness of studying reactions induced by heavy beams. Unfortunately, with the closure of the facility early next year, a very versatile accelerator facility will be lost. Only recently has the SISI8 accelerator at GSI been able to reproduce the range of particles, both in

mass and energy, that the Bevalac has provided over the years. Currently, the MSU superconducting cyclotron can only provide beams as heavy as Xe up to E/A=60 MeV with a reasonable beam current. It also cannot accelerate light ions to high energies as the Bevalac can. The GANIL facility in France is comparable to the MSUNSCL, capable of accelerating all ion species from E/A=30 to 100 MeV. The SIS accelerator in Germany is comparable to the Bevalac, but does not have an intermediate energy program. The closure of the Bevalac will leave a gap in the study of reactions induced by heavy beams at intermediate and high energies. This work has shown that these reactions can produce phenomena that are not well understood, and should be further studied.

APPENDIX A Electronics Diagrams

The electronics used in any nuclear chemistry experiment is an important part of the entire experiment. They interface the detectors with the data acquisition system, so that the correct parameters can be determined for each particle detected.

Briefly, a coincidence between the energy signals of a particle entering a 300μm Si (ΔE or DE) and a 5mm detector (E) in the same detector telescope is used to generate a master gate as long as the VME controller (which controls the interfacing of the electronics to the computer) is not busy. At the same time, a bit is set in the bit register for each telescope in which a ΔE-E coincidence is detected. The VME controller reads the bit register, and only telescopes for which the bit has been set have their parameters read by the VME controller. For the recoil detectors, a signal in any of the fourteen detectors sets the bit in the bit register and also starts the TAC for the time-of-flight measurement. The TAC is stopped by a delayed plastic signal, so that the time-of-flight clock runs backwards. (This ensures a coincidence between a recoil detector and a scintillator.) The electronics diagrams for this experiment are shown in Figures A.1, A.2, and A.3. Figure A.1 shows the electronics used for an individual telescope of the Si-Si(Li)-plastic array. Figure A.2 shows the logic for all of the elements of the array (starting with the OR, which is an OR of all the separate telescopes). Additionally, the logic diagram for the recoil Si detectors is shown in Figure A.3. Table A.1 shows the definitions of the abbreviations used in the electronics diagrams.

Table A.1 Definitions of abbreviations used in the electronics diagrams.

ADC- analog to digital converter	PA pre-amplifier
QDC- charge to digital converter	Amp- amplifier
TAC- time to amplitude converter	CFD- constant fraction discriminator
DGG- delay and gate generator	FIFO- fan in-fan out
Anti- anti-coincidence	AND- coincidence
OR- or	MG- master gate

Figure A.1: Electronics diagram for an individual telescope of the Si-Si(Li)-plastic array.

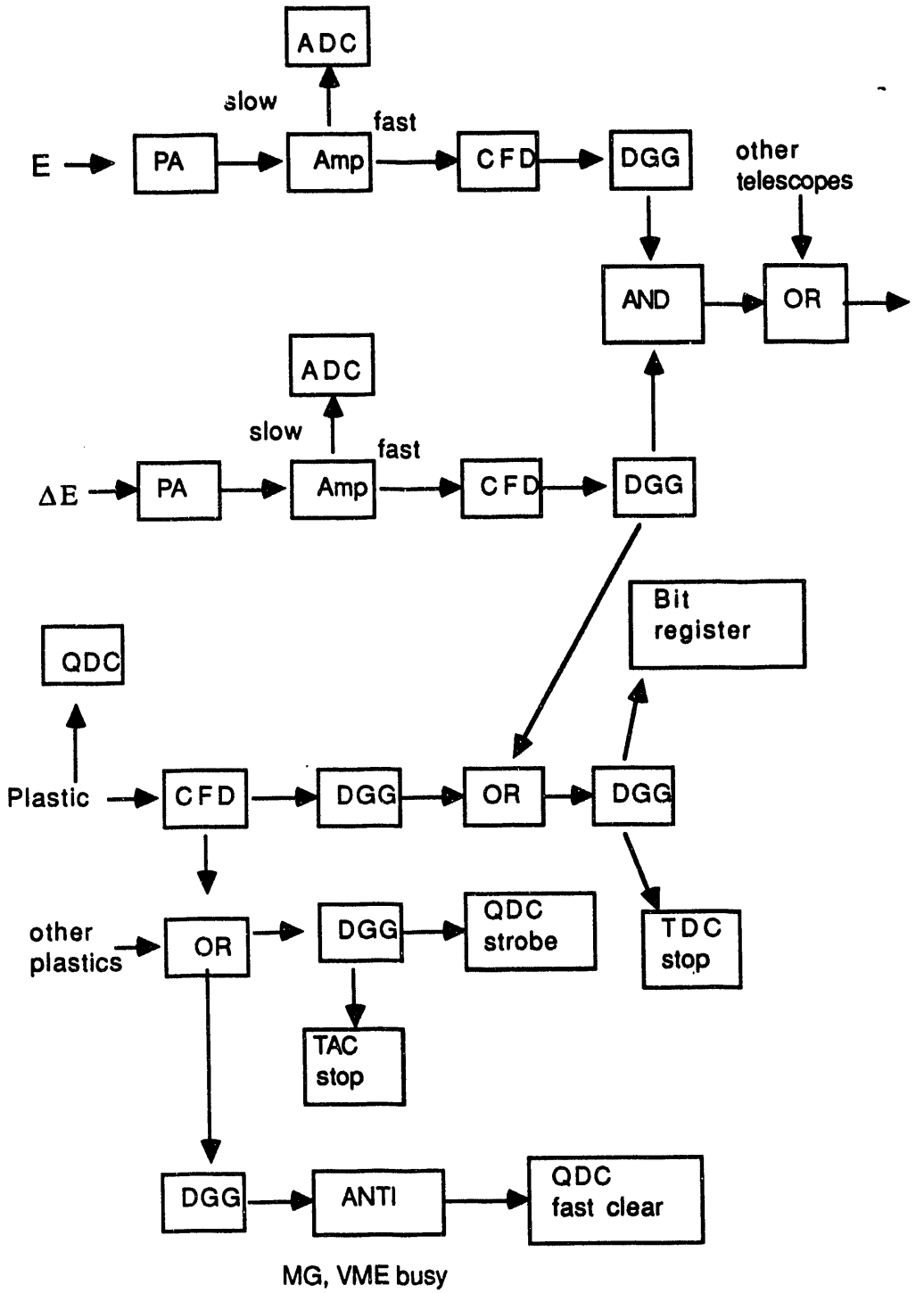
ADC
slow
fast
E
PA
Amp
CFD
DGG
other
telescopes
AND
OR
ADC
slow
fast
ΔE
PA
Amp
CFD
DGG
Bit
register
QDC
Plastic
CFD
DGG
OR
DGG
other
plastics
OR
DGG
QDC
strobe
TDC
stop
TAC
stop
DGG
ANTI
QDC
fast clear
MG, VME busy

Figure A.2: Electronics diagram for the entire array.

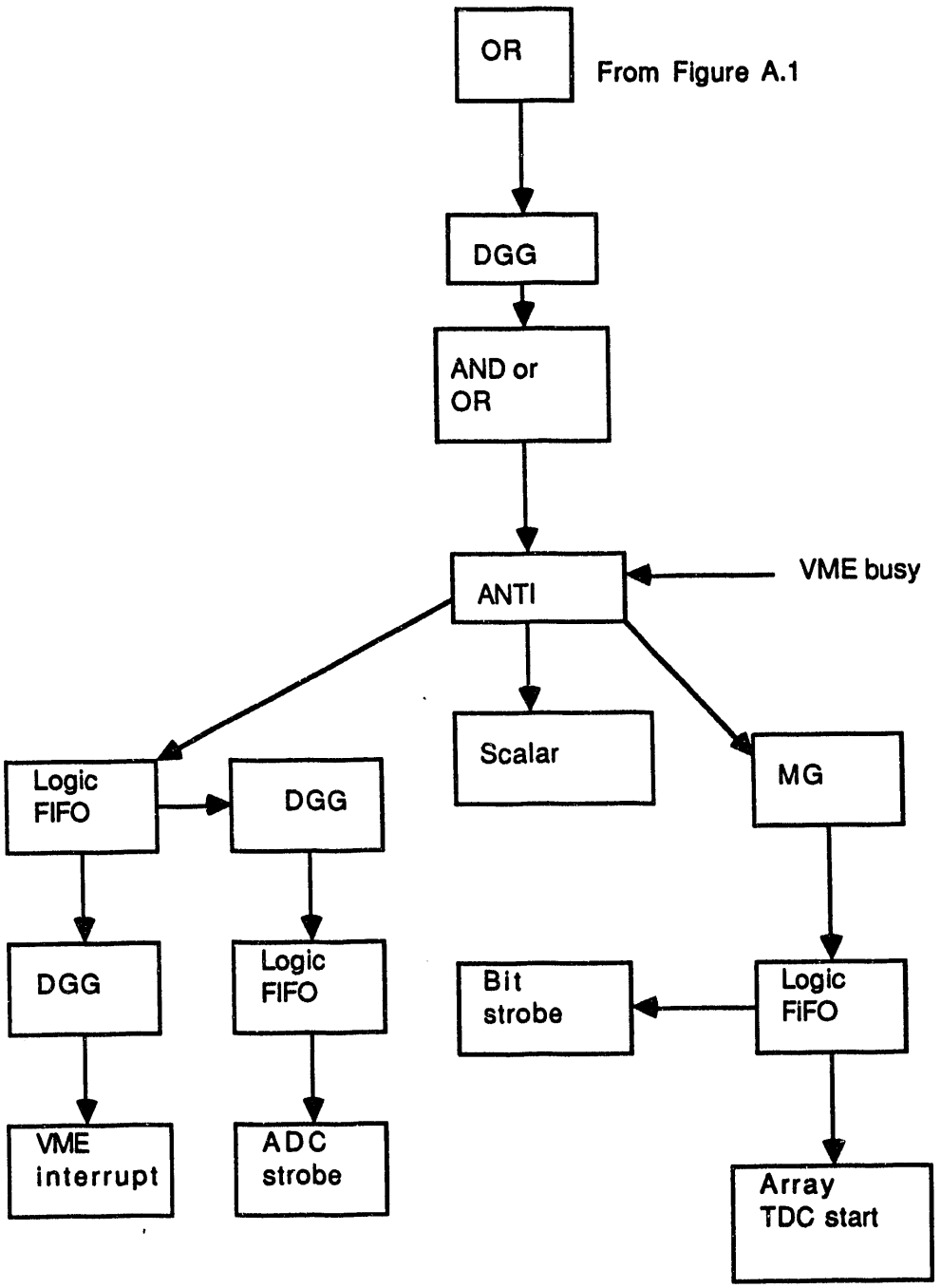
OR
From Figure A.1
DGG
AND or
OR
ANTI
VME busy
Logic
FIFO
DGG
Scalar
MG
DGG
Logic
FIFO
Bit
strobe
Logic
FiFO
VME
interrupt
ADC
strobe
Array
TDC start

Figure A.3: Electronics diagram for the recoil detectors.

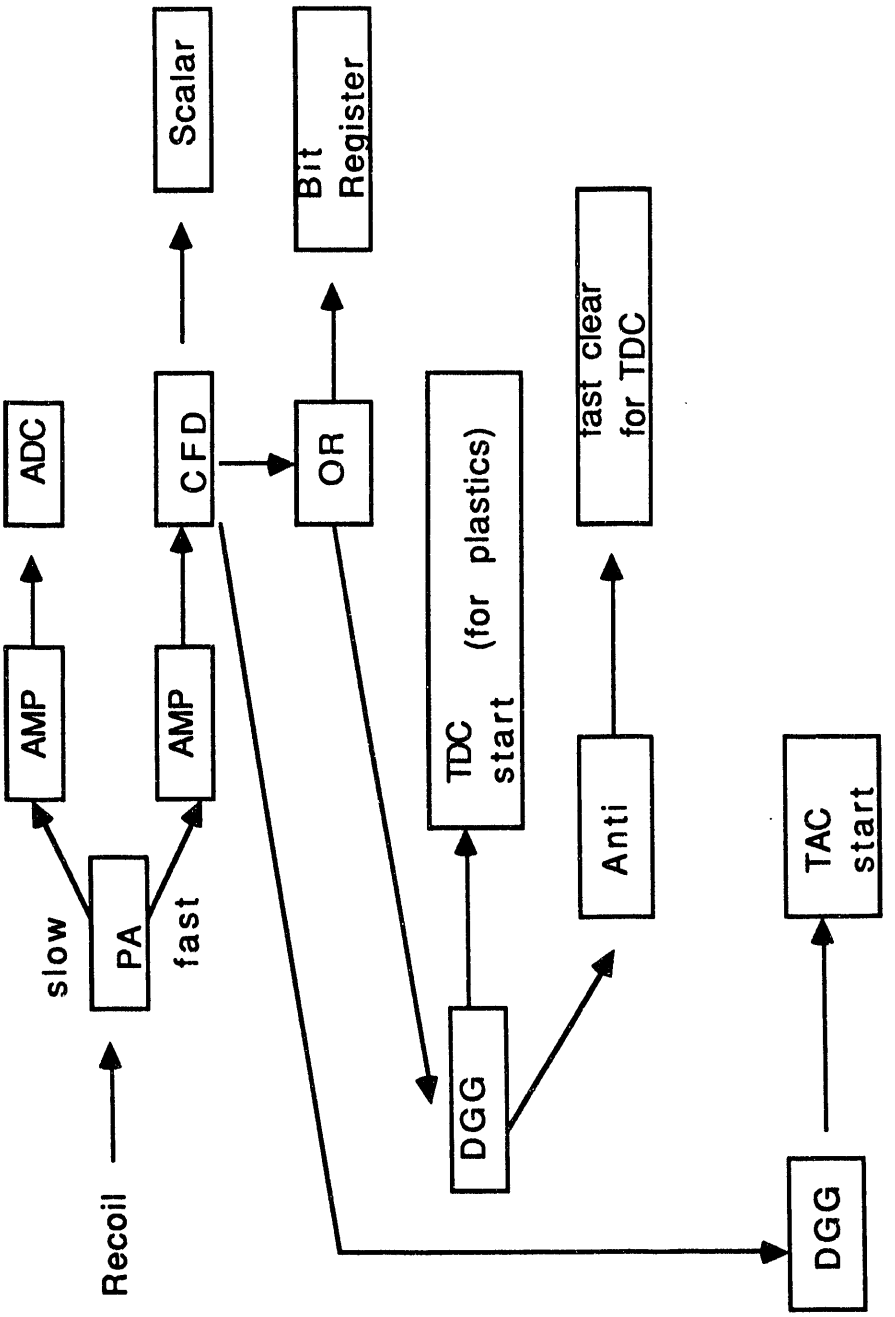
Recoil
PA
slow
fast
AMP
AMP
ADC
CFD
Scalar
OR
Bit Register
DGG
TDC start (for plastics)
Anti
fast clear for TDC
DGG
TAC start

APPENDIX B DATA ANALYSIS

The data analysis program LISA was developed in Germany and modified at Lawrence Berkeley Laboratory for analysis of Bevalac experiments. It was used for all calibrations and further data analysis for this experiment. The program LISA is a FORTRAN program that reads data from tape or disk, performs calibrations and calculations, and generates one- and two-dimensional spectra. It can also be used to rewrite the data back onto disk or tape once the calibrations have been performed and the data has been presorted by Z, energy, angle, and detector number. A flow chart of the program LISA is shown in Figure B.1.

Figure B.1: Flow chart of the data analysis program LISA.

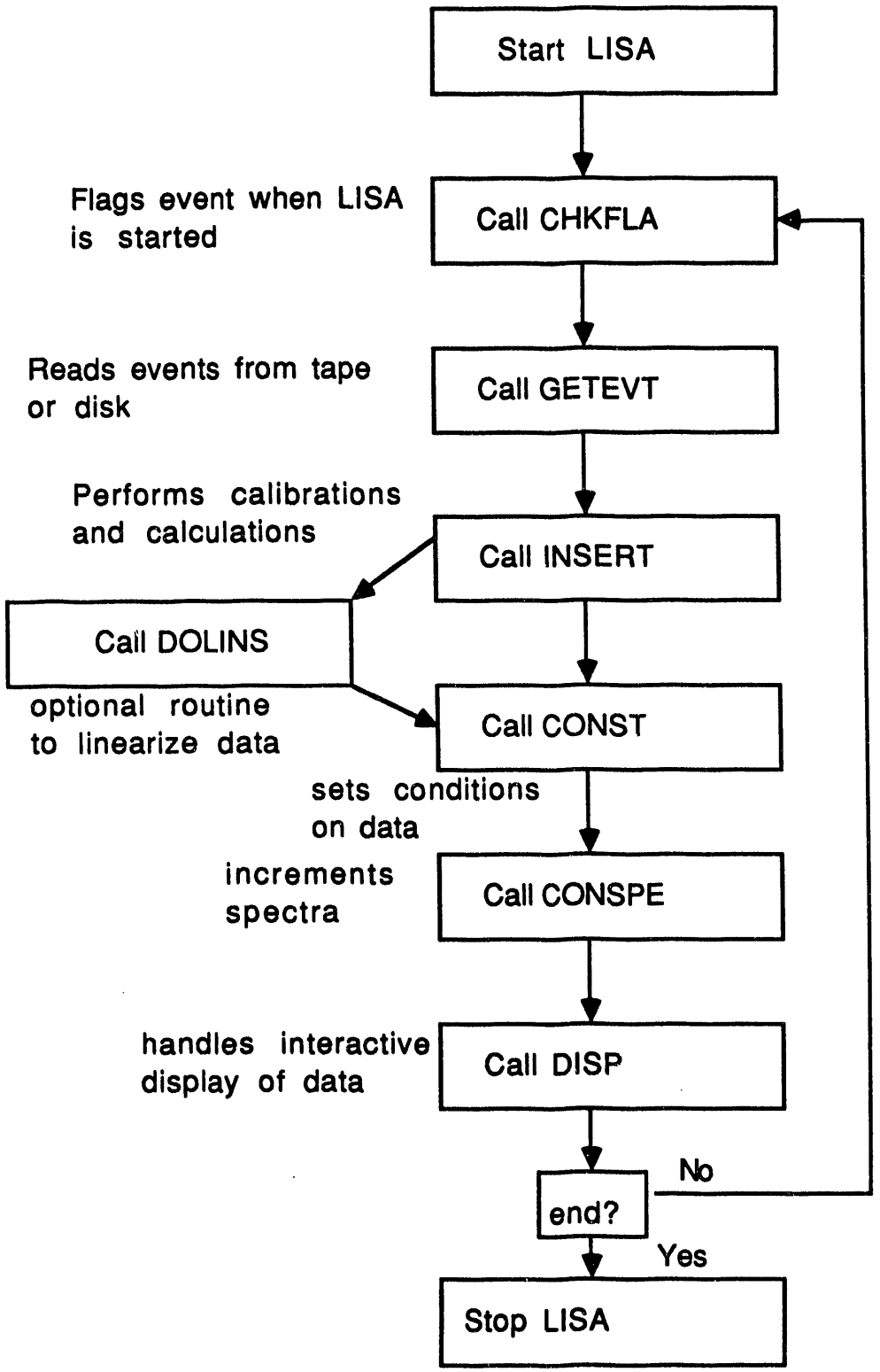
Start LISA
Flags event when LISA is started
Call CHKFLA
Reads events from tape or disk
Call GETEVT
Performs calibrations and calculations
Call INSERT
Call DOLINS
optional routine to linearize data
Call CONST
sets conditions on data
increments spectra
Call CONSPE
handles interactive display of data
Call DISP
No
end?
Yes
Stop LISA

REFERENCES

ADO91 A. Adorno, A. Bonasera, M. Cavinato, M. Colonna, A. Cunsolo, G.C. DiLeo, M. DiToro, and F. Gulminelli, *Nucl. Phys.* **A529**, 565 (1991)

AIC88 J. Aichelin, G. Peilert, A. Bohnet, A. Rosenhauer, H. Stocker, and W. Greiner, *Phys. Rev* **C37**, 2451 (1988).

BAU92 W. Bauer, G.F. Bertsch, and H. Schulz, preprint MSUCL-840, 1992.

BER83 G. Bertsch and P.J. Siemens, *Phys. Lett* **126B**, 9 (1983).

BLU91 Y. Blumenfeld, N. Colonna, P. Roussel-Chomaz, D.N. Delis, K. Hanold,J.C. Meng, G.F. Peaslee, Q.C. Sui, G.J. Wozniak, L.G. Moretto, B. Libby, A.C. Mignerey, G. Guarino, N. Santoruvo, and I. Iori, *Phys. Rev. Lett.* **66**, 576 (1991).

BON85 J.P. Bondorf, R. Donangelo, I.N. Mishutin, and H. Schulz, *Nucl. Phys.* **A444**, 460 (1985).

BON89 A. Bonasera, G.F. Burgio, and M. DiToro, *Phys. Lett.* **221B**, 233 (1989).

BON90 A. Bonasera, M. Colonna, M. DiToro, F. Gulminelli, and H.H. Wolter, *Phys. Lett.* **244B**, 169 (1990).

BOR88 B. Borderie, M. Montoya, M.F. Rivet, D. Jouan, C. Cabot, H. Fuchs, D. Gardes, H. Gauvin, D. Jacquet, and F. Monnet, *Phys. Lett* **205B**, 26 (1988).

BOU88 R. Bougault, F. Delaunay, A. Genoux-Lubain, C. LeBrun, J.F. Lecolley, F. Lefebvres, M. Louvel, J.C. Steckmeyer, J.C. Adloff,

B. Bilwes, R. Bilwes, M. Glaser, G. Rudolf, F. Scheibling, L. Stuttge, and J.L. Ferrero, *Nucl. Phys.* **A488**, 255c, (1988).

BOU89 R. Bougault, J. Colin, F. Delaunay, A. Genoux-Lubain, A. Hafjani, C. LeBrun, J.F. Lecolley, M. Louvel, and J.C. Steckmeyer, *Phys. Lett.* **232B**, 291 (1989).

BOW87 D.R. Bowman, W.L. Kehoe, R.J. Charity, M.A. Mcmahan, A. Moroni, A. Bracco, S. Bradley, I. Iori, R.J. McDonald, A.C. Mignerey, L.G. Moretto, M.N. Namboodiri, and G.J. Wozniak, *Phys. Lett.* **189B**, 282 (1987).

BOW89 D.R. Bowman, Ph.D. thesis, Lawrence Berkeley Laboratory Report LBL-27691 (1989).

BOW91a D.R. Bowman, G.F. Peaslee, R.T. DeSouza, N. Carlin, C.K. Gelbke, W.G. Gong, Y.D. Kim, M.A. Lisa, W.G. Lynch, L. Phair, M.B. Tsang, C. Williams, N. Colonna, K. Hanold, M.A. McMahan, G.J. Wozniak, L.G. Moretto, and W.A. Friedman, *Phys. Rev. Lett.* **67**, 1527 (1991).

BOW91b D.R. Bowman, G.F. Peaslee, N. Colonna, R.J. Charity, M.A. McMahan, D.Delis, H. Han, K. Jing, G.J. Wozniak, L.G. Moretto, W.L. Kehoe, B. Libby, A.C. Mignerey, A. Moroni, S. Angius, I. Iori, A. Pantaleo, and G. Guarino, *Nucl. Phys.* **A523**, 386 (1991).

BOW92a D.R. Bowman, private communication (1992).

BOW92b D.R. Bowman, C.M. Mader, G.F. Peaslee, W. Bauer, N. Carlin, R.T. DeSouza, C.K. Gelbke, W.G. Gong, Y.D. Kim, M.A. Lisa, W.G. Lynch, L. Phair, M.B. Tsang, C. Williams, N. Colonna, K. Hanold, M.A. McMahan, G.J. Wozniak, L.G. Moretto, and W.A. Friedman, preprint MSUCL-850 (1992).

CAR58 A.A. Caretto, J. Hudis, and G. Friedlander, *Phys. Rev.* **110**, 1130 (1958)

CAS89 C. Casey, W. Loveland, Z. Zhu, L. Sihver, K. Aleklett, and G.T. Seaborg, *Phys. Rev.* **C40**, 1244 (1989).

CEB90 D.A. Cebra, S. Howden, J. Karn, A. Nadasen, C.A. Ogilvie, A. VanderMolen, G.D. Westfall, W.K. Wilson, J.S. Winfield, and E. Norbeck, *Phys. Rev. Lett.* **64**, 2246 (1990).

CHA88a R.J. Charity, D.R. Bowman, Z.H. Liu, R.J. McDonald, M.A. McMahan, G.J. Wozniak, L.G. Moretto, S. Bradley, W.L. Kehoe, and A.C. Mignerey, *Nucl. Phys.* **A476**, 516 (1988).

CHA88b R.J. Charity, M.A. McMahan, G.J. Wozniak, R.J. McDonald, L.G. Moretto, D.G. Sarantides, L.G. Sobotka, G. Guarino, A. Pantaleo, L. Fiore, A. Gobbi, and K.D. Hildebrand, *Nucl. Phys.* **A483**, 371 (1988).

COL89 N. Colonna, R.J. Charity, D.R. Bowman, M.A. McMahan, G.J. Wozniak, G. Guarino, A. Pantaleo, L. Fiore, A. Gobbi, and K.D. Hildebrand, *Phys. Lett.* **62B**, 1833 (1989).

COL90 N. Colonna, private communication (1990).

COL91 M. Colonna, P. Roussel-Chomaz, N. Colonna, M. DiToro, L.G. Moretto, and G.J. Wozniak, Lawrence Berkeley Laboratory preprint LBL-30810 (1991).

CUM64 J.B. Cumming, S. Katcoff, N.T. Porile, S. Tanaka, and A. Wyttenbach, *Phys. Rev.* **134**, B1262 (1964).

DES87 J. Desbois, R. Boisgard, C. Ngo, and J. Nemeth, *Z. Phys.***A328**, 101 (1987).

FRI90 W.A. Friedman, *Phys. Rev.* **C42**, 667 (1990).

GEL87 C.K. Gelbke and D.H. Boal, *Prog. Part. and Nucl. Phys.* **19**, 33 (1987).

GRE82 C. Gregoire, C. Ngo, and B. Remaud, *Nucl. Phys.* **A383**, 392 (1982).

GRE85a C. Gregoire, Invited talk given at the Topical Meeting on the Phase Space Approach to Nuclear Dynamics, Trieste, Italy (1985).

GRE85b C. Gregoire, B. Remaud, F. Sebille, L. Vinet, and Y. Raffray, *Nucl. Phys.* **A436**, 365 (1985).

GRE87 C. Gregoire, B. Remaud, F. Sebille, L. Vinet, and Y. Raffray, *Nucl. Phys.* **A465**, 317 (1987).

GRO88 D.H.E. Gross, *Phys. Lett.* **203B**, 26 (1988).

GRO92 D.H.E. Gross, B.A. Li, and A.R. DeAngelis, Hahn-Meitner Institute preprint (1992).

HAG92 K. Hagel, M. Gonin, R. Wada, J.B. Natowitz, B.H. Sa, Y. Lou, M. Gui, D. Utley, G. Nebbia, D. Fabris, G. Prete, J. Ruiz, D. Drain, B. Chambon, B. Cheynis, D. Guinet, X.C. Hu, A. Demeyer, C. Pastor, A. Giorni, A. Lleres, R. Stassi, J.B. Viano, and P. Gonthier, *Phys. Rev. Lett.* **68**, 2141 (1992).

HAR88 C. Hartnack, H. Stocker, and W. Greiner, *Phys. Lett.* **215B**, 33 (1988)

HIN89 D.J. Hinde, D. Hilscher, and H. Rossner, *Nucl. Phys.* **A502**, 497c (1989).

HYD71 E.K. Hyde, G.W. Butler, and A.M. Poskanzer, *Phys. Rev.* **C4**, 1759 (1971).

JAC83 B.V. Jacak, G.D. Westfall, C.K. Gelbke, L.H. Harwood, W.G. Lynch, D.K. Scott, H. Stoker, M.B. Tsang, and T.J.M. Symons, *Phys. Rev. Lett.* **51**, 1846 (1983).

JAC85 B.V. Jacak, D. Fox, and G.D. Westfall, *Phys. Rev.* **C31**, 704 (1985).

KAU70 S.B. Kaufman, B.D. Wikins, M.J. Fluss, and E.B. Steinberg, *Nucl. Instt. and Meth.* **82**, 117 (1970).

KAU74 S.B. Kaufman, E.B. Steinberg, B.D. Wikins, J. Unik, A.J. Gorski, and M.J. Fluss, *Nucl. Instr. and Meth.* **115**, 47 (1974).

KEH89 W.L. Kehoe, University of Maryland Ph.D. thesis (1989).

KEH92 W.L. Kehoe, A.C. Mignerey, A. Moroni, I. Iori, G.F. Peaslee, N. Colonna, K. Hanold, D.R. Bowman, L.G. Moretto, M.A. McMahan, J.T. Walton, and G.J. Wozniak, *Nucl. Instr. and Meth.* **A311**, 258 (1992).

KIM89 Y.D. Kim, M.B. Tsang, C.K. Gelbke, W.G. Lynch, N. Carlin, Z. Chen, R. Fox, W.G. Gong, T. Murakami, T.K. Nayak, R.M. Ronningen, H.M. Zhu, W. Bauer, L.G. Sobotka, D. Stracener, D.G. Sarantides, Z. Majka, V. Abenante, and H.Griffin, *Phys. Rev. Lett.* **63**, 494 (1989).

KIM91 Y.D. Kim, R.T. DeSouza, D.R. Bowman, N. Carlin, C.K. Gelbke, W.G. Gong, W.G. Lynch, L. Phair, M. B. Tsang, F. Zhu, S. Pratt, *Phys. Rev. Lett.* **67**, 14 (1991).

LER90 S. Leray, C. Ngo, M.E. Spina, B. Remaud, and F. Sebille, *Nucl. Phys.* **A511**, 414 (1990).

LEV85 S. Levit and P. Bonche, *Nucl. Phys.* **A437**, 426 (1985).

LOP84 J.A. Lopez and P.J. Siemens, *Nucl. Phys.* **A431**, 728 (1984).

LOT92 B. Lott, S.P. Baldwin, B.M. Szabo, B.M. Quednau, W.U. Schroder, J. Toke, L.G. Sobotka, J. Barreto, R.J. Charity, L. Gallamore, D.G. Sarantides, D.W. Stracener, and R.T. DeSouza, *Phys. Rev. Lett.* **68**, 3141 (1992).

LUT86 K. Lutzenkirchen, J.V. Kratz, G. Wirth, W. Bruchle, K. Summere, R. Lucas, J. Poitou, and C. Gregoire, *Nucl. Phys.* **A452**, 351 (1986).

MIG92 A.C. Mignerey, Annual Progress Report, (1992).

MOR75 L.G. Moretto, *Nucl. Phys.* **A247**, 211 (1975).

MOR88 L.G. Moretto and G.J. Wozniak, *Prog. Part. and Nucl. Phys.* **21**, 401 (1988).

MOR92 L.G. Moretto, K. Tso, N. Colonna, and G.J. Wozniak, Lawrence Berkeley Laboratory preprint LBL-31812 (1992).

NEU84 H. Neunzert, Lecture Notes in Mathematics 1984, ed. by A. Dold and B. Eckman; Springer-Verlag: Berlin, 1984; p. 60.

PAN84 A.D. Panagioutou, M.W. Curtin, H. Toki, D.K. Scott, and P.J. Siemens, *Phys. Rev. Lett.* **52**, 496 (1984).

PEA90 G.F. Peaslee, L.G. Moretto, and G.J. Wozniak, Lawrence Berkeley Laboratory preprint LBL-29014 (1990).

PI91 M. Pi, E. Suraud, and P. Schuck, *Nucl. Phys.* **A524**, 537 (1991).

POS71 A.M. Poskanzer, G.W. Butler, and E.K. Hyde, *Phys. Rev.* **C3**, 882 (1971).

REM85a B. Remaud, F. Sebille, C. Gregoire, and L. Vinet, *J. de Physique* **C2**, 195 (1985).

REM85b B. Remaud, F. Sebille, C. Gregoire, L.Vinet, and Y. Raffray, *Nucl. Phys.* **A447**, 555c (1985).

REM88 B. Remaud, C. Gregoire, F. Sebille, and P. Schuck, *Nucl. Phys.* **A488**, 423c (1985).

ROU92 P. Roussel-Chomaz, N. Colonna, Y. Blumenfeld, B. Libby, G.F. Peaslee, D.N. Delis, K. Hanold, M.A. McMahan, J.C. Meng, Q.C. Sui, G.J. Wozniak, L.G. Moretto, H. Madani, A.A. Masrchetti,

A.C. Mignerey, G. Guarino, N. Santoruvo, I. Iori, S. Bradley, Lawrence Berkeley Laboratory preprint LBL-32433

SEB89 F. Sebille, G. Royer, C. Gregoire, B. Remaud, and P. Schuck, *Nucl. Phys.* **A501**, 137 (1989).

SUG54 N. Sugarman, R.B. Duffield, G. Friedlander, and J.M. Miller, *Phys. Rev.* **95**, 1704 (1954).

SUR89 E. Suraud, M. Pi, P. Schuck, B. Remaud, F. Sebille, C. Gregoire, and F. Saint-Laurent, *Phys. Lett.* **229B**, 359 (1989).

TOK85 J. Toke, R. Bock, G.X. Dai, A. Gobbi, S. Gralla, K.D. Hildebrand, J. Kuzminski, W.F.J. Muller, A. Olmi, H. Stelzer, B.B. Back, and S. Bjornholm, *Nucl. Phys.* **A440**, 327 (1985).

TRO89 R. Trockel, K.D. Hildebrand, U. Lynen, W.F.J. Muller, H.J. Rabe, H. Sann, H. Stelzer, W. Trautmann, R. Wada, E. Eckert, P. Kreutz, A. Kuhmichel, J. Pochadzalla, and D. Pelte, *Phys. Rev.* **C39**, 729 (1989).

WAL90 J.T. Walton, H.A. Sommer, G.J. Wozniak, G.F. Peaslee, D.R. Bowman, W.L. Kehoe, and A. Moroni, *IEEE Trans. Nucl. Sci.* **NS-37**. 1578 (1990)

WES76 G.D. Westfall, J. Gosset, P.J. Johansen, A.M. Poskanzer, W.G. Meyer, H.H. Gutbrod, A. Sandoval, and R. Stock, *Phys. Rev. Lett.* **37**, 1202 (1976).

WES85 G.D. Westfall, J.E. Yurkon, J. van der Plicht, Z.M. Koenig, B.V. Jacak, R. Fox, G.M. Crowley, M.R. Maier, B.E. Hasselquist, R.S. Tickle, and D. Horn, *Nucl. Instr. and Meth.* **A238**, 347 (1985).

WOL56 R. Wolfgang, E.W. Baker, A.A. Caretto, J.B. Cumming, G. Friedlander, and J. Hudis, *Phys. Rev.* **103**, 394 (1956).

YEN91 S.J. Yenello, E.C. Pollacco, K. Kwiatkowski, C. Volant, R. Dayras, Y. Cassagnou, R. Legrain, E. Norbeck, V.E. Viola, J.L. Wile, and N.R. Yoder, *Phys. Rev. Lett.* **67**, 671 (1991).

END

DATE
FILMED
6/18/93